

Spring 1998

Thin-Layer Prestressed Composite Ferroelectric Driver and Sensor Characterization with Application to Separation Flow Control

Karla M. Mossi
Old Dominion University

Follow this and additional works at: https://digitalcommons.odu.edu/mae_etds

 Part of the [Mechanical Engineering Commons](#)

Recommended Citation

Mossi, Karla M.. "Thin-Layer Prestressed Composite Ferroelectric Driver and Sensor Characterization with Application to Separation Flow Control" (1998). Doctor of Philosophy (PhD), dissertation, Mechanical Engineering, Old Dominion University, DOI: 10.25777/g85r-r918
https://digitalcommons.odu.edu/mae_etds/152

This Dissertation is brought to you for free and open access by the Mechanical & Aerospace Engineering at ODU Digital Commons. It has been accepted for inclusion in Mechanical & Aerospace Engineering Theses & Dissertations by an authorized administrator of ODU Digital Commons. For more information, please contact digitalcommons@odu.edu.

**THIN-LAYER PRE-STRESSED COMPOSITE FERROELECTRIC DRIVER
AND SENSOR CHARACTERIZATION WITH APPLICATION TO
SEPARATION FLOW CONTROL**

by

Karla M. Mossi

B.S., May 1987, Universidad Nacional Autonoma de Honduras
M.S., May 1992, Old Dominion University

A Dissertation submitted to the Faculty of
Old Dominion University in Partial Fulfillment
of the Requirements for the Degree of

DOCTOR OF PHILOSOPHY


MECHANICAL ENGINEERING

OLD DOMINION UNIVERSITY

May 1998

Approved by:



 Gregory V. Selby (Director)

A. Sidney, Roberts, Jr. (Member)

Linda L. Vahala (Member)

Robert G. Bryant (Member)

Jen-Kuang Huang (Member)

ABSTRACT

THIN-LAYER COMPOSITE FERROELECTRIC DRIVER AND SENSOR CHARACTERIZATION WITH APPLICATION TO SEPARATION FLOW CONTROL

Karla M. Mossi

Old Dominion University, 1998

Director: Dr. Gregory V. Selby

Experiments were conducted in two different stages — general piezoelectric actuator characterization and flow separation control applications. The characterization of the piezoelectric devices was performed in several stages, due to the many variables that affect performance. The first stage of the characterization consisted of tests conducted on 13 different THUNDER™ (thin-layer composite unimorph ferroelectric driver and sensor) configurations. These configurations consisted of a combination of 1, 3, 5, 7, and 9 layers of 25 μ thick aluminum as backing material, with and without a top layer of 25 μ aluminum. All of these configurations used the same piezoelectric ceramic wafer (PZT-5A) with dimensions of 5.1 x 3.8 x 0.018 cm. The above configurations were tested at two stages of the manufacturing process: before and after re-poling. The parameters measured included frequency, driving voltage, displacement, capacitance, and radius of curvature. An optical sensor recorded the displacement at a fixed voltage (100-400 Vpp) over a predetermined frequency range (1-1000 Hz). These displacement measurements were performed using a computer that controlled the process of activating and measuring the

displacement of the device. A parameter β was defined which can be used to predict which configuration will produce maximum displacement for a partially constrained device. The second phase of the characterization was conducted using two different types of piezoelectric devices. Actuators were made with PZT wafers of 3.8 x 1.9 x 0.025cm, and 3.8 x 1.3 x 0.02 cm. These models consisted of a combination of top layers of 1 mil (0.0254 mm) aluminum and brass, and bottom layers of stainless steel, aluminum, and brass of varying thickness [3, 4, 5, 7, 9, 10 mil (0.076, 0.102, 0.127, 0.178, 0.229, 0.254 mm)]. Displacement was measured for 12 configurations at 1 Hz and 200 Vpp under loads of 0, 0.2, 0.4, 0.5, and 1.0 Kg using an optical sensor. Again the parameter β was used to predict the configuration with the maximum displacement for a partially constrained device, as well as with the device under load. Finally, a THUNDER™-based actuator was used to deploy submerged vane-type vortex generators which were used to control turbulent separated flow associated with flow over a backward-facing ramp. Effectiveness of the vortex generator array was demonstrated using wall pressure measurements, velocity surveys, and smoke-oil flow visualization photographs which showed that the nominal flow separation region was reduced by 35-40%.

ACKNOWLEDGMENTS

This work was supported and encouraged by many different people. I would like to thank my advisor, Dr. Greg V. Selby for his guidance and support. Also, my Ph.D. guidance committee for their helpful comments, Dr. Jen-Kuang Huang, Dr. Linda L. Vahala, Dr. Sidney Roberts, and Dr. Robert G. Bryant. Special thanks to Dr. Bryant, inventor of THUNDER™, for his invaluable guidance, dedication, and patience with this research.

I am very thankful to Brad Face, and Chris Busacco of the FACE® International Companies for generously allowing me the full use of the laboratory and equipment. I am especially grateful to Sam Face for building a pressure rake, for his enthusiasm, and for his confidence in this research. Thanks too, to Richard Bishop for proofreading this dissertation. I would also like to thank *everyone* at FACE® International for their recent help.

Special thanks are extended to Mr. Tim Bryant for his invaluable expertise, and incalculable assistance. Besides building numerous probes and instrumentation, he was responsible for securing a wind tunnel appropriate for this research. Tim recommended and located specialized hardware, and created many of the technical drawings included in this work. Finally, Tim proposed model construction methods, and assisted with the development of ideas to test flow visualization.

For my friends Lisa Scott, Scott Staylor, and Dr. Ali Kheireddine, for their technical input, moral support, and continuing encouragement, I am very grateful. Most of all I wish to thank my family who patiently waited for me to finally finish school and pushed me to go ahead when it was necessary. *Gracias Lolilos.*

Part of this work was performed under memorandum of agreement SAA No.326, with NASA Langley Research Center.

TABLE OF CONTENTS

Abstract	i
Acknowledgments	iii
Table of Contents	iv
List of Tables	vi
List of Figures	viii
Nomenclature	xvi
CHAPTER I. INTRODUCTION	1
1.1 General Background	1
1.2 Smart materials	3
1.2.1 Magnetostrictive Alloys	4
1.2.2 Shape Memory Alloys	5
1.2.3 Electrorheological Fluids	5
1.2.4 Piezoelectric Materials and Polymers	6
1.2.5 Unimorphs [®] and Bimorphs [®]	8
1.2.6 MOONIES	8
1.2.7 RAINBOW [®]	9
1.2.7 THUNDER [™]	9
1.3 Flow Separation Control	10
1.3.1 Vortex Generator Jets	12
1.3.2 Large-Eddy Breakup Devices at Angle of Attack	13
1.3.3 Submerged Vortex Generators	13
1.4 Research Objectives	14
CHAPTER II. EXPERIMENTAL SETUP	16
2.1 NASA Langley Research Center Tests	16
2.1.1 Displacement Measurements	18
2.1.2 Capacitance Measurements	19
2.2 Experimental Setup at Face International Corporation	19
2.2.1 Force Measurements	20
2.2.2 Life Cycling Measurements	20
2.3 Wind-Tunnel Setup	21
2.3.1 Model Description	23
CHAPTER III. THUNDER [™] CHARACTERIZATION	43
3.1 General	43
3.1.2 Displacement-Frequency Profiles	44
3.1.3 Capacitance Measurements	46
3.1.4 Displacement-Voltage Profiles	47
3.1.5 Hysteresis	48
3.1.6 Summary Graphs	48

3.2 Specialized Designs	49
3.2.1 Load-Displacement Profiles	50
3.2.2 Impedance Measurements	50
3.3.3 Life-Cycle Tests	51
CHAPTER IV. THEORETICAL FORMULATIONS	133
CHAPTER V. APPLICATIONS TO FLOW CONTROL	148
5.1 General	148
5.2 Boundary - Layer Parameters	149
5.3 Submerged Vane - Type Vortex Generators	152
5.4 Pressure Distribution	154
5.5 Flow Visualization Results	155
CHAPTER VI. SUMMARY, CONCLUSIONS, AND RECOMMENDATIONS ...	167
REFERENCES	170
APPENDIX A THUNDER™ Manufacturing Process	178
APPENDIX B Equivalent Circuit	182

LIST OF TABLES

<u>Table</u>	<u>Page</u>
3.1 Test Configurations	52
3.2 Performance at 1, 10, and 100 Hz at 200Vpp for All Configurations before Re-Poling	53
3.3 Performance at 1, 10, and 100 Hz at 200Vpp for All Configurations after Re-Poling	54
3.4 Ceramics for Model Types I and II	55
3.5 Cases Studied with Model Type I Ceramics	55
3.6 Cases Studied with Model Type II Ceramics	56
3.7 Coefficient for Exponential Fit for Devices under Load	57
3.8 Equivalent Circuit Parameters for all Cases	58
4.1 Location of Neutral Axis for x/Al Configurations Using Theoretical Thickness	140
4.2 Location of Neutral Axis for x/Al Configurations Using Measured Thickness	140
4.3 Location of Neutral Axis for Al/Al Configurations Using Theoretical Thickness	141
4.4 Location of Neutral Axis for Al/Al Configurations Using Measured Thickness	141
4.5 Radius of Curvature for all Configurations before and after Re-Poling	142
4.6 Location of Neutral Axis for Cases 1a thru 7a	143
4.7 Location of Neutral Axis for Cases 1b thru 5b	143

LIST OF FIGURES

<u>Figure</u>	<u>Page</u>	
2.1	Calibration Curve for the Optic Sensor Measurement Probe (Taken From: Ångstrom Resolver Series Dual Channel Models 201, Opto Acoustic Sensors, Inc.)	24
2.2	Schematic of the Operating Principle for a Basic 7-Fiber Optic Lever (Taken From: Ångstrom Resolver Series Dual Channel Models 201, Opto Acoustic Sensors, Inc.)	25
2.3	Experimental Setup Control Loop	26
2.4	Monitor Display from LabVIEW™ Poling Program	27
2.5	Monitor Display from LabVIEW™ Piezoelectric Displacement Measurement Program	28
2.6	Schematic of the Experimental Setup for Displacement Measurements	29
2.7	Schematic of Data Acquisition Setup	30
2.8	Monitor Display from LabVIEW™ Program for Controlling Displacement Measurements at Varying Frequency	31
2.9	Monitor Display from LabVIEW™ Program for Impedance Analysis	32
2.10	Structure Used to Attach Loads to THUNDER™ Devices	33
2.11	THUNDER Actuator under a Load, W, in a Pin-Free Configuration	34
2.12	Open-Loop Subsonic Wind Tunnel	35
2.13	Wind Tunnel Test Section (55.8 x 5.08 x 15.2 cm)	36
2.14	Wind Tunnel Drive System	37

Figure	Page
2.15 Flow-Visualization System	38
2.16 Illumination System	39
2.17 Schematic of Setup for Wind Tunnel Measurements	40
2.18 Two-Dimensional Backward-Facing Ramp	41
2.19 Monitor Display from LabVIEW™ Program to Control Wind Tunnel Measurements	42
3.1 Displacement vs. Frequency for Varying Voltage Levels for Configuration 0/1-x/Al, with No Re-Poling	59
3.2 Displacement vs. Frequency for Varying Voltage Levels for Configuration 0/3-x/Al, with No Re-Poling	60
3.3 Displacement vs. Frequency for Varying Voltage Levels for Configuration 0/5-x/Al, with No Re-Poling	61
3.4 Displacement vs. Frequency for Varying Voltage Levels for Configuration 0/7-x/Al, with No Re-Poling	62
3.5 Displacement vs. Frequency for Varying Voltage Levels for Configuration 0/9-x/Al, with No Re-Poling	63
3.6 Displacement vs. Frequency for Varying Voltage Levels for Configuration 1/3-Al/Al, with No Re-Poling	64
3.7 Displacement vs. Frequency for Varying Voltage Levels for Configuration 1/5-Al/Al, with No Re-Poling	65
3.8 Displacement vs. Frequency for Varying Voltage Levels for Configuration 1/7-Al/Al, with No Re-Poling	66

<u>Figure</u>	<u>Page</u>
3.9 Displacement vs. Frequency for Varying Voltage Levels for Configuration 1/9-Al/Al, with No Re-Poling	67
3.10 Displacement vs. Frequency for Varying Voltage Levels for Configuration 0/1-x/Al-5, with No Re-Poling	68
3.11 Displacement vs. Frequency for Varying Voltage Levels for Configuration 0/1-x/SS-1, with No Re-Poling	69
3.12 Displacement vs. Frequency for Varying Voltage Levels for Configuration 0/1-x/SS-3, with No Re-Poling	70
3.13 Displacement vs. Frequency for Varying Voltage Levels for Configuration 0/1-x/BeCu-2, with No Re-Poling	71
3.14 Displacement of x/Al Configurations vs. Theoretical Total Bottom-Layer Thickness at 1, 10, and 100 Hz Before Re-Poling.	72
3.15 Displacement of Al/Al Configurations vs. Theoretical Total Bottom-Layer Thickness at 1, 10, and 100 Hz before Re-Poling.	72
3.16 Probable Trends in Displacement vs. Number of Backing Layers before Re-Poling	73
3.17 Displacement vs. Frequency for Varying Voltage Levels for Configuration 0/3-x/Al, after Re-Poling	74
3.18 Displacement vs. Frequency for Varying Voltage Levels for Configuration 0/5-x/Al, after Re-Poling	75
3.19 Displacement vs. Frequency for Varying Voltage Levels for Configuration 0/7-x/Al, after Re-Poling	76

<u>Figure</u>	<u>Page</u>
3.20 Displacement vs. Frequency for Varying Voltage Levels for Configuration 0/9-x/Al, after Re-Poling	77
3.21 Displacement vs. Frequency for Varying Voltage Levels for Configuration 1/3-Al/Al, after Re-Poling	78
3.22 Displacement vs. Frequency for Varying Voltage Levels for Configuration 1/5-Al/Al, after Re-Poling	79
3.23 Displacement vs. Frequency for Varying Voltage Levels for Configuration 1/7-Al/Al, after Re-Poling	80
3.24 Displacement vs. Frequency for Varying Voltage Levels for Configuration 1/9-Al/Al, after Re-Poling	81
3.25 Displacement vs. Frequency for Varying Voltage Levels for Configuration 0/1-x/SS-1, after Re-Poling	82
3.26 Displacement vs. Frequency for Varying Voltage Levels for Configuration 0/1-x/SS-3, after Re-Poling	83
3.27 Displacement vs. Frequency for Varying Voltage Levels for Configuration 0/1-x/BeCu-2, after Re-Poling	84
3.28 Displacement of x/Al Configurations vs. Theoretical Total Bottom-Layer Thickness at 1, 10, and 100 Hz after Re-Poling.....	85
3.29 Displacement of Al/Al Configurations vs. Theoretical Total Bottom-Layer Thickness at 1, 10, and 100 Hz after Re-Poling.....	85
3.30 Performance of re-Poled vs. non re-Poled Devices at an Applied Voltage of 200Vpp.	86

Figure	Page
3.31 Capacitance vs. Frequency for Configuration 0/1-x/Al at Different Processing Stages	87
3.32 Capacitance vs. Frequency for Configuration 0/3-x/Al at Different Processing Stages	88
3.33 Capacitance vs. Frequency for Configuration 0/5-x/Al at Different Processing Stages	89
3.34 Capacitance vs. Frequency for Configuration 0/9-x/Al at Different Processing Stages	90
3.35 Capacitance vs. Frequency for Configuration 0/1-x/SS-3 at Different Processing Stages	91
3.36 Capacitance vs. Frequency for Configuration 0/1-x/BeCu-2 at Different Processing Stages	92
3.37 Capacitance vs. Frequency for Al/Al Configurations after Re-Poling	93
3.38 Displacement vs. Voltage at 1 Hz for Configuration 0/1-x/Al	94
3.39 Displacement vs. Voltage at 1 Hz for Configuration 0/3-x/Al	95
3.40 Displacement vs. Voltage at 1 Hz for Configuration 0/5-x/Al	96
3.41 Displacement vs. Voltage at 1 Hz for Configuration 0/7-x/Al	97
3.42 Displacement vs. Voltage at 1 Hz for Configuration 0/9-x/Al	98
3.43 Displacement vs. Voltage at 1 Hz for x/Al Configurations	99
3.44 Displacement vs. Voltage at 1 Hz for Configuration 0/1-x/SS, 0/1-x/SS-3, and x/BeCu-2	100

<u>Figure</u>	<u>Page</u>
3.45 Driving Voltage Waveform and Displacement Waveform for Configuration 0/7-x/Al at 1 Hz.	101
3.46 Hysteresis Curve for Configuration 0/7-x/Al at 1 Hz	101
3.47 Driving Voltage Waveform and Displacement Waveform for Configuration 0/7-x/Al at 350 Hz.	102
3.48 Hysteresis Curve for Configuration 0/7-x/Al at 350 Hz	102
3.49 Summary of the Performance of x/Al Configurations at 200 Vpp with No Re-Poling	103
3.50 Summary of the Performance x/Al Configurations At 200 Vpp after Re-Poling	104
3.51 Summary of the Performance x/Al Configurations with SS, Al, and BeCu at 200Vpp, No Re-Poling	105
3.52 Summary of the Performance x/Al Configurations with SS, Al, and BeCu at 200Vpp, after Re-Poling	106
3.53 Load Performance of THUNDER Type I	107
3.54 Load Performance of THUNDER Type II	108
3.55 Load vs Displacement Performance for Case 1a	109
3.56 Load vs Displacement Performance for Case 2a	110
3.57 Load vs Displacement Performance for Case 3a	111
3.58 Load vs Displacement Performance for Case 4a	112
3.59 Load vs Displacement Performance for Case 5a	113
3.60 Load vs Displacement Performance for Case 6a	114

<u>Figure</u>	<u>Page</u>
3.61 Load vs Displacement Performance for Case 7a	115
3.62 Load vs Displacement Performance for Case 1b	116
3.63 Load vs Displacement Performance for Case 2b	117
3.64 Load vs Displacement Performance for Case 3b	118
3.65 Load vs Displacement Performance for Case 4b	119
3.66 Load vs Displacement Performance for Case 5b	120
3.67 Impedance and Phase angle vs Frequency for Case 1a	121
3.68 Impedance and Phase angle vs Frequency for Case 2a	122
3.69 Impedance and Phase angle vs Frequency for Case 3a	123
3.70 Impedance and Phase angle vs Frequency for Case 4a	124
3.71 Impedance and Phase angle vs Frequency for Case 5a	125
3.72 Impedance and Phase angle vs Frequency for Case 6a	126
3.73 Impedance and Phase angle vs Frequency for Case 7a	127
3.74 Impedance and Phase angle vs Frequency for Case 1b	128
3.75 Impedance and Phase angle vs Frequency for Case 2b	129
3.76 Impedance and Phase angle vs Frequency for Case 3b	130
3.77 Impedance and Phase angle vs Frequency for Case 4b	131
3.78 Impedance and Phase angle vs Frequency for Case 5b	132
4.1 Equivalent Cross-Sections for THUNDER Type I	146
4.2 Equivalent Cross-Sections for THUNDER Type II	147
5.1 Velocity Profile for Turbulent Flow Over a Flat Plate, $x/h=5.0$	157
5.2 Baseline Velocity Profiles for a Backward-Facing Ramp	158

<u>Figure</u>	<u>Page</u>
5.3 Baseline Boundary-Layer Parameters	159
5.4 Schematic of Submerged Vane-Type Vortex Generators	160
5.5 Velocity Profiles for a Backward-Facing Ramp with Deployed Vortex Generators	161
5.6 Boundary Layer Parameters for Deployed Vortex Generators	162
5.7 Boundary-Layer Shape Factor (Baseline and with Vortex Generators Deployed)	163
5.8 Wall Pressure Coefficient Distribution over a Backward-Facing Ramp (Baseline and with Vortex Generators Deployed)	164
5.9 Smoke-Oil Flow Visualization over a Backward-Facing Step (a) Baseline and (b) Vortex Generators Deployed	165
5.10 Modified Flow Visualization Photographs of Separated-Flow Region	166
5.11 Smoke-Oil Flow Visualization for Vortex Generators Oscillating at 12 Hz ...	167

NOMENCLATURE

C_p	pressure coefficient, $2(P - P_\infty)/\rho U_\infty^2$
h	ramp height (distance from the floor)
l	device chord (streamwise) length
P	pressure
P_∞	freestream static pressure
s	device spanwise width
u	local mean velocity in the x-direction
U_∞	freestream velocity
V_{pp}	peak-to-peak voltage
x	coordinate along the freestream direction with origin at the nose of the model
y	coordinate normal to the wall with origin at the surface
W	load
Greek Symbols	
α	active to inactive layer ratio
β	neutral axis location parameter
δ	boundary-layer thickness (based on $u/U_\infty = 0.99$)
δ^*	displacement thickness, $\int_0^\delta (1 - u/U_\infty) dy$
H	shape factor, $H = \delta^*/\theta$
η	device height (distance from wall)
θ	momentum thickness, $\int_0^\delta (u/U_\infty)(1 - u/U_\infty) dy$
λ	spanwise or lateral distance between each geometric cycle
ρ	density
ψ	device azimuthal angle (angle between the device axis and the freestream direction in a x-z plane)
Subscripts	
w	wall value
∞	freestream value

CHAPTER I

INTRODUCTION

1.1 General Background

The physics of fluid flows and consequently, the control of fluid flow, involves a wide variety of research areas and industries, including physics, biology, medicine, construction, manufacturing, aerospace, and others. For this reason, a multidisciplinary approach to fluid-flow problems is often necessary. Such approaches may find applications in any research area in the natural sciences and engineering which involves the control and analysis of fluid flow. In biology for example, the high-aspect-ratio propulsion system used by most of the fastest aquatic animals [1]¹ is suitable for analysis by airfoil theory. In medicine, "work in the physiological fluid dynamics needs very close and intimate collaboration between specialists in physiological science and specialists in the dynamics of fluids." [2] For instance, studies indicate that turbulent blood flow, possibly induced by flow separation, makes aneurysms (intercranial saccular aneurysm) self-aggravating. [2] Such studies form the research area known as biofluidmechanics and indicate the importance of flow control research and a wide range of potential applications.

In order to exert applicable control over a fluid system (or a structure), an adaptive control scheme using an adaptive structure may be necessary, and during the past few years a significant amount of research has been performed on the control of fluid and structural systems using smart sensors and actuators. [3, 4, 5, 6, 7, 8] Some of these systems can sense changes in their environment and respond accordingly. [9, 10] The field of smart structures

The journal model used on this dissertation was AIAA Journal.

and systems. These systems can sense and control their own behavior to achieve much higher levels of operational performance than conventional materials and structures.[11]

In particular, smart materials have been widely used in aerospace research. For instance, smart materials have been used in acoustic control (to make aircraft quieter), active damage control (for extending a wing structure's fatigue life), aircraft wings that stiffen in rough weather, flutter suppression, and vibration control.[6, 12, 13, 14]

Smart or intelligent structures are made with adaptive materials that can change their properties (i.e., stiffness, shape, etc.) through an external stimulus (such as electricity, heat, or a magnetic field).[15] These structures can be used as control systems or complete integrated structures containing embedded sensors, actuators, etc.[11] Therefore, adaptive materials can replace some functions presently performed by mechanical actuators. Such materials have the advantage over mechanical actuators in weight and volume, depending on the desired use. For example, the requirement of small cooling units with rotating fans, has resulted in the use of smart materials to create designs without moving mechanical parts.[12]

Some of these recent developments in smart materials and actuation mechanisms provide new approaches in health monitoring and methods of feedback control. Such developments promote the analysis, design, and development of controlled smart systems which are effective either as passive or active control systems as shown by many researchers.[12, 16, 17, 18, 19, 20]

Due to the advantages of smart actuators over mechanical parts, active or passive control of a system often becomes more feasible particularly in aerodynamic applications such as flow-separation control. Flow-separation control is important because separation

usually causes large energy losses [21] that affect airfoil, diffuser, and transportation systems performance.[22] For instance, excessive separation on wings and other lifting surfaces, may cause stalling, leading to catastrophic results.[23] Furthermore, non-aerodynamic surfaces on building structures produce flow separation on the upwind side of the building, and reattachment on the downwind side, creating a recirculation zone on the leeward side of the building with a high level of turbulence and low mean velocity. Consequently, several passive and active methods exist for the artificial prevention of flow separation, when it occurs.

A system which will effectively and efficiently control flow separation can often be designed using smart materials. Such a system can have significant advantages over traditional passive and active flow control systems. For this reason, a detailed review of the general characteristics of smart materials is important and is given below.

1.2 Smart Materials

There are several materials classified and tested as smart materials due to their unique physical properties and characteristics.[8] They have been used as a combination of sensor and actuator to control a system,[24] so that an electrical input can be converted into mechanical distortion. The ideal sensor would convert mechanical distortion directly into an electrical potential. Generally, a smart material is one that is not simply an actuator or a sensor, but functions as both, and senses a change and responds to that change in some manner. [25]

Piezoelectric layers, for example, bonded to the surface or manufactured and embedded into a flexible structural member can act as either control actuators or sensors.

One advantage is that the load transfer from the piezoelectric material to the host structure is enhanced and the surface of the structure is free of fragile components and connections. However, potential complications include electrical insulation and manufacturing of the actuators, sensors, and electrical leads into the laminate. The successful implementation of intelligent structures depends not only on the development of suitable actuators and sensors, but processors and control algorithms as well. Warkentin [26] studied the feasibility of embedded electronics for intelligent structures. He concluded that the processing components can also be surface-mounted or embedded, with both approaches having advantages and disadvantages.

Surface-bonded components would offer ease of access and maintenance, but would be easily damaged in service and would place functional demands on the structural surface that may conflict with existing requirements. Components embedded within the structure would provide better protection of the devices and simpler interconnections to the embedded actuators and sensors.

Some of the materials used to build smart systems are shape memory alloys(SMA), polymers, piezoelectric ceramics, magnetostrictive alloys, optical fibers, conductive polymers, and electrorheological fluids.[9] Piezoelectric materials and magnetostrictive materials are the "fast-twitch muscles of power" for short duration at high strain rates. Shape-memory alloys can transform heat into mechanical work.[9] A brief description of the most utilized materials is presented below.

1.2.1 Magnetostrictive Alloys

When a magnetostrictive material is magnetized, it changes shape which in turn introduces elastic strains in the material; e.g., Terfenol-D, Metglass, etc.[27, 28] Terfenol-D is the most commonly-known magnetostrictive material which is capable of strains up to 0.2%. Advantages over piezoelectric ceramics include reliability, stable material properties, ability to manufacture and flexibility. Disadvantages are that most magnetostrictive materials require large magnetic fields for actuation, and some of them (e.g., Terfenol-D) cannot be build into composites.[22] Applications include sonic actuators, active vibration control, geophysical exploration, and ultrasonics. [29]

1.2.2 Shape Memory Alloys

A shape memory alloy (SMA) is a material with the ability to recover its shape when activated by an external thermal stimulus. [22] William Buehler found that nickel-titanium alloy, called nitinol, held a special property. It remembered and returned to its original shape after being formed into a second shape and then heated. [30]

The SMAs are capable of directly transforming heat (produced by fluids, gases, or electricity) into mechanical work. Disadvantages of SMAs are large hysteresis and a low bandwidth during the cooling half-cycle. Advantages are high force output and high resistivity. [22]

1.2.3 Electrorheological Fluids

Electrorheological Fluids (ER) are actuator materials containing particles suspended in a non-conducting fluid. The fluid solidifies when exposed to an electric field. [9] The ER

fluids exhibit coupling between their fluid dynamic and electrical behavior. When exposed to an electrical field, their viscosity, damping capability and shear strength increase. [22]

Applications include aircraft that stiffen in rough weather, automotive shock absorbers, and marine hulls that flex to escape detection by enemy sonar. [9]

1.2.4 Piezoelectric Materials and Polymers

The label “smart” materials originated with the discovery called piezoelectricity made by Jacques and Pierre Curie in 1880. They discovered piezoelectricity in quartz and Rochelle salt where the piezoelectric effect is inherent to the material.[31]

There are various crystals that exhibit polar effects such as piezoelectricity, pyroelectricity, and ferroelectricity. Piezoelectric crystals become electrically polarized or undergo a change in polarization when subjected to stress. Pyroelectric crystals are spontaneously polarizable where a temperature change in these materials produces a change in polarization. A limited number of pyroelectric crystals can change the direction of spontaneous polarization by application of an electric field. Such materials are termed ferroelectric. Hence, all ferroelectric crystals are pyroelectric and all pyroelectric crystals are piezoelectric, but not vice versa. [26] Ferroelectricity is the presence of a spontaneous momentum on a crystal which can be changed in its orientation between two or more distinct crystallographic directions by the application of an external electric field. [25, 26]

Piezoelectricity can be induced, since for a piezoelectric interaction to exist, it is necessary that certain crystalline axes possess polarity [25]. Polarity can be induced in an otherwise isotropic polycrystal ceramics permanently, by the application of a strong electric field. This process is called *poling*.

Poling is analogous to magnetizing a ferrous metal, such as iron. Iron must be poled to become active; hence, piezoelectric ceramics are ferroelectrics. For piezoelectric materials, poling is accomplished by the application of a strong DC electric field to the electroded ceramic shape, generally in a fluid with high dielectric constant.[25] The stronger the field and the longer it is applied, the higher the degree of orientation and the stronger the piezoelectricity. This is valid only to a point in which any additional effect is not really noticeable. The magnitude of the strength of this effect depends strongly on material composition. Because of the different compositions among ceramics, poling conditions must be determined experimentally, making the discovery of the poling process one of the basic steps in the understanding of piezoelectricity in ceramics.[26]

Materials such as PVDF (poly-vinylidene fluoride) polymer, and PZT (lead zirconate titanate) can act as smart material actuators or sensors depending upon their polarity. [9]. The film product, poly-vinylidene fluoride polymer (PVDF), discovered by Kawai[32], is characterized by flexibility, light weight, and inexpensiveness. It has a higher voltage limit with lower stiffness and coupling coefficients than other materials mentioned above, and it is better used for sensor applications. PVDF materials are available in large sheets of thin film that are easy to shape into specific geometries to implement modal actuators and modal sensors for the control and sensing of flexible structures.[9, 33] Conversely, the discovery of a very strong and stable piezoelectric effect in PZT solid solutions constituted an advance of great practical importance, making lead zirconate titanate with various additives the most important group of piezoelectric materials.[34] Also, $\text{Pb}(\text{Zr}, \text{Ti})\text{O}_3$, lead zirconate titanate, is the most widely used piezoceramic in various solid solutions because of its large degree

of orientation and high spontaneous polarization, combined with high permanent polarization and high dielectric constant. [35]

Because of their unique properties, a variety of PZT materials have been developed to suit a wide range of signal transmission and reception requirements. [36] Among them are, Unimorphs[®], Bimorphs[®], RAINBOW[™] (Reduced And Internally Biased Oxide Wafers), Moonies, Stacks, and THUNDER[™] (THin layer composite UNimorph ferroelectric Driver and sensor).

1.2.5 Unimorphs[®] and Bimorphs[®]

These materials are defined by the number of piezoelectric ceramic plates - one plate is bonded onto an elastic shim (Unimorph[®]) or two ceramic plates are bonded together on a common electrode plate (Bimorph[®]). Bimorphs[®] cause bending deformation because two piezoelectric plates are bonded together and each plate simultaneously produces an extension and contraction under an electric field.[13, 22]

Since the fabrication process is simple, and large magnification of the displacement is easily obtained, this structure has been widely used. However, it has a low response frequency (1 kHz) and low generative force. [13]

1.2.6 MOONIES

The origin of the name “Moonie” comes from the moon-shaped spaces between metal end caps and the piezoelectric ceramic.[37] The Moonie has intermediate characteristics between the conventional multilayer and Bimorph[®] actuators, exhibits an order-of-

magnitude larger displacement (100 μ m), and much larger generative force (10Kgf) with quicker response (100 μ s) than the Bimorph[®]. [13]

1.2.7 RAINBOW™

RAINBOW™, Reduced And INternally Biased Oxide Wafers, are structurally similar to standard piezoelectric Unimorphs[®]. [38, 39] A RAINBOW™ ceramic is a monolithic structure with an integral electrode that is fabricated to place an internal compressive stress bias on the piezoelectric element. [40] The process renders one side of lanthanum zirconium titanate (PLZT) ceramic inactive, making it act like an integral stationary metal shim. The RAINBOW™ reduction process involves placing graphite (carbon) block on one side of the wafer and a zirconia plate to protect the active side. The assembly is then put in a furnace heated to 975°C for an hour. [23, 24, 25, 33, 41, 42]

Typical performance ranges for the RAINBOW™ actuator are displacements of less than 1000 μ m, forces of less than 500N, frequencies of less than 10kHz, and temperatures below 100°C. [43] However, a 10% decrease in displacement after 10⁷ cycles under no load has been measured, along with a 40% decrease in displacement after 10⁷ cycles under 300grf. [34]

1.2.7 THUNDER™

The new piezoelectric device, THUNDER™, developed at NASA Langley Research Center, is composed of a ferroelectric material which is prestressed against a foundation material (glass, metal, etc). This new piezoelectric device is based on a piezoelectric ceramic wafer attached to a metal backing using a polyimERIC adhesive. [44] The ferroelectric

material used in the manufacturing process consists of a piezoelectric wafer laminated between layers of materials, such as aluminum, stainless steel, beryllium, etc., bonded with a polyimide adhesive created at NASA.[45, 46] In this manner, a more durable, rugged, and more flexible actuator and sensor is obtained.[47, 48, 49, 50, 51, 52] Two clear advantages of this new piezoelectric device class over others are ease of fabrication and the ability to create application-specific devices.

Because of the diversity of construction techniques for a THUNDER™ device, its characteristics vary from configuration to configuration. This fact makes THUNDER™ a flexible actuator that can be adapted for each particular application. For example, a device can be designed that produces more force than displacement at a particular frequency. Since a THUNDER™ device behavior is dependent on several factors, such as mounting, poling, voltage, frequency, metallic layer thickness, and shape, most of these are addressed herein.

The subject of smart materials was investigated specifically for the purpose of creating an actuator suitable to be used in flow-separation control applications. Hence, a review of the traditional passive and active devices used in this area is appropriate and is presented below.

1.3 Flow-Separation Control

Flow separation can cause loss of energy and instability, in such a manner that it can reduce the performance of fluid-handling machinery such as pumps, turbines, fans, etc., as well as airborne or seaborne vehicles. When flow separates, more power is required to compensate for energy loss, stalling, etc., which can destroy or damage human bodies and machines. [53]

The onset of flow separation is determined by the characteristics of the flow along a wall, so that in two-dimensional flow, the criterion for separation is zero pressure gradient at the wall or zero wall friction.[56] In another words, the interconnection between surface streamlines and viscosity in a flow separated region, may be found by surface streamlines which define a skeleton structure of the viscous region. In this manner the separation criterion is given by,

$$\frac{\partial q}{\partial y} \Big|_{y=0} = 0 \quad (1)$$

where q is the component of the velocity in the direction perpendicular to the separation line. In short, adverse pressure gradient and fluid viscosity are two key factors that affect flow separation.[54]

Many techniques have been utilized to detect the onset of flow separation over the years. Flow visualization is one of the techniques most frequently used, since it is simple and the overall flow pattern can help to determine whether or not separation takes place. Parameters observable include pathlines or particle paths, streaklines, and in limited cases, streamlines. [53] Consequently, smoke flow visualization has been widely utilized by many researchers to investigate the steady and unsteady effects of geometry and other parameters on flow separation. [55, 56, 57, 58] Other techniques include hot-film gages, [59, 60, 61] surface pressure measurements, [62, 63] and computational methods. [64, 65]

Once flow separation can be identified, techniques to control it can be investigated and successfully tested in theory, as well as in practical applications. For instance, suction, blowing, riblets, etc., have proven to be successful techniques for delaying or preventing the

onset of separation. [66, 67] The choice of flow-separation-control technique is dictated by system considerations, such as parasite or device drag, system complications (due to weight, volume, complexity, and structural considerations), cost, reliability, performance sensitivity, and geometry.[68, 69] Typically, research on separation control devices involves limited parametric studies of a particular device or approach, as applied to a particular flow situation. For example, on a pitching delta wing, separation occurs in a cyclic manner, making its control more difficult, [70] and techniques for its control have been proposed. [71] If this type of flow is suitably controlled, dramatically enhanced agility could be conferred to aircraft performance. [72]

The optimum standby separation control scheme for an application should use the best combination of the following criteria: minimum system penalty when not deployed (minimum volume and weight addition, low pressure drag), effectiveness in controlling turbulent flow separation, passive operation, and rapid deployability.[46] Some techniques for controlling flow separation are, transverse and longitudinal surface grooves, riblets, passive porous surfaces, vortex generators (VG's), large-eddy breakup device (LEBU) at an angle of attack, spanwise cylinders, arches, Helmholtz resonators, Viets' fluidic flappers, vortex generator jets, and wall cooling.[46] Of all these techniques, the most effective are briefly introduced in the following sections.

1.3.1 Vortex Generator Jets

Vortex generator Jets (VGJ), consist of holes in the surface inclined at an angle to the surface, skewed with respect to the freestream direction, and arrayed along the surface much like classical vortex generators. Their effectiveness on separation control has been

studied by many researchers. [73, 74, 75] For instance, Selby, et al., investigated VGJ effectiveness over a two-dimensional rearward-facing ramp. They found that VGJs are effective in reducing separation by up to 90%, and their effect lasted for at least 40 times the boundary-layer thickness. [46] Applications include air injection on an axial compressor to control rotating stall and theoretical models to actively control stall have been proposed. [76]

1.3.2 Large-Eddy Breakup Device at Angle of Attack

A Large-Eddy Breakup Device (LEBU) is a thin spanwise ribbon or airfoil, with chord on the order of magnitude of the boundary-layer thickness, placed in the outer part of the boundary layer (parallel to the wall in order to alter the turbulence structure). [45] Under laboratory conditions, it has been established that LEBUs reduce the local skin friction downstream of tandem ribbons in a turbulent boundary layer by a large percentage. [77] However, LEBUs produce a net drag increase. A very detailed summary and study of the effectiveness of LEBU's has been published by Lynn, et al.[78]

1.3.3 Submerged Vortex Generators

Of the techniques mentioned above, classical vortex generators are of particular interest because of their overall characteristics. In internal flows, they are used to prevent flow separation and to reduce total pressure distortion.[79]

There are many kinds of VG's, such as small transverse and swept grooves, boundary layer fences, and vertical flaps.[46, 80] Among the most used are the vane-type VGs introduced by Taylor.[81] They consist of a row of small plates or airfoils that project

normal to the surface and are set at an angle of incidence to the local flow to produce single trailing vortices. Flow visualization results for a pair of vane-type vortex generators have indicated that each pair provides attached flow directly downstream.

Several passive and active separation control techniques, of the ones mentioned above, were investigated by John Lin, et al., for controlling two-dimensional turbulent flow separation over a backward-facing ramp.[46] They concluded that the vane-type vortex generators (VG's) reduced the extent of separation by almost 90%, when placed properly. However, since the VG represents an obstruction in the flow, there is a drag penalty for its use.[46] Furthermore, vortex generator position and geometry are key factors in achieving control of the flow around a body.[82]

Actively-controlled VG's, which would automatically deploy when separation is imminent, would be a major advance in research involving flow separation control and drag reduction, for both aerospace and non-aerospace applications. Many researchers have proven the effectiveness of submerged flow control devices in different flow situations. [83, 84, 85, 86, 87, 88, 89] Attempts to study the effects of an oscillating plate immersed in a turbulent boundary layer were performed by Miao, Cheng, and Chou [90] and they found that there is a critical frequency for the oscillating plate where the flow becomes quasi steady, which suggests that a moving vortex generator may alter the flow favorably and can be controlled depending on the physical conditions (landing, angle of attack, etc.) Other studies which include mechanical actuators embedded in a delta wing, discuss the feasibility of active control of the pitching of the wing.[91] The major disadvantage of such an approach is added weight and the difficulty of installing a device on the original structure.

1.4 Research Objectives

The objective of the present research is to design, construct, test, and characterize an actuator to be used in a flow-separation-control system. This project is multidisciplinary in nature and requires knowledge of flow physics, automatic control theory, design of mechanical systems, and materials science. Because of the unique characteristics of THUNDER™, it was desirable to determine if it can be used in flow-separation control, especially in conjunction with vortex generators.

Performance characteristics of a specially designed THUNDER™ actuator have been investigated. Parameters such as displacement, frequency, size, shape, mounting, and effects as a vortex generator on the separated flow over a ramp has been investigated.

CHAPTER II

EXPERIMENTAL SETUP

Experiments were conducted in two different stages—general THUNDER™ characterization and wind tunnel THUNDER™ applications. The first part of the experiments were conducted at NASA Langley Research Center and the Face R&D Laboratories. The wind tunnel experiments were conducted at Old Dominion University. A description of the equipment used in each facility and each experimental setup utilized is presented below.

2.1 Experimental Setup at NASA Langley Research Center

The electromechanical characterization of the present class of piezoelectric devices was performed at NASA Langley Research Center using a data acquisition system composed of computer controlled hardware and software that provided flexibility in measuring the pertinent parameters. The hardware used included a portable computer equipped with an IEEE 488 interface card; a Wavetek Synthesized Function Generator (Model 23) with an IEEE interface; a TREK Power Supply/ Amplifier (Model 70/750); an optical-fiber-based Angstrom Resolver Series (Dual Channel Model 201); a Dual Channel Low Pass Filter (Model SR640); a Hewlett-Packard 4-channel Oscilloscope (HP54601A with an IEEE interface); and a Hewlett Packard Impedance Analyzer (HP-4192A with an IEEE interface). All of the hardware was monitored and controlled using LabVIEW™ software .

The function generator had a range of 10mHz to 12MHz frequency range and was equipped with an IEEE interface card that allowed it to communicate with the personal computer. The power supply had a 0 - 1500 volt output range at 50mA, 100 mA peak

current (for 10 s into capacitive or resistive loads). It used a floating output driver, allowing the instrument to be configured to produce an output voltage range of 0 V to +1500 V, 0 to -1500 V or -750 V to +750 V. It featured adjustable DC gain in the range of 15 to 300 V/V and AC response controls that permitted handling of different capacitive loads.

The Angstrom Resolver Series is an optical fiber based, non-contacting, high frequency, high resolution surface motion transducer system. Each sensor was calibrated and a linear relationship between voltage measured and travel distance was used to reduce data. Each calibration curve had two linear ranges and depending on the ranges expected, front or back slope was chosen. (See Figure 2.1) Also each sensor operated over a different measurement range. Channel B was used to perform the present measurements with a linear range between 0 to 0.635 mm (25 mils, back slope), and an accuracy of $0.127\mu/\sqrt{\text{Hz}}$. A schematic of a basic 7-fiber optic lever is shown in Figure 2.2.

The Impedance Analyzer was used to measure parameters such as capacitance as a function of frequency. It can operate on frequencies between 5 and 13MHz with a 1mHz resolution. This device measures 11 impedance parameters (i.e., capacitance, impedance, phase angle, etc.) and has a DC bias of up to 35V.

2.1.1 Displacement Measurements

A schematic of the control loop for displacement measurements is presented in Figure 2.3. This control loop is composed of the computer, which is connected to the function generator that controls the power supply to drive the piezoelectric device. The optic sensor

measures the displacement through a filtered signal fed back to the computer through a digitizing oscilloscope.

Since many variables affect the behavior of the THUNDER™ elements, the characterization was divided into several phases. The first phase involved poling of the elements. The second phase consisted of measurements of displacement as a function of voltage at a constant frequency, and the third phase consisted of measurements of displacement as a function of frequency at a constant voltage.

Poling, the first phase, was controlled using a LabVIEW™ program (see Figure 2.4), which activated the function generator, resulting in the input of a voltage offset to the power amplifier. This was the DC voltage required to pole the THUNDER™ element. This DC voltage was applied for a predetermined period of time (usually 2 minutes) and then was reduced to zero.

The second stage was facilitated using LabVIEW™ software, shown in Figure 2.5. The program controlled variables such as voltage, frequency, voltage offset, and channel over which the optic sensor displacement measurements were transmitted.

The control loop for data acquisition began with a signal transmitted from the computer to the function generator, which produced a small AC signal (0-5 VAC) at a particular frequency. This AC signal was an input to the amplifier, which amplified the signal 150 times, producing the desired voltage in a range between 100 to 400 VAC, depending on the desired voltage to drive the THUNDER™ element. Modeling clay was used to freely attach (at four corners) the piezoelectric device to a stationary platform (see Figure 2.6), and an optical-fiber-based sensor measured and monitored the displacement at a location near the center of the piezoelectric device. This displacement signal was passed

through a filter set at 5 kHz in order to eliminate noise. The signal from the filter was then displayed on the oscilloscope, along with the signal driving the piezoelectric device, so that the performance of the device under study could be actively monitored. The oscilloscope digitized the signal and transmitted it to the computer, where all the necessary conversions were performed to obtain displacement of the THUNDER™ device. See Figure 2.7 for a schematic of the aforesaid setup.

The LabVIEW™ program used during the last phase of the characterization was designed to drive the THUNDER™ element at a constant voltage, and perform a sweep through predetermined frequencies. A view of the monitor output associated with this program is presented in Figure 2.8.

2.1.2 Capacitance Measurements

The Impedance Analyzer was used to measure the capacitance of the piezoelectric devices over a range of frequencies. This was accomplished using another LabVIEW™ data acquisition program (see Figure 2.9), that stored the values measured for further processing.

2.2 Experimental Setup at Face International Corporation

This section was performed at the Face R&D laboratories using a data acquisition system which included an optical-fiber-based Angstrom Resolver Series (Dual Channel Model 201, manufactured by Opto Acoustic Sensors); a Tektronix 4-channel Digitizing Oscilloscope (model TDS-420A); a Hewlett Packard Synthesizer/Function Generator (model HP-3325A); a National Instruments data acquisition card (model LabPC+); a TREK Power Supply/Amplifier (Model 70/750); and a Hewlett Packard Impedance Analyzer (HP-4192A

with an IEEE interface). All of the devices described were monitored and controlled using LabVIEW™ software.

2.2.1 Force Measurements

Force measurements were performed using a specially designed attachment for THUNDER™ rectangular devices. See Figure 2.10 for more details. This mechanism allowed the THUNDER™ device to be loaded with different masses, and at the same time, the THUNDER™ performance could be monitored (See Figure 2.11). The purpose of the rod on the mechanism was to keep the mass balanced while the THUNDER™ actuator was moving. Measurements performed in this manner were applicable for low frequencies only.

2.2.2 Life-Cycling Measurements

Life-cycling tests were performed on an accelerated basis. The test consisted of monitoring the displacement of a selected type of THUNDER element, with the equipment described above, at set intervals of time, besides visual inspection of cracks. The power supply (Face International Corporation) utilized produced a square wave at 375 Vpp. The specimens were tested close to their first mechanical resonance in order to accelerate the results of these tests, since the number of cycles is defined by the following equation.

$$\text{No. of cycles} = f \cdot t \quad (2.1)$$

where f is the operating frequency in Hz, and t is the time in seconds.

2.3 Wind Tunnel Setup

Flow visualization and other experiments were performed in an open-loop subsonic wind tunnel with a test section of 55.8 x 5.08 x 15.2 cm (22 x 2 x 6 in). This facility can achieve speeds of up to 30 m/s. In order to ensure uniform flow conditions, a speed of 24 m/s was used for all experiments. The length of the tunnel was 3.83 m, which included the inlet section, the settling chamber, the contraction, the test section, the diffuser, driver system, the exhaust, and a smoke flow visualization system. See Figure 2.12.

The wind tunnel was mounted on 0.483 cm (19 in) relay racks 121.9 cm (48 in) tall that were reinforced with aluminum stock to provide stability, as well as support for the tunnel. The test section, the drive system, and the diffuser were mounted on a rail system to allow movement and precise alignment between sections, which provided high quality flow as well as accessibility. The tunnel was built with several additional features to ensure flow quality; a test section inlet and diffuser made of hand laid fiberglass-epoxy; the test section precisely aligned with the end of the contraction (See Figure 2.13); the contraction with a sinusoidal profile; the motor fan assembly mounted on isolation mounts balanced with static weights; and the drive system isolated with a flexible rubber coupler from the diffuser. Finally, the test section was designed so that front and rear wall could be independently and simply removed for ease of access. The drive system (See Figure 2.14) consisted of a squirrel cage fan (Daytona model 1C792), an AC drive motor (Reliance Electric, 0.75 hp, and 1725 rpm), an industrial motor speed control with a tachometer feedback, and an anti-vibration system. The AC motor drive and the tachometer feedback helped provide the tunnel test section with constant speed flow.

The flow visualization system (built by NASA Langley Research Center, Microelectronics Development Section) consisted of a power supply, three timers, an automatic oiler system, and a light system (See Figure 2.15). The power supply provided current to a 0.010 cm (4 mil) diameter *Inconel resistance wire* which carried the oil (SAE - 10W40). The three timers controlled current flow through the wire, trigger time, and perform other auxiliary events. The oiler system consisted of a reservoir located at the interface of the inlet and settling chamber of the wind tunnel, which had a wire passing through it, cable connections to the wire, and a built-in slider system. The first timer controlled the amount of current supplied to the wire, and needed to be monitored and adjusted, depending on the tunnel flow rate, in order to produce full burning of the oil. The second timer controlled the triggering of the flash and the third timer was used for auxiliary purposes. Finally, the flash had a focused light beam with a conventional zeon light system. A cylindrical lens produced a uniform sheet of light (See Figure 2.16).

Two different cameras were used to capture flow visualization images a Polaroid with bellow system for daylight and room photography and a 35 mm camera. The Polaroid camera was mounted on a tripod and the 35 mm camera was mounted on the wind tunnel camera support system. The mounting system allowed for movement along the test section and out of the plane of the tunnel. In this manner, the position of the camera was fixed with respect to the tunnel in order to allow a high degree of repeatability for the flow visualization experiments.

2.3.1 Model Description

The baseline separation model was a two dimensional 25° ramp with an 20.32 cm shoulder radius. The width of the model was 5.08 cm, which spanned the test section. The length was 27.84 cm. This model produced reasonably two-dimensional separated flow at approximately the beginning of the ramp. See Figure 2.17 for a schematic of the wind tunnel setup.

Two backward-facing steps were built based on the results produced by Lin.[54] The first model was 5.08 cm wide and 27.84 cm long with a rounded nose and a smooth ramp (See Figure 2.18). The purpose of this model was to conduct preliminary tests to determine the optimum location of vortex generators. Using the results presented by Lin, several locations were tested using a 0.025cm-diameter boundary-layer probe and a height gage. The second model (same dimensions) was made hollow to include a THUNDER™ device, and a support structure spanning the width of the inner section of the model. The electrical connections to the THUNDER™ device were made through an aperture of 0.004 cm diameter in the rear of the tunnel test section.

The piezoelectric device was powered by a TREK power supply with connections to a PC (data acquisition card). The computer transmitted a signal to the power supply for DC voltage or an AC signal that could be selected at a particular frequency. See Figure 2.19 for a schematic of this control loop.

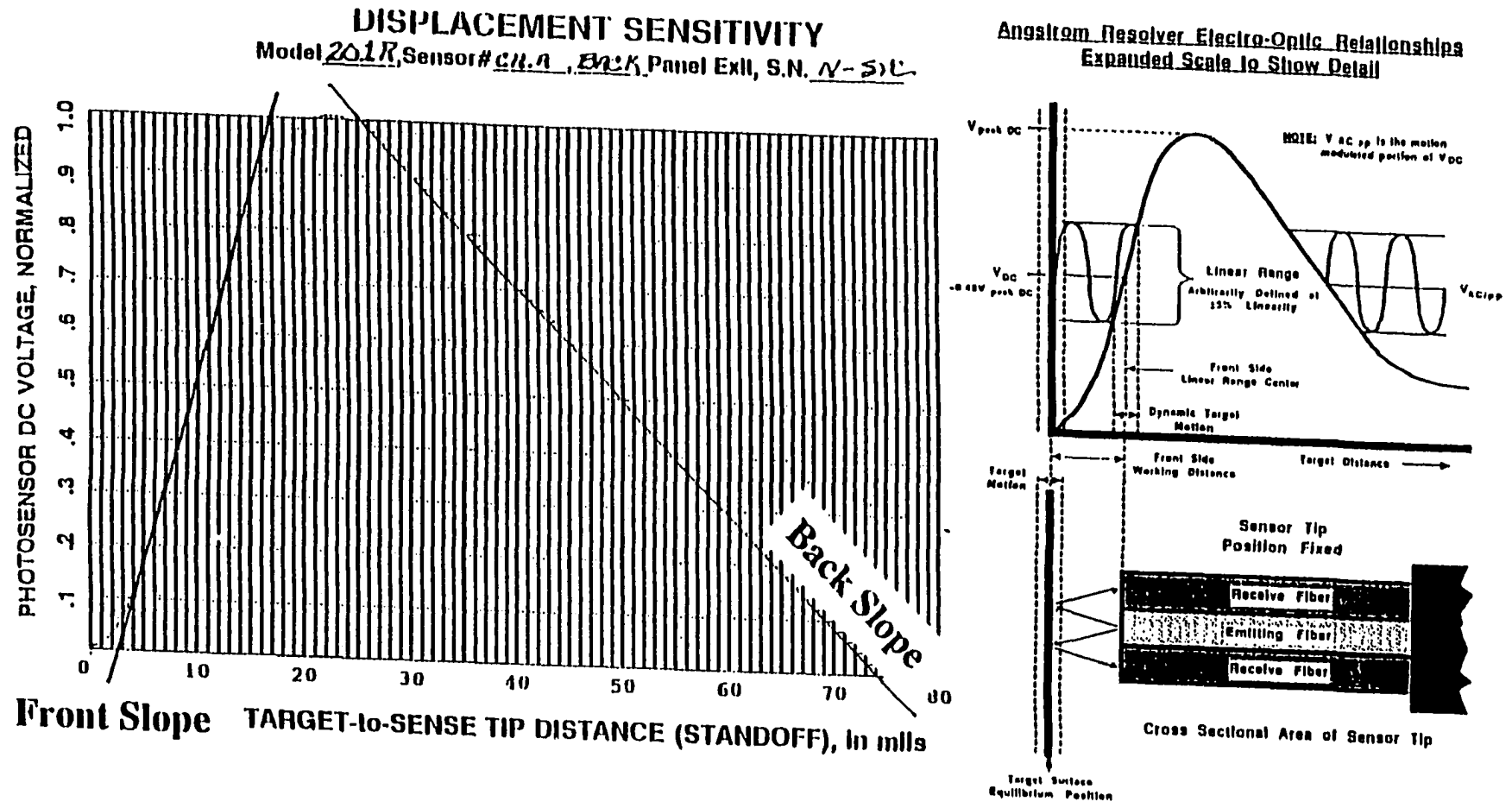
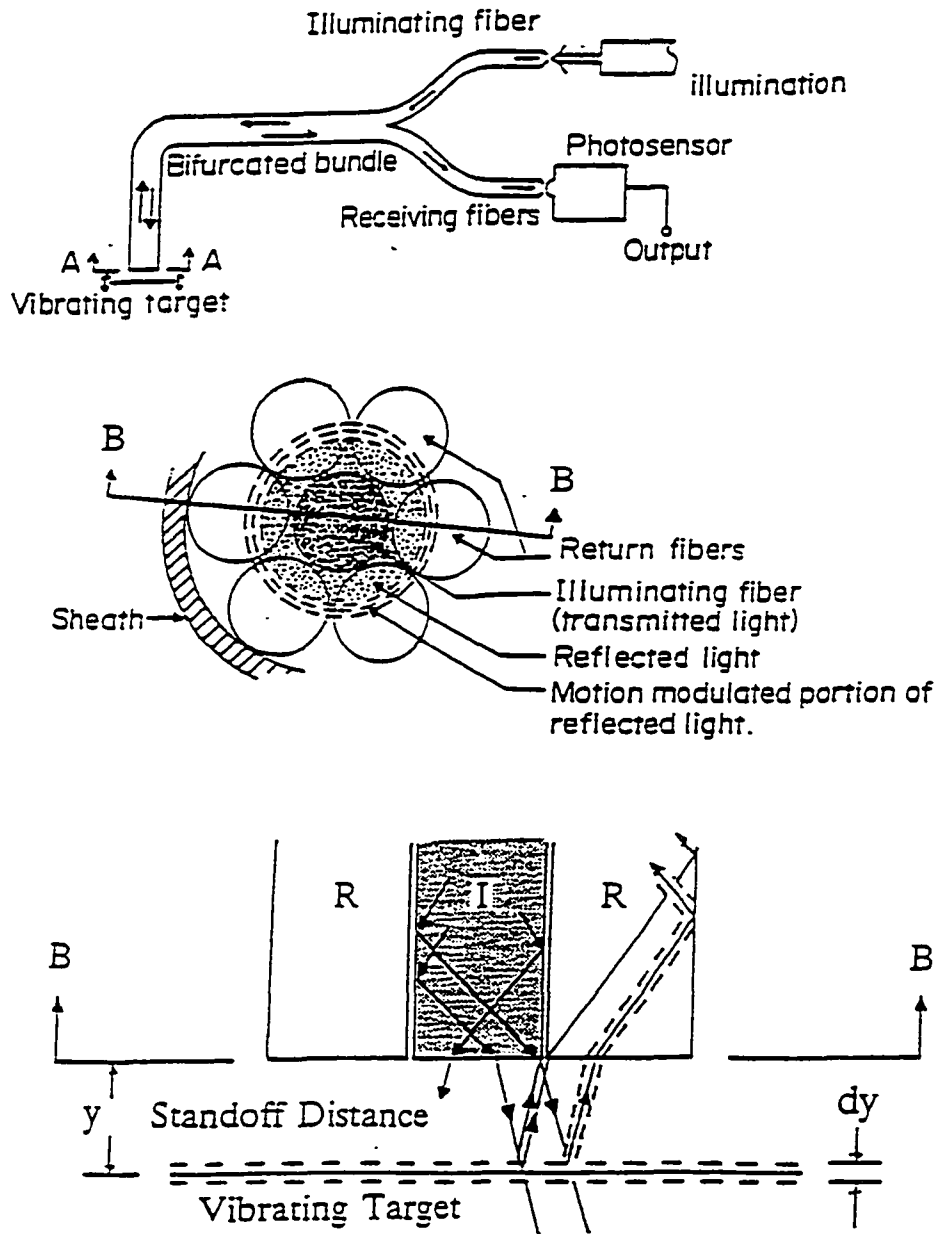


Figure 2.1 Calibration Curve for the Optic Sensor Measurement Probe
(Taken From: Ångstrom Resolver Series Dual Channel Models 201,
Opto Acoustic Sensors, Inc.)



Schematic of a Basic 7-Fiber Optic Lever

Figure 2.2 Schematic of the Operating Principle for a Basic 7-Fiber Optic Lever (Taken From: Ångstrom Resolver Series Dual Channel Models 201, Opto Acoustic Sensors, Inc.)

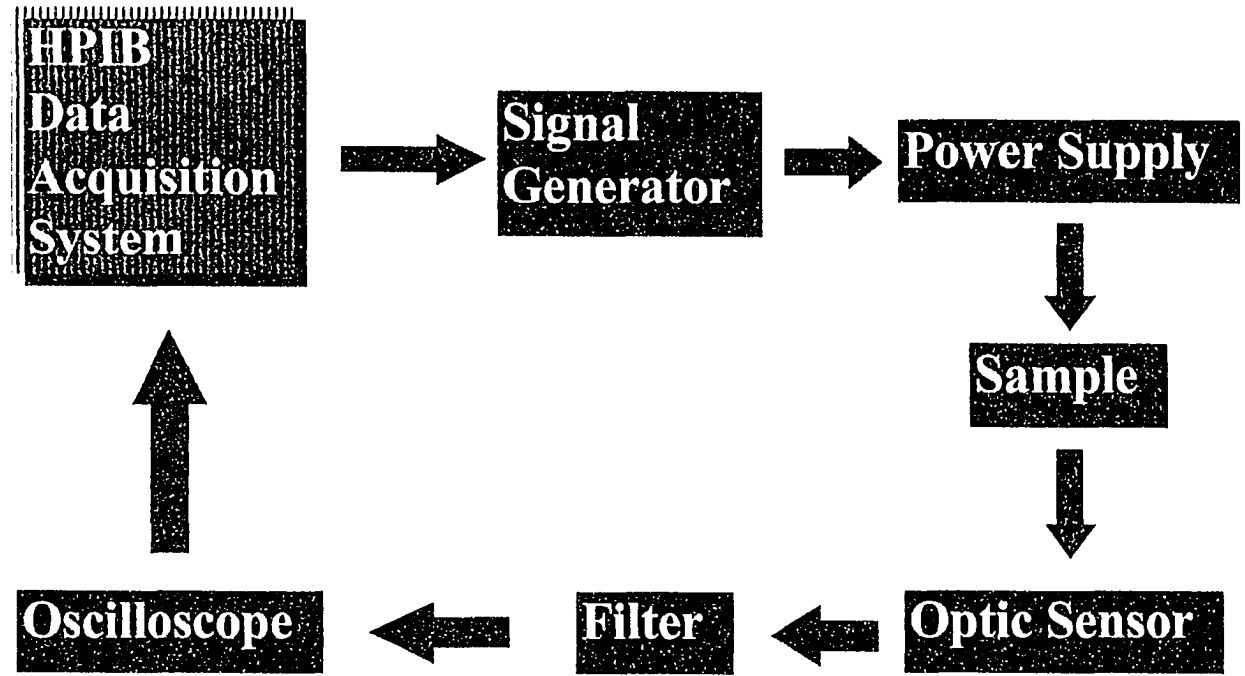


Figure 2.3 Experimental Setup Control Loop

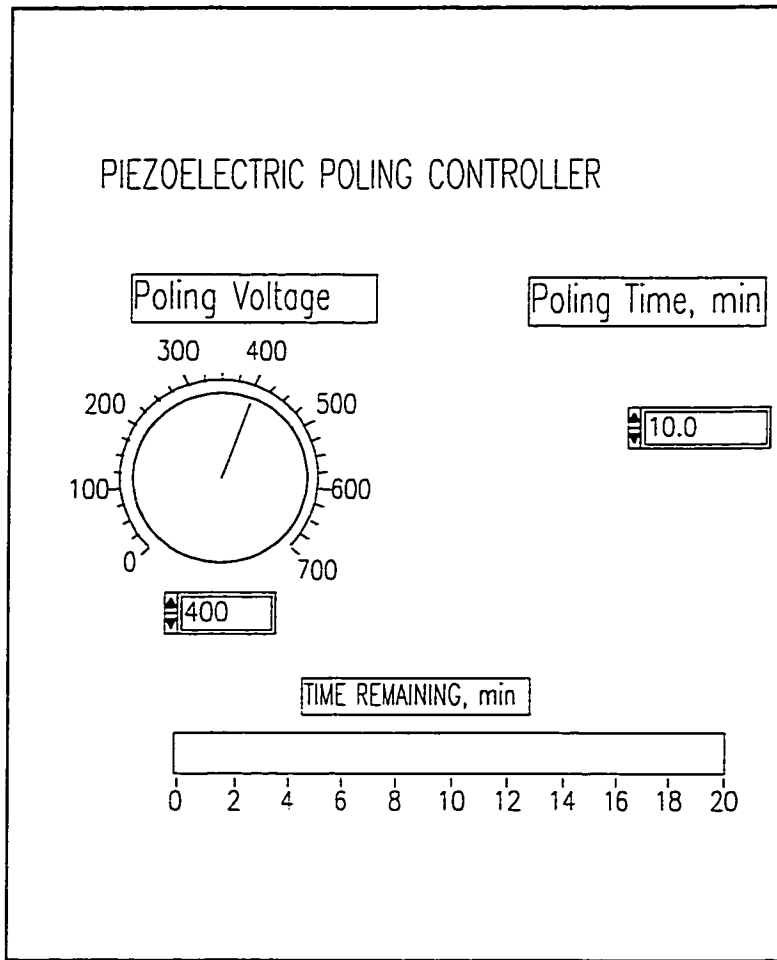


Figure 2.4 Monitor Display from LabVIEW® Poling Program

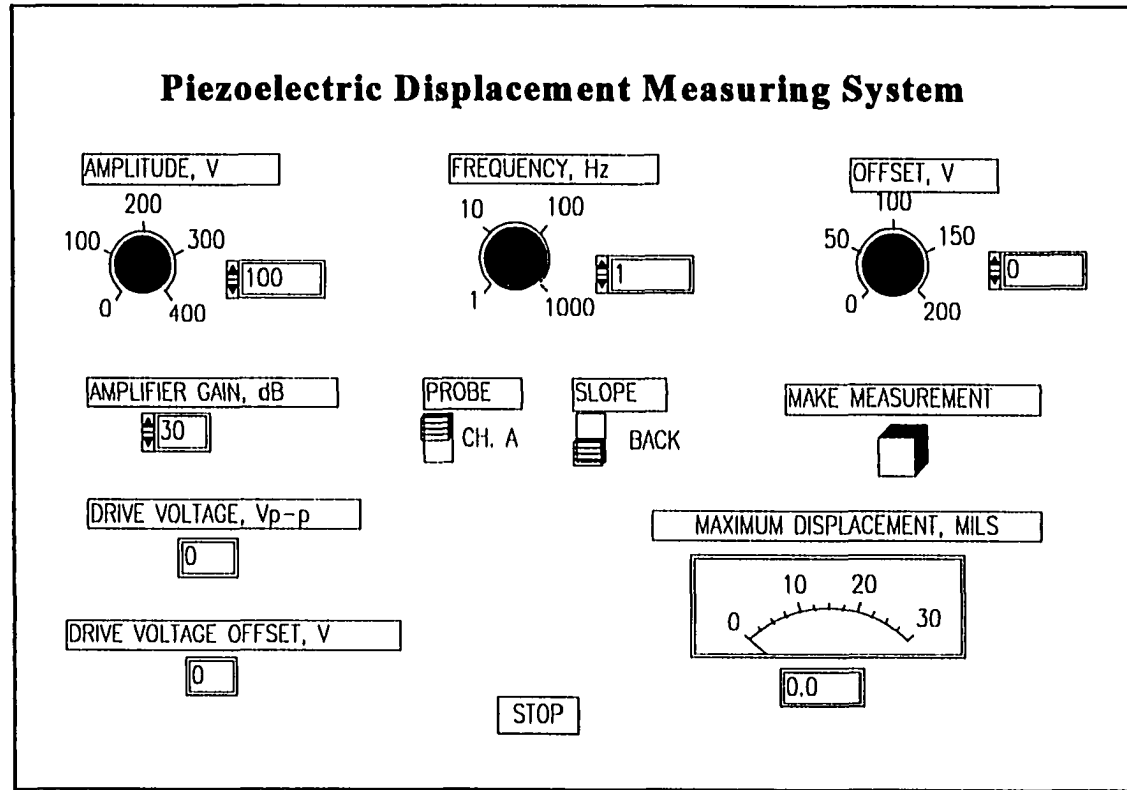


Figure 2.5 Monitor Display from LabVIEW® Piezoelectric Displacement Measurement Program

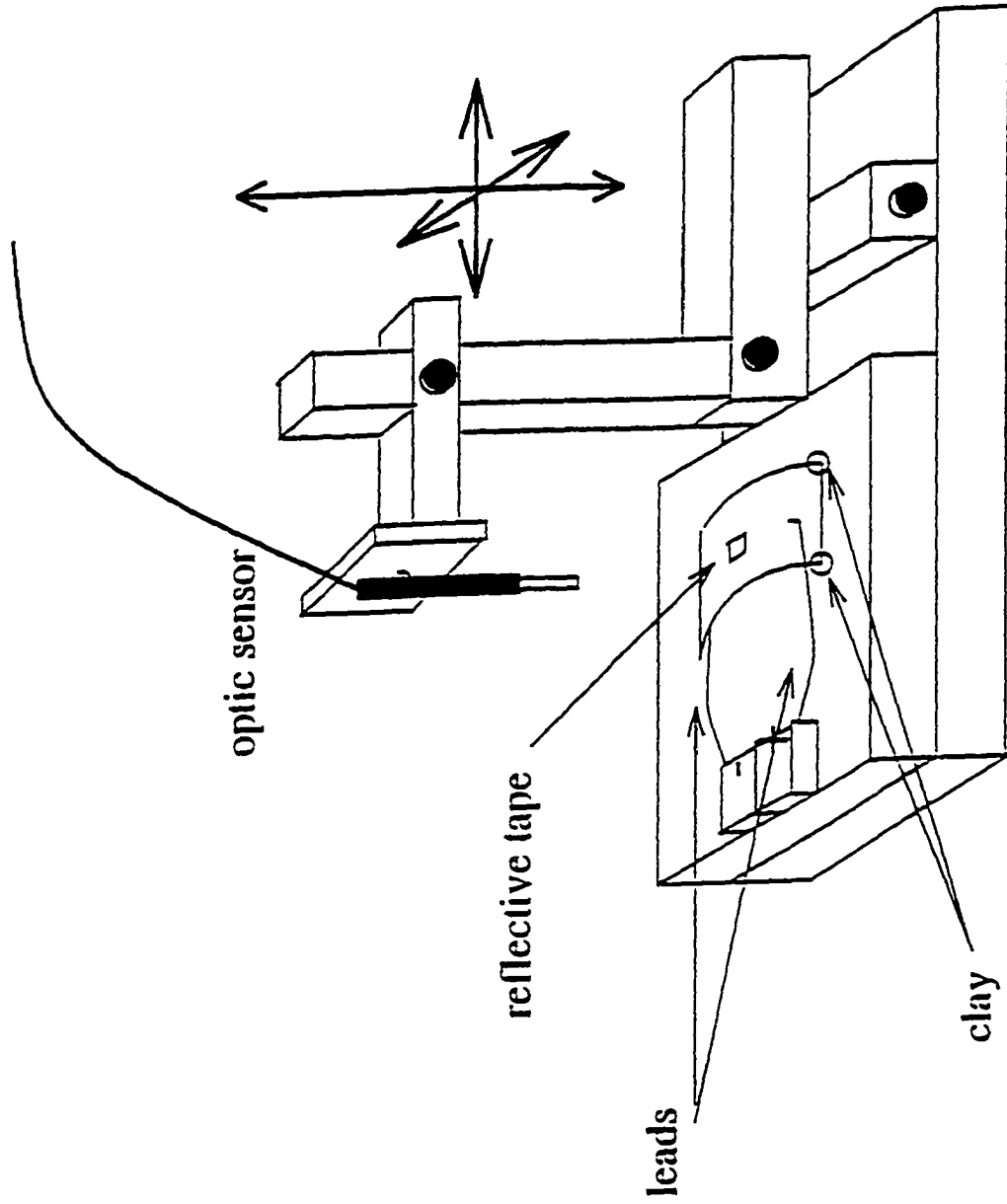


Figure 2.6 Schematic of the Experimental Setup for Displacement Measurements

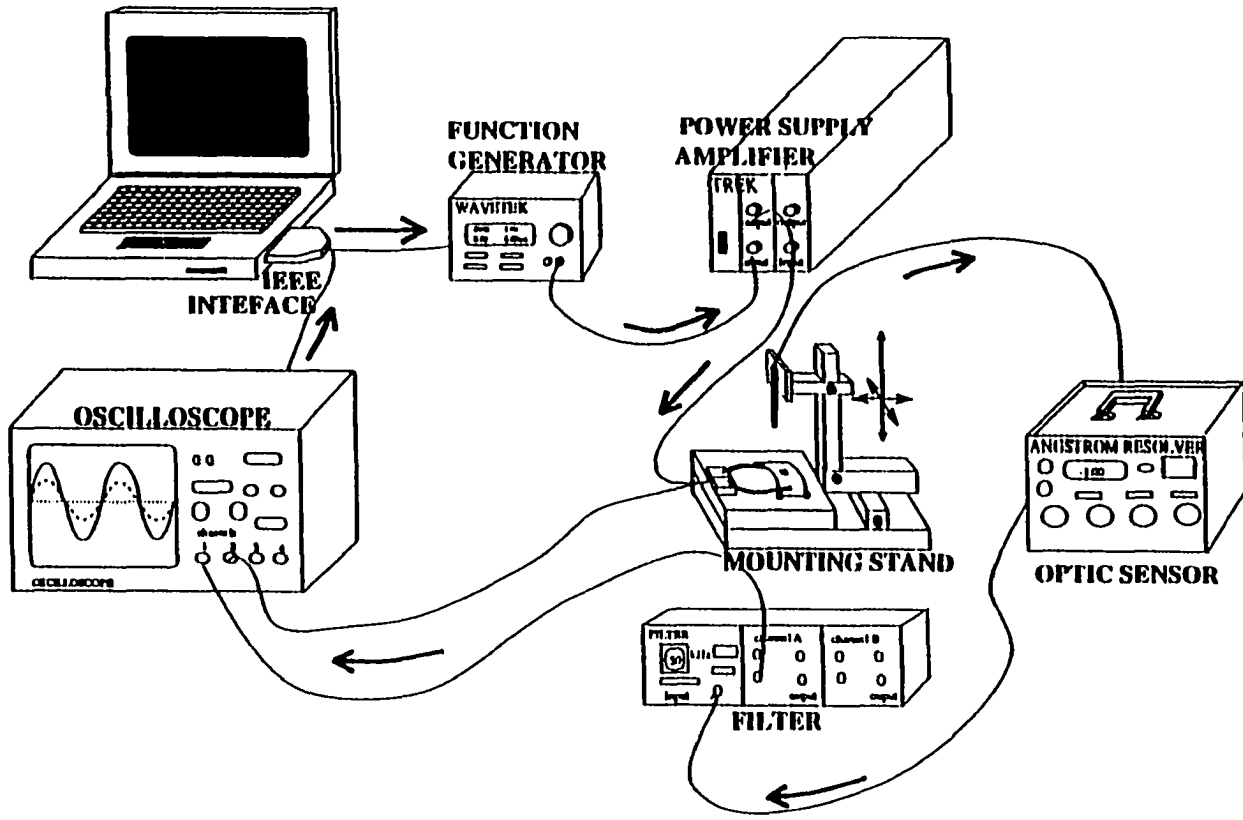


Figure 2.7 Schematic of Data Acquisition Setup

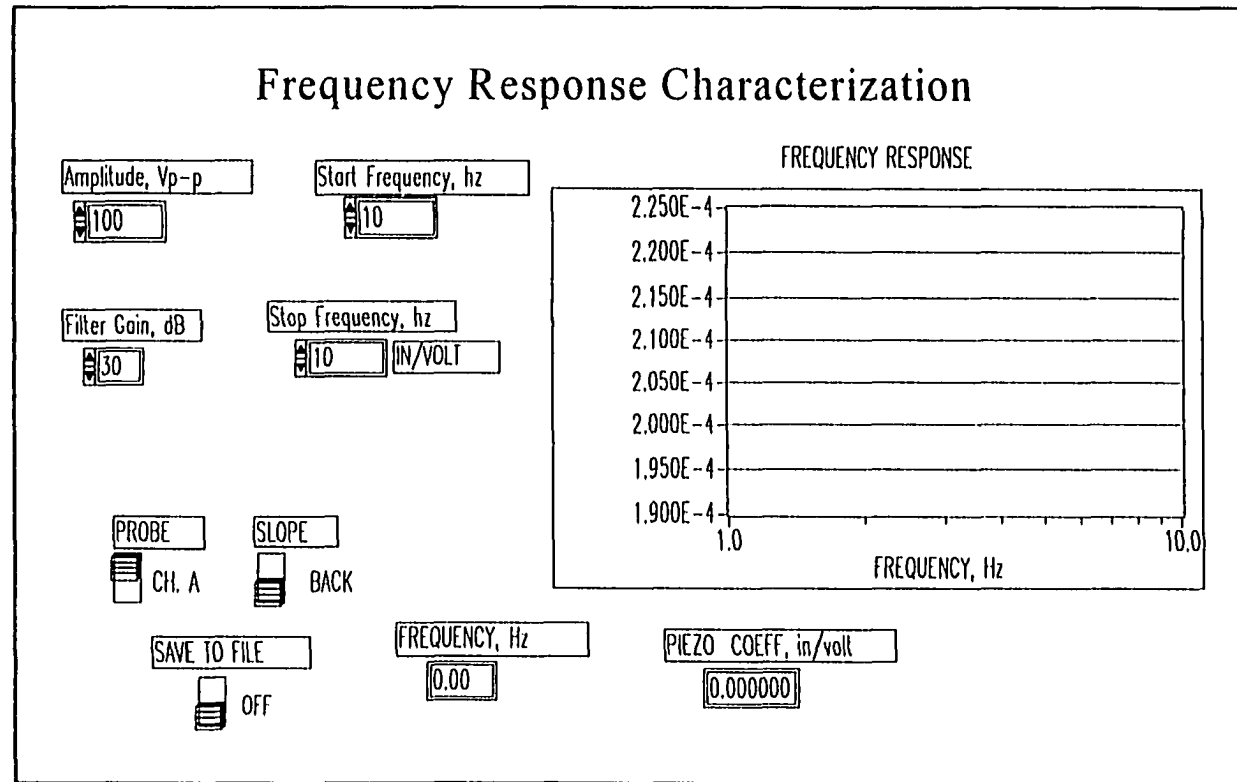


Figure 2.8 Monitor Display from LabVIEW[®] Program for Controlling Displacement Measurements at Varying Frequency

PIEZOELECTRIC MATERIAL CHARACTERIZATION

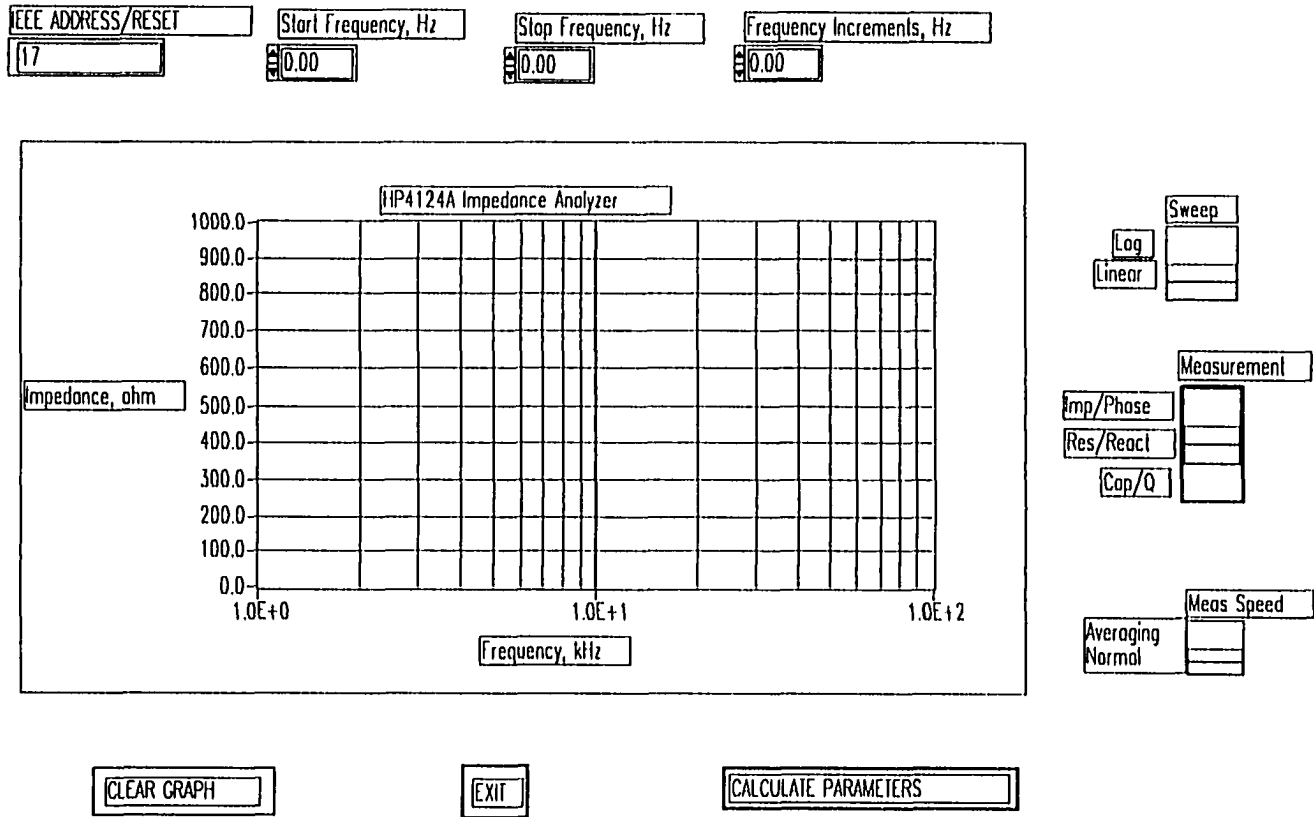


Figure 2.9 Monitor Display from LabVIEW® Program for Impedance Analysis

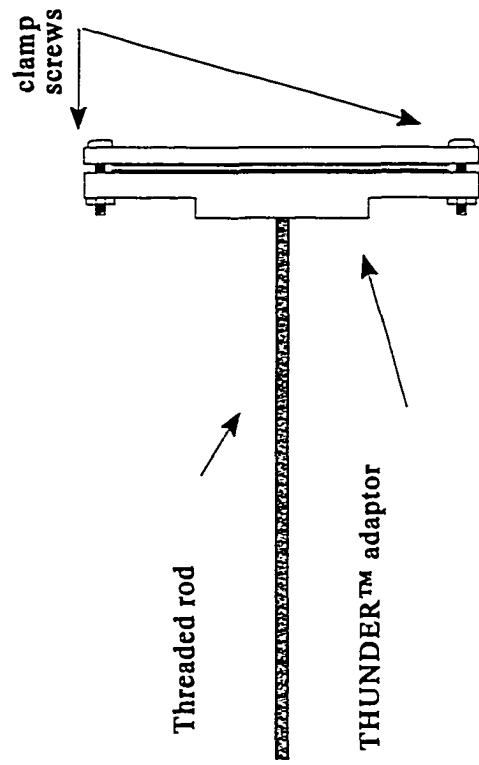


Figure 2.10 Structure Used to Attach Loads to the THUNDER™ Devices

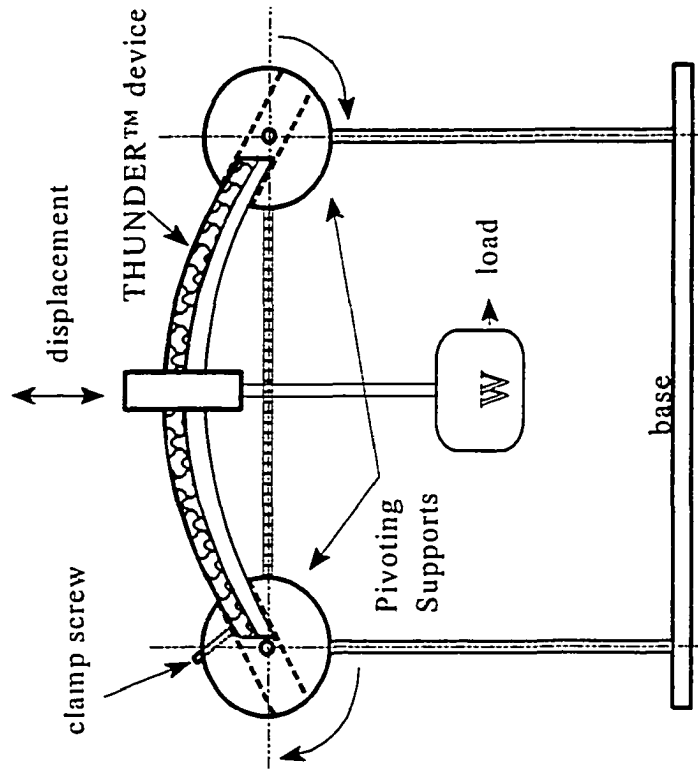


Figure 2.1.1 THUNDER™ Actuator under a Load, W, in a Pin-Free Configuration



Figure 2.12 Open-Loop Subsonic Wind Tunnel



Figure 2.13 Wind Tunnel Test Section (55.8 x 5.08 x 15.2 cm)

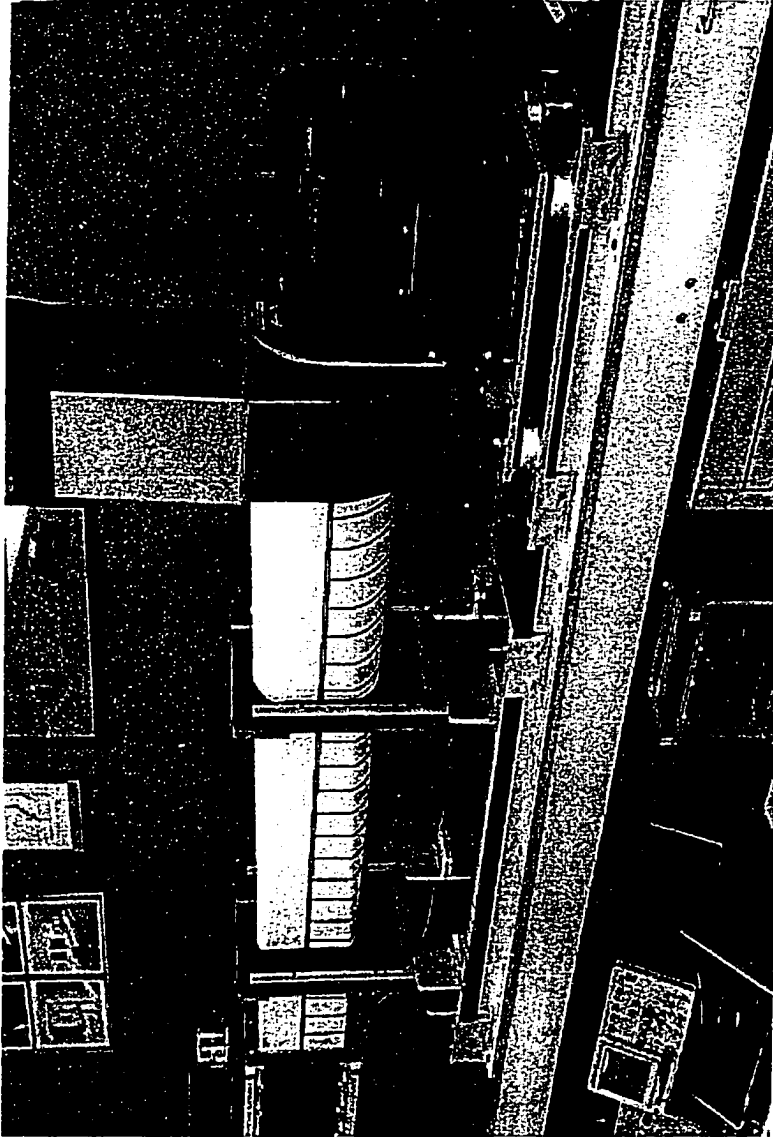


Figure 2.14 Wind Tunnel Drive System



Figure 2.15 Flow Visualization System

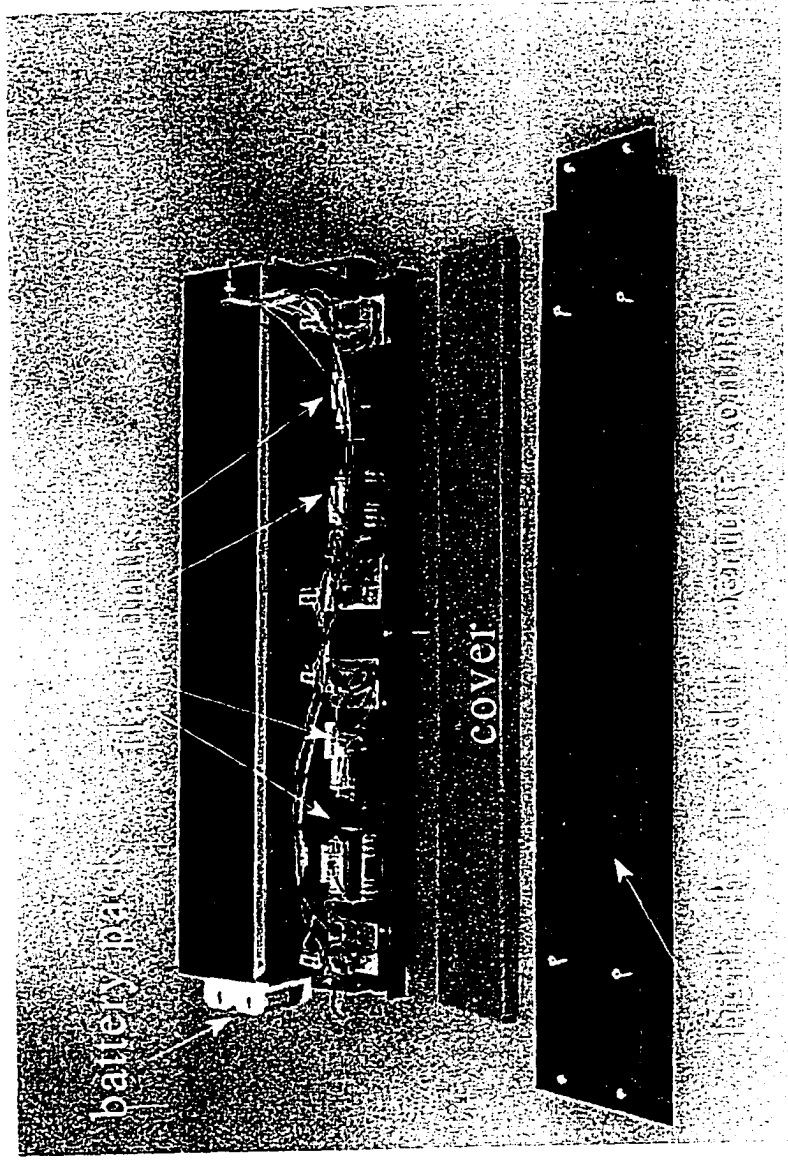


Figure 2.16 Illumination System

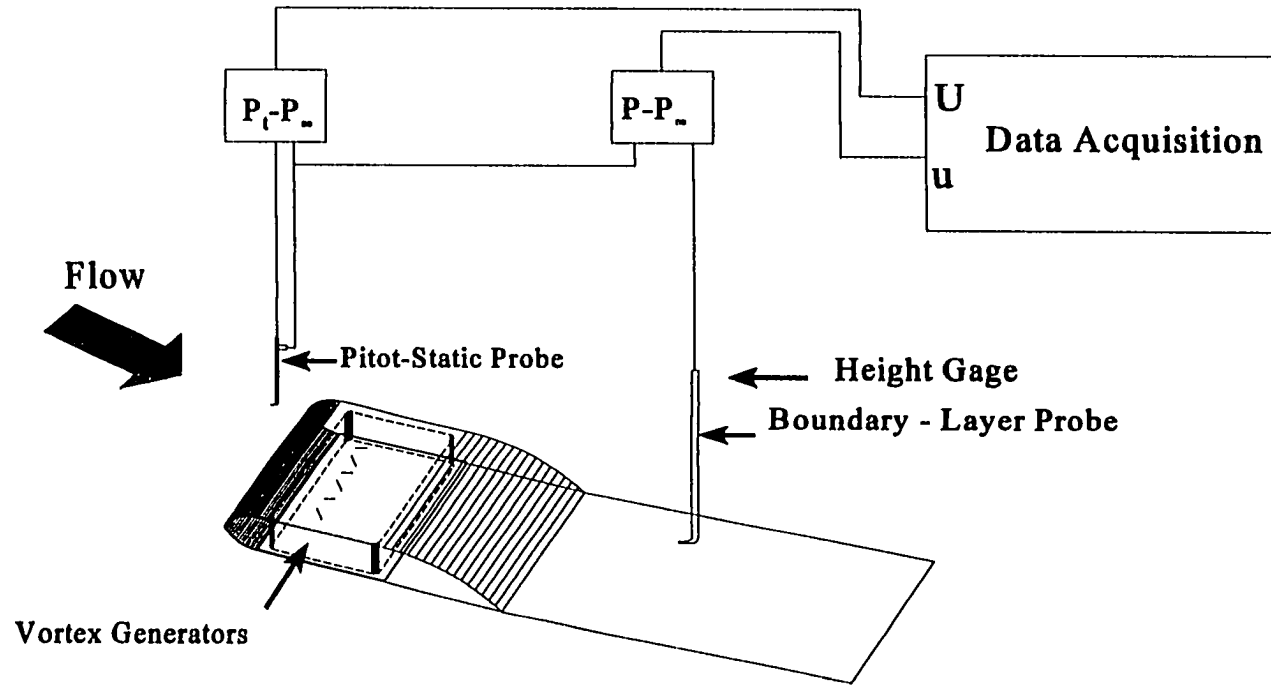
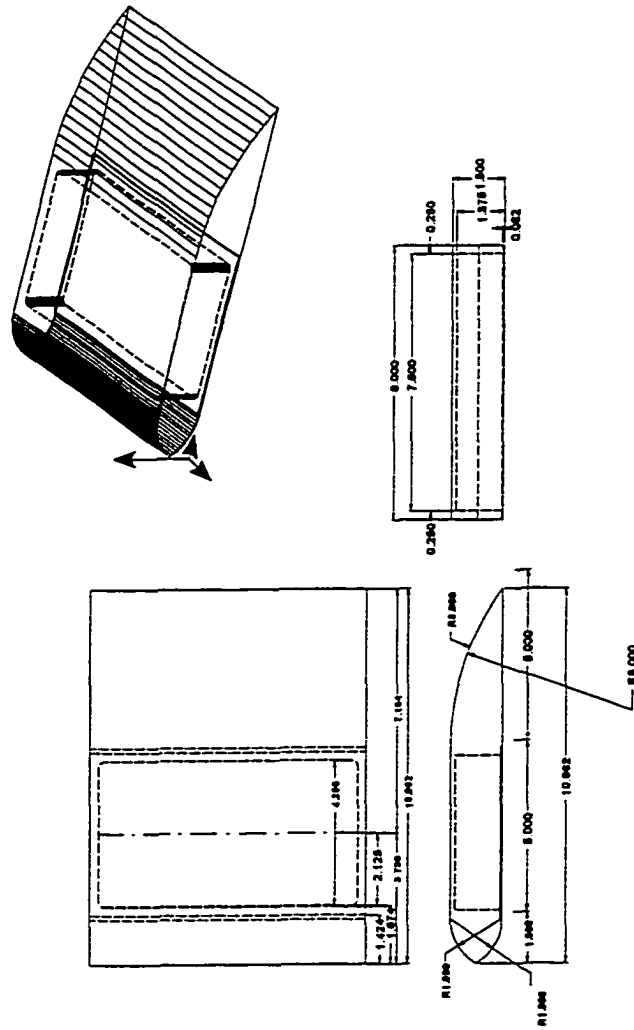


Figure 2.17 Schematic of Setup for Wind Tunnel Measurement Setup



all dimensions in inches

Figure 2.18 Two-Dimensional Backward - Facing Ramp

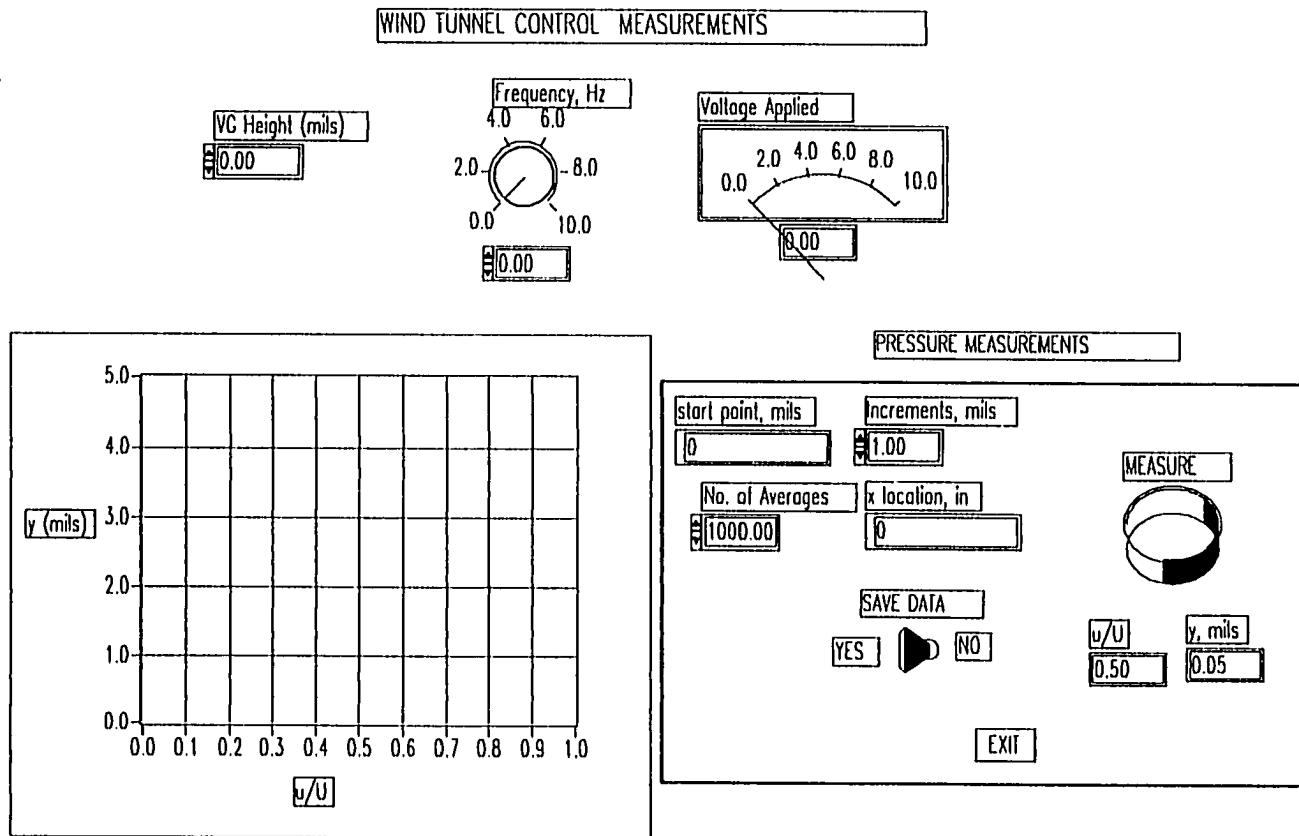


Figure 2.19 Monitor Display from LabVIEW[®] Program to Control Wind Tunnel Measurements

CHAPTER III

THUNDER™ CHARACTERIZATION

3.1 General

The characterization of the piezoelectric devices was performed in several stages, due to the many variables that affect their performance. Among those variables, the most important are frequency, voltage, shape (radius of curvature), physical dimensions, number of layers and amount of pre-stressing material, type of material, poling voltage, and clamping procedure. In order to control these variables, all the ceramic wafers used in the first stage of the characterization were poled PZT-5A wafers manufactured by MORGAN MATROC, Inc., with dimensions of 6.35 x 3.81 x 0.018 cm. Furthermore, the piezoelectric devices were clamped using modeling clay to allow relatively unrestrained motion with a physical boundary.

Since the ceramic type (PZT-5A), dimensions, and clamping procedure were kept constant, the remaining variables were driving voltage, frequency, shapes, number of layers and backing material. The driving voltage was varied between 100 and 400 Vpp in 50-volt increments and the frequency was varied between 1 and 1000 Hz for each case tested. The device configurations included three different metals - aluminum, stainless steel, and beryllium copper of different thicknesses and number of layers. Each configuration had a layer of 1-mil of 3% offset LaRC-SI film between the layers, and all materials were primed with LaRC-SI solution in a 10% solid concentration. All the metallic foils used were 1-mil thick, except where noted. One set of configurations of piezoelectric devices had 1, 3, 5, 7,

or 9 layers of 1-mil thick aluminum as the backing material, in order to determine the effect of backing thickness on device performance. A second set of devices was prepared with one layer of 1-mil thick aluminum above the ceramic wafer and 1, 3, 5, 7, or 9 layers of aluminum as the backing material. A description of the manufacturing process of a Typical THUNDER™ device is described in detail in Appendix A, and a summary of the configurations tested is presented in Table 3.1.

3.1.2 Displacement-Frequency Profiles

The first set of experiments involved measurements of displacement as a function of frequency (between 1 and 1000 Hz) at a fixed voltage. The objective of these tests was to determine if the process of manufacturing the piezoelectric devices resulted in a loss of polarization. Hence, this set of tests was performed on devices with poled ceramic wafers, as they were obtained from the manufacturer. Voltages were varied between 100 and 350 Vpp. These results are presented in Figures 3.1 through 3.13 for the thirteen configurations tested during this phase. It is important to note the resonant frequency for most configurations tested occurred between 100 and 200 Hz, suggesting that the resonant frequency is independent of configuration (thickness, driving voltage, etc.), but related to other geometric constants such as mounting and dimension. Although data points are often connected in Figures 3.1 to 3.13 in the region above the probe limit and near resonance, trends may be different than inferred in those regions.

In order to compare the performance of the various configurations, data were examined at three values of frequency at 200 Vpp. The frequencies chosen were 1, 10, and

100 Hz. These measurements should only be interpreted as characteristic of trends in piezoelectric device behavior. A summary is presented in Table 3.2.

These results are better analyzed if they are arranged differently. Taking into account all configurations that do not have a layer of material on top of the ceramic wafer (designated as x/Al) and using the theoretical backing thickness of the piezoelectric device, Figure 3.14 was produced. This figure generally indicates an increase in device displacement as the number of layers of backing material is increased, except for the configuration with 5 layers of backing material at the bottom. This graph also shows that when the backing material exceeds 7 layers, the displacement decays. The theoretical bottom thickness was determined in the following manner:

Configuration 3(0/3- x/Al): 3 layers of backing material

Configuration 8(1/7- Al/Al): 7 layers of backing material

The same data for configurations with a metallic top layer (Al/Al configurations) are presented in Figure 3.15. It is evident that displacement for Al/Al configurations is generally significantly less than for x/Al configurations, indicating that the top layer of material attenuates the movement of the piezoelectric device.

Since Figure 3.14 for x/Al configurations shows an irregular value for the configuration 3, a suggested trend is shown in Figure 3.16, upon including data for configuration 10. These two configurations are equivalent, since the total backing thickness is approximately equal for the configurations.

In order to verify that piezoelectric device performance was independent of the degree of poling of the devices, additional tests were performed after the devices were re-poled. A DC voltage of 420 V was applied for 5 minutes to each device. The poling time

of 5 minutes was chosen because the capacitance of the piezoelectric device was found to be constant for poling times of 1, 3, 5, and 10 minutes.

After re-poling, a sequence of tests was performed on all configurations. The capacitance was measured as a function of frequency and displacement was again measured as a function of frequency (between 1 and 1000 Hz) at fixed voltages. These results are presented in Figures 3.17 through 3.27. Once again, selected displacement data (at frequencies of 1, 10, and 100 Hz) are presented in Table 3.3 at an applied voltage of 200Vpp.

It can be observed that the resonant frequency still occurs between 100 and 200 Hz after re-poling. This observation reinforces the conclusion that resonant frequency appears independent of the variables examined in the present research. These data are presented again in Figures 3.28 and 3.29. These figures show a clear relationship between the total bottom layer thickness and device displacement, and an overall performance improvement over the results obtained before re-poling (see Figures 3.14 and 3.15). A more detailed comparison can be seen in Figure 3.30. In addition, a different trend is shown for the Al/Al configurations in Figure 3.29, as compared to the results for the same configuration as shown in Figure 3.15. The latter pattern is in better agreement with data for the x/Al configurations.

3.1.3 Capacitance Measurements

To further identify the causes for the differences in displacement performance, capacitance measurements were made at different processing/testing stages. The results are shown in Figures 3.31 through 3.37. The capacitance measurements were performed on the poled ceramic wafer before processing, the piezoelectric device after being processed prior to being re-poled, and finally, the piezoelectric device after re-poling. Interesting device

behavior can be observed in Figures 3.31 through 3.34. For these configurations (1, 2, 3, and 5), there is a significant variation in capacitance for the three tests. The most significant differences are between measurements obtained before and after re-poling. These data suggest that the piezoelectric devices may become depoled at the time of fabrication and therefore, need to be re-poled. However, not all configurations displayed this behavior. For instance, Figures 3.35 and 3.36 show almost no change in capacitance during the processing stages. This fact may be due to the use of different metals in the piezoelectric devices (stainless steel versus aluminum).

3.1.4 Displacement-Voltage Profiles

Due to the vast amount of data available, displacement as a function of voltage is only presented at 1 Hz for some of the most relevant configurations. Figures 3.38 through 3.42 show a linear relationship between applied voltage and displacement with only a small hysteresis effect.

The slope of the displacement-voltage curve for configuration 1 (Figure 3.38) is less than the slope of the curves for configurations 2 through 5 (Figures 3.39 through 3.42, respectively). However, the slopes for configurations 2 through 5 display little variation. Figure 3.43 shows displacement-voltage data for configurations 6 through 9 (Al/Al configurations) and Figure 3.44 shows the same data for configurations 10, 12, and 13. These figures indicate that the slopes for configurations 2 through 5 are greater than the values for configuration 6 through 9. However, the greatest slopes are exhibited for configurations 11 and 13 (Figure 3.44).

3.1.5 Hysteresis

The oscilloscope plots presented as Figures 3.45 through 3.49 show the response of the piezoelectric devices to an applied AC sinusoidal signal. As Figure 3.45 shows, at 1 Hz there is no phase shift between the driving voltage ($V_{pp}(1)$), and the measured displacement ($V_{pp}(2)$) for configuration 4. Furthermore, the hysteresis is very small at this frequency, as can be seen in Figure 3.46. However, as the frequency increases, a phase shift between the driving voltage and the displacement of the device appears (Figure 3.47), as well as an increase in hysteresis (Figure 3.48). These results are consistent with data presented in Figures 3.4 and 3.19, that show that a frequency of 350 Hz is close to the resonant frequency, and therefore results in unreliable measurements.

3.1.6 Summary Graphs

In order to show the difference in performance among the x/Al configurations before and after re-poling, Figures 3.49 and 3.50 are presented for an applied voltage of 200 Vpp. This value of voltage was chosen for convenience, since all the piezoelectric devices had measurable displacement values at this voltage. These figures indicate that the configuration that produced the most displacement (under no load) was configuration 4 (0/7-x/Al) at all frequencies measured (1-1000 Hz).

Finally, Figures 3.51 and 3.52 show the data for configurations with different backing materials. These data indicate that stainless steel may be the most effective material to use as a backing for the lower layers of the present class of piezoelectric devices at low frequencies (1-10 Hz).

3.2 Specialized Designs

In order to corroborate the theories mentioned above, other THUNDER™ designs were considered, as well as more specific parameters tested. The different THUNDER™ devices tested were measured in a pin-free configuration (see Figure 2.11) at a relatively low voltage ($200 V_{pp}$), at a frequency of 1 Hz, and under loads of 0, 0.2, 0.4, 0.5, and 1 Kgf. The load was attached to the THUNDER™ device using the structure shown in Figure 2.10. This structure has a threaded bar that keeps the weight balanced while the THUNDER™ actuator is moving, to facilitate accurate monitoring of displacement performance. This procedure is valid only for measurements at low frequencies. Two sets of models (I and II) were designed with different dimensions, but the same PZT properties (such as dielectric constant, density, etc.). See Table 3.4 for a description the ceramics materials used in these models. The two sets of models included a different combination of top layers of 1 mil (0.0254 mm) aluminum and brass and bottom layers of stainless steel, aluminum, and brass of varying thicknesses (3, 4, 5, 7, 9, 10 mil [0.076, 0.102, 0.127, 0.178, 0.229, 0.254 mm]). A description of the construction of each set is presented in Tables 3.5 (model type I) and 3.6 (model type II).

For the two sets of THUNDER™ models, displacement was measured and the results are presented in Figures 3.53 and 3.54. It can be observed from these results that there is a particular case that generally has a higher displacement than the others. For model type I (Figure 3.53) the case that usually produced the most displacement with or without load was 3a. However, when the load became greater than 0.5 Kgf, all the models essentially displayed the same displacement. For model type II (Figure 3.54) the case that produced the

most displacement was 2b. Again, with a load of 1 Kgf, most models performed similarly (less than 1 mil displacement).

3.2.1 Load-Displacement Profiles

Non-dimensional displacement as a function of applied load for all models described above is presented in Figures 3.55 through 3.66. Measured displacement has been non-dimensionalized with respect to initial displacement. These results fit an exponential equation of the form,

$$\frac{\delta}{\delta_0} = a e^{-bW} \quad (3.1)$$

where δ is the displacement of the device with a load W in grams, and δ_0 is the displacement under no-load. A summary of these results is presented in Table 3.7.

3.2.2 Impedance Measurements

The models mentioned above were also tested for impedance and phase, so that an equivalent circuit could be calculated (a description of the equivalent circuit used is presented in Appendix B). These tests were performed with the impedance analyzer with the device free (resting on a flat surface). Impedance curves, as well as phase angle data, are shown in Figures 3.67 thru 3.78. The equivalent circuit tested, shown in Figure 2.21, and the values for each component are shown in Table 3.8.

Note that the impedance curves show two basic resonant points at 350 and 780 Hz, between the measured frequencies of 100 to 1000 Hz, which makes the impedance values

used for the calculation of an equivalent circuit in that range, unusually large. This is due to the resonant points that again seemed to be mechanical.

3.2.3. Life-Cycle Tests

In order to perform accelerated life-cycle tests on the THUNDER™ devices, one model was chosen to be tested at frequencies close to a resonant point. These devices were clamped at the middle section of the device, between two pieces of plastic with elastomeric gum between them (to provide damping). For this case, the mechanical resonance was 75 Hz. Displacement was monitored daily, as well as visual inspections for cracks or other defects associated with the elements.

One of the major concerns, during the two million cycles tested, was failure of the connections to the THUNDER™ device. The wires included in the models were not capable of sustaining the cyclic stresses associated with the movement of the device.

Table 3.1 Test Configurations

CONFIGURATION	DESIGNATION	TOP LAYER	BOTTOM LAYERS
1	0/1-x/Al [†]	none	1 layer of Al
2	0/3-x/Al [†]	none	3 layers of Al
3	0/5-x/Al [†]	none	5 layers of Al
4	0/7-x/Al [†]	none	7 layers of Al
5	0/9-x/Al [†]	none	9 layers of Al
6	1/3-Al/Al [†]	1 layer of Al	3 layers of Al
7	1/5-Al/Al [†]	1 layer of Al	5 layers of Al
8	1/7-Al/Al [†]	1 layer of Al	7 layers of Al
9	1/9-Al/Al [†]	1 layer of Al	9 layers of Al
10	0/1-x/Al-5	none	1 layer of 5 mil Al
11	0/1-x/SS [†]	none	1 layer of 1 mil SS
12	0/1-x/SS-3	none	1 layer of 3 mil SS
13	0/1-x/BeCu-2	none	1 layer of 2 mil BeCu

[†] 1 mil (25.4 microns = 0.0254 mm) layers of Al

Table 3.2
Performance at 1, 10, and 100 Hz at 200 Vpp
for all Configurations before Re-poling

CONFIGURATION	Displacement (mm)		
	At 1 Hz	At 10 Hz	At 100 Hz
1	0.14	0.12	0.09
2	0.33	0.26	0.26
3	0.26	0.22	0.20
4	0.38	0.32	0.38
5	0.32	0.29	0.32
6	0.12	0.10	0.11
7	0.16	0.12	0.12
8	0.20	0.15	0.15
9	0.34	0.30	0.36
10	0.35	0.30	0.31
11	0.12	0.06	0.05
12	0.40	0.26	0.17
13	0.22	0.22	0.19

Table 3.3
Performance at 1, 10, and 100 Hz at 200 Vpp
for all Configurations after Re-Poling

Configuration	Displacement (mm)		
	At 1 Hz	At 10 Hz	At 100 Hz
1	broke	—	—
2	0.32	0.28	0.27
3	0.42	0.36	0.36
4	0.64*	0.58	0.64
5	0.36	0.34	0.42
6	0.26	0.24	0.36
7	0.36	0.34	0.46
8	0.27	0.24	0.26
9	0.24	0.21	0.19
10	broke	—	—
11	0.30	0.26	0.21
12	0.64*	0.64*	0.64*
13	0.36	0.34	0.36

*out of range, used maximum measurable value

Table 3.4 Ceramic Wafers for Models Types I and II

Model Type	Manufacturer	Classification	Dimensions (cm)		
			length	width	thickness
I	Morgan Matroc	PZT-5A	3.810	1.905	0.025
II	Motorola	PZT-3195HD	3.810	1.270	0.0203

Table 3.5 Cases Studied with Model Type I Ceramics

Case	Top Layers	Bottom Layers		
		First	Second	Third
1a	1 layer of Al	1 mil Al ¹	1 mil SS	1 mil SS
2a	1 layer of Al	1 mil Al	3 mil SS	none
3a	1 layer of Al	1 mil Al	4 mil SS	none
4a	1 layer of Al	1 mil Al	3 mil SS	3 mil SS
5a	1 layer of Al	1 mil Al	4 mil SS	4 mil SS
6a	1 layer of Al	1 mil Al	7 mil SS	none
7a	1 layer of Al	1 mil Al	9 mil SS	none

¹ 1 mil = 0.0254 mm

Table 3.6 Cases Studied with Model Type II Ceramics

Case	Top Layers	Bottom Layers	
		First	Second
1b	1 layer of Brass	4 mil SS	none
2b	1 layer of Brass	5 mil SS	none
3b	1 layer of Brass	6 mil SS	none
4b	1 layer of Brass	9 mil SS	none
5b	1 layer of Brass	5 mil SS	7 mil SS

Table 3.7
Coefficients for an Exponential Fit

$\frac{\delta}{\delta_0} = a \cdot e^{-b \cdot W}$	a	b	R ²
Cases Units	non-dimensional	units/g	non-dimensional
1a	1.0021	0.008	0.99
2a	0.9602	0.0028	0.95
3a	0.9785	0.0027	0.97
4a	0.9755	0.0029	0.99
5a	0.9596	0.0017	0.98
6a	0.9907	0.0033	0.99
7a	0.9499	0.0015	0.97
1b	1.0533	0.0011	0.97
2b	1.0483	0.0012	0.96
3b	1.0600	0.0014	0.97
4b	1.0771	0.0008	0.94
5b	1.0113	0.0003	0.94

Table 3.8 Equivalent Circuit Parameter Values

Case	R (k Ω)	L (H)	Ca (nF)	Cb(nF)
1a	242	41	0.64	35
2a	277	53	0.61	34
3a	171	66	1.00	34
4a	49	24	1.21	29
5a	20	24	1.11	26
6a	147	97	0.34	30
7a	106	40	0.76	29
1b	105	72	0.53	24
2b	103	118	0.60	23
3b	158	116	0.47	23
4b	195	110	0.39	21
5b	350	554	0.05	20

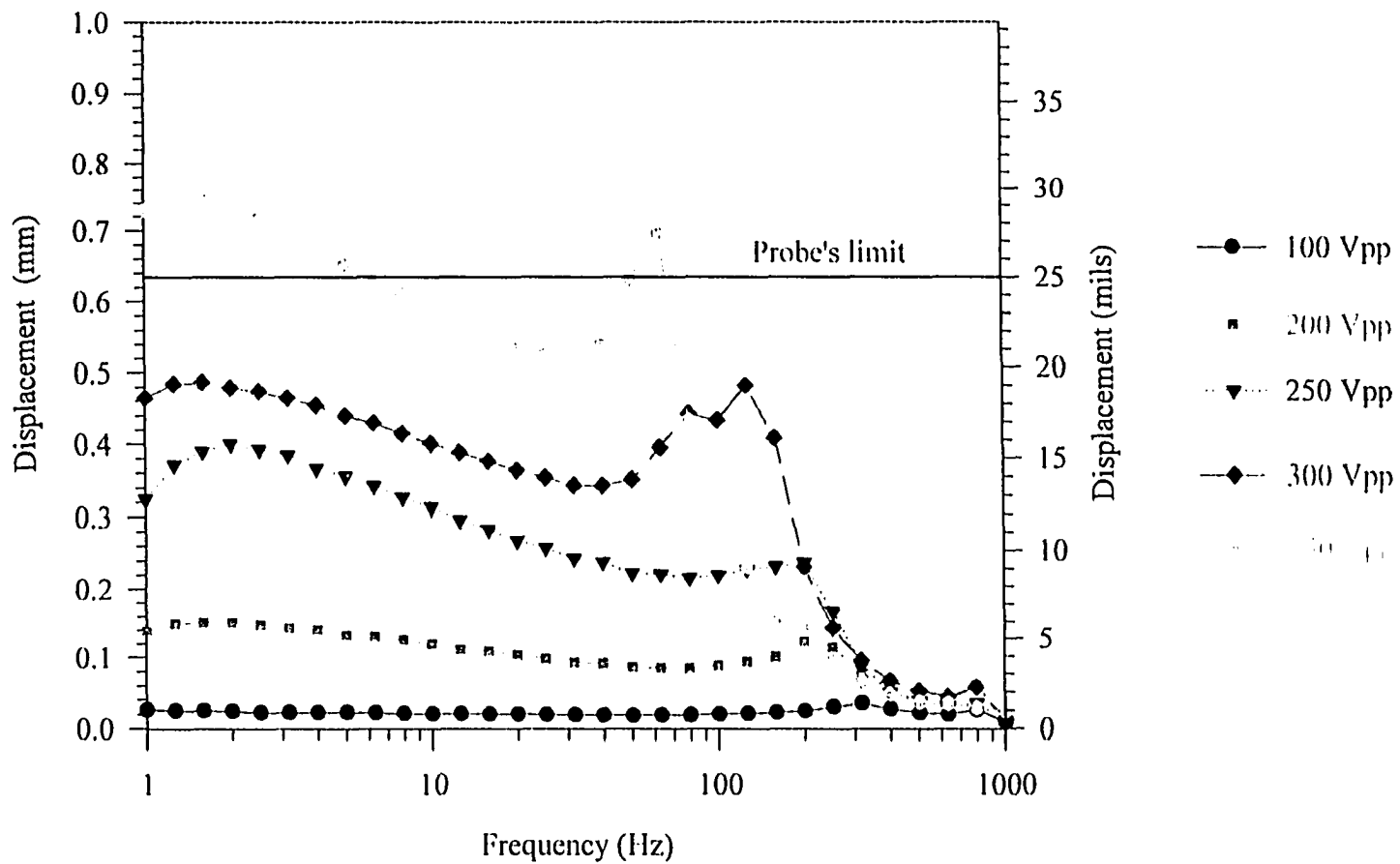


Figure 3.1 Displacement vs. Frequency for Varying Voltage Levels for Configuration 0/1-x/Al, with No Re-Poling

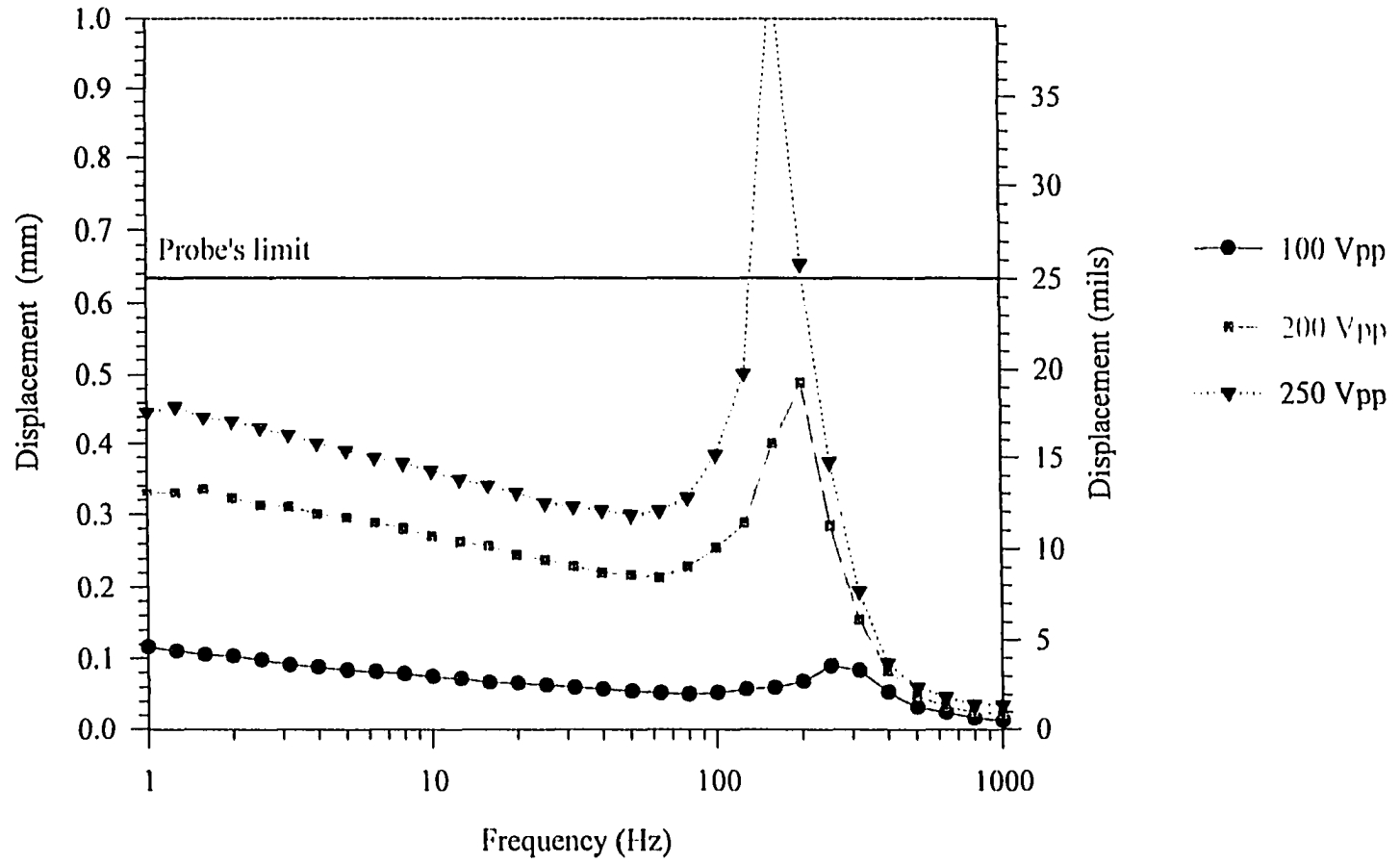


Figure 3.2 Displacement vs. Frequency for Varying Voltage Levels for Configuration 0/3-x/A1, with No Re-Poling

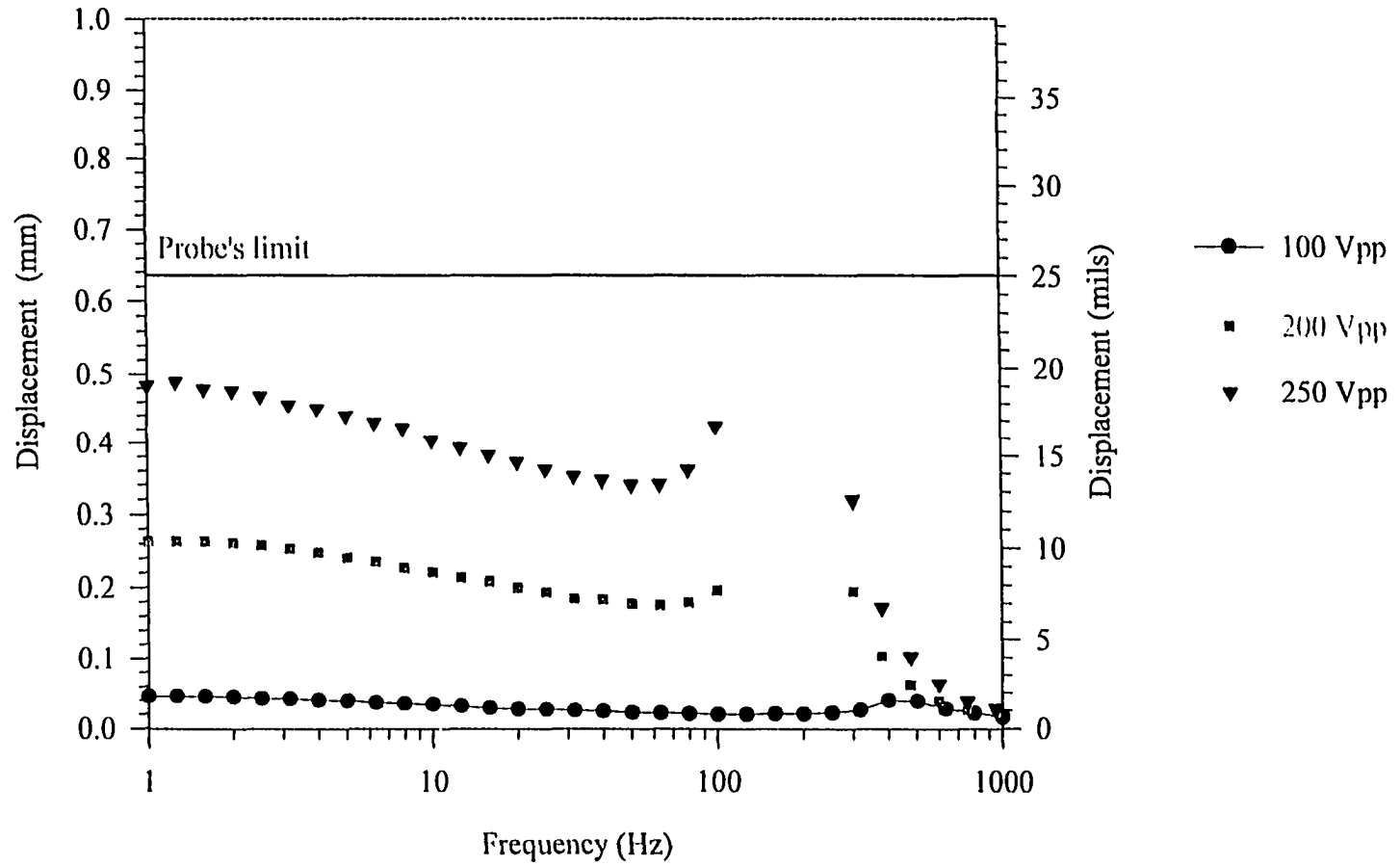


Figure 3.3 Displacement vs. Frequency for Varying Voltage Levels for Configuration 0/5-x/A1, with No Re-Poling

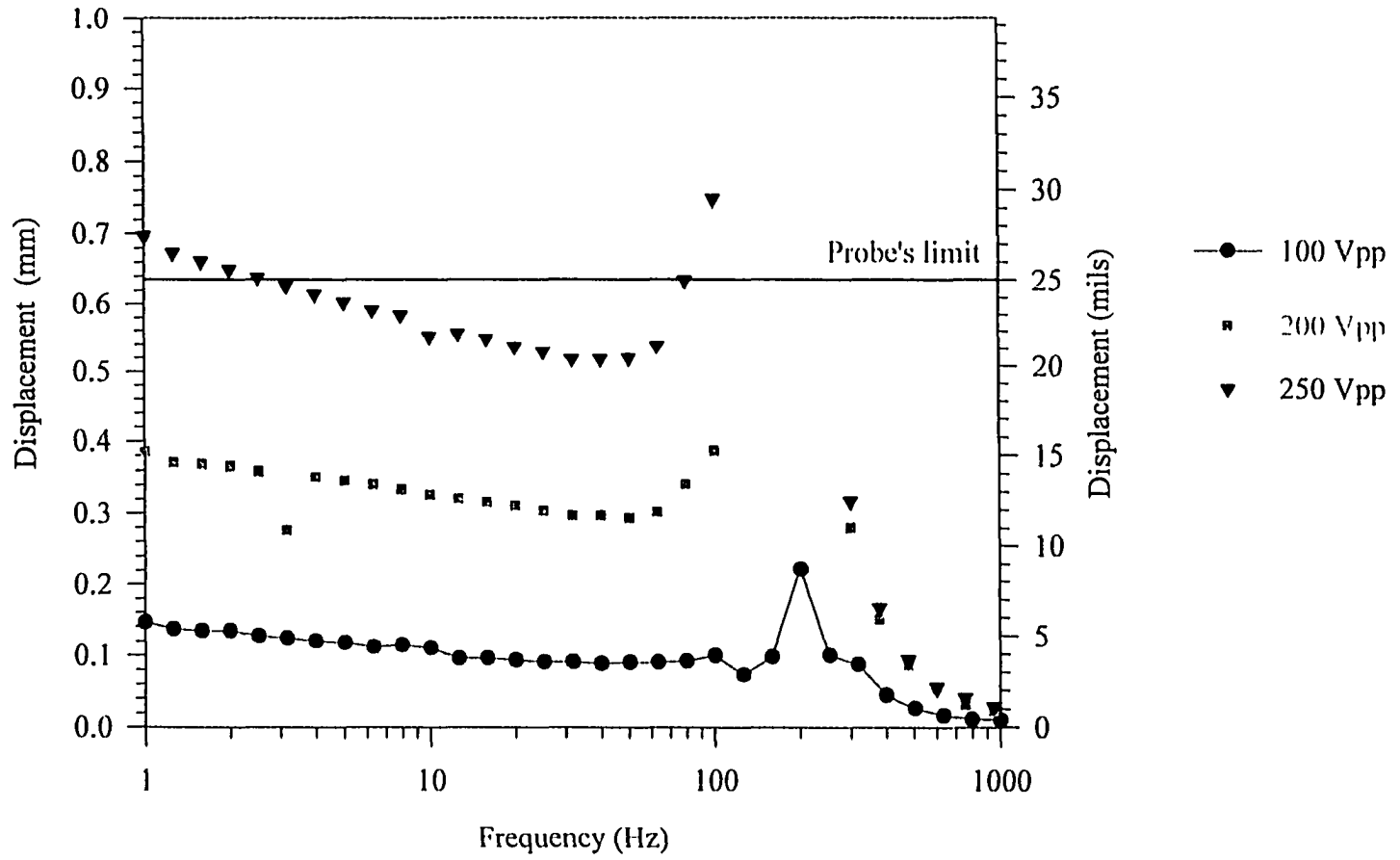


Figure 3.4 Displacement vs. Frequency for Varying Voltage Levels for Configuration 0/7-x/Al, with No Re-Poling

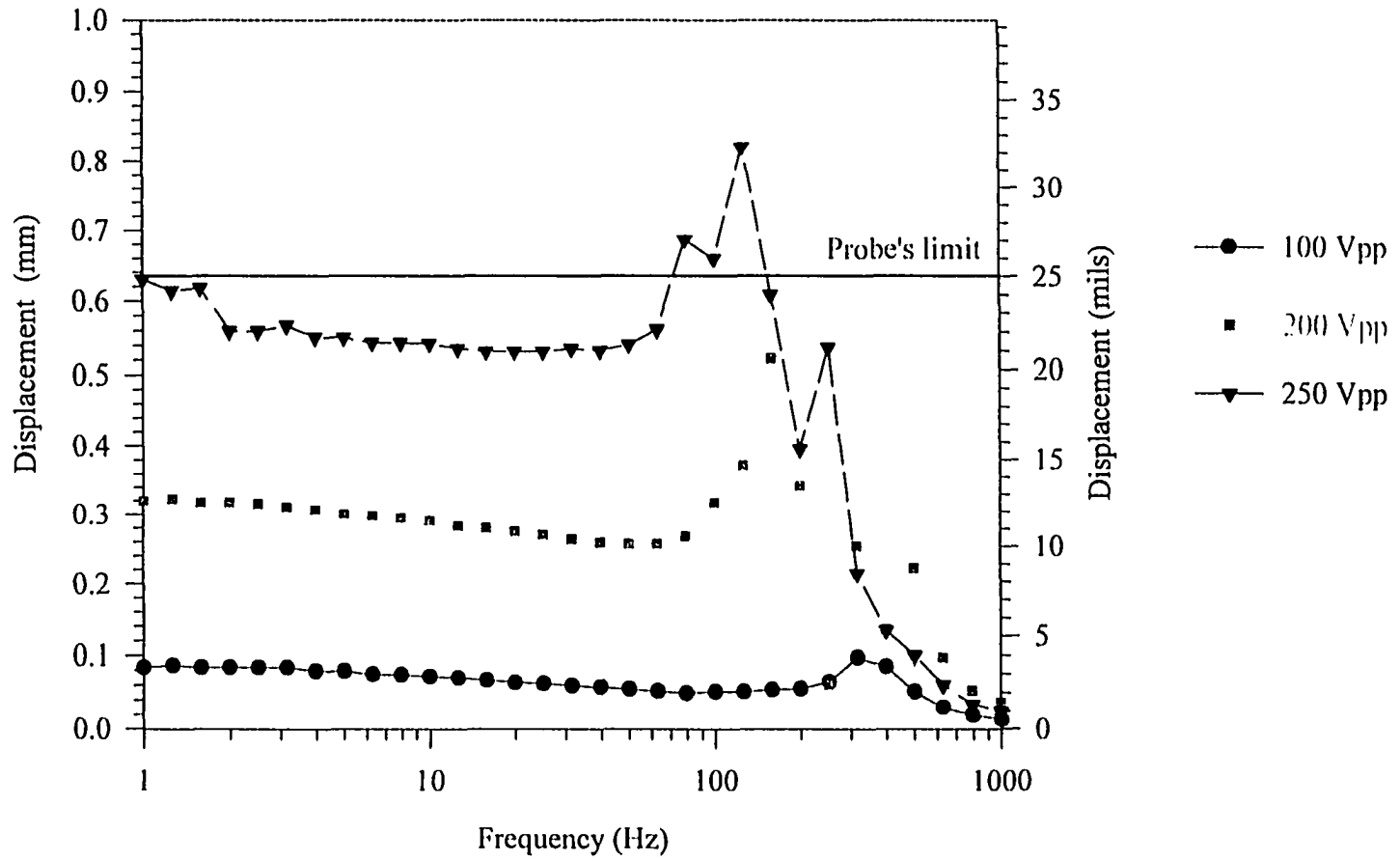


Figure 3.5 Displacement vs. Frequency for Varying Voltage Levels for Configuration 0/9-x/A1, with No Re-Poling

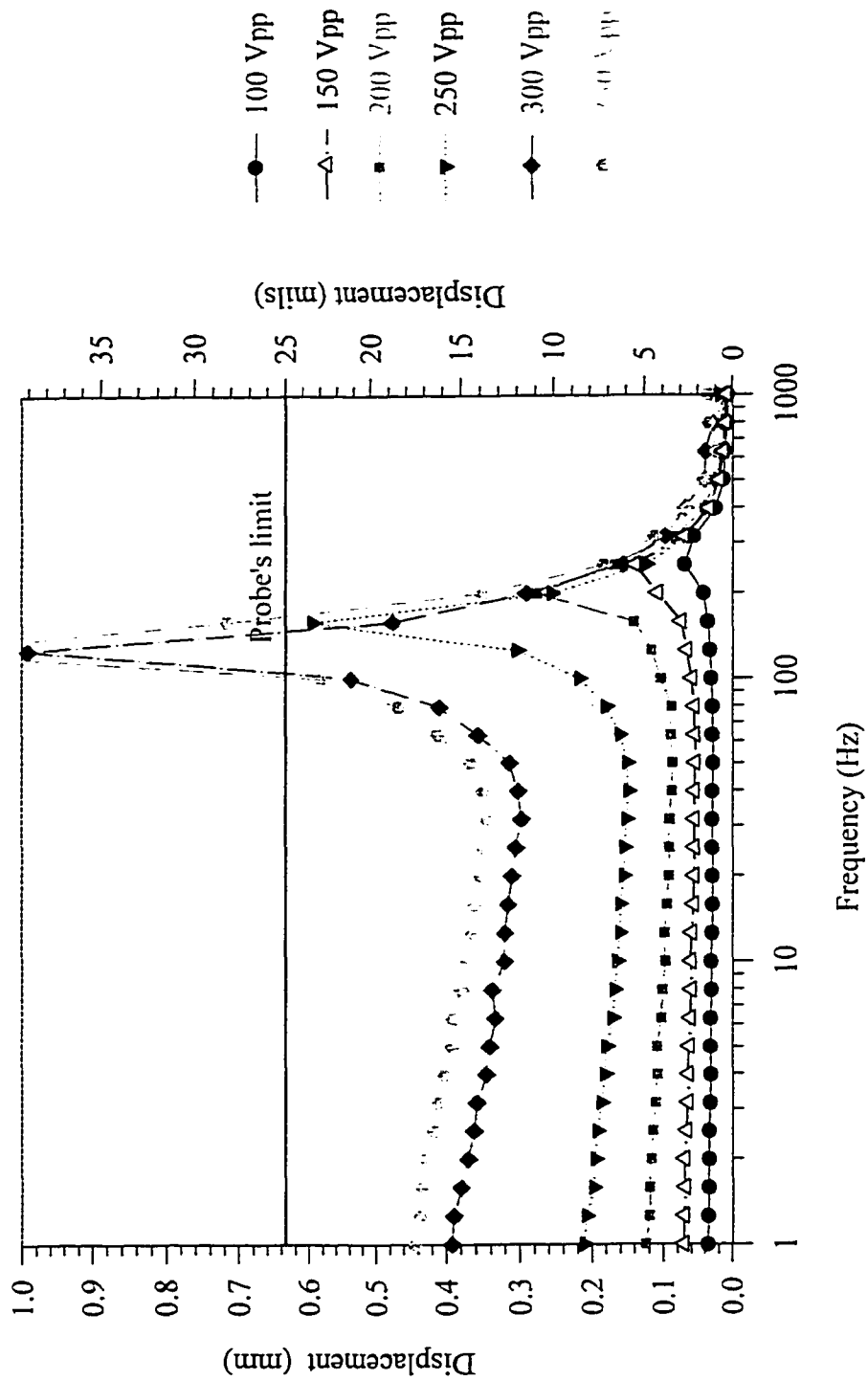


Figure 3.6 Displacement vs. Frequency for Varying Voltage Levels for Configuration 1/3-Al/Al, with No Re-Poling

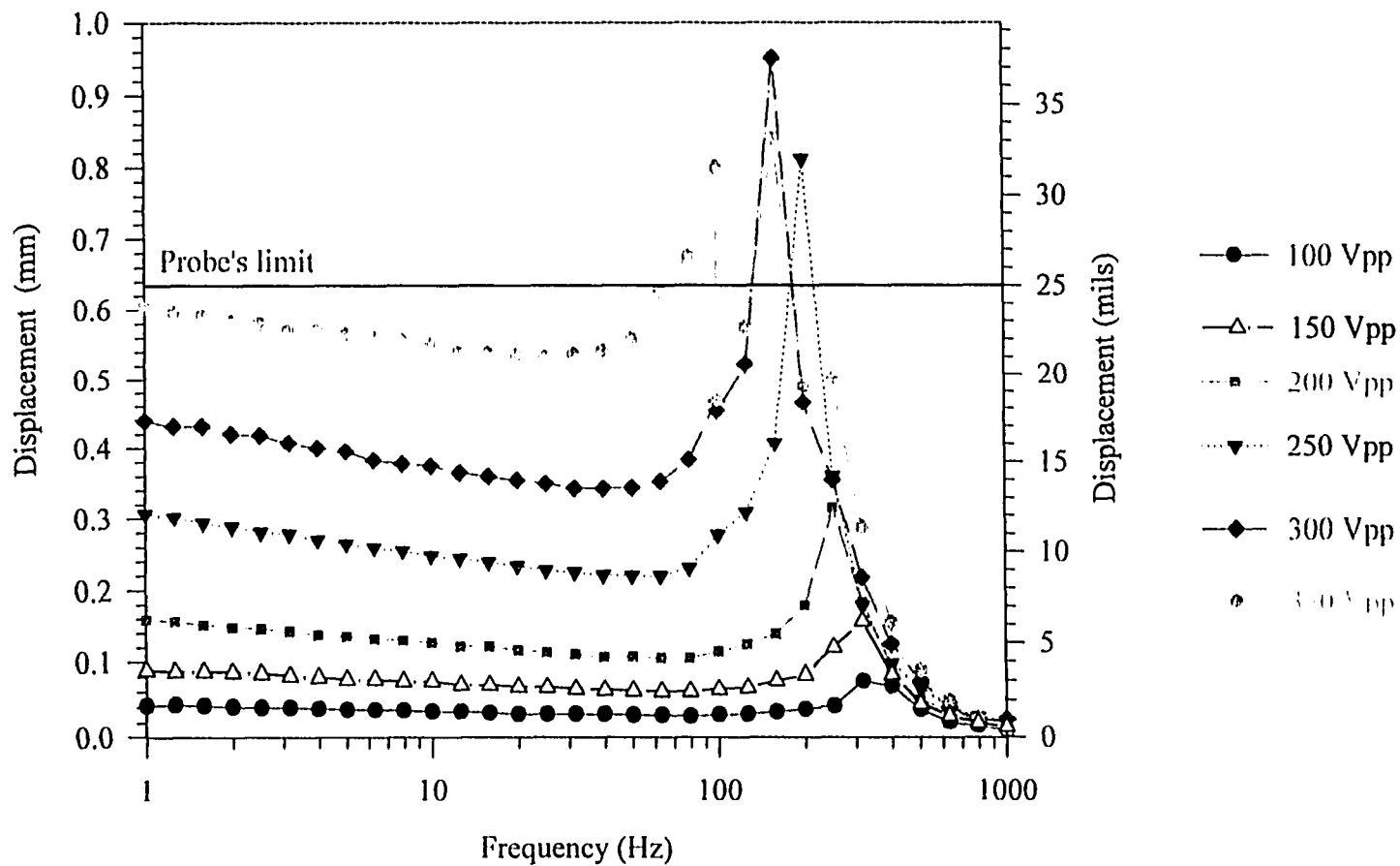


Figure 3.7 Displacement vs. Frequency for Varying Voltage Levels for Configuration 1/5-Al/Al, with No Re-Poling

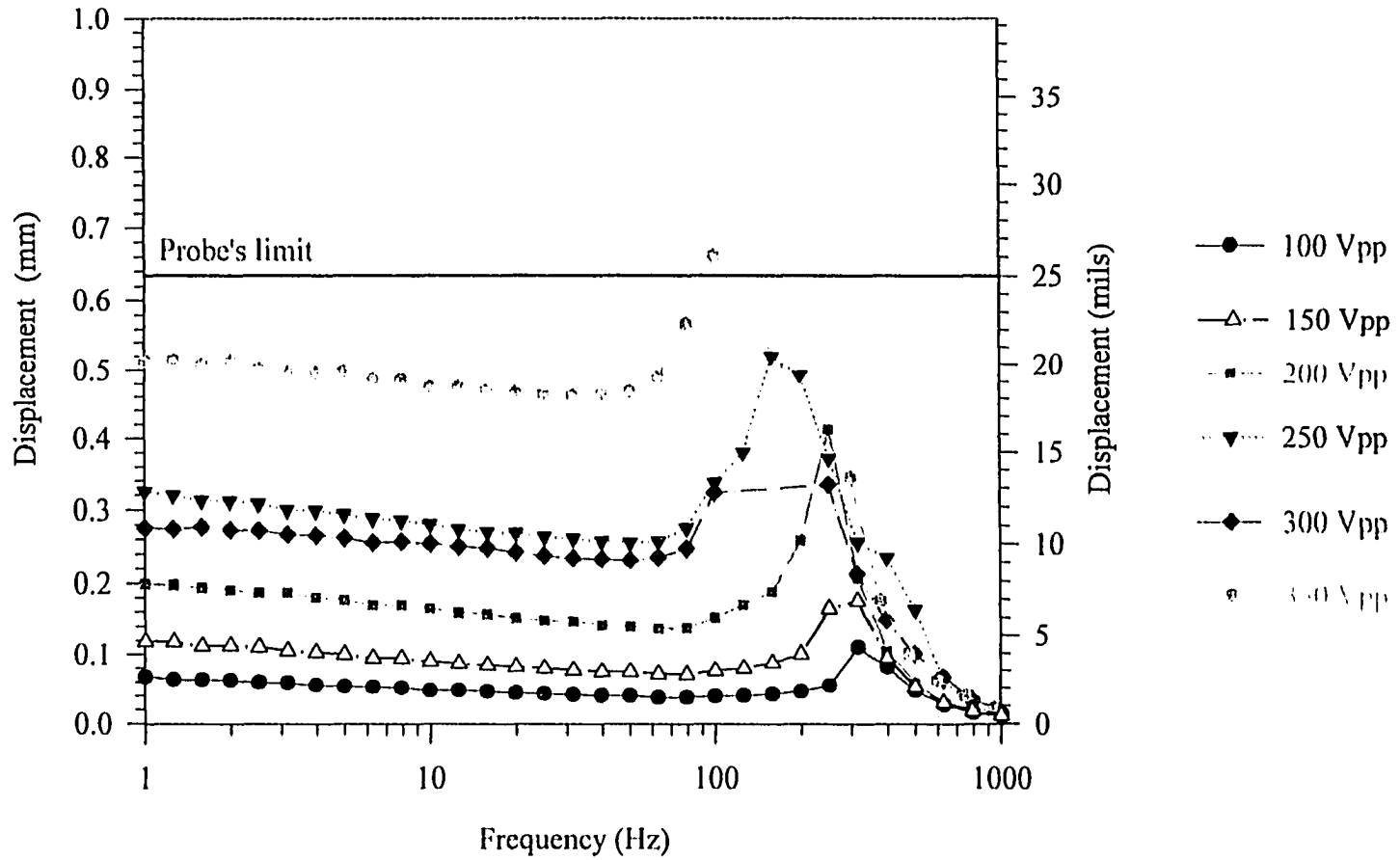


Figure 3.8 Displacement vs. Frequency for Varying Voltage Levels for Configuration 1/7-Al/Al, with No Re-Poling

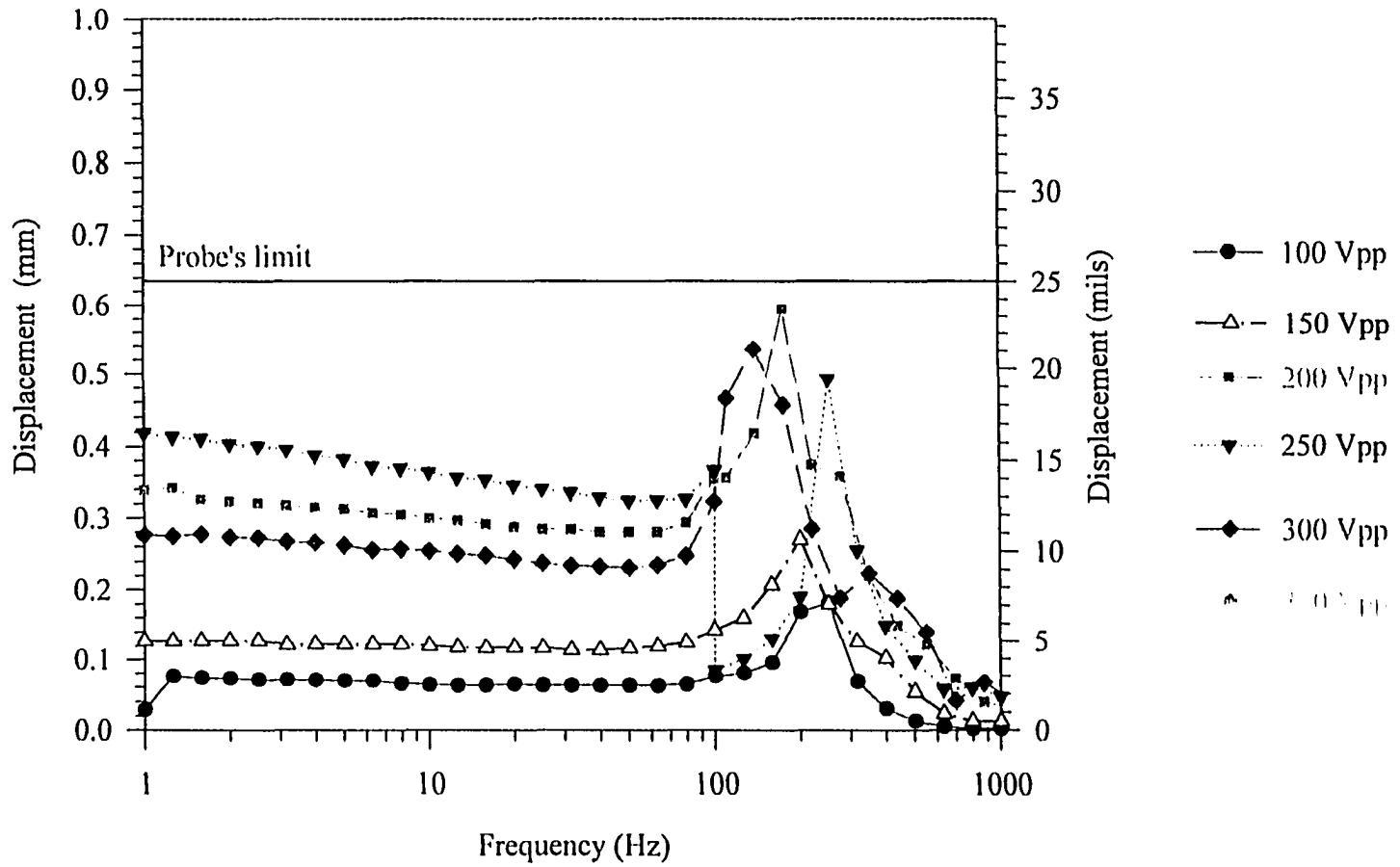


Figure 3.9 Displacement vs. Frequency for Varying Voltage Levels for Configuration 1/9-Al/Al, with No Re-Poling

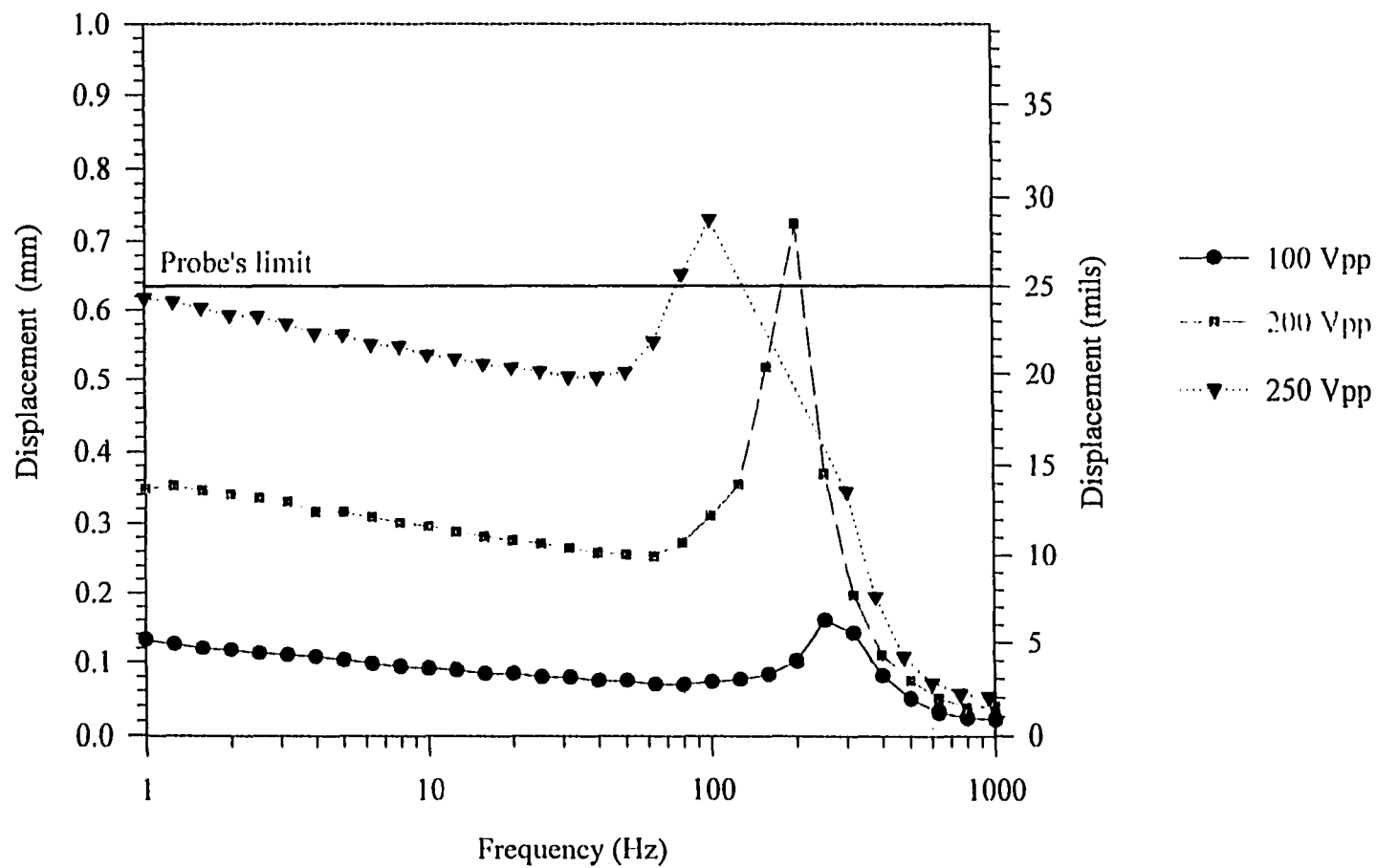


Figure 3.10 Displacement vs. Frequency for Varying Voltage Levels for Configuration 0/1-x/Al-5, with No Re-Poling

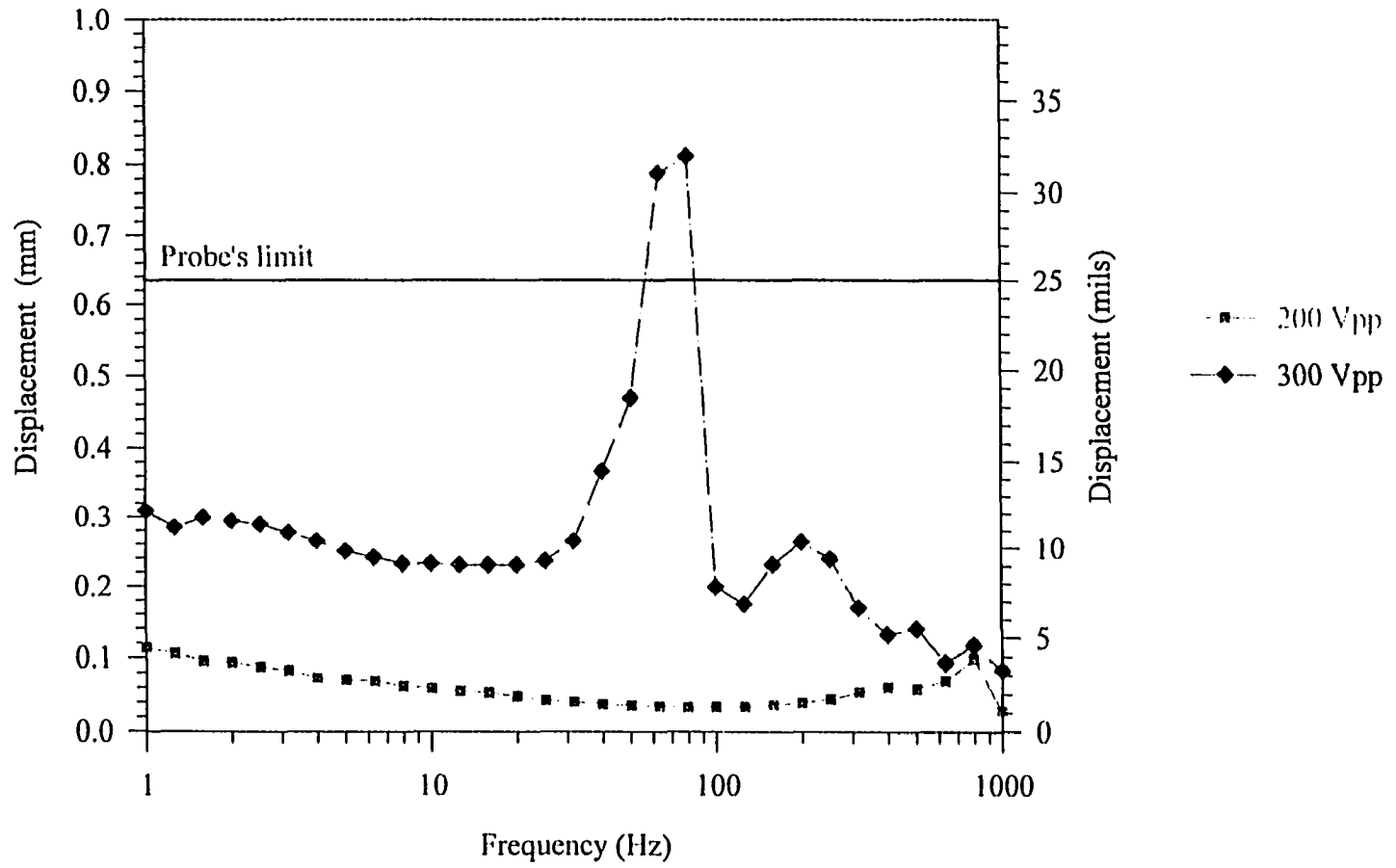


Figure 3.11 Displacement vs. Frequency for Varying Voltage Levels for Configuration 0/1-x/SS-1, with No Re-Poling

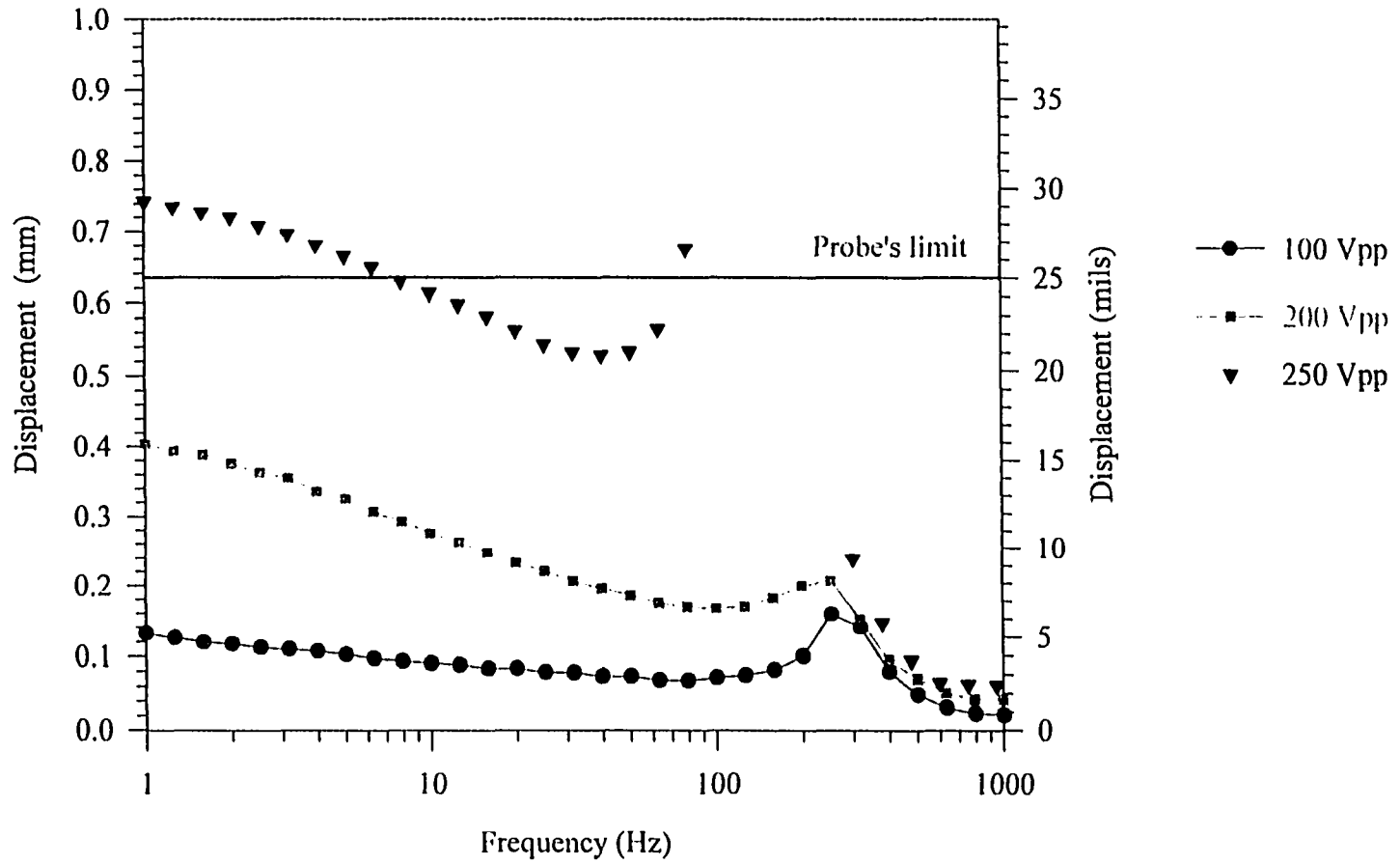


Figure 3.12 Displacement vs. Frequency for Varying Voltage Levels for Configuration 0/1-x/SS-3, with No Re-Poling

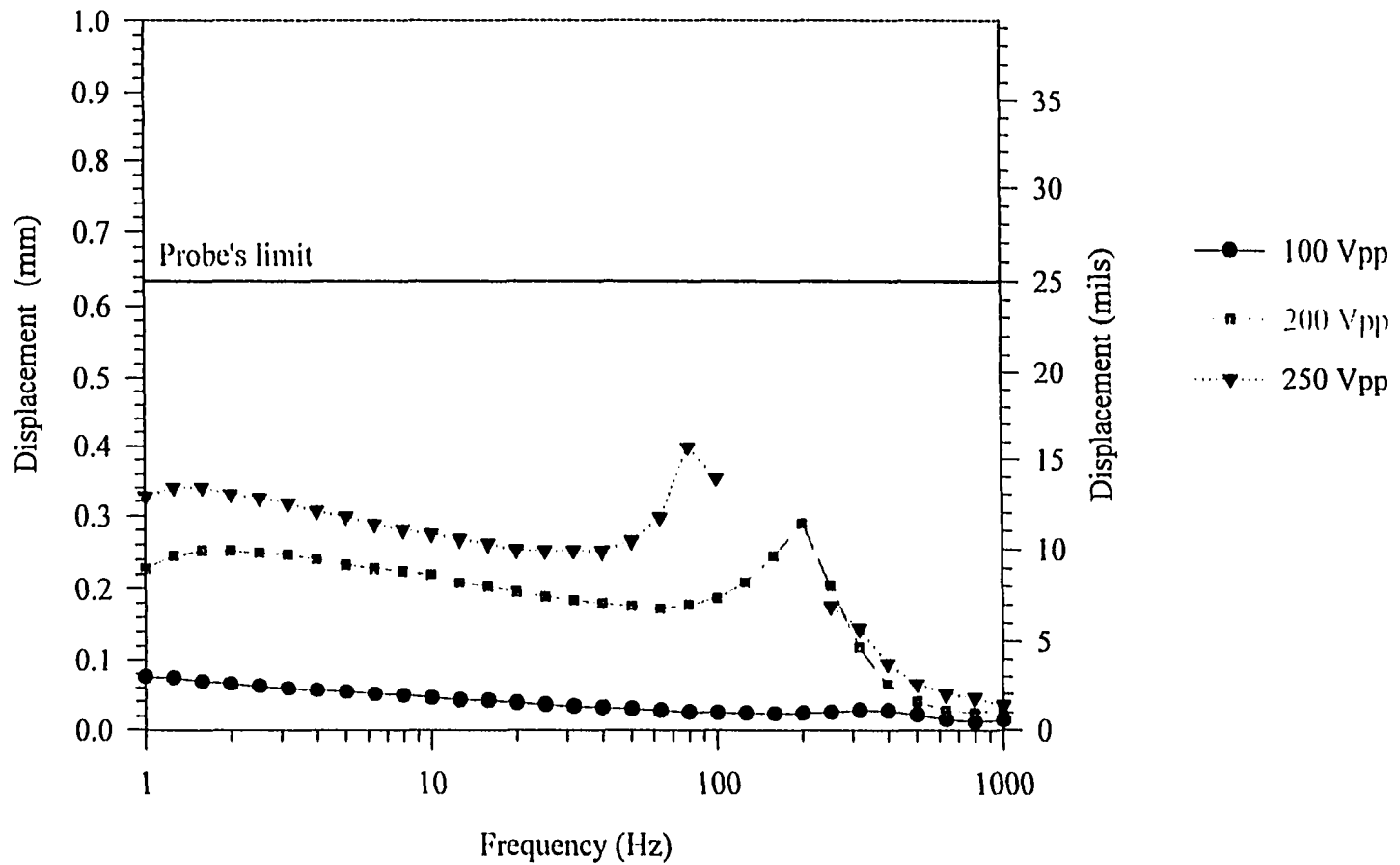


Figure 3.13 Displacement vs. Frequency for Varying Voltage Levels for Configuration 0/1-x/BeCu-2, with No Re-Poling

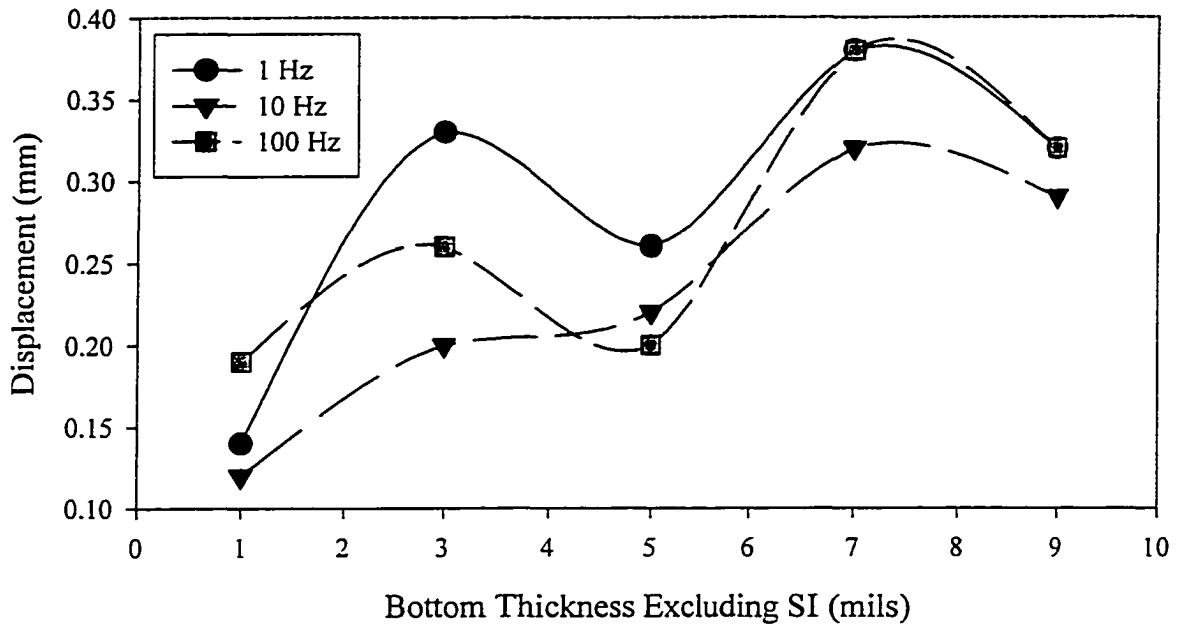


Figure 3.14 Displacement of x/Al Configuration vs. Theoretical Total Bottom-Layer Thickness at 1, 10, and 100 Hz before Re-Poling

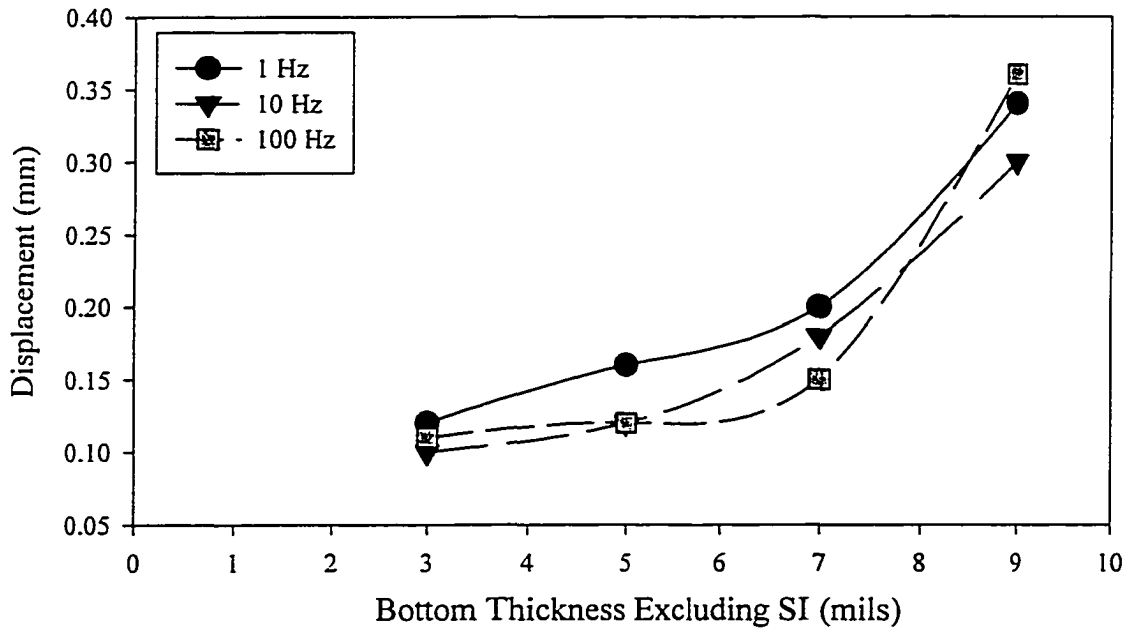


Figure 3.15 Displacement of Al/Al Configuration vs. Theoretical Total Bottom-Layer Thickness at 1, 10, and 100 Hz before Re-Poling

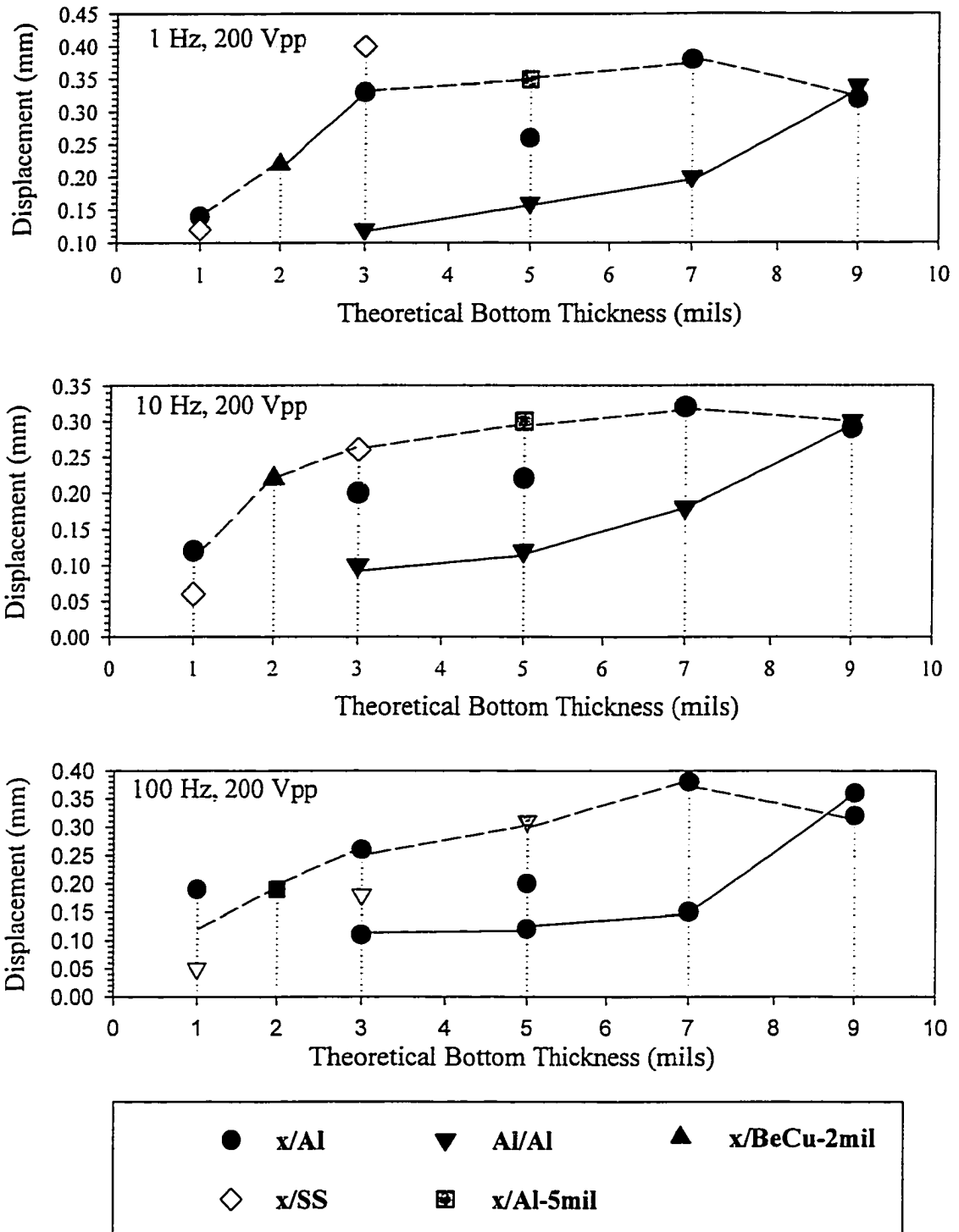


Figure 3.16 Probable Trends in Displacement vs. Number of Backing Layers before Re-Poling.

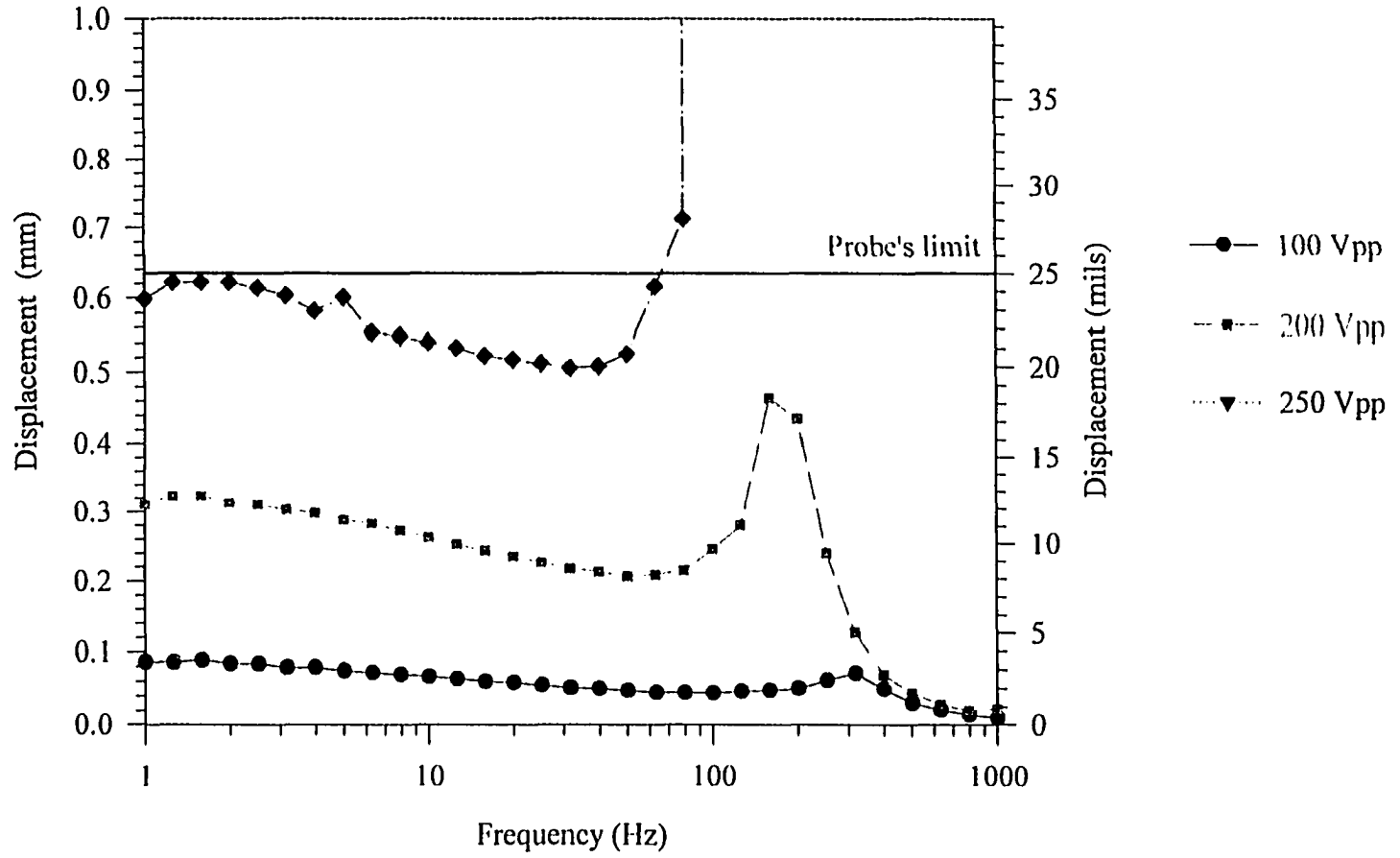


Figure 3.17 Displacement vs. Frequency for Varying Voltage Levels for Configuration 0/3-x/A1, after Re-Poling

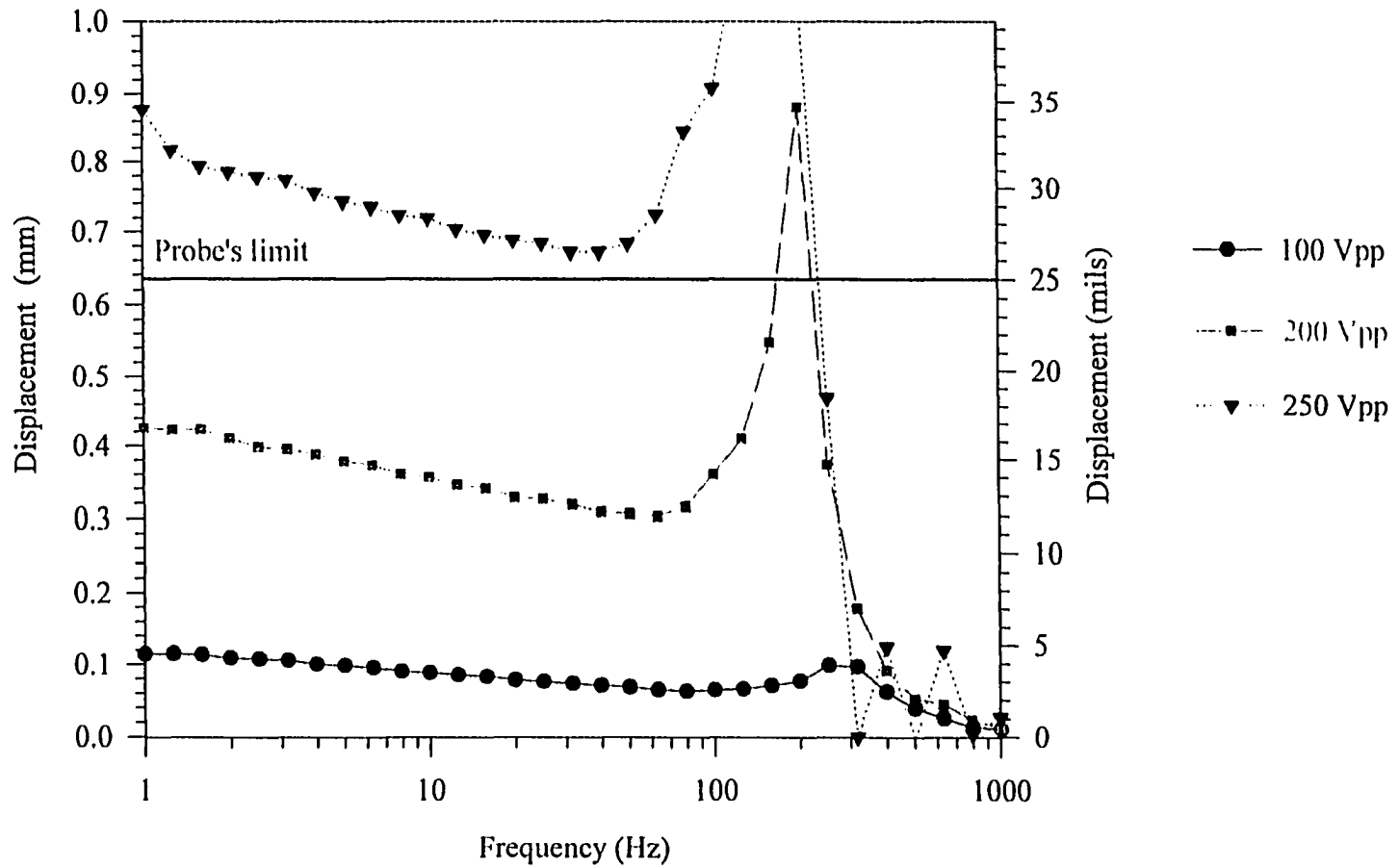


Figure 3.18 Displacement vs. Frequency for Varying Voltage Levels for Configuration 0/5-x/Al, after Re-Poling

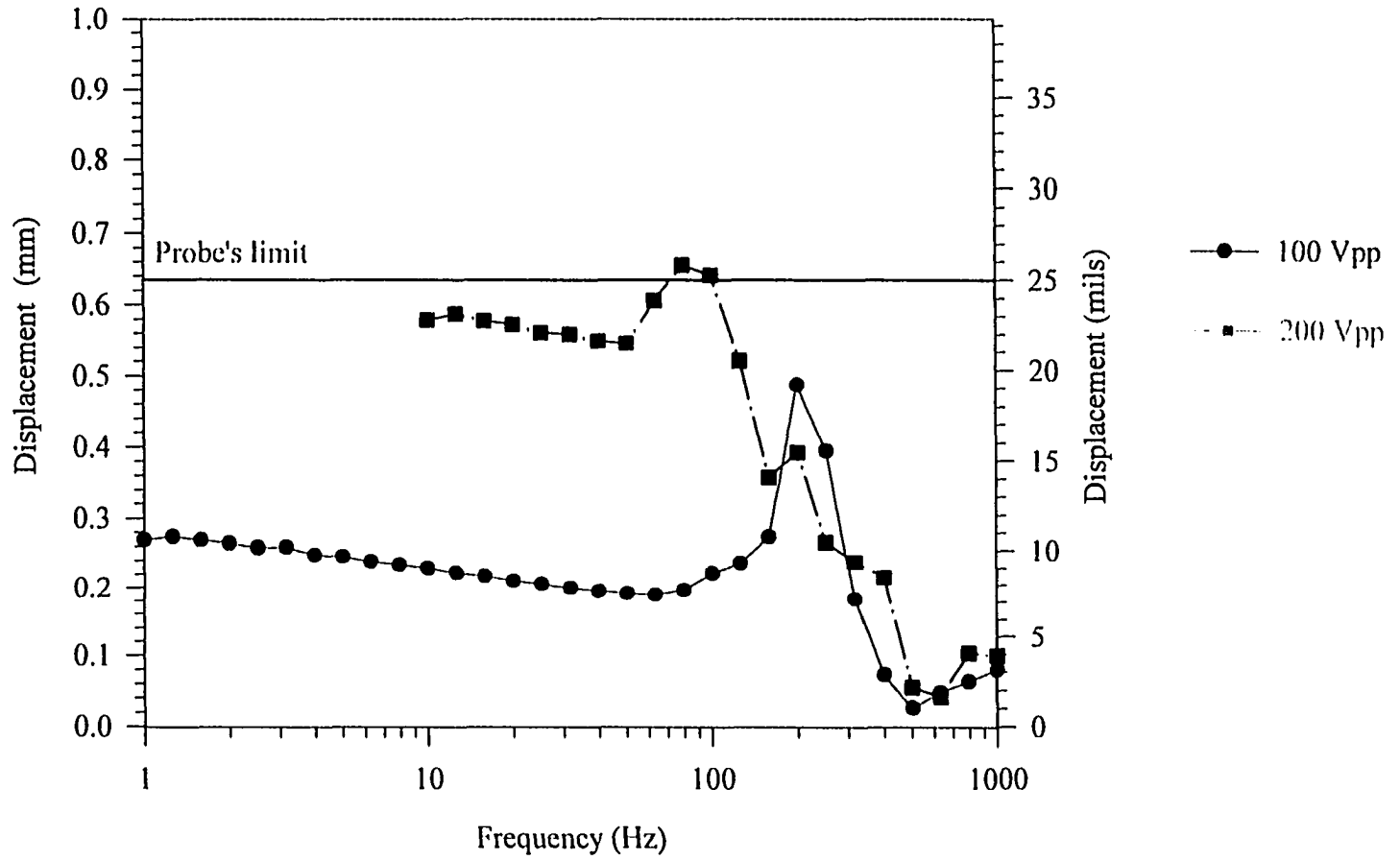


Figure 3.19 Displacement vs. Frequency for Varying Voltage Levels for Configuration 0/7-x/Al, after Re-Poling

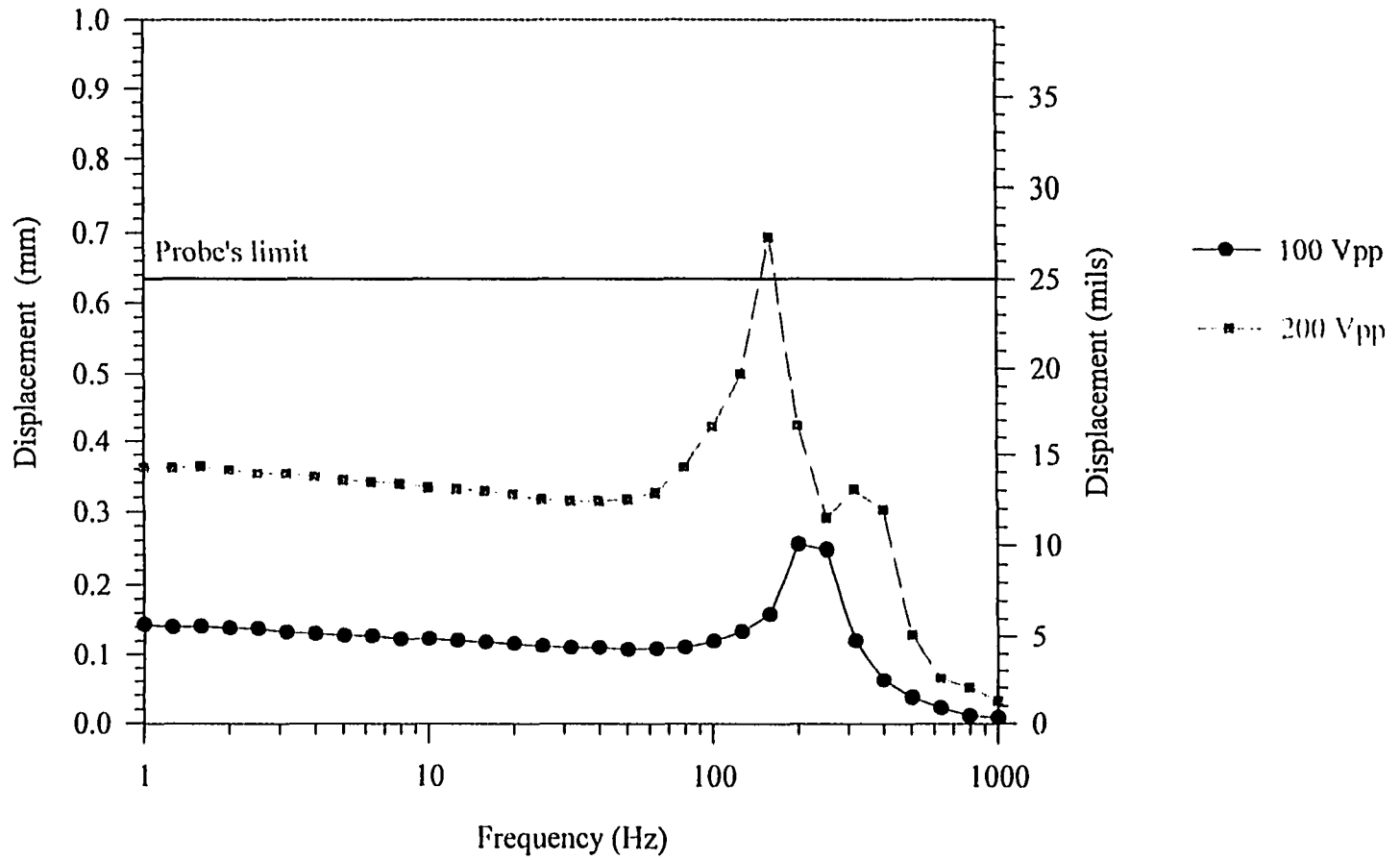


Figure 3.20 Displacement vs. Frequency for Varying Voltage Levels for Configuration 0/9-x/A1, after Re-Poling

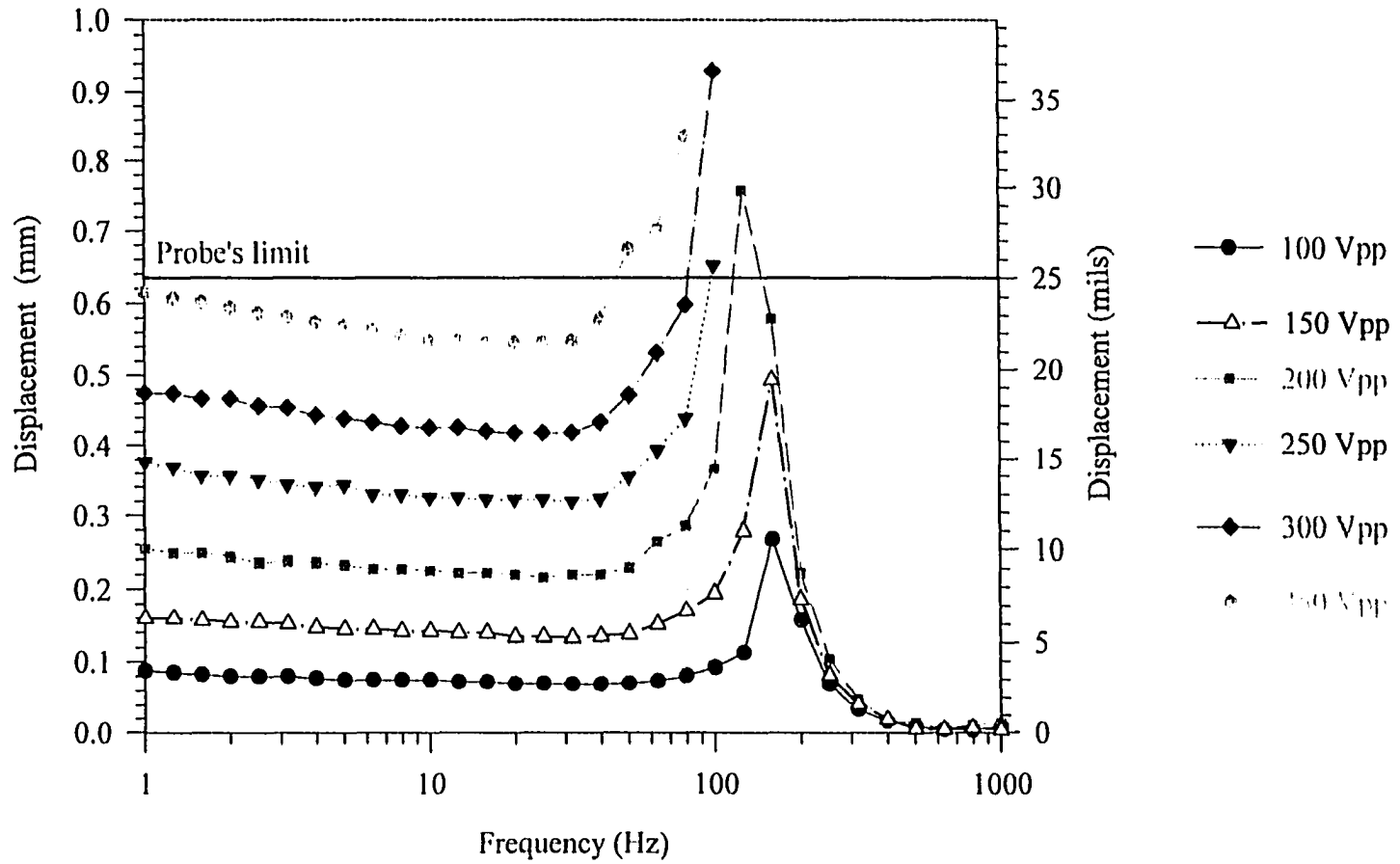


Figure 3.21 Displacement vs. Frequency for Varying Voltage Levels for Configuration 1/3-Al/Al, after Re-Poling

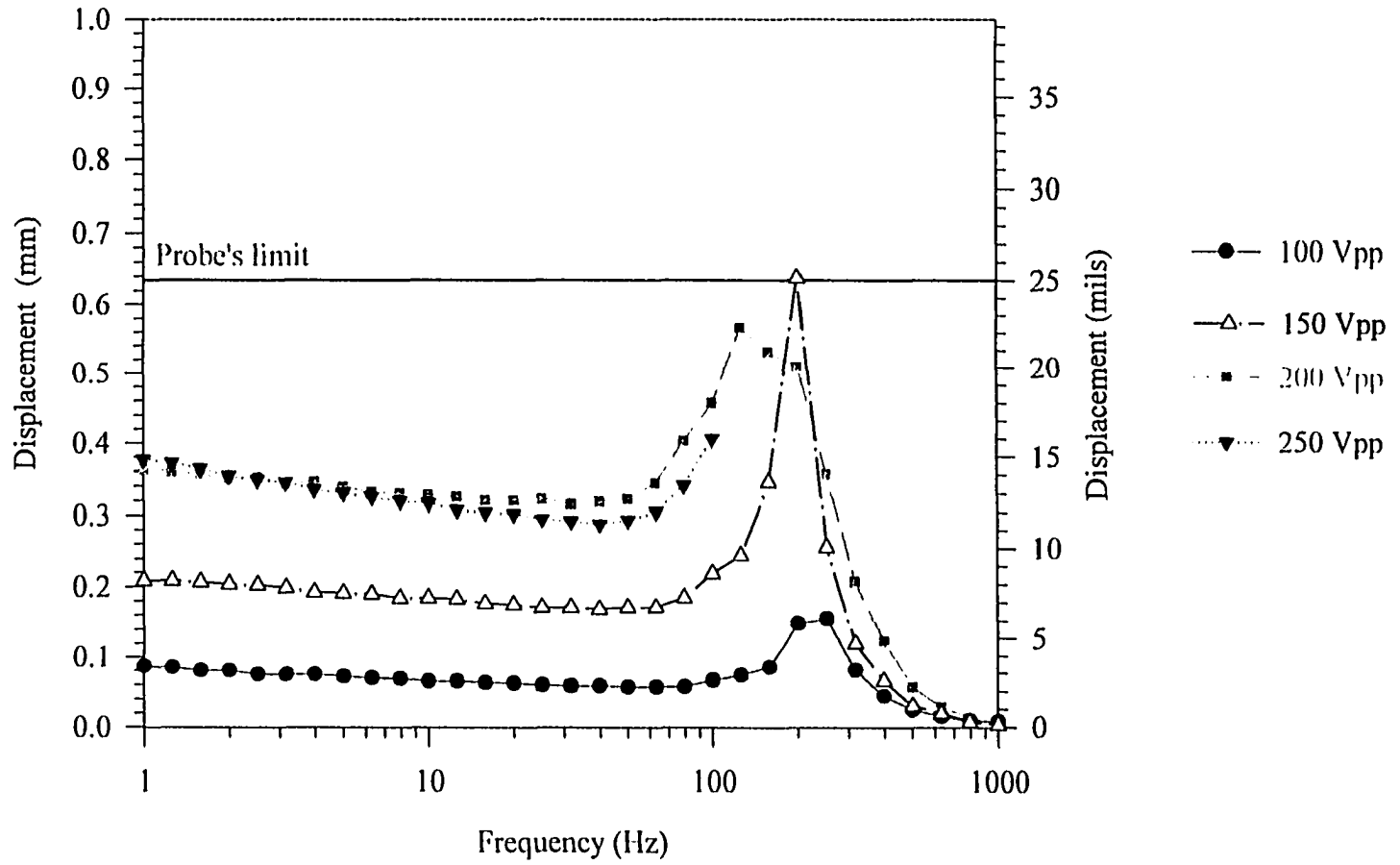


Figure 3.22 Displacement vs. Frequency for Varying Voltage Levels for Configuration 1/5-Al/Al, after Re-Poling

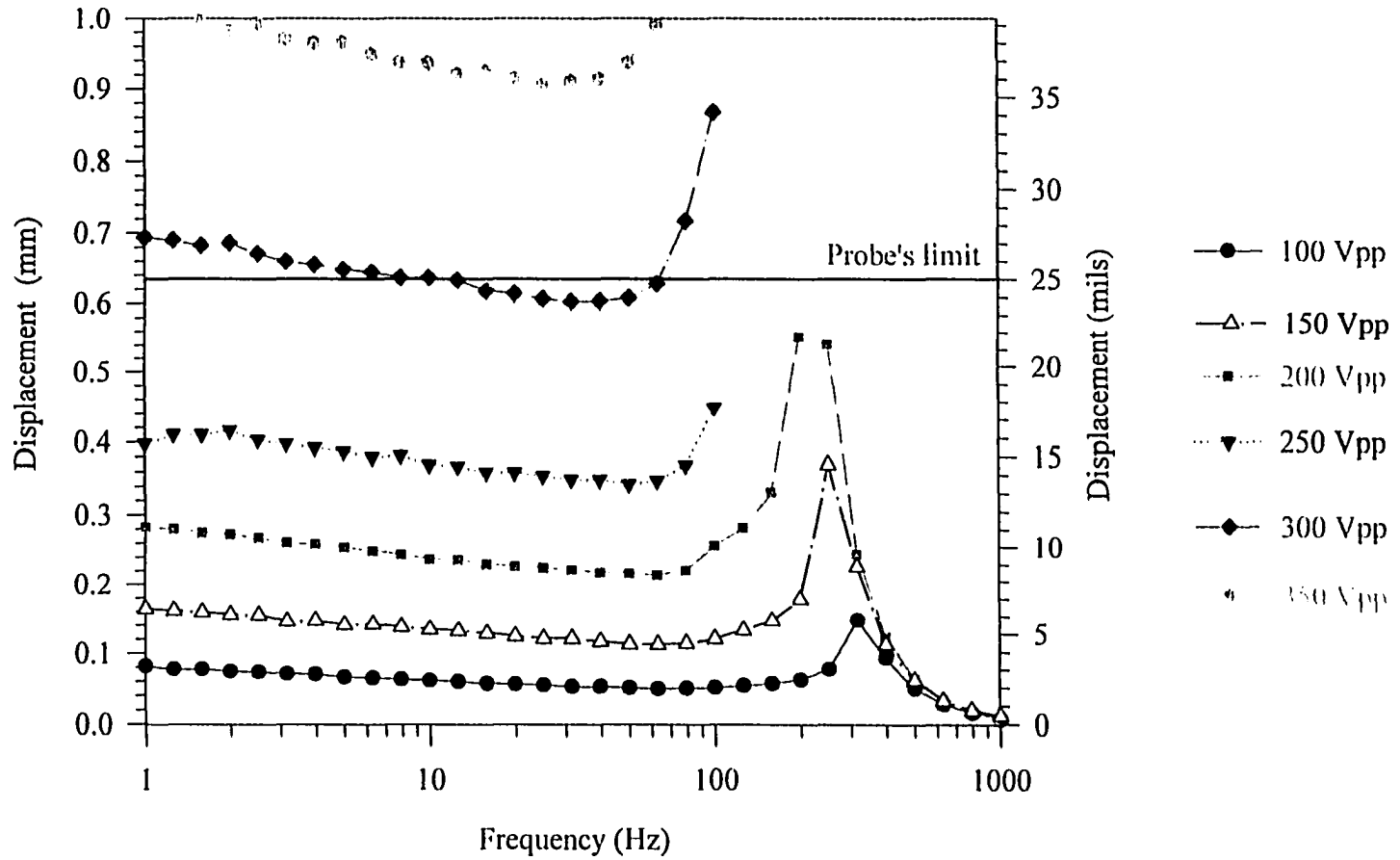


Figure 3.23 Displacement vs. Frequency for Varying Voltage Levels for Configuration 1/7-Al/Al, after Re-Poling

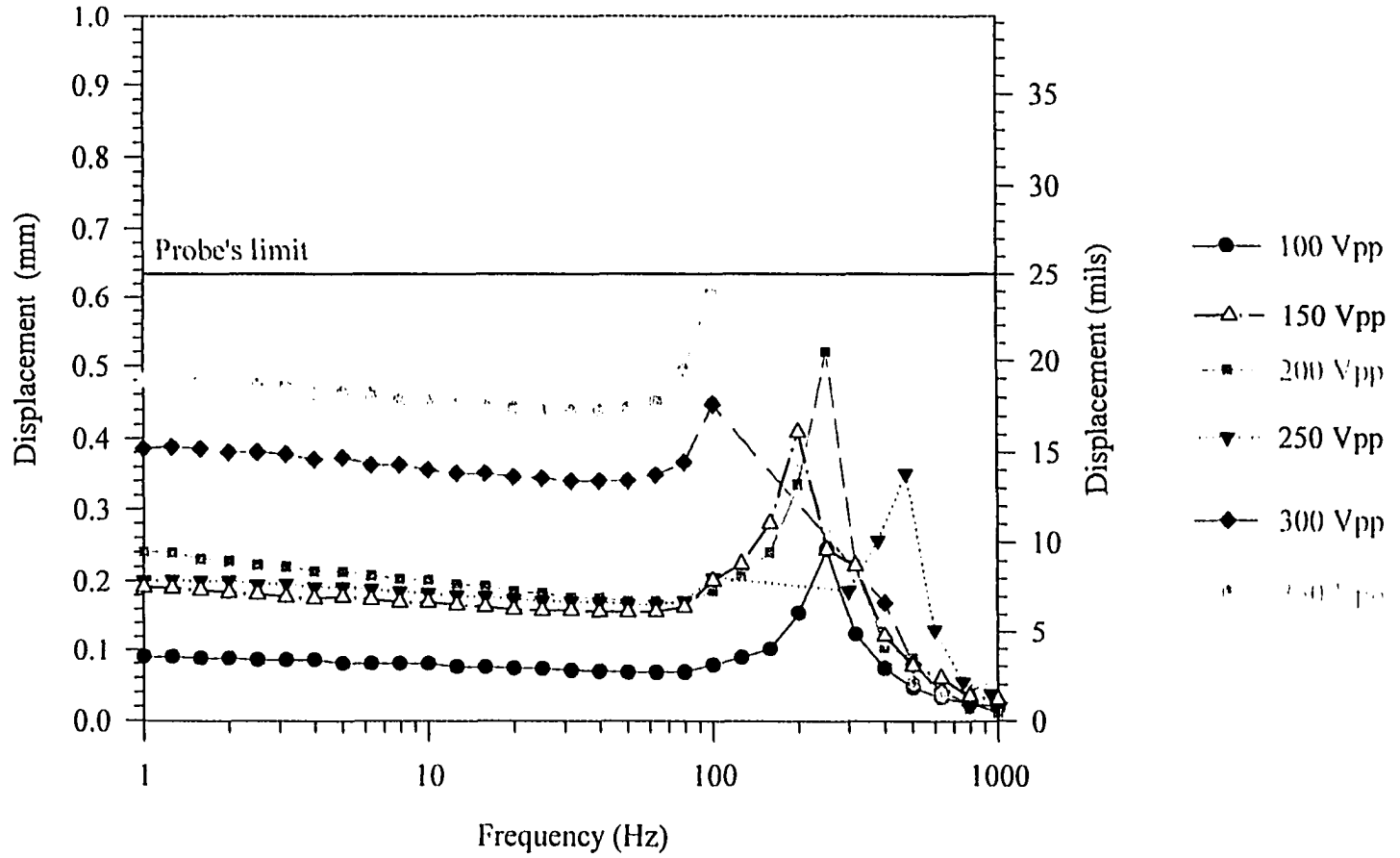


Figure 3.24 Displacement vs. Frequency for Varying Voltage Levels for Configuration 1/9-Al/Al, after Re-Poling

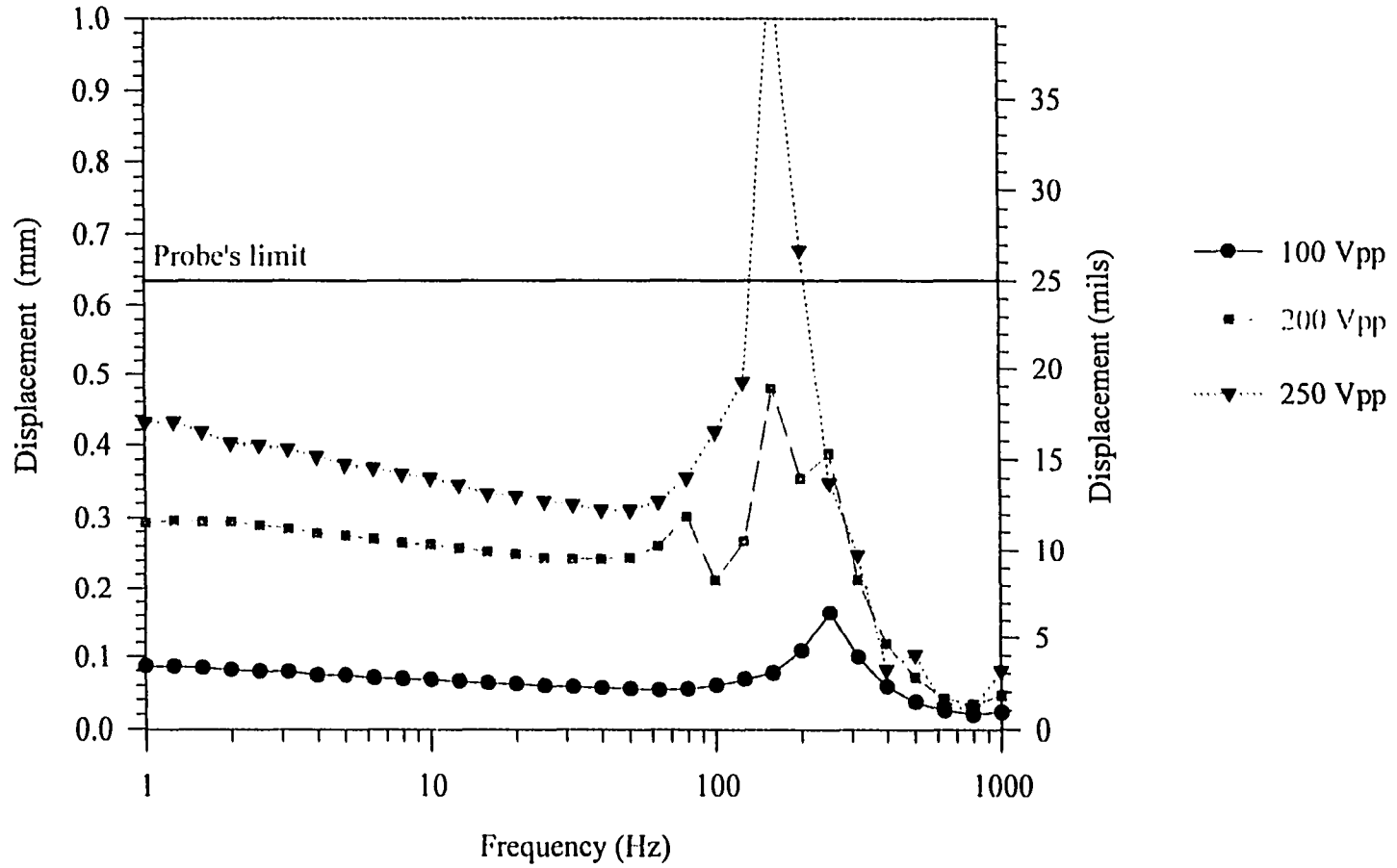


Figure 3.25 Displacement vs. Frequency for Varying Voltage Levels for Configuration 0/1-x/SS, after Re-Poling

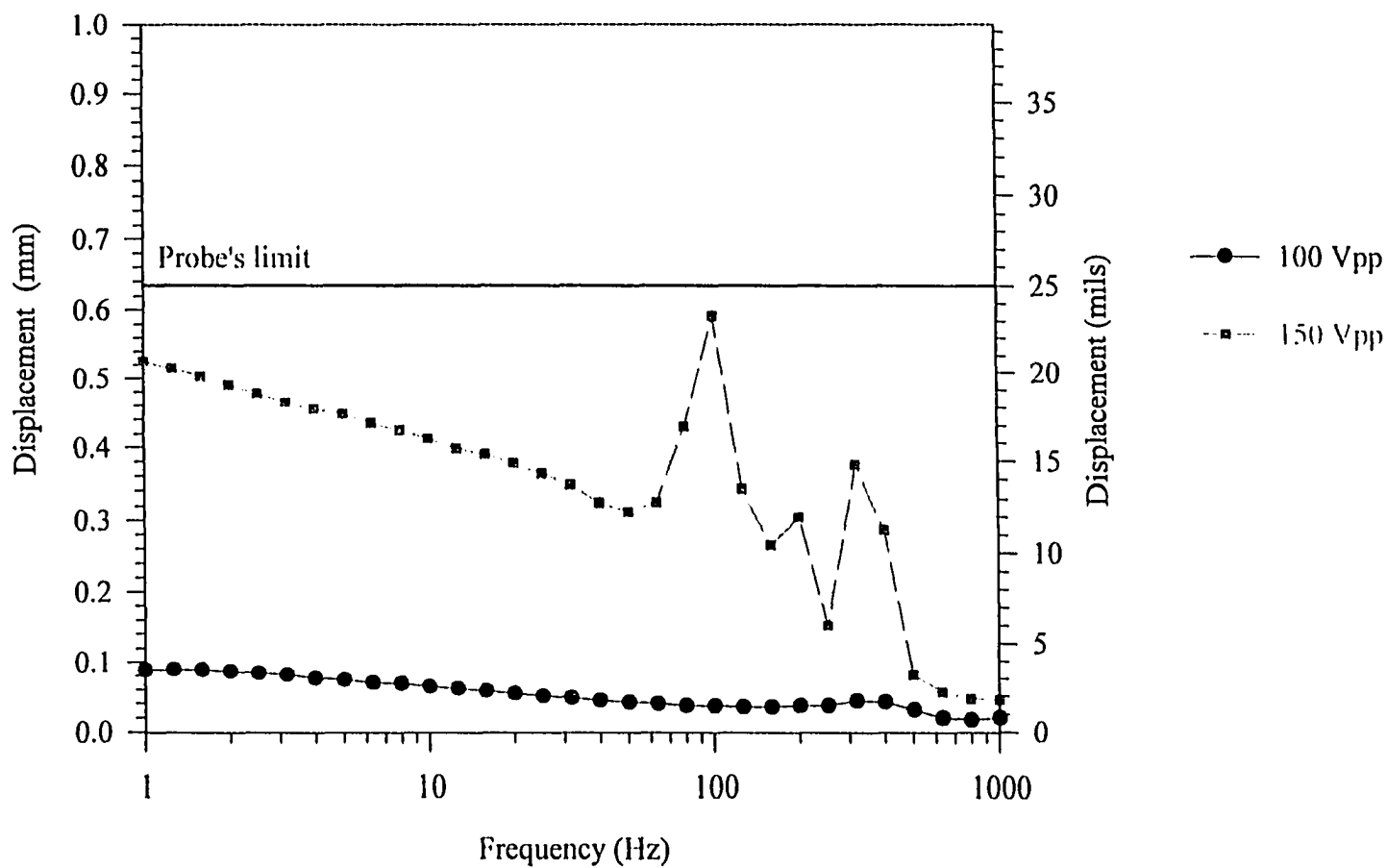


Figure 3.26 Displacement vs. Frequency for Varying Voltage Levels for Configuration 0/1-x/SS-3, after Re-Poling

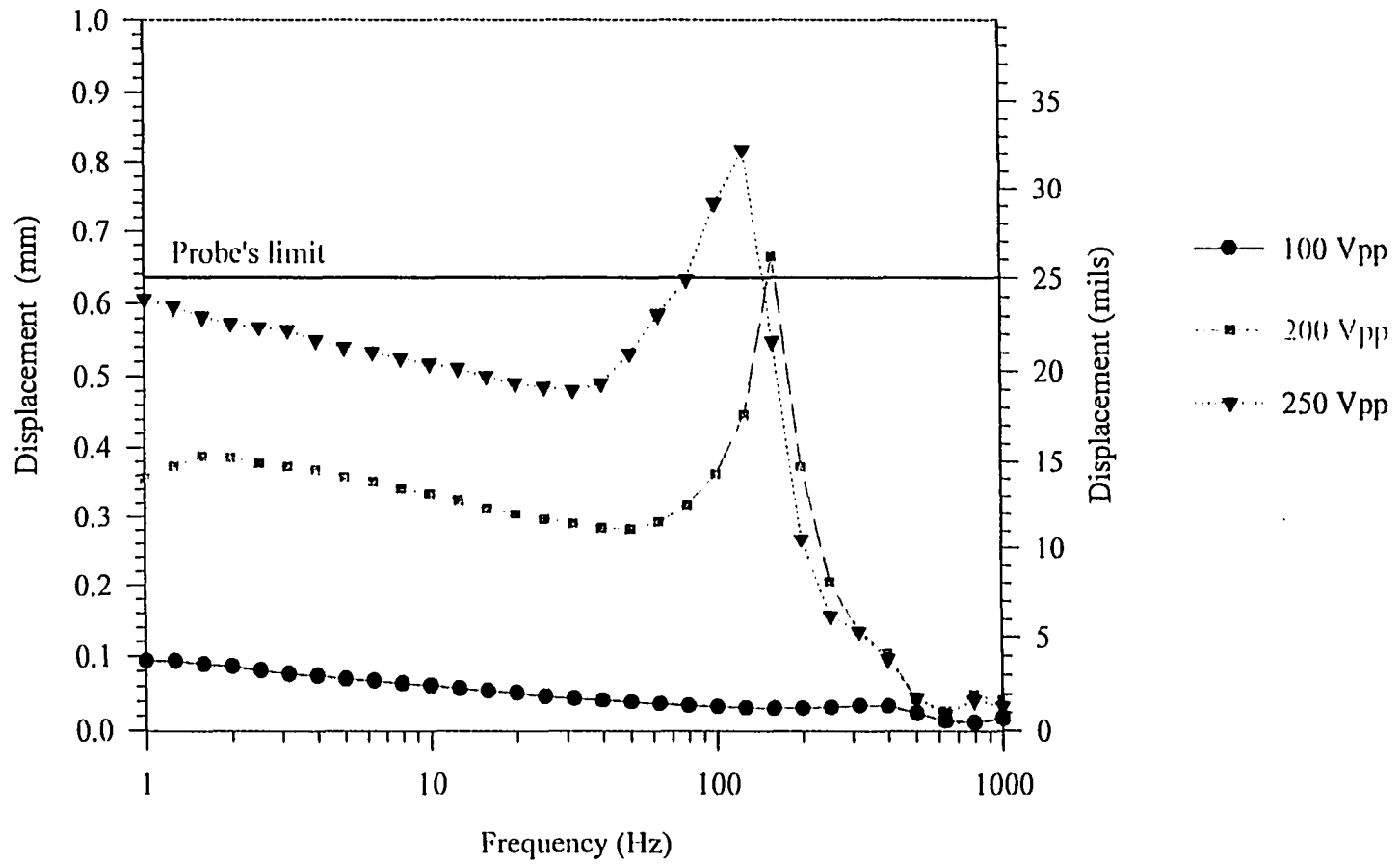


Figure 3.27 Displacement vs. Frequency for Varying Voltage Levels for Configuration 0/1-x/BeCu-2, after Re-Poling

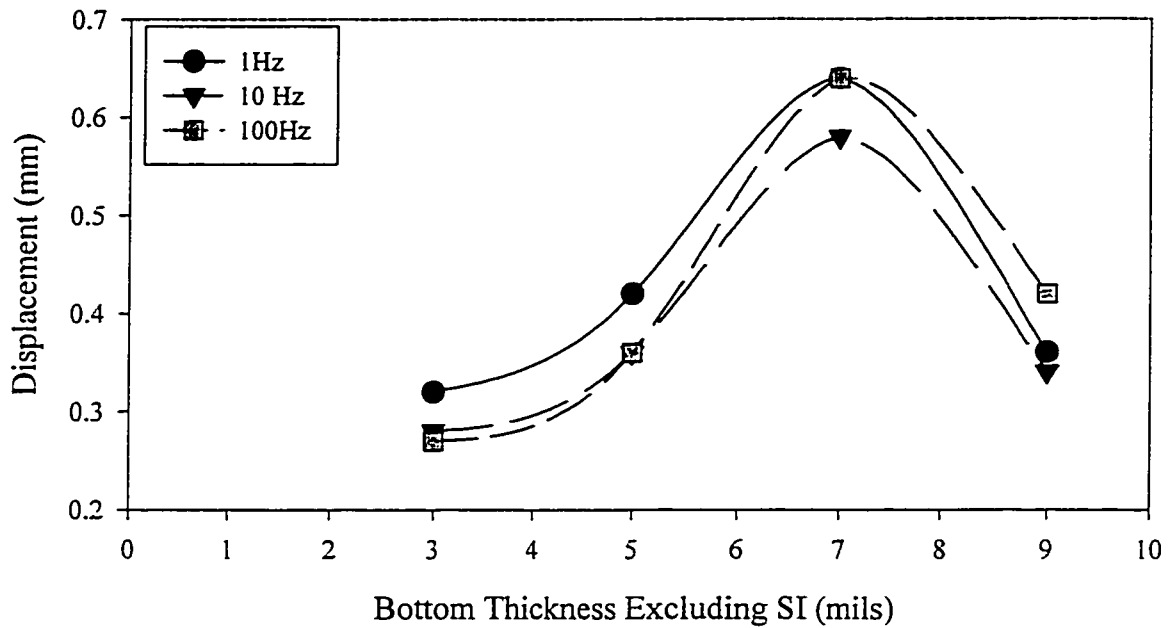


Figure 3.28 Displacement of x/Al Configuration vs. Theoretical Total Bottom-Layer Thickness at 1, 10, and 100 Hz after Re-Poling

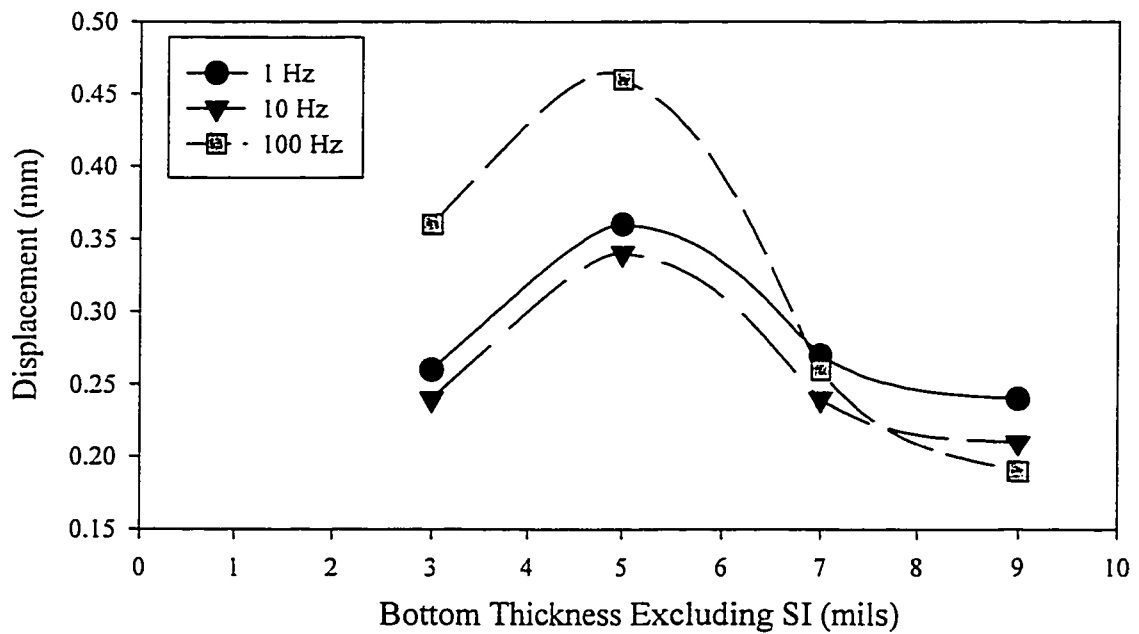


Figure 3.29 Displacement of Al/Al Configuration vs. Theoretical Total Bottom-Layer Thickness at 1, 10, and 100 Hz after Re-Poling

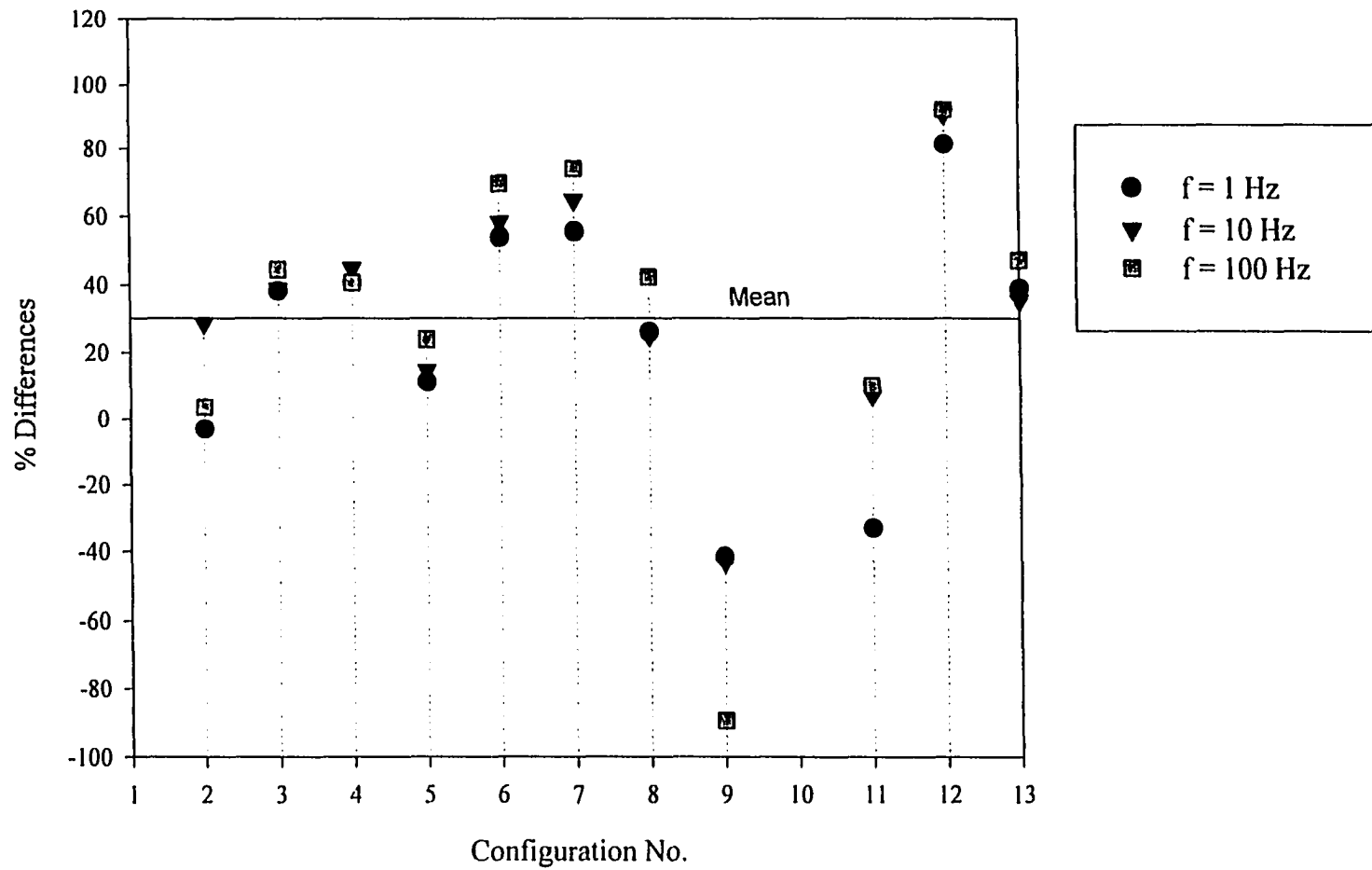
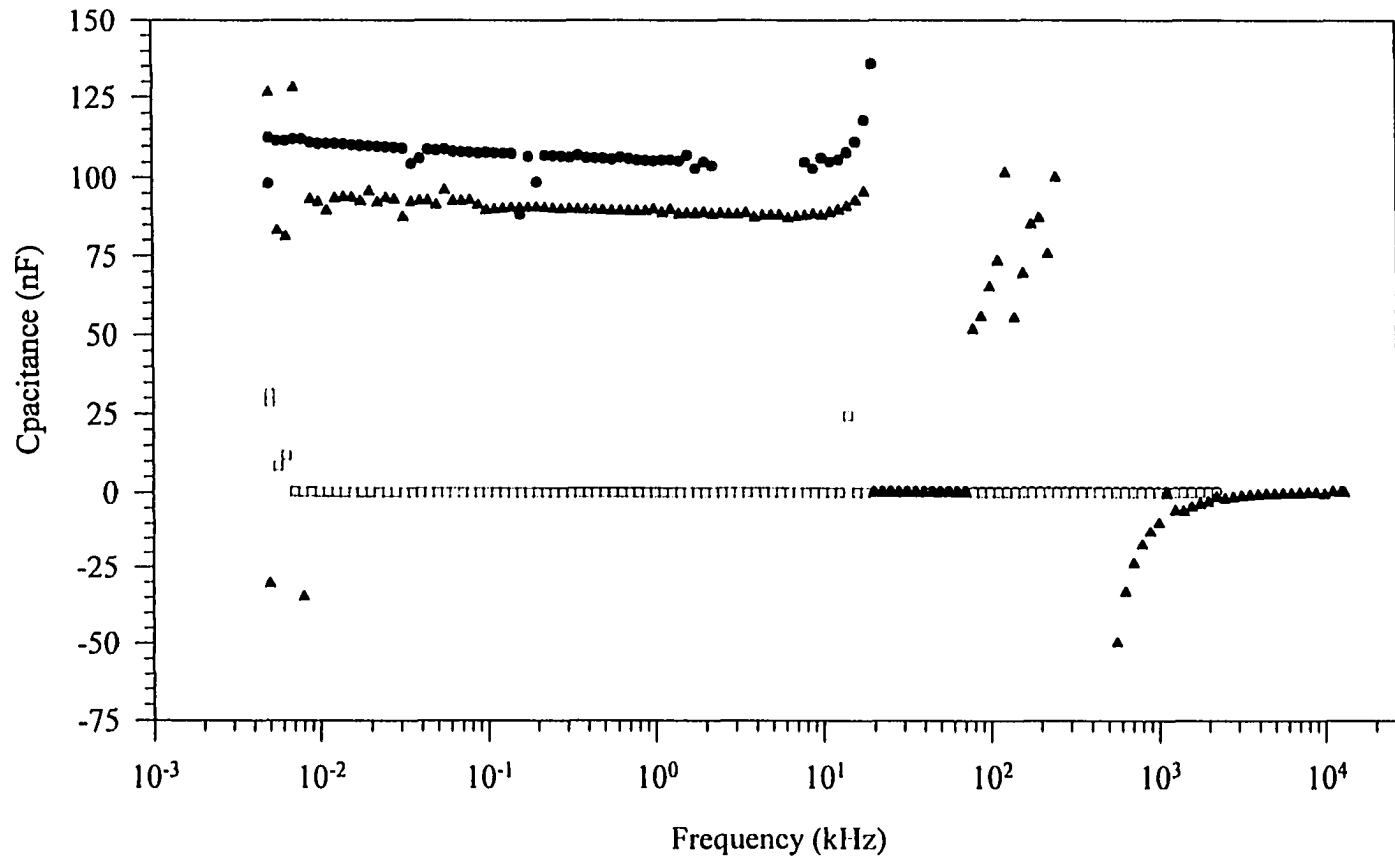


Figure 3.30 Performance of Re-Poled vs. Non Re-Poled Devices at an Applied Voltage of 200Vpp



● before autoclave / before processing /PZT-5A □ after autoclave/no re-poling ▲ after autoclave/after re-poling

Figure 3.31 Capacitance vs. Frequency for Configuration 0/1-x/Al at Different Processing Stages

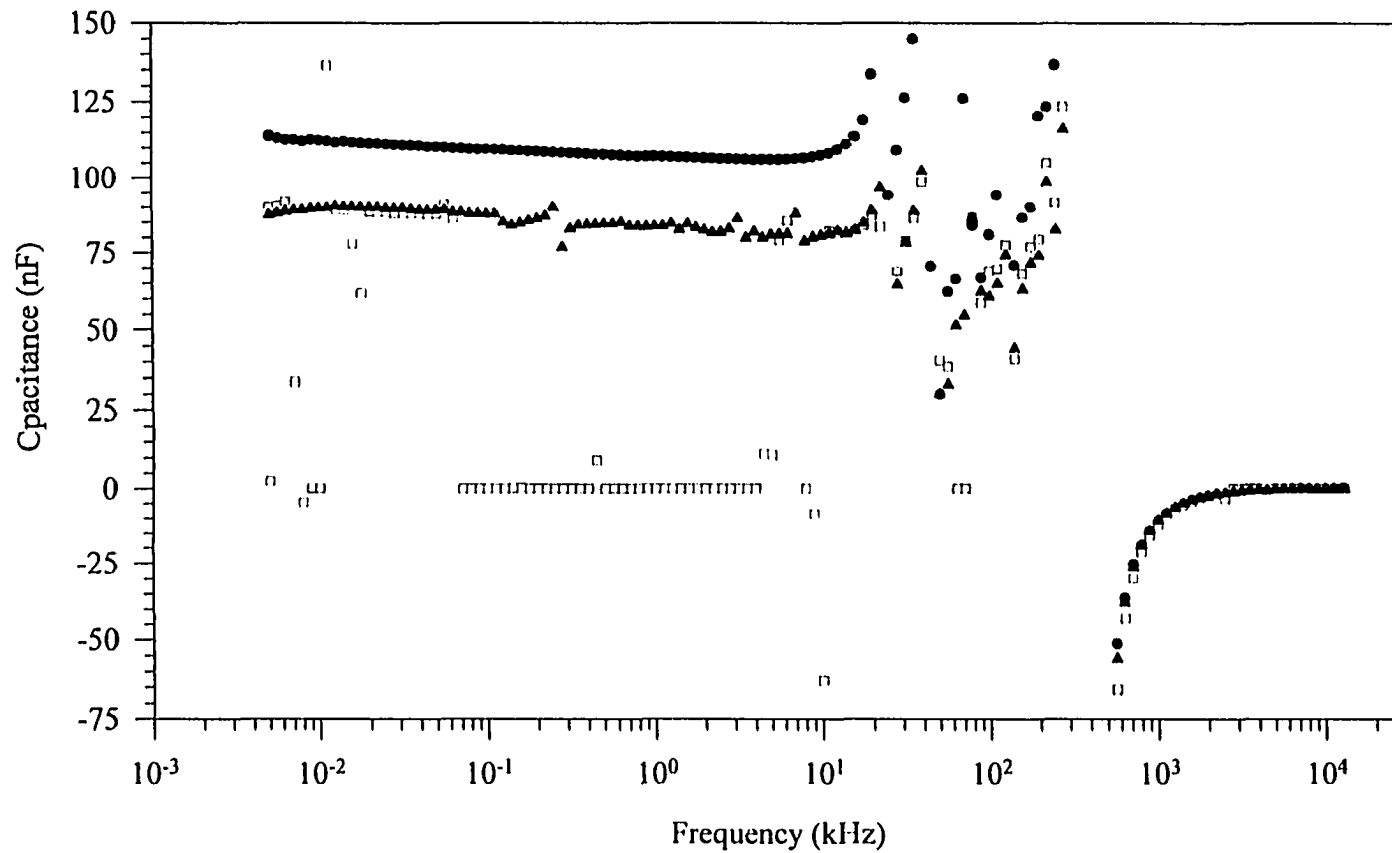
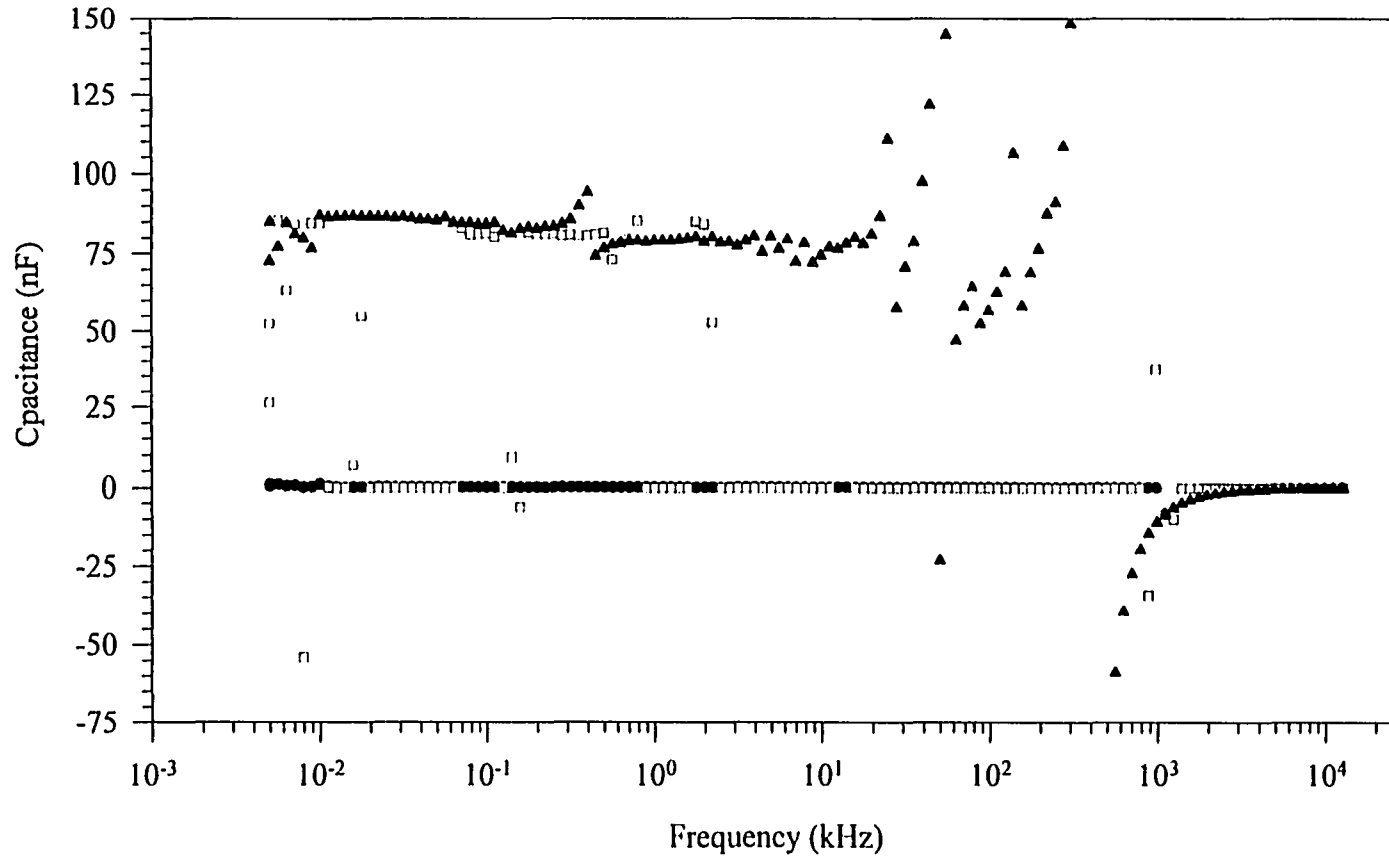
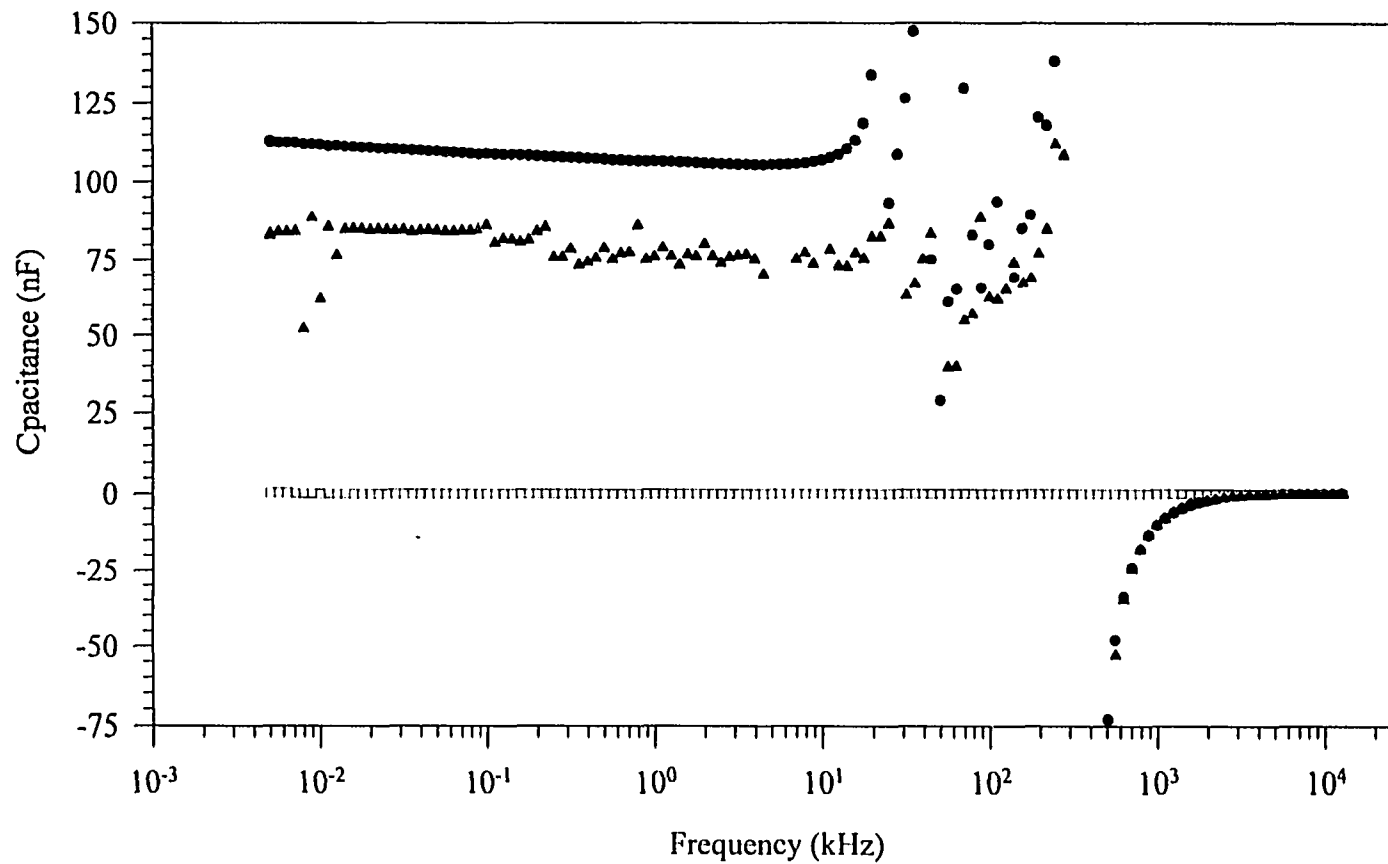


Figure 3.32 Capacitance vs. Frequency for Configuration 0/3-x/Al at Different Processing Stages



•	□	▲
before autoclave / before processing /PZT-5A	after autoclave/no re-poling	after autoclave/after re-poling

Figure 3.33 Capacitance vs. Frequency for Configuration 0/5-x/Al at Different Processing Stages



● before autoclave / before processing /PZT-5A ◻ after autoclave/no re-poling ▲ after autoclave/after re-poling

Figure 3.34 Capacitance vs. Frequency for Configuration 0/9-x/Al at Different Processing Stages

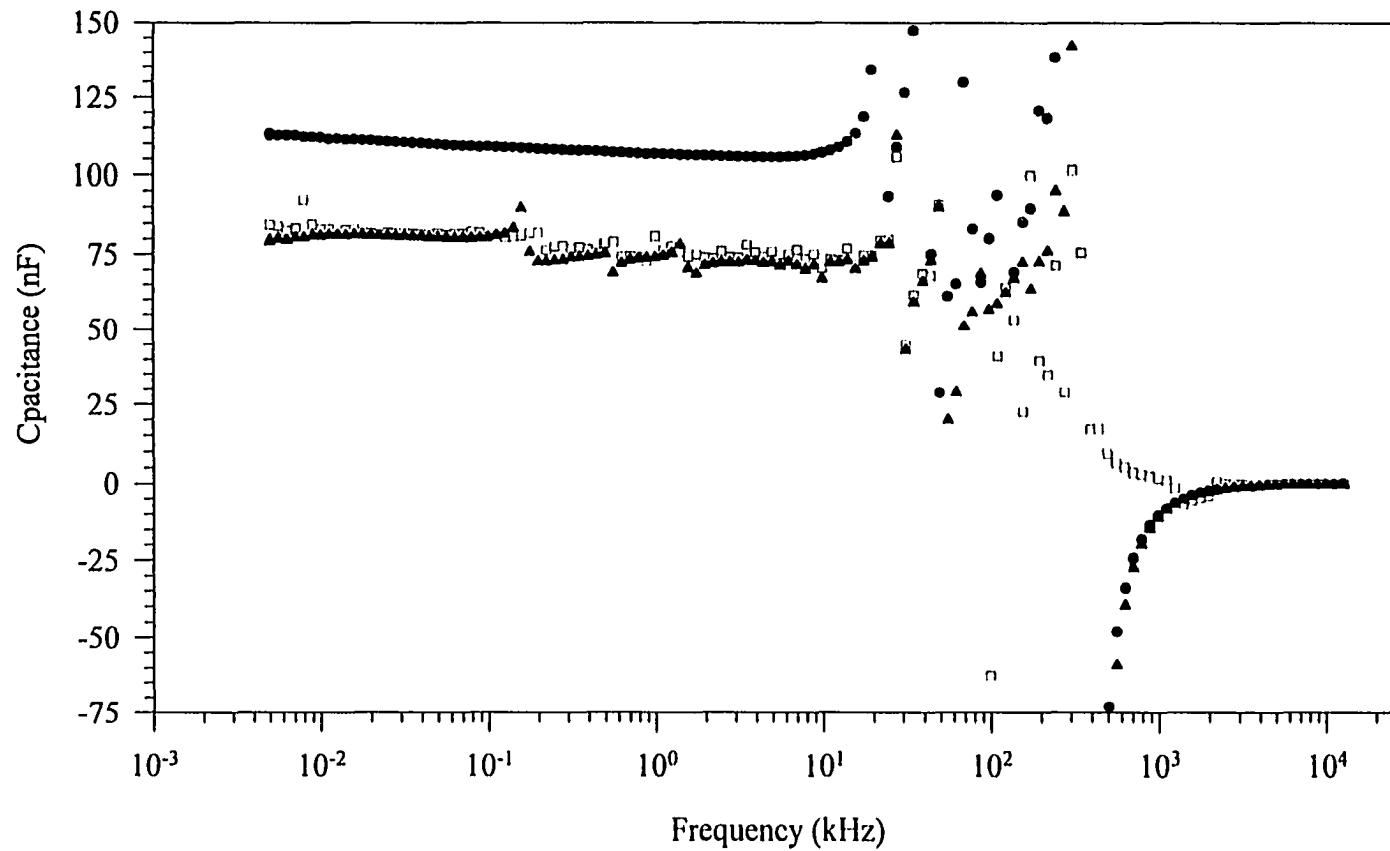
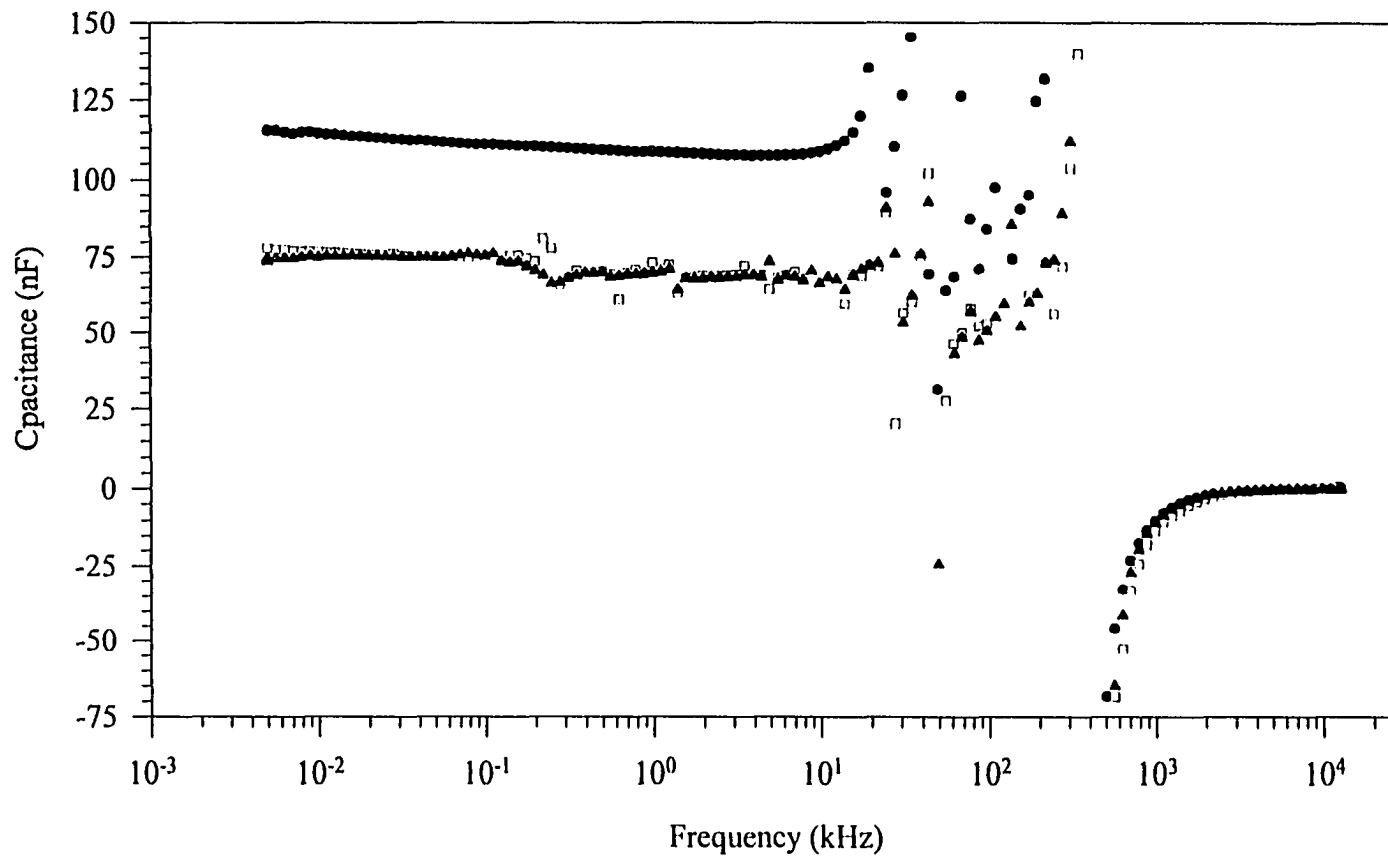


Figure 3.35 Capacitance vs. Frequency for Configuration 0/1-x/SS-3mil at Different Processing Stages



• before autoclave / before processing / PZT-5A □ after autoclave/no re-poling ▲ after autoclave/after re-poling

Figure 3.36 Capacitance vs. Frequency for Configuration 0/1-x/BeCu-2mil at Different Processing Stages

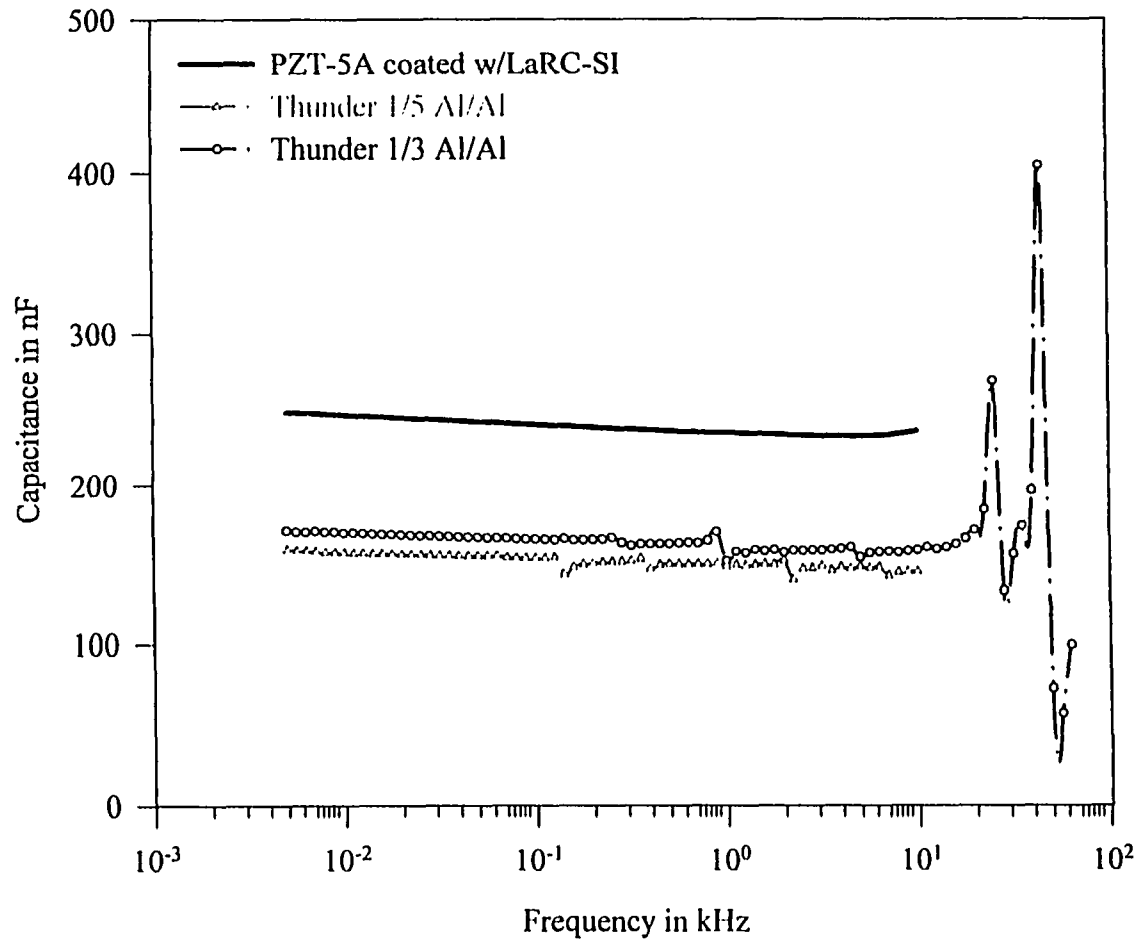


Figure 3.37 Capacitance vs. Frequency for Al/Al Configurations after Re-Poling

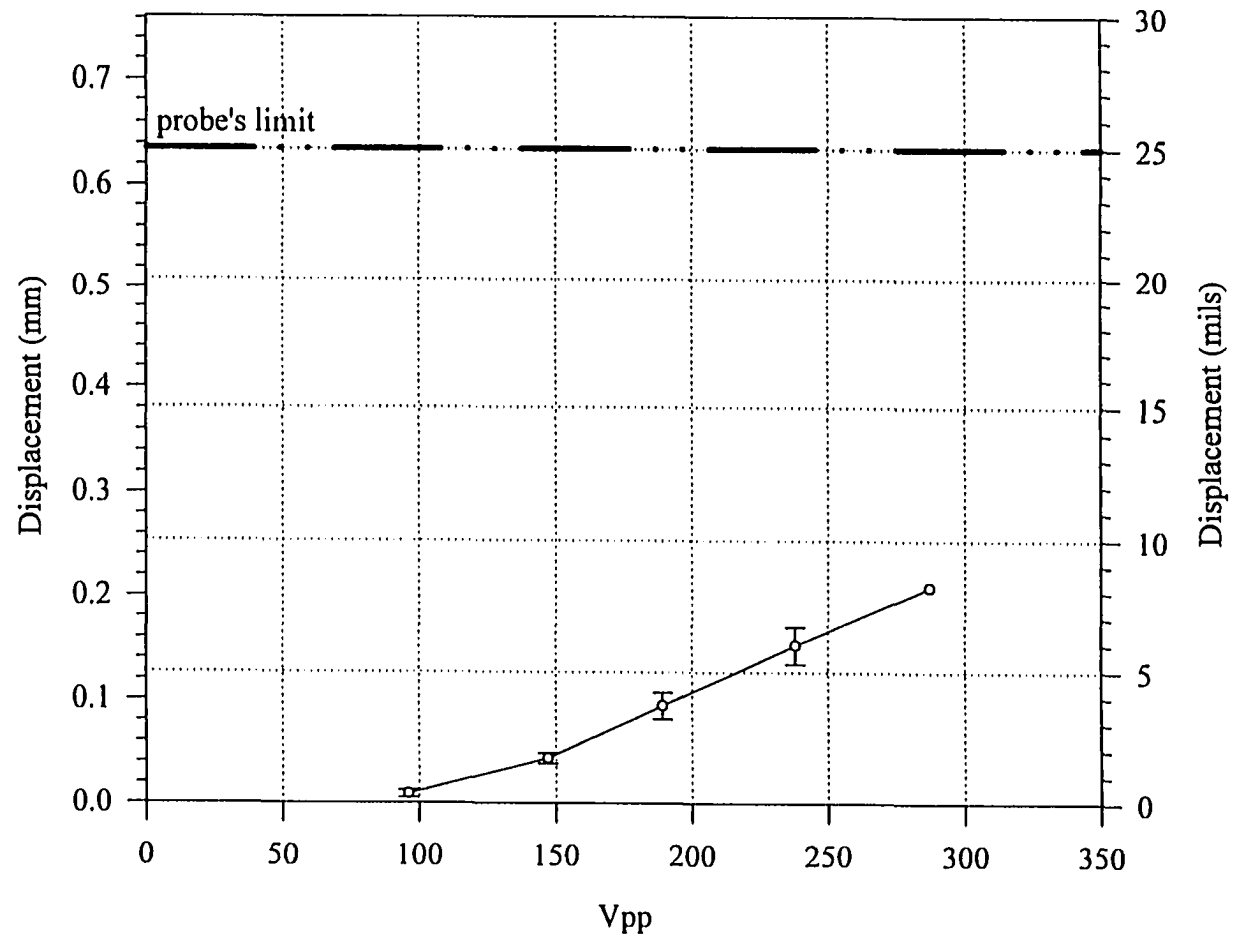


Figure 3.38 Displacement vs. Voltage at 1 Hz for Configuration 0/1-x/Al

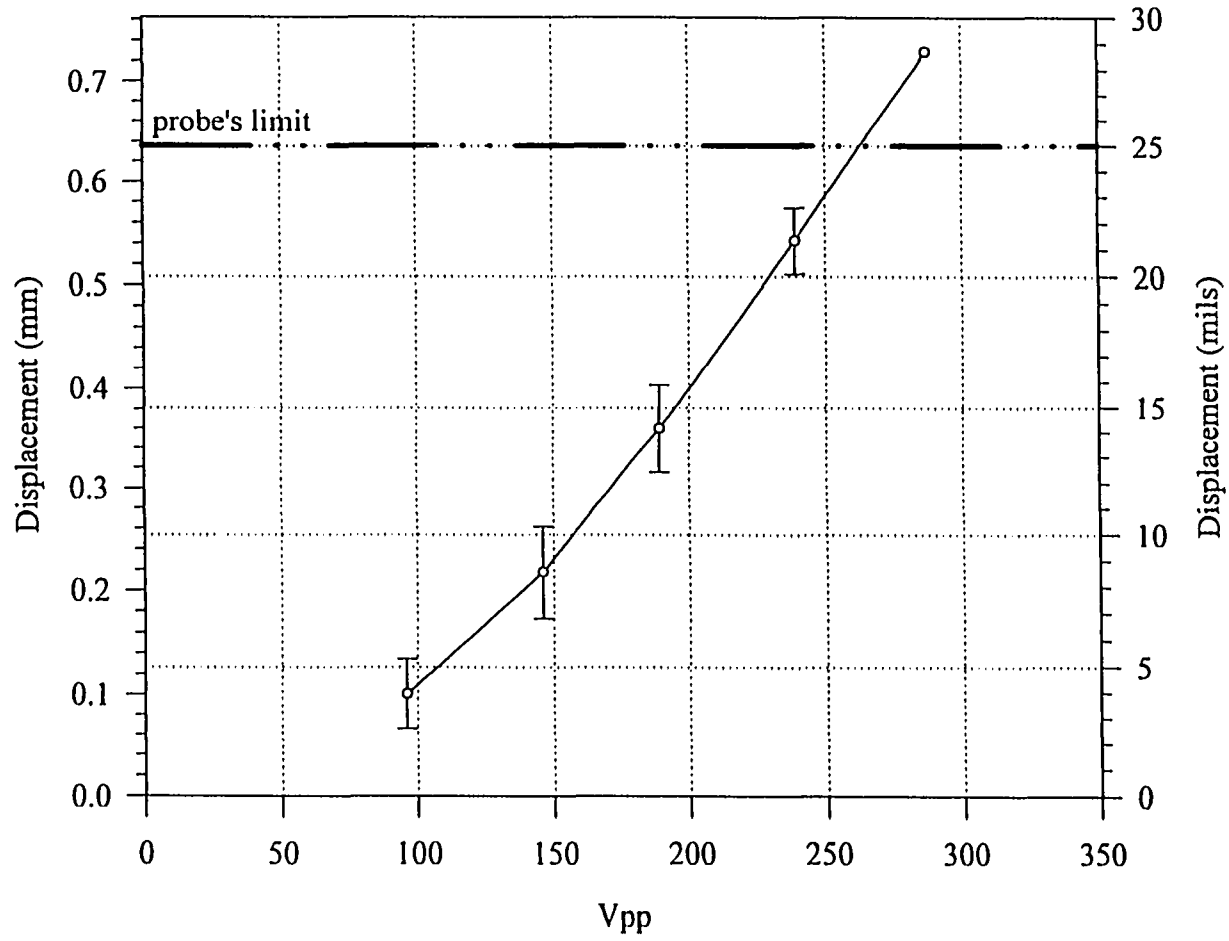


Figure 3.39 Displacement vs. Voltage at 1 Hz for Configuration 0/3-x/A1

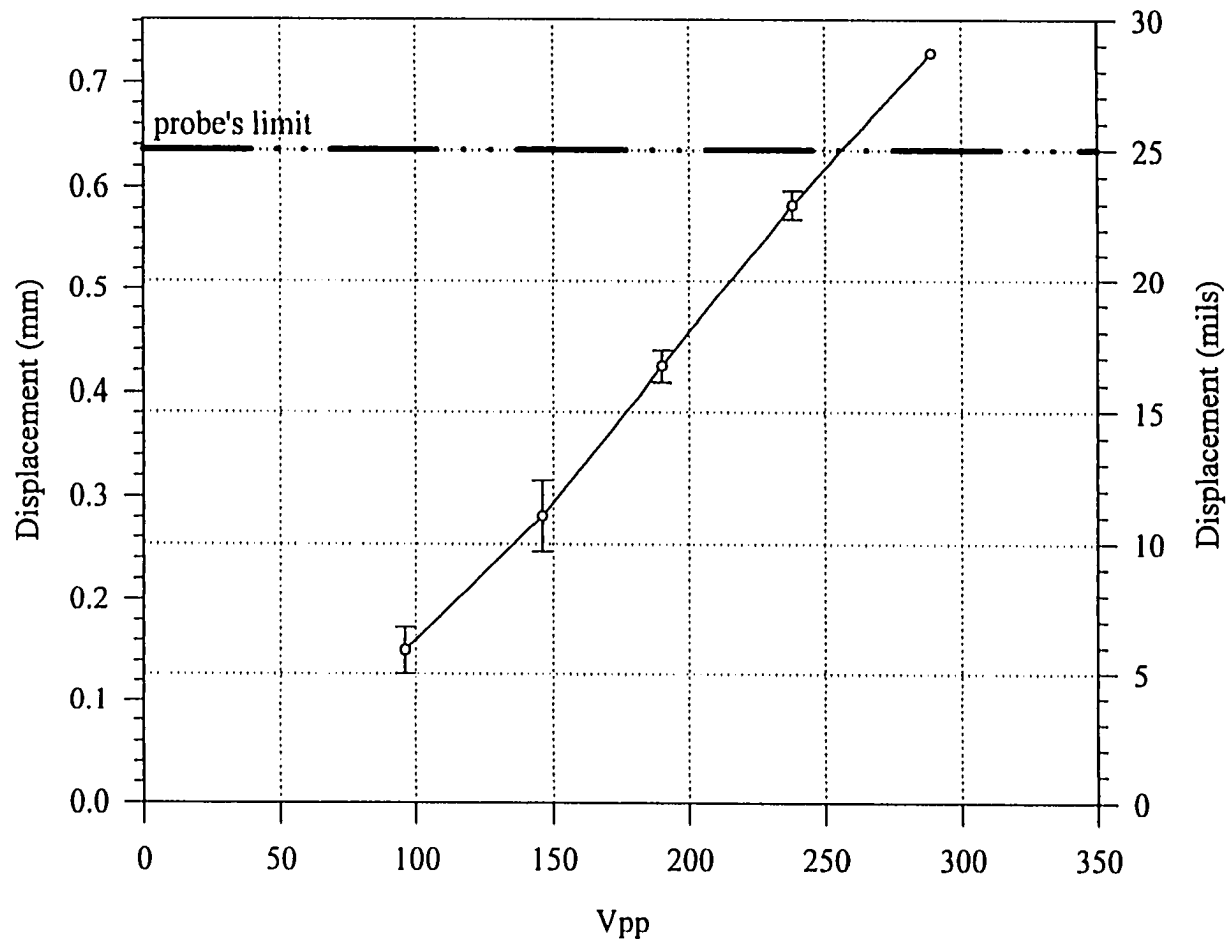


Figure 3.40 Displacement vs. Voltage at 1 Hz for Configuration 0/5-x/A1

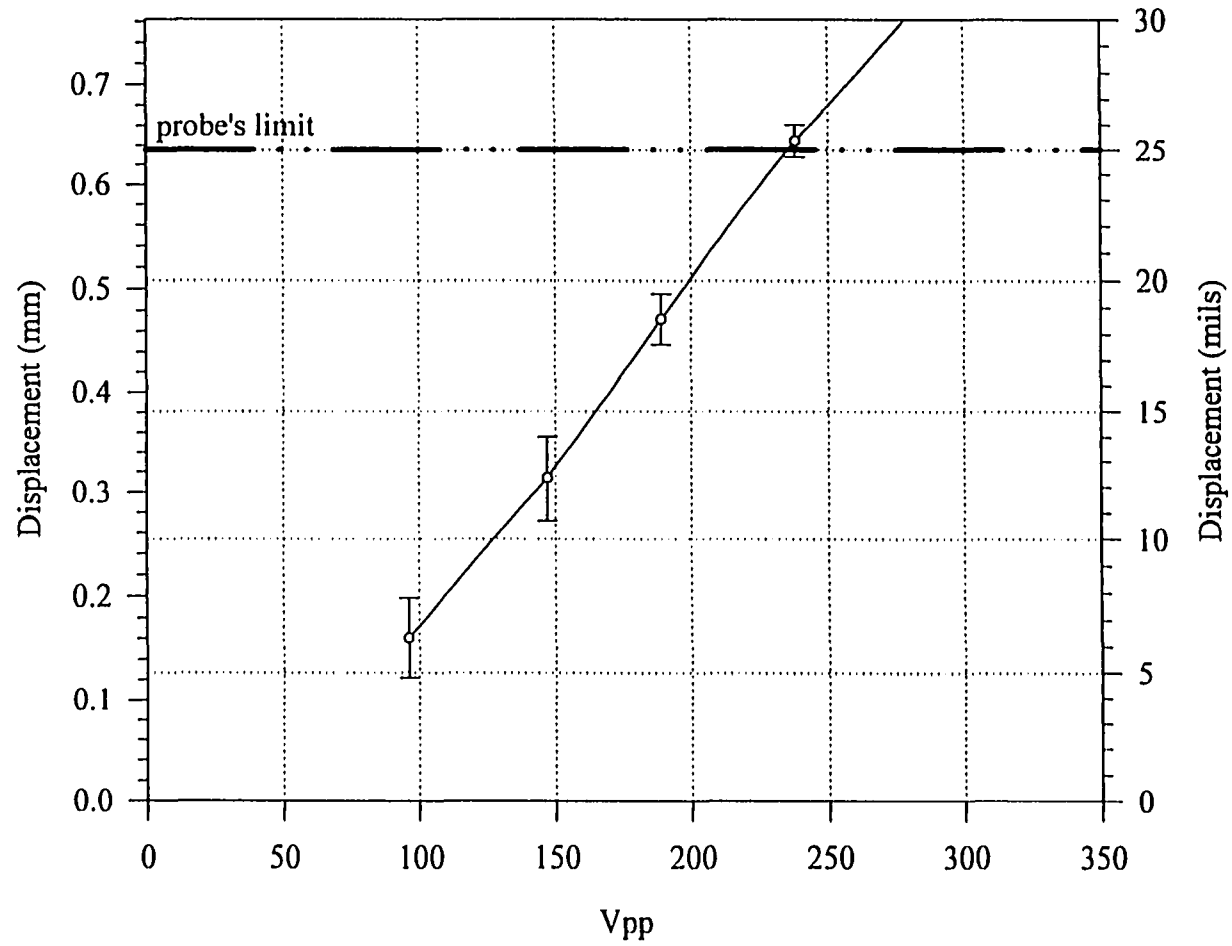


Figure 3.41 Displacement vs. Voltage at 1 Hz for Configuration 0/7-x/Al

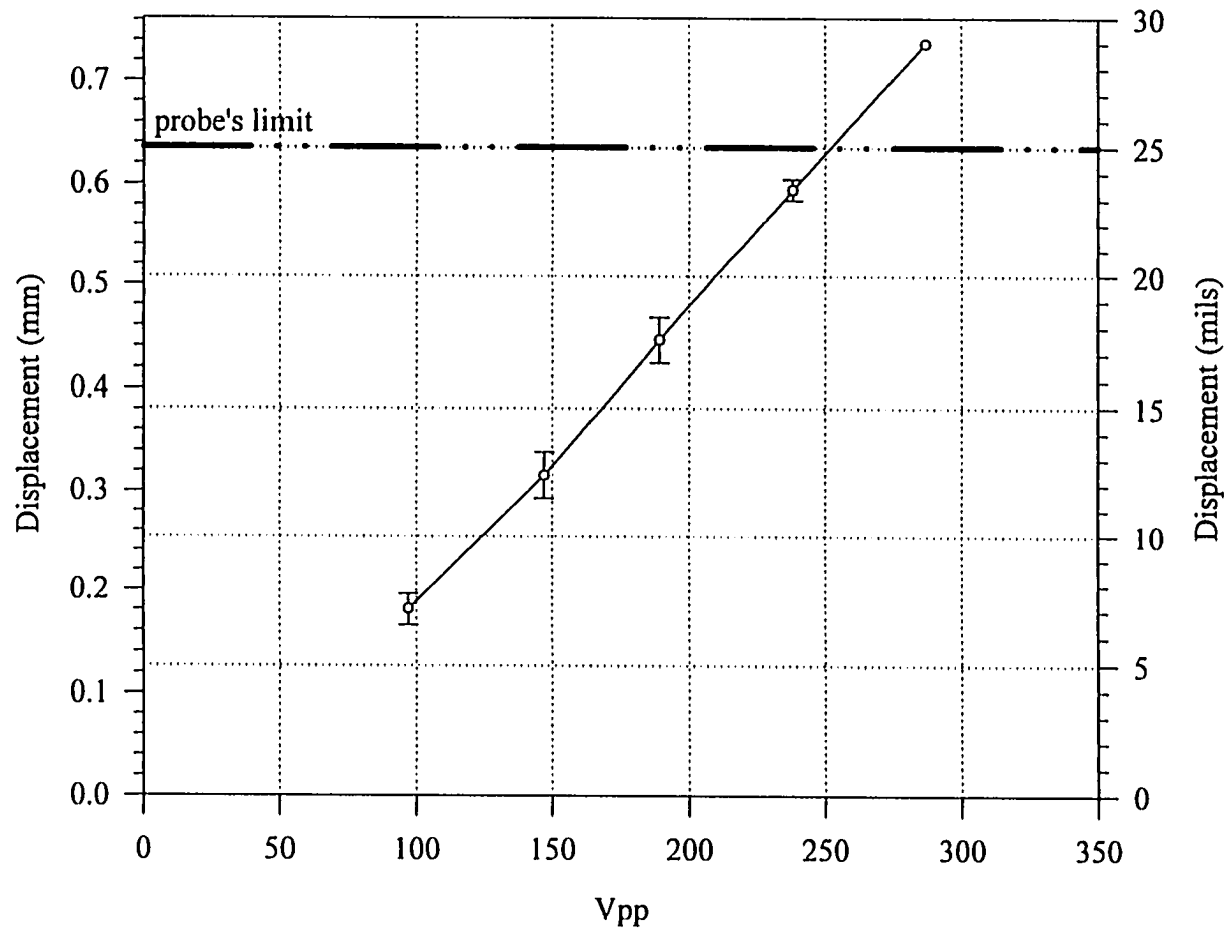


Figure 3.42 Displacement vs. Voltage at 1 Hz for Configuration 0/9-x/A1

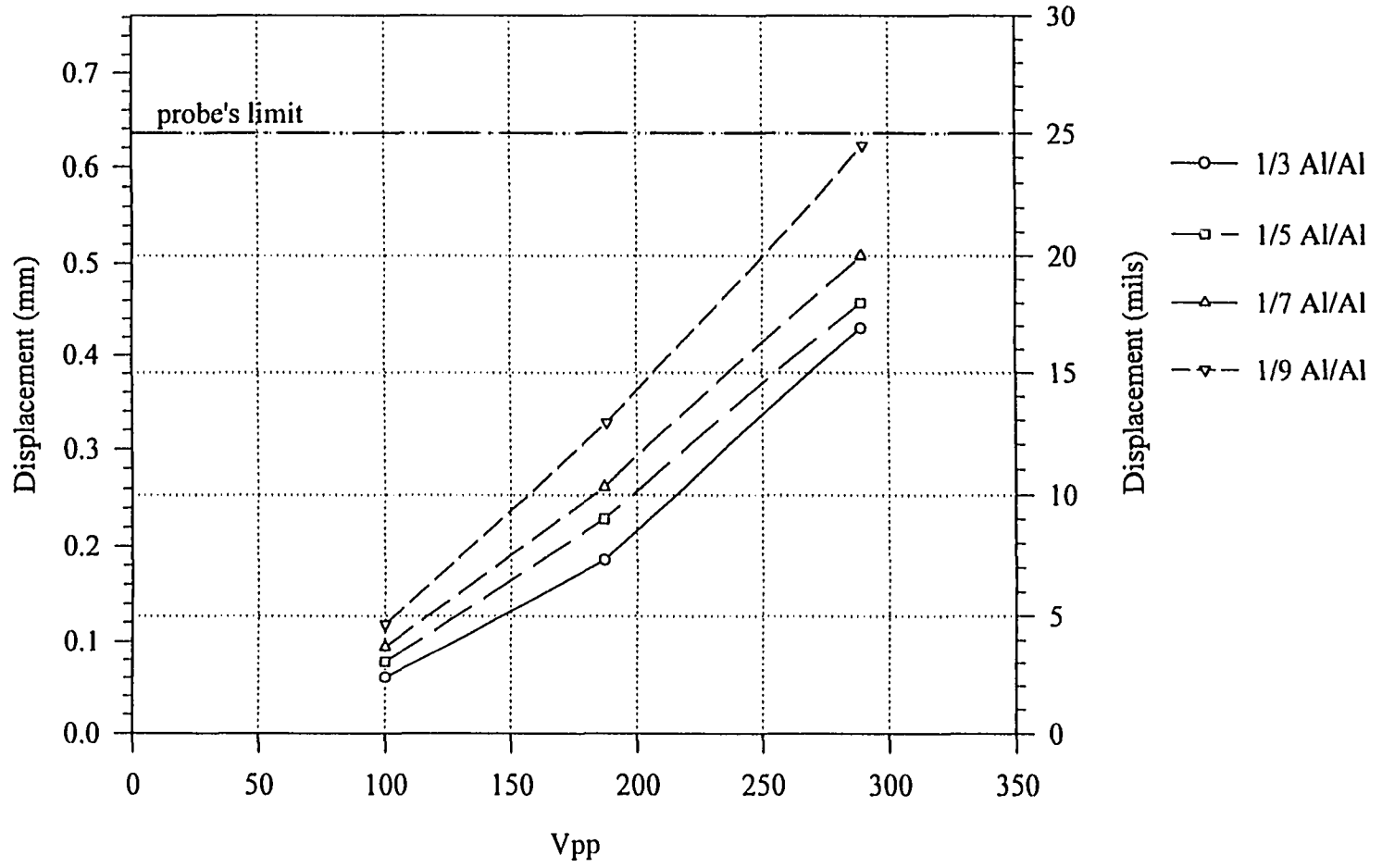


Figure 3.43 Displacement vs. Voltage at 1 Hz for x/Al Configurations

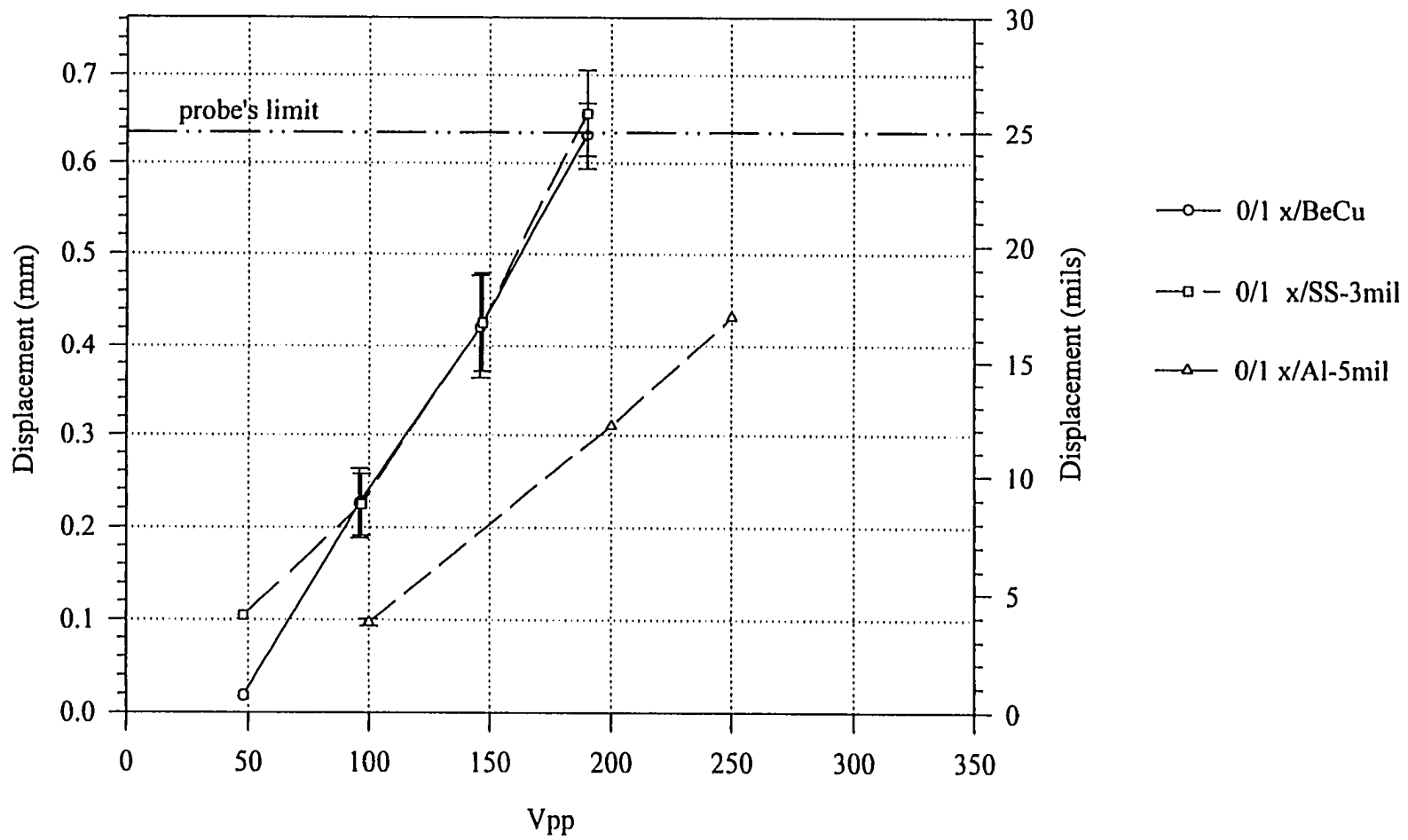


Figure 3.44 Displacement vs. Voltage at 1 Hz for Configuration 0/1-x/SS, 0/1-x/SS-3, and x/BeCu-2

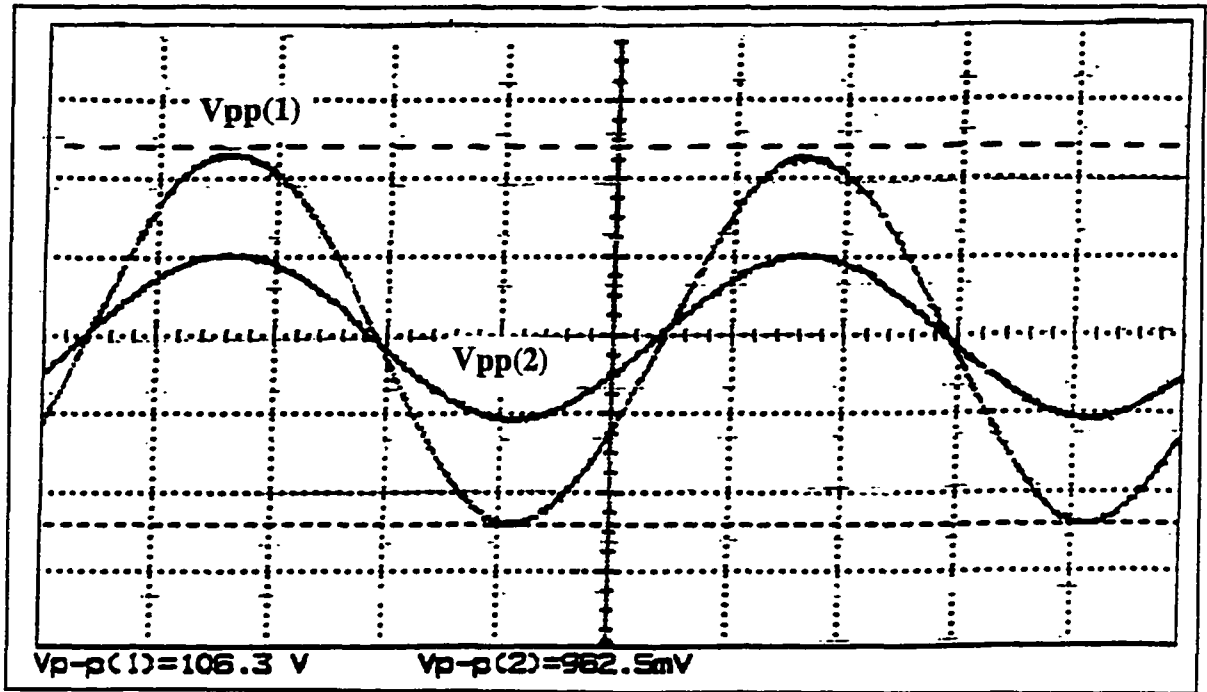


Figure 3.45 Driving Voltage Waveform and Displacement Waveform for Configuration 0/7-x/A1 at 1 Hz

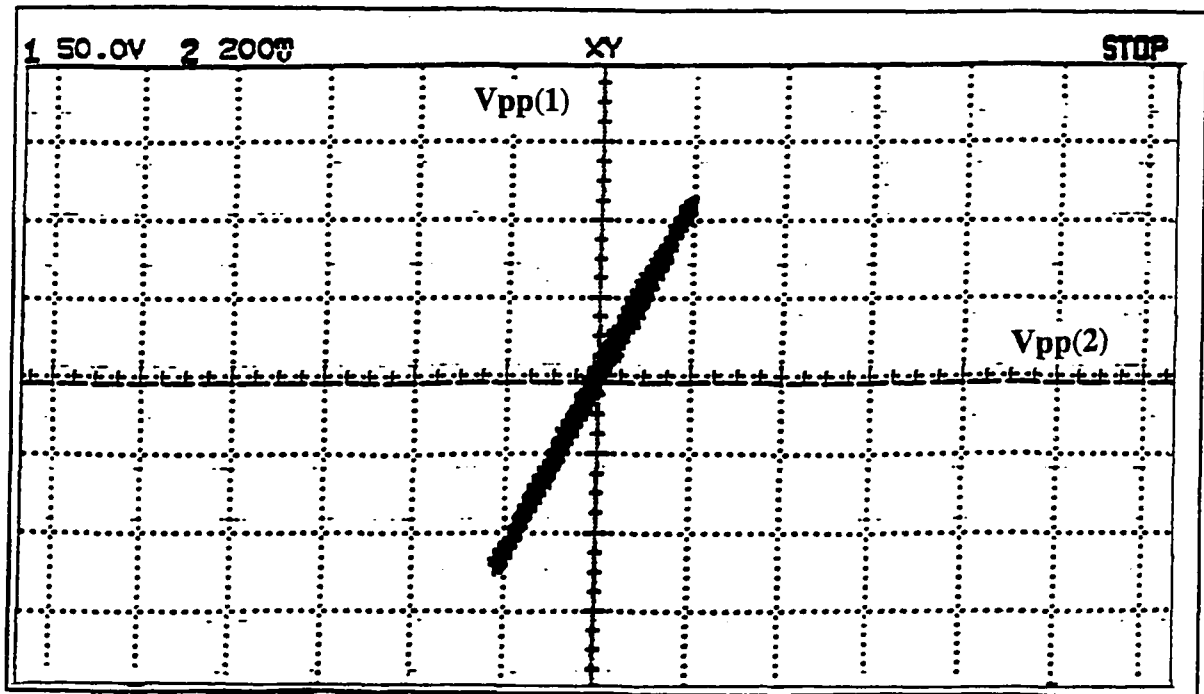


Figure 3.46 Hysteresis Curve for Configuration 0/7-x/A1 at 1 Hz

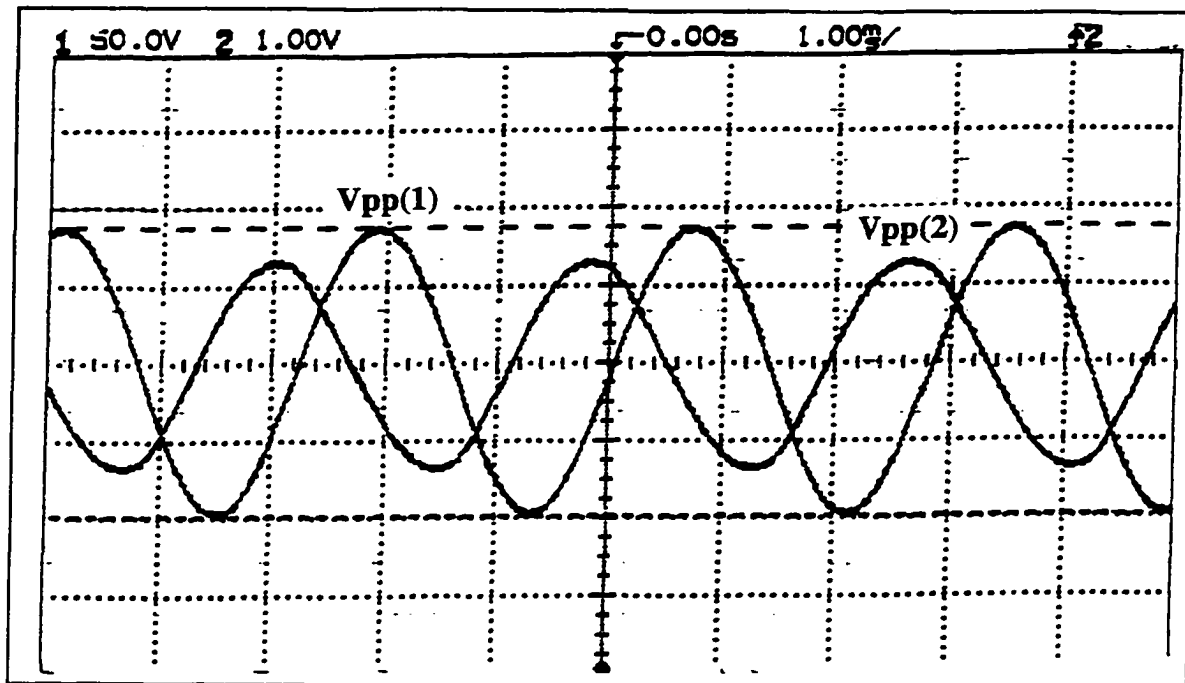


Figure 3.47 Driving Voltage Waveform and Displacement Waveform for Configuration 0/7-x/A1 at 350 Hz

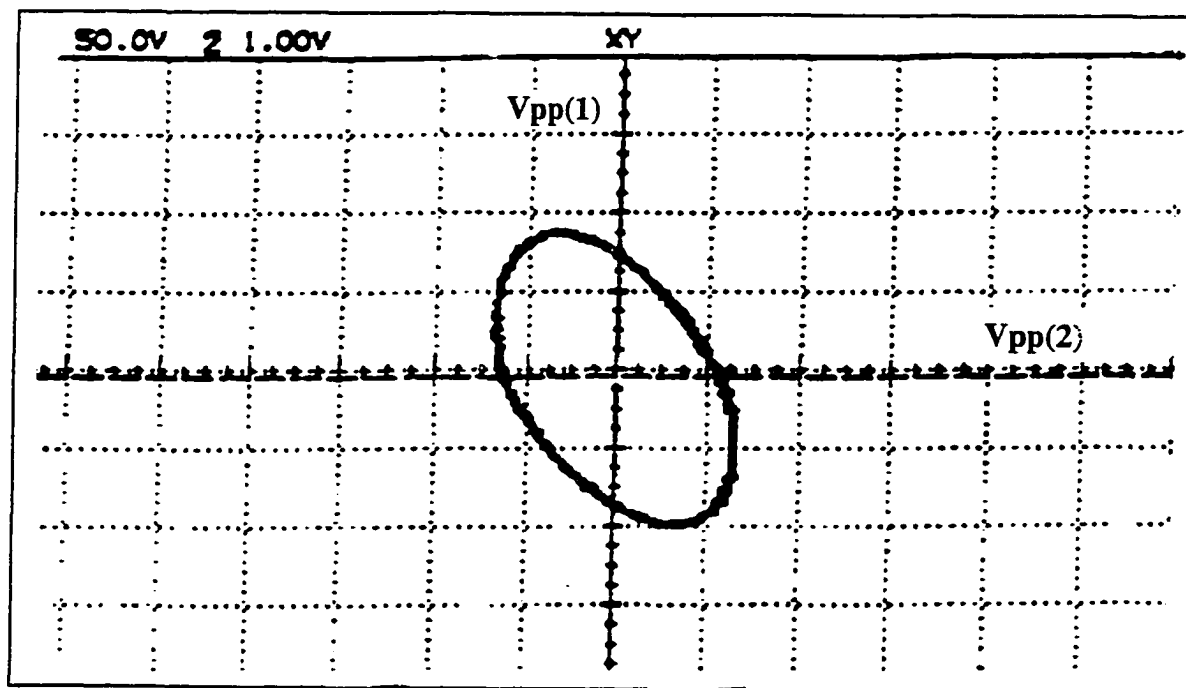


Figure 3.48 Hysteresis Curve for Configuration 0/7-x/A1 at 350 Hz

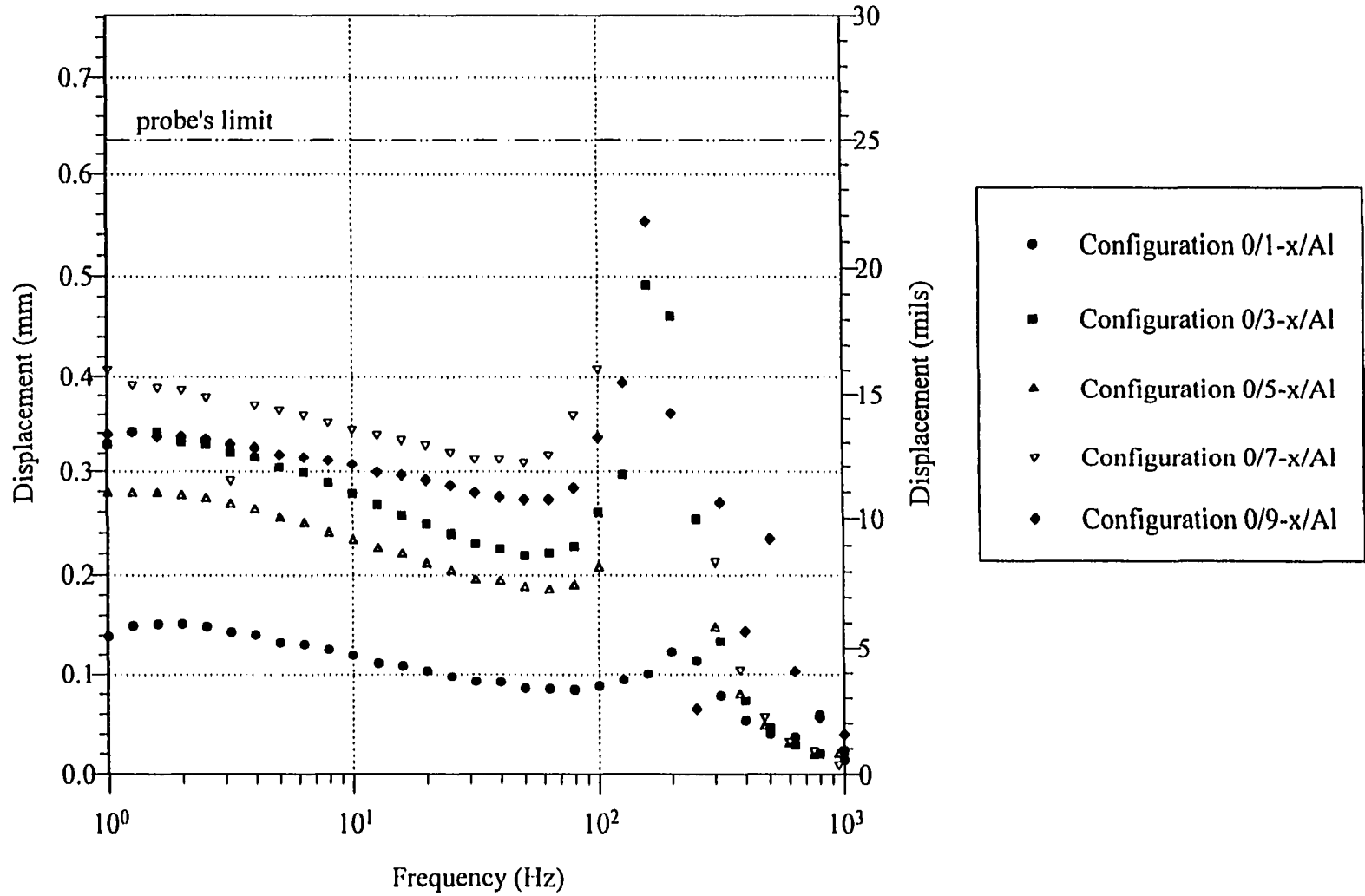


Figure 3.49 Summary of the Performance of x/Al Configurations at 200 Vpp with No Re-Poling

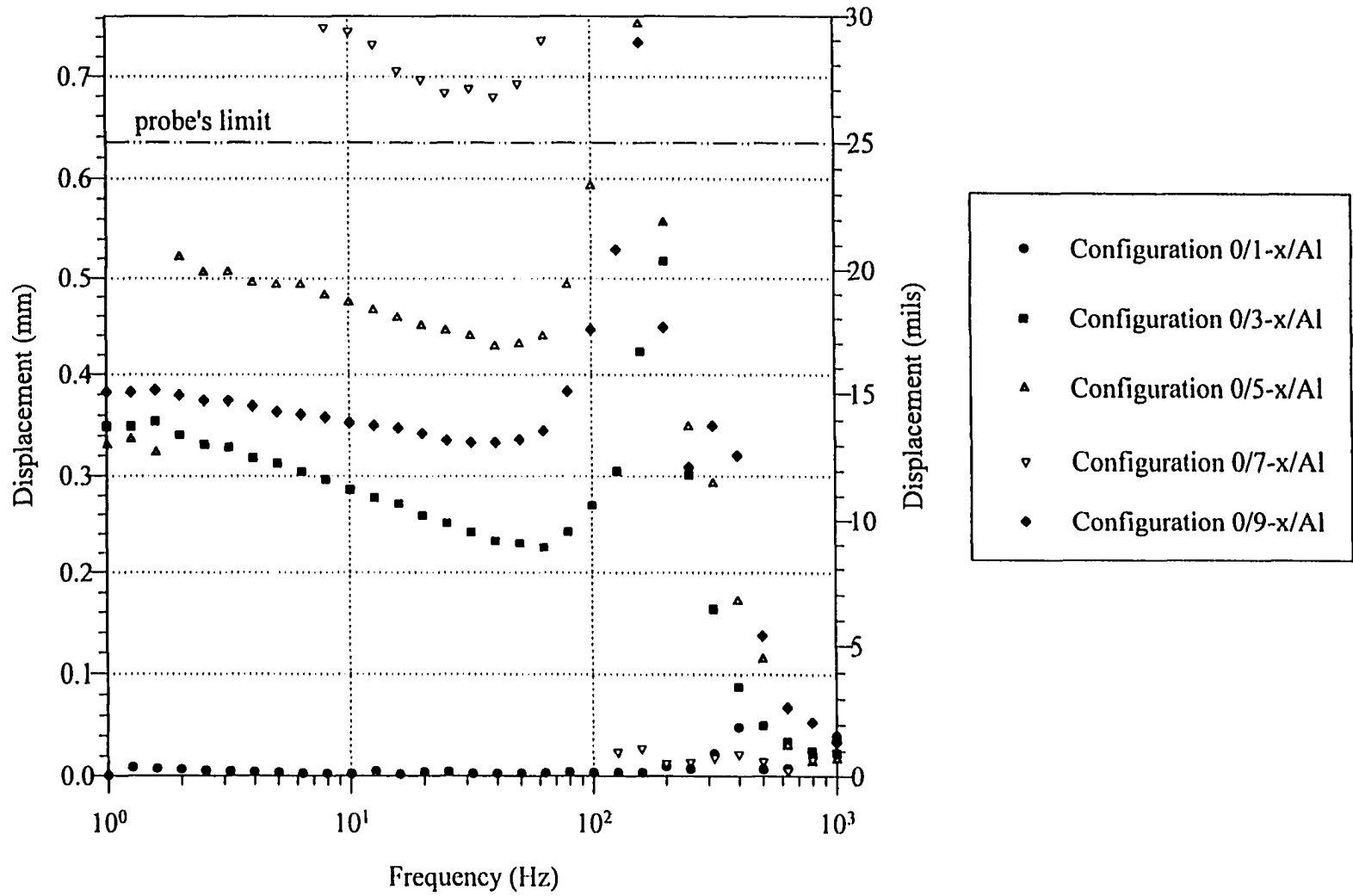


Figure 3.50 Summary of the Performance of x/Al Configurations at 200 Vpp after Re-Poling

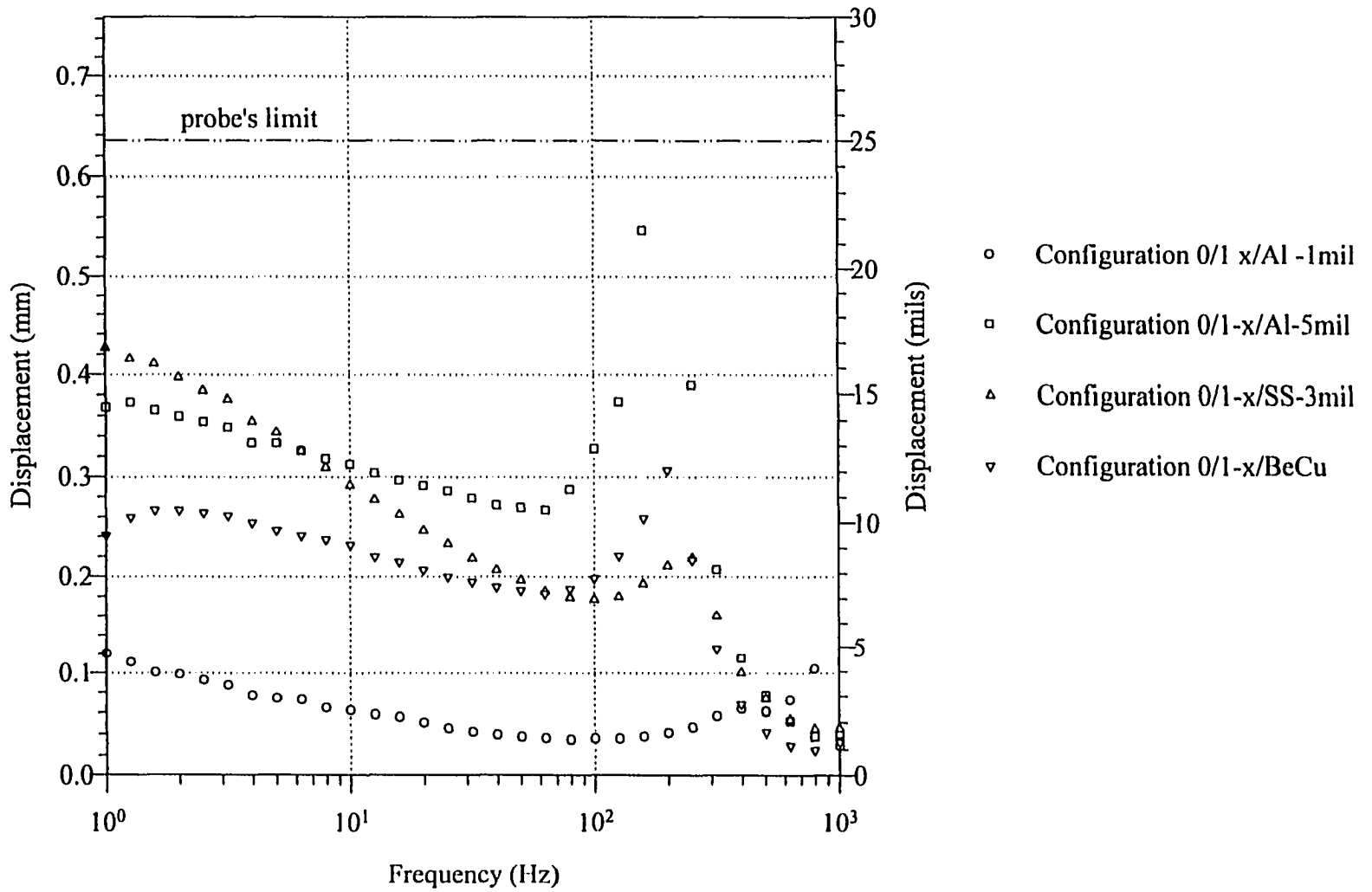


Figure 3.51 Summary of the Performance x/Al Configurations with SS, Al, BeCu at 200Vpp, No Re-Poling

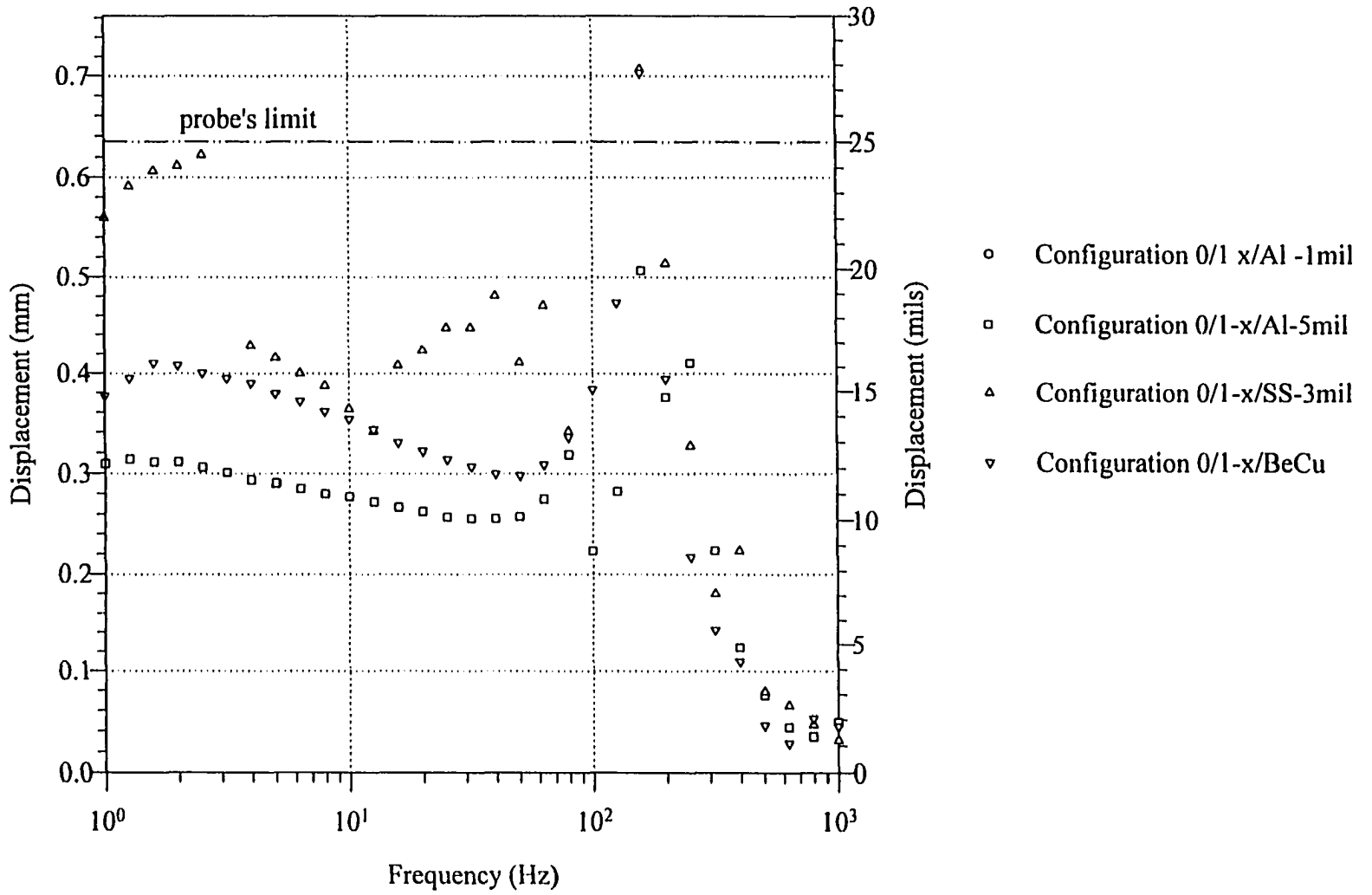


Figure 3.52 Summary of the Performance x/Al Configurations with SS, Al, BeCu at 200Vpp, after Re-Poling

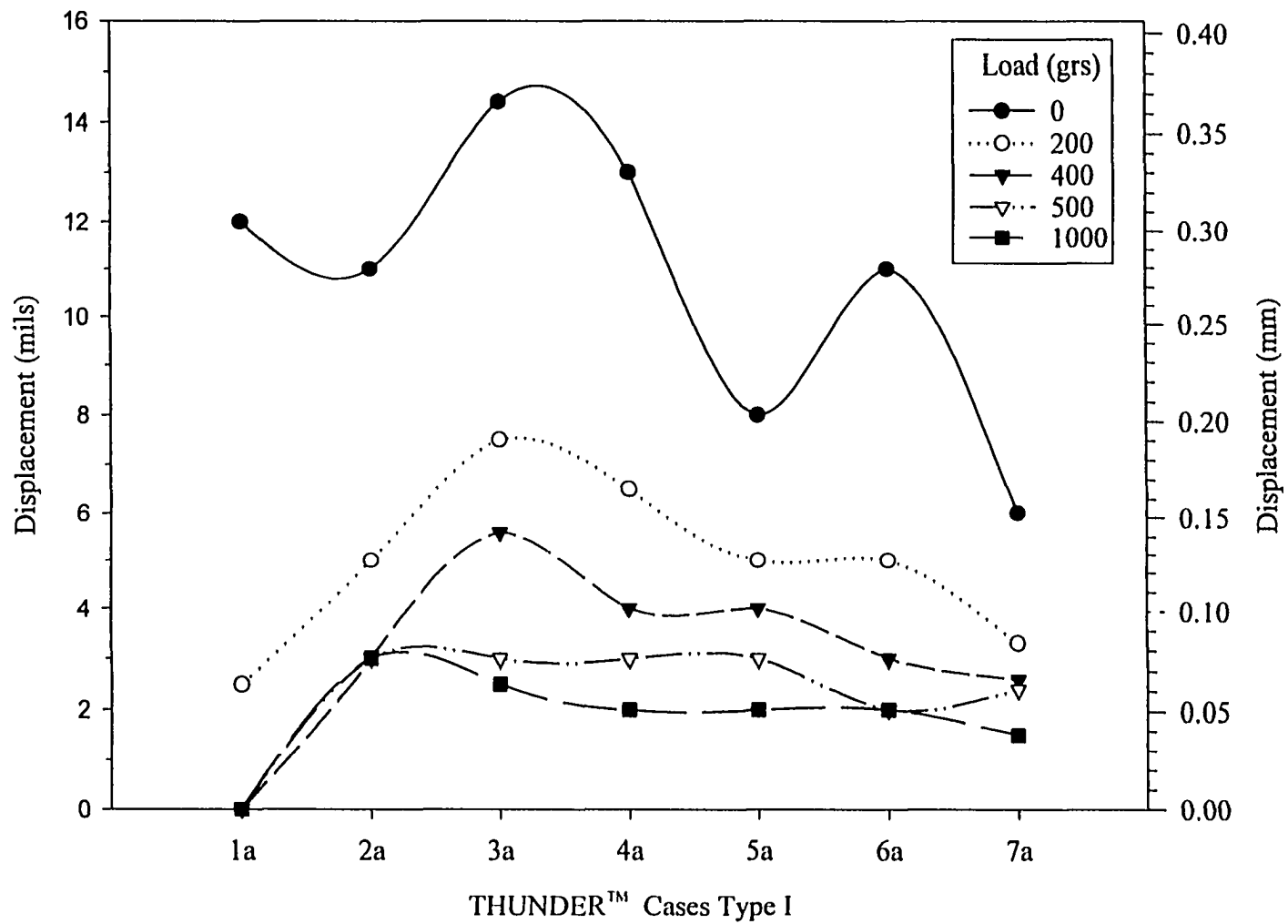


Figure 3.53 Load Performance of THUNDER™ Type I

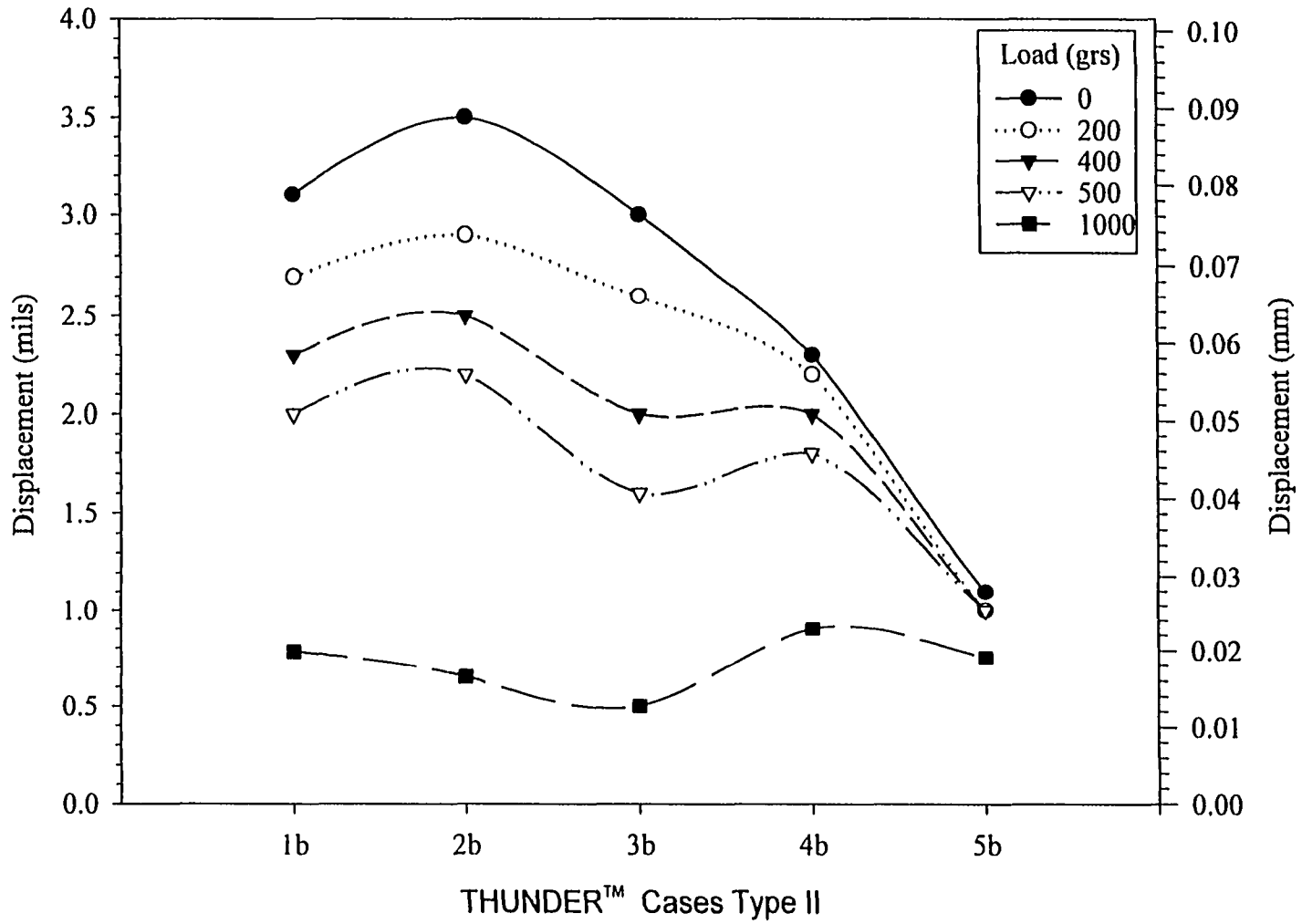


Figure 3.54 Load Performance of THUNDER™ Type II

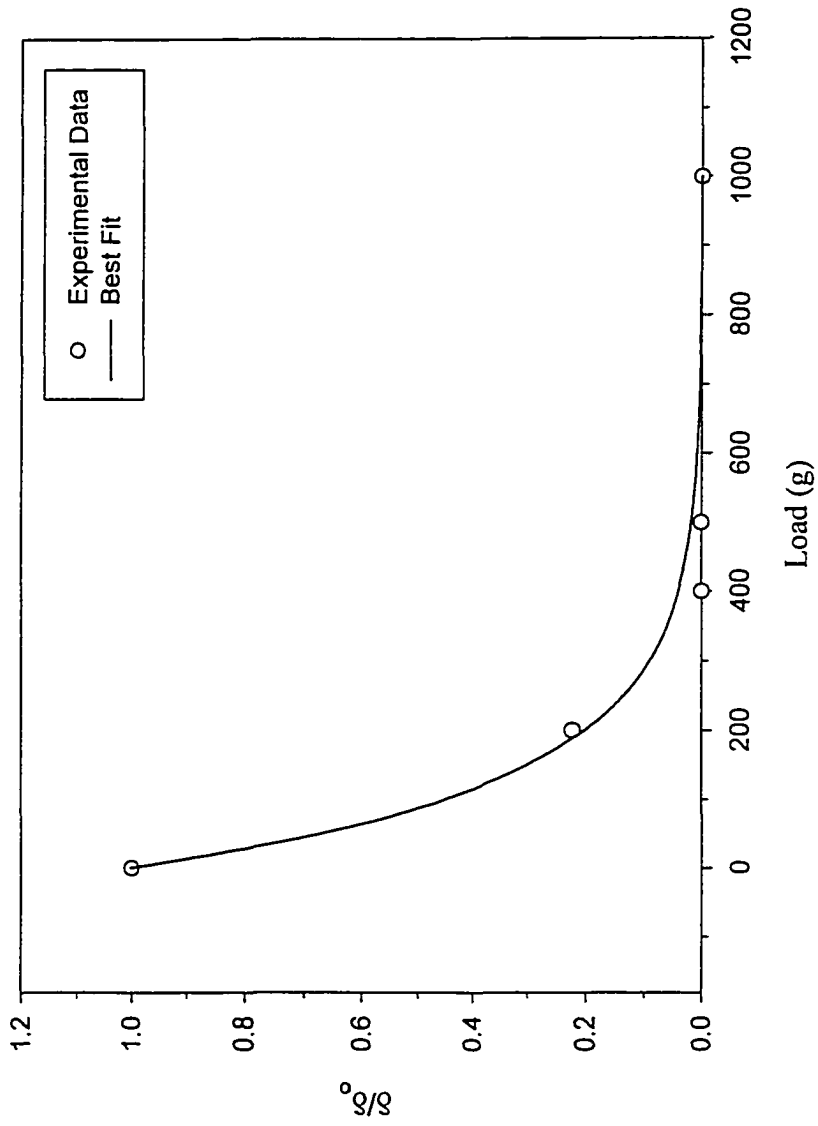


Figure 3.55 Load vs. Displacement for Case 1a

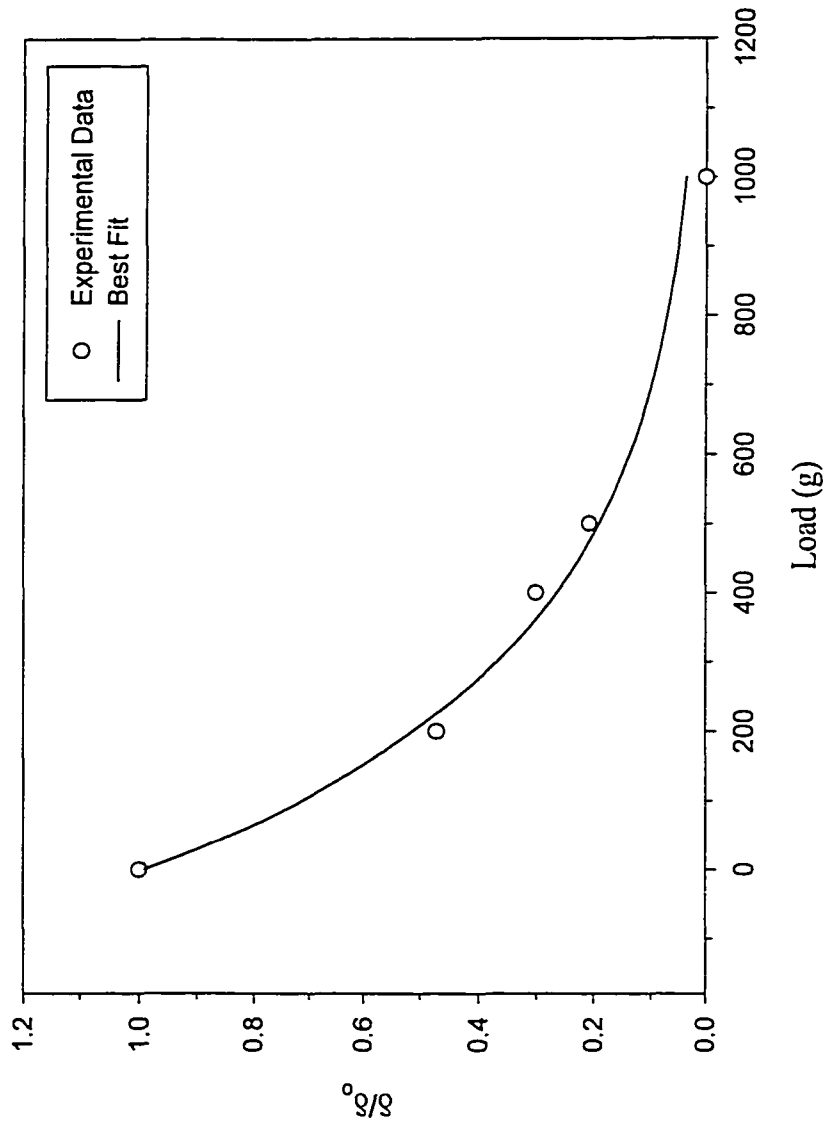


Figure 3.56 Load vs. Displacement for Case 2a

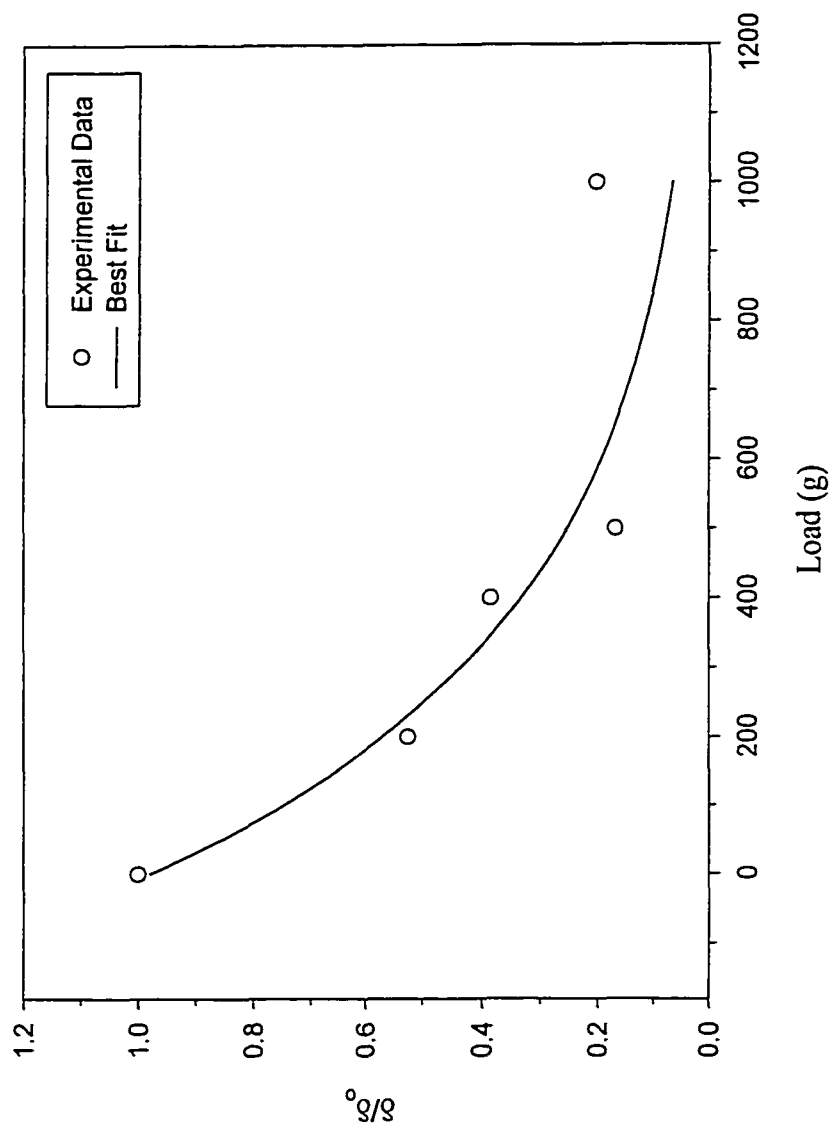


Figure 3.57 Load vs. Displacement for Case 3a

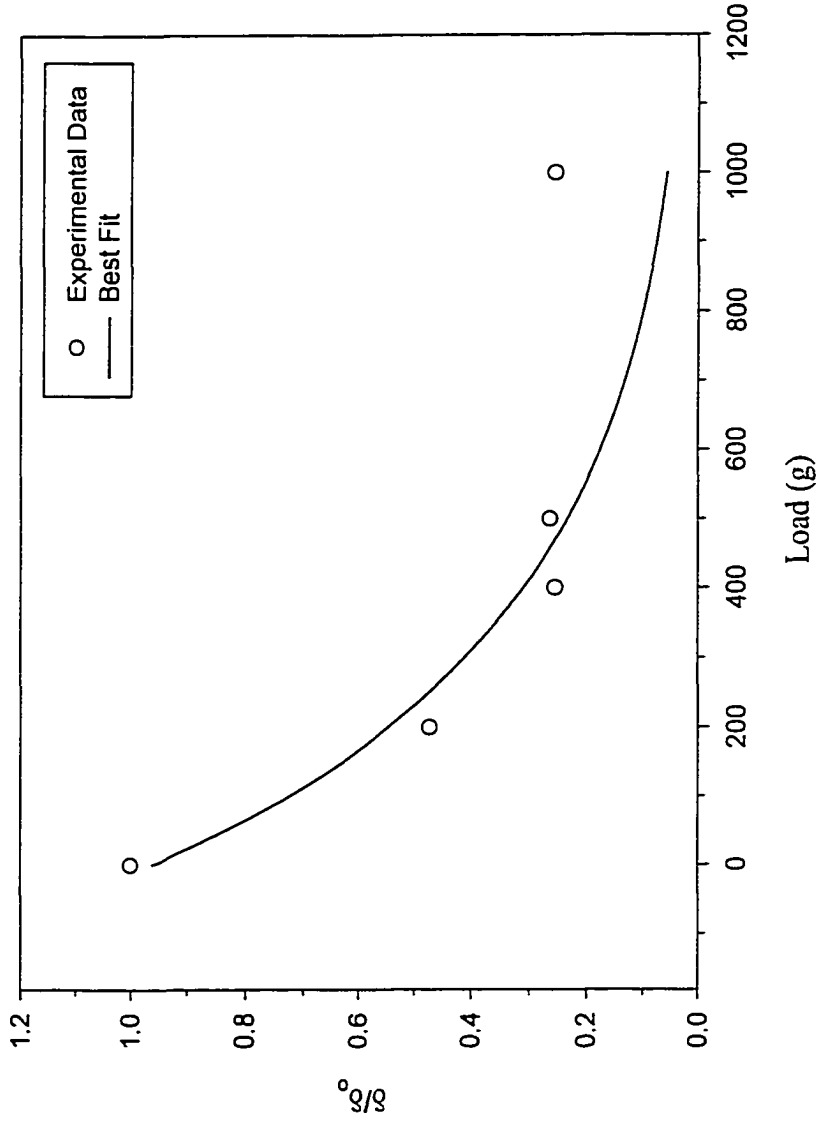


Figure 3.58 Load vs. Displacement for Case 4a

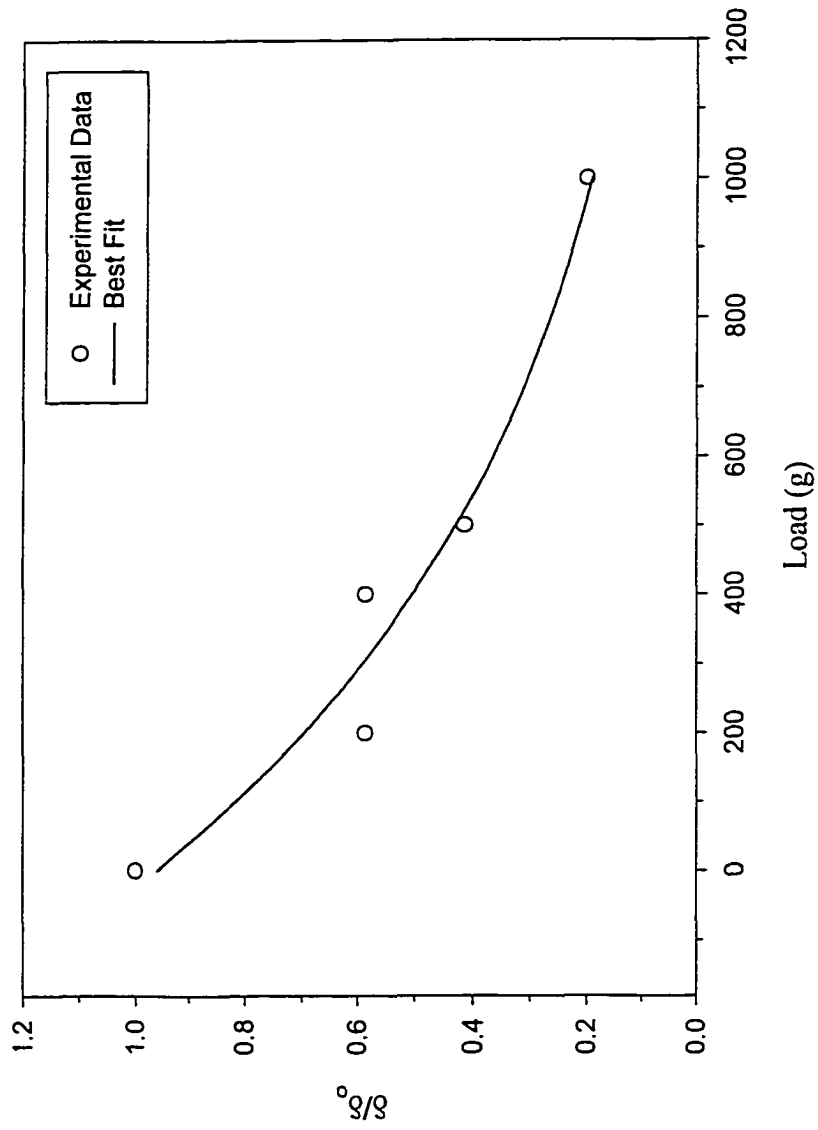


Figure 3.57 Load vs. Displacement for Case 5a

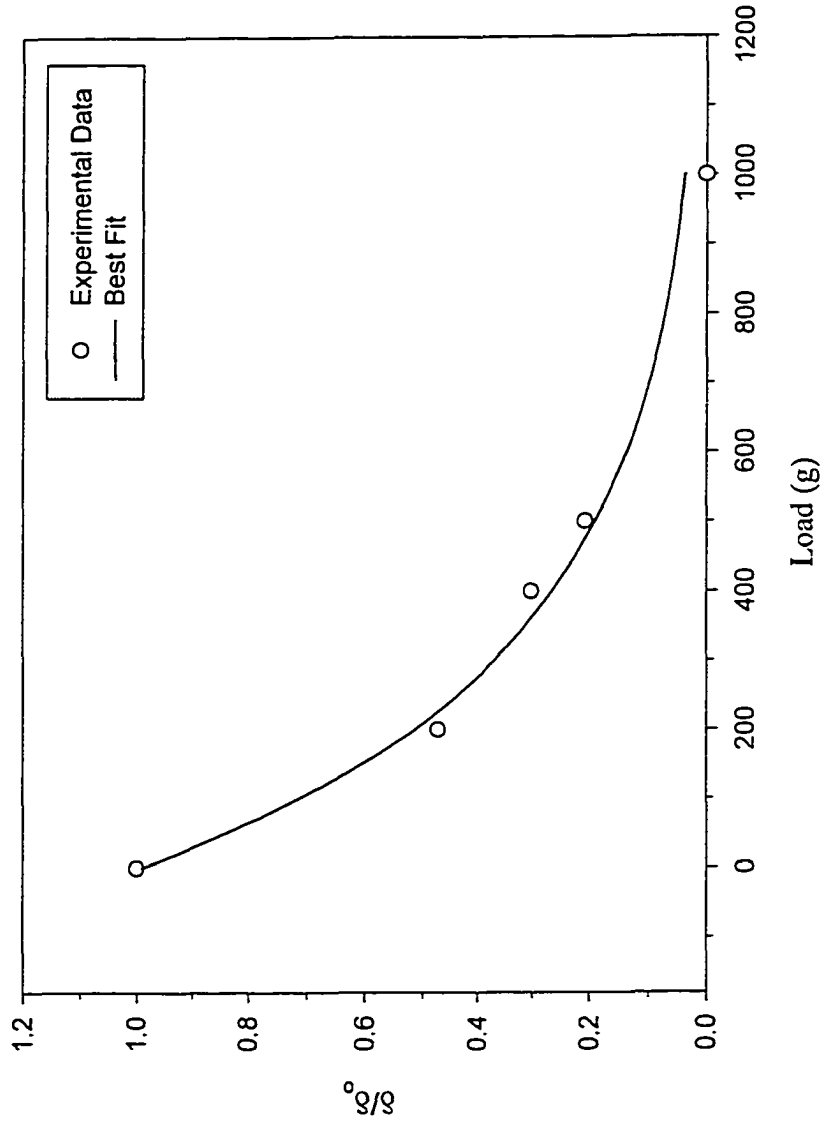


Figure 3.60 Load vs. Displacement for Case 6a

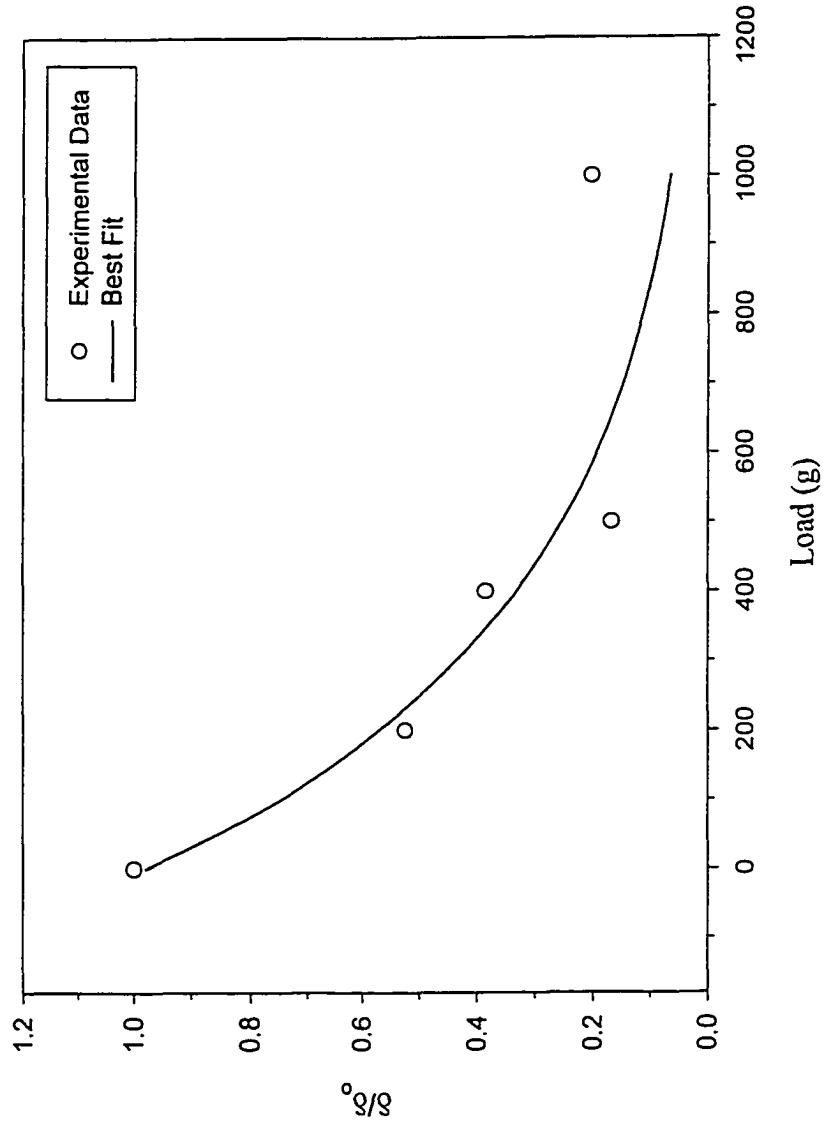


Figure 3.61 Load vs. Displacement for Case 7a

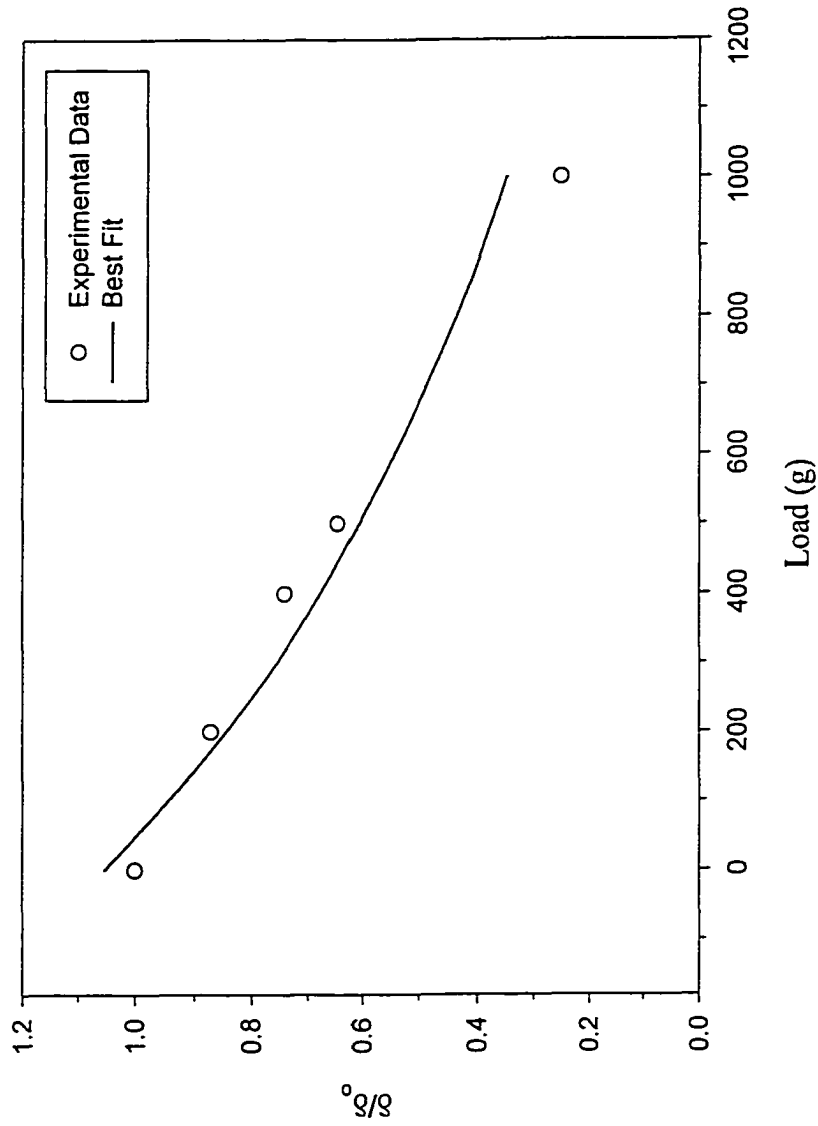


Figure 3.62 Load vs. Displacement for Case 1b

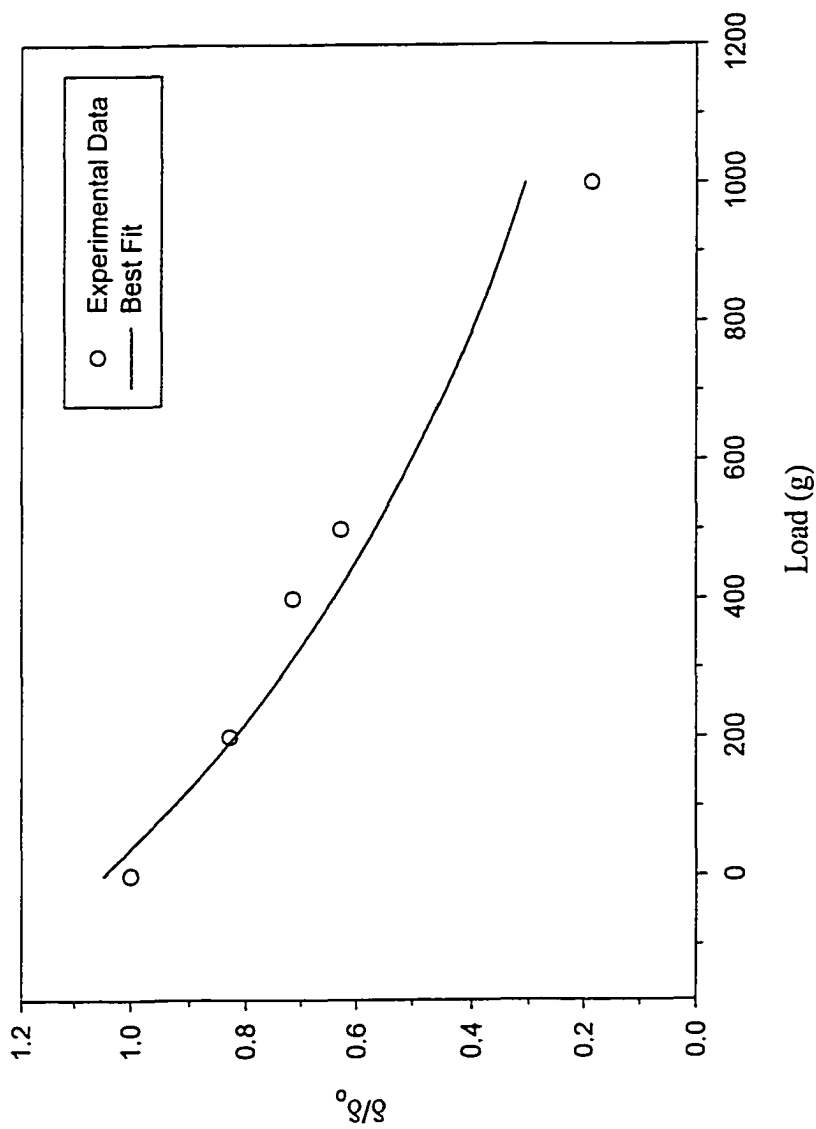


Figure 3.63 Load vs. Displacement for Case 2b

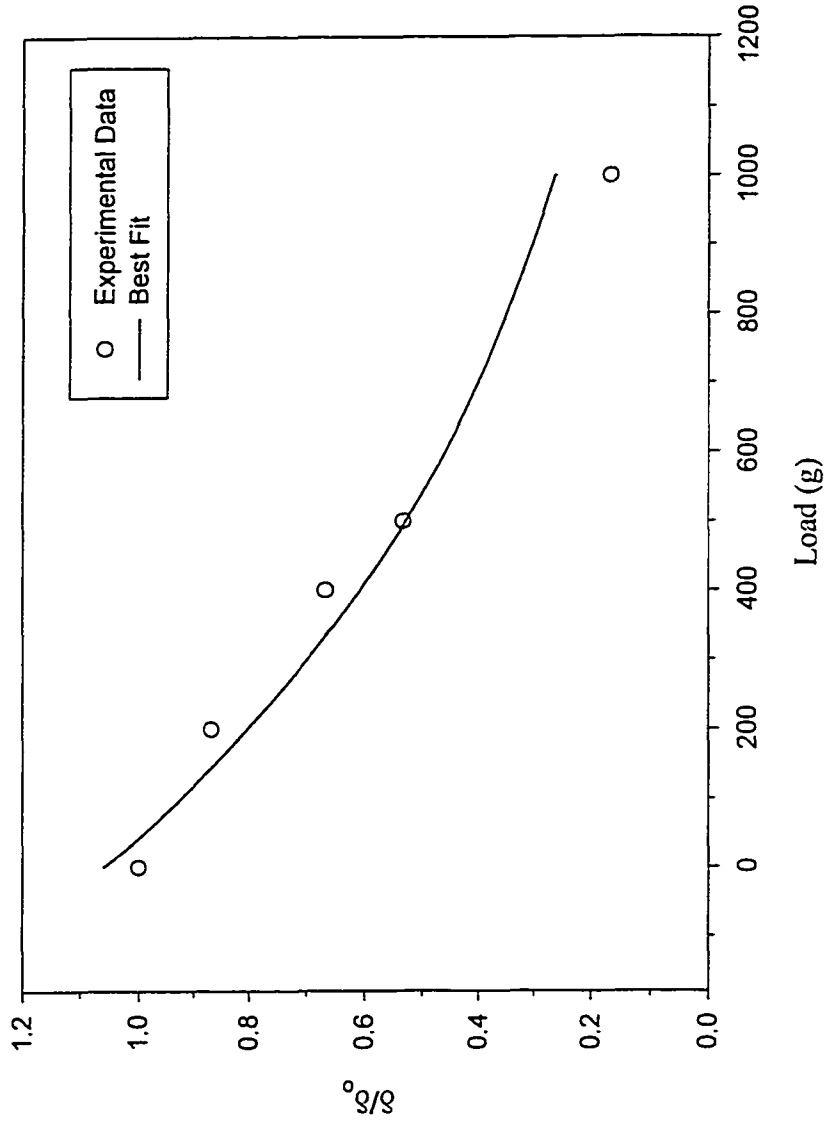


Figure 3.64 Load vs. Displacement for Case 3b

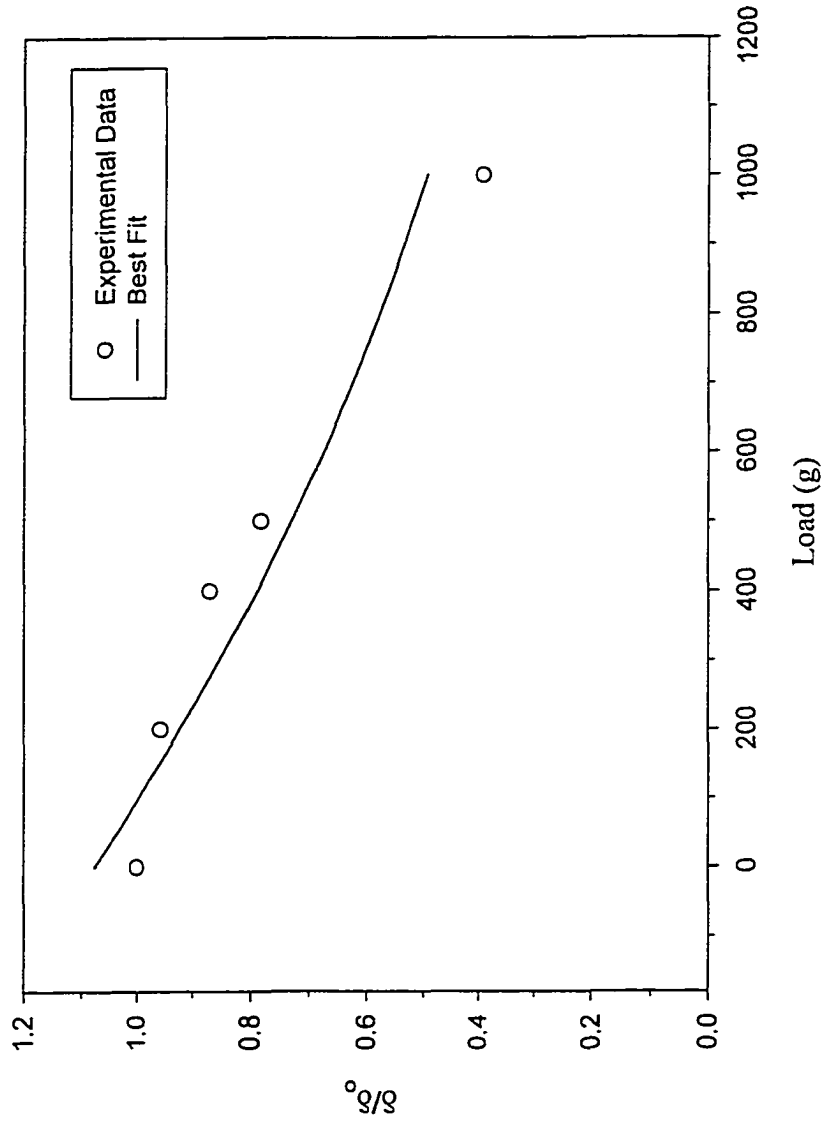


Figure 3.65 Load vs. Displacement for Case 4b

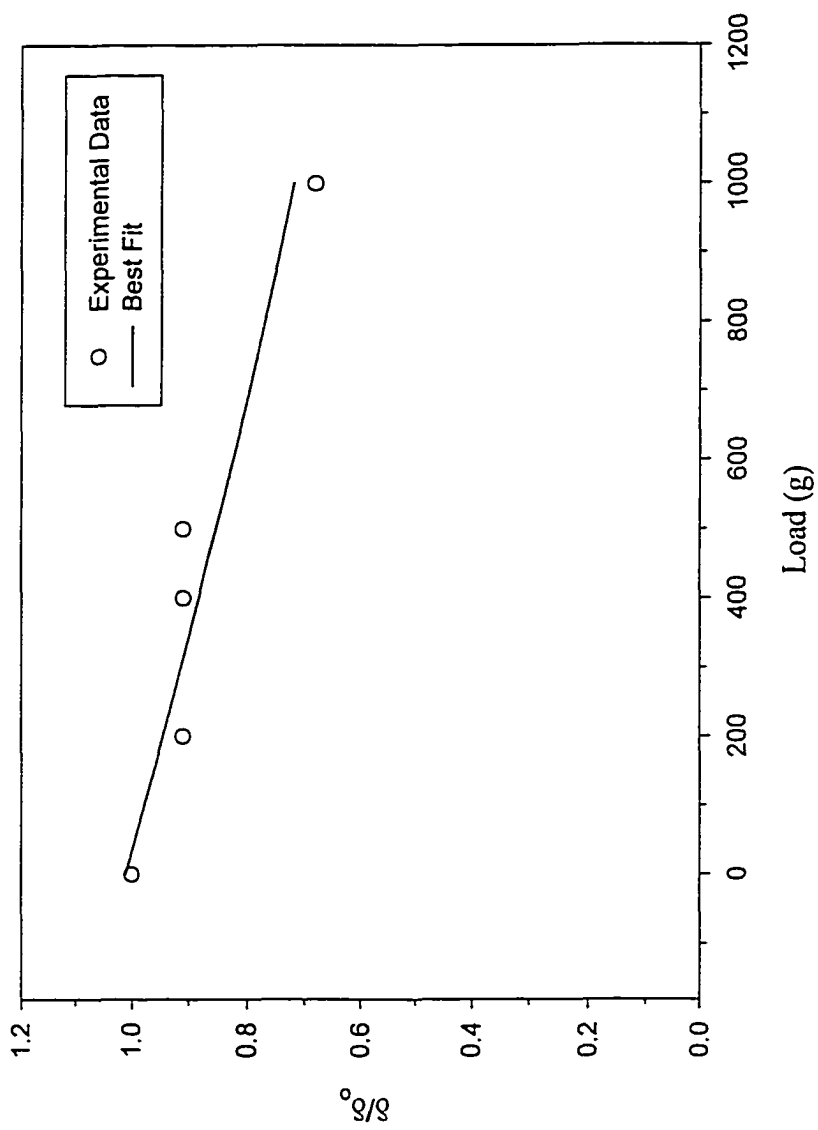


Figure 3.66 Load vs. Displacement for Case 5b

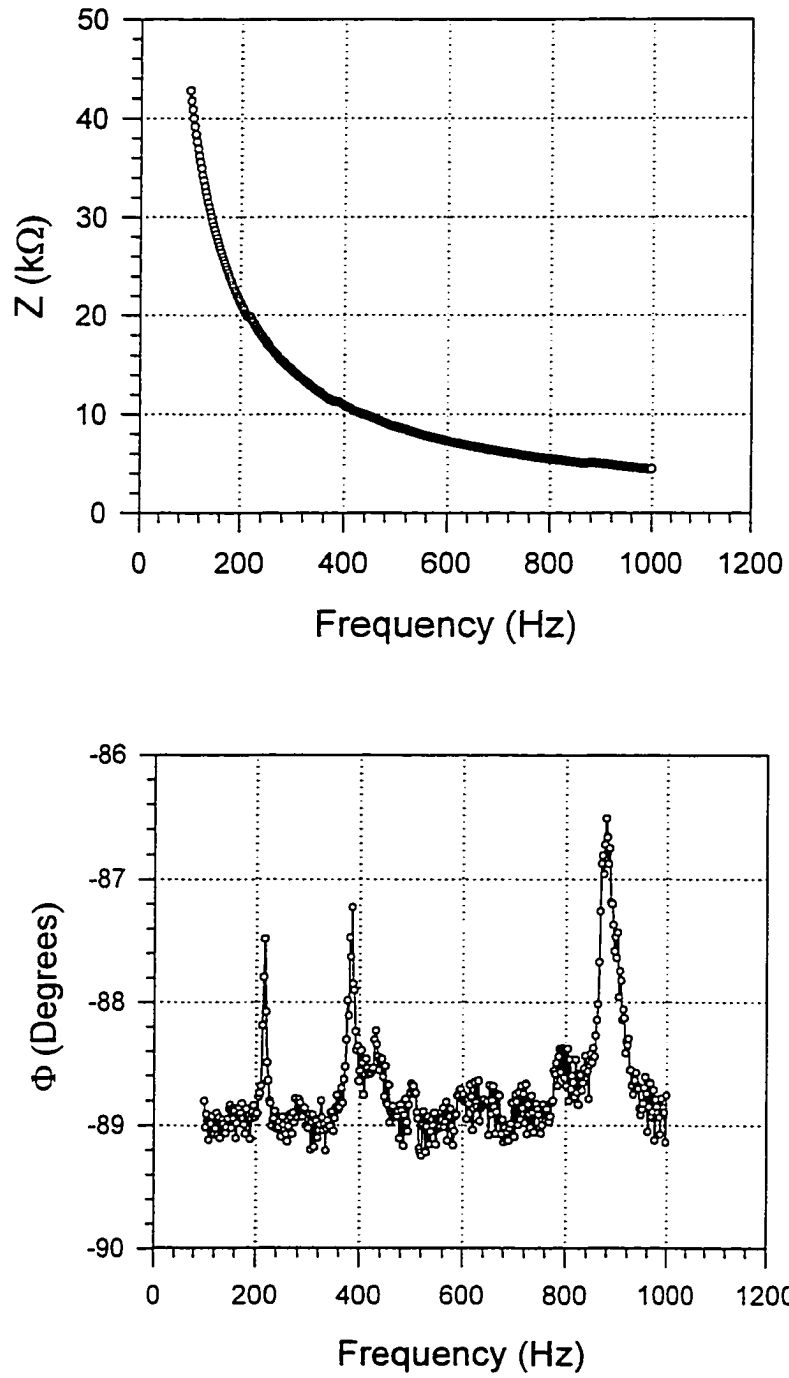


Figure 3.67 Impedance and Phase angle vs Frequency for Case 1a

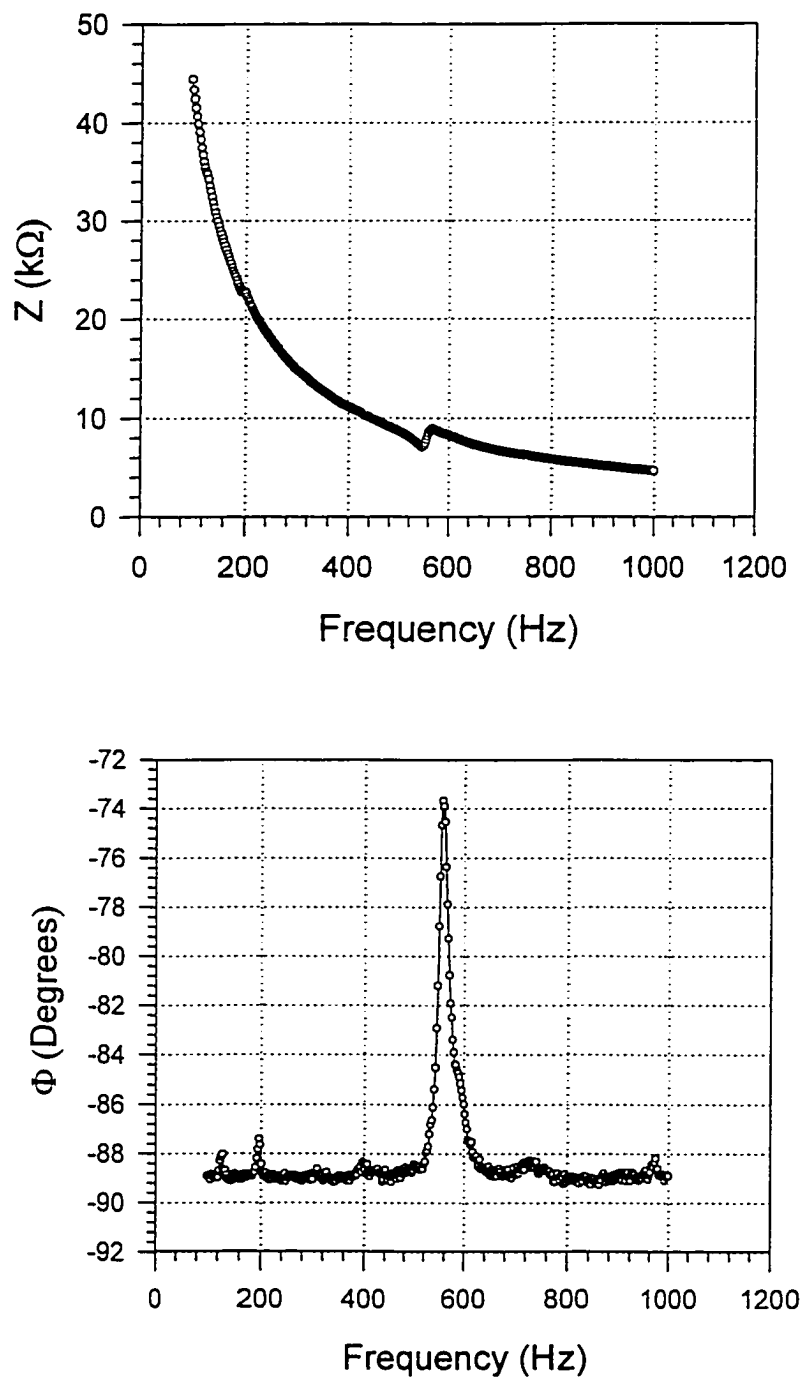


Figure 3.68 Impedance and Phase Angle vs Frequency for Case 2a

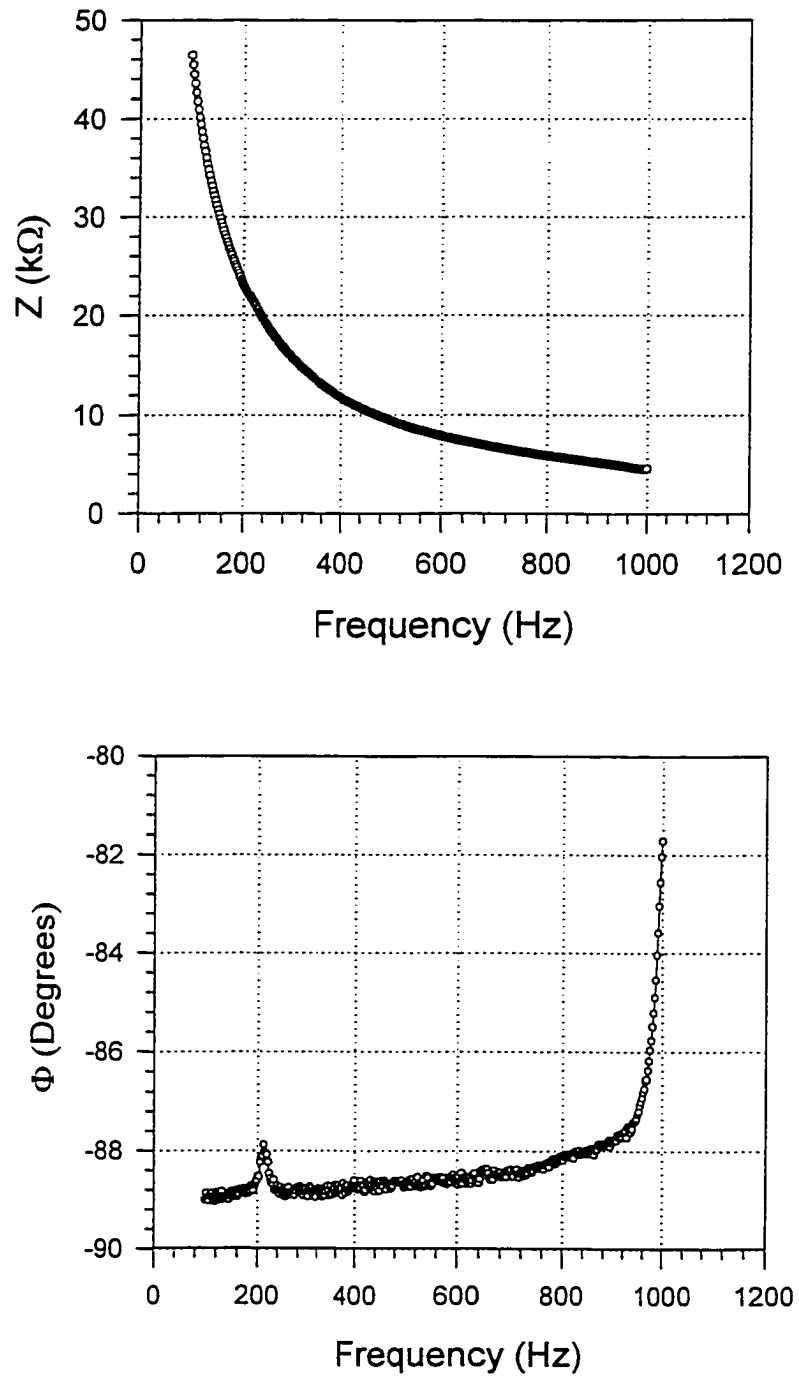


Figure 3.69 Impedance and Phase Angle vs Frequency for Case 3a

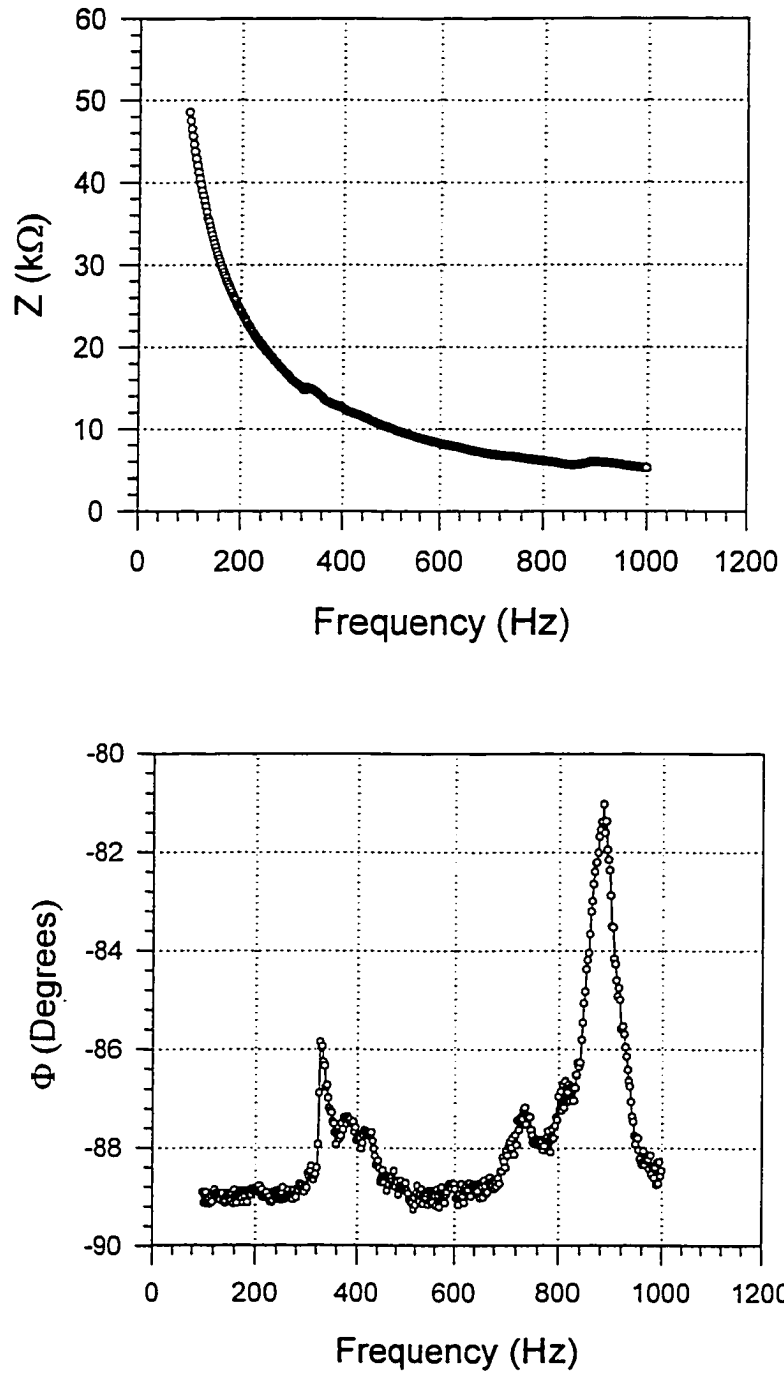


Figure 3.70 Impedance and Phase Angle vs Frequency for Case 4a

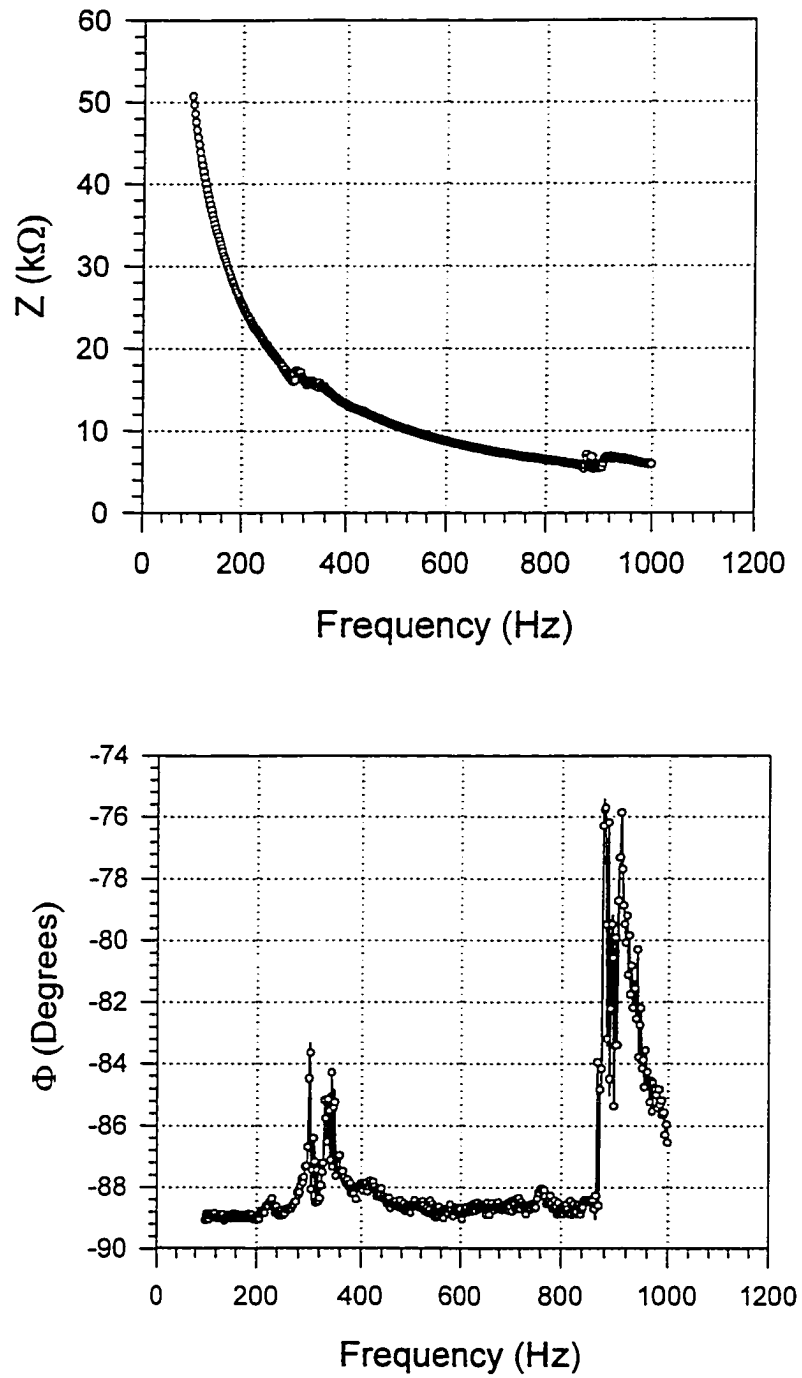


Figure 3.71 Impedance and Phase Angle vs Frequency for Case 5a

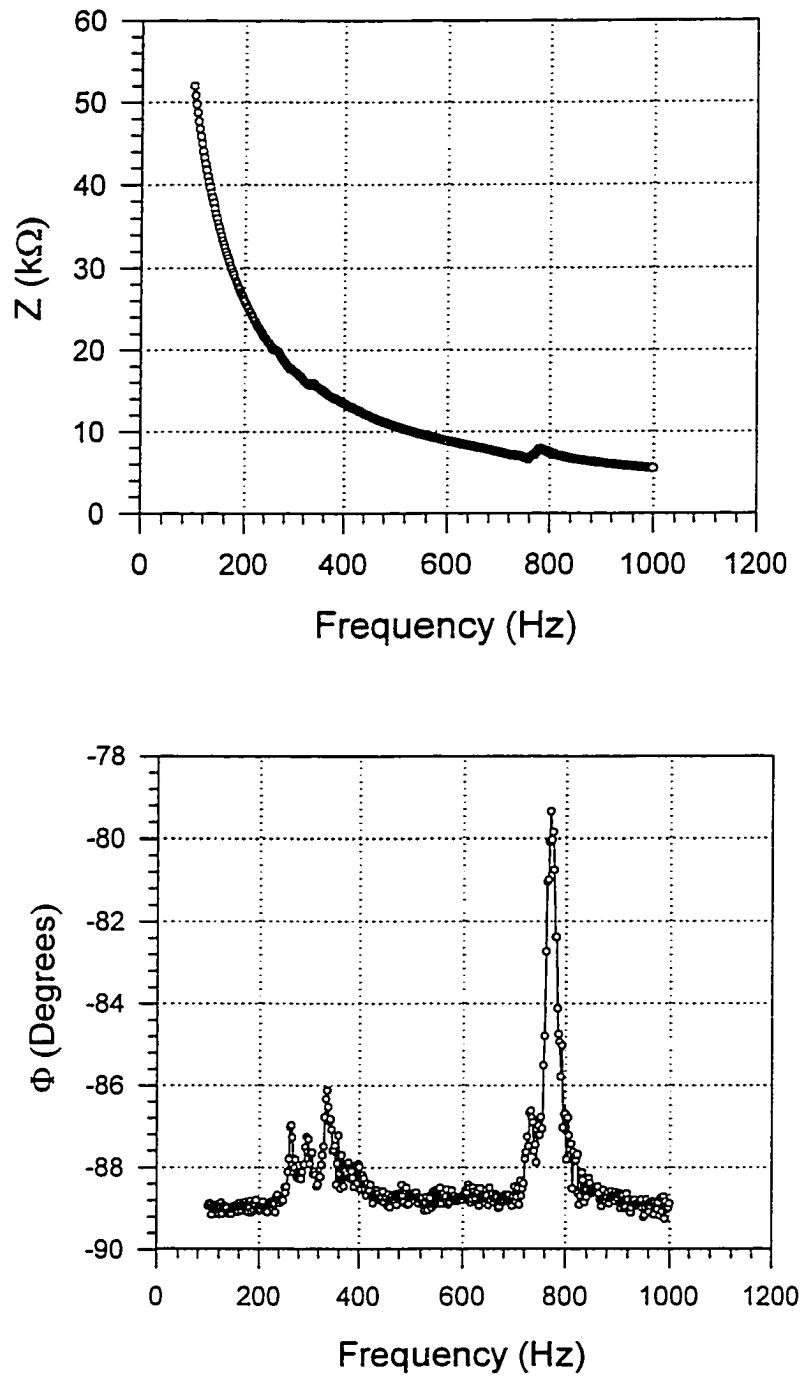


Figure 3.72 Impedance and Phase Angle vs Frequency for Case 6a

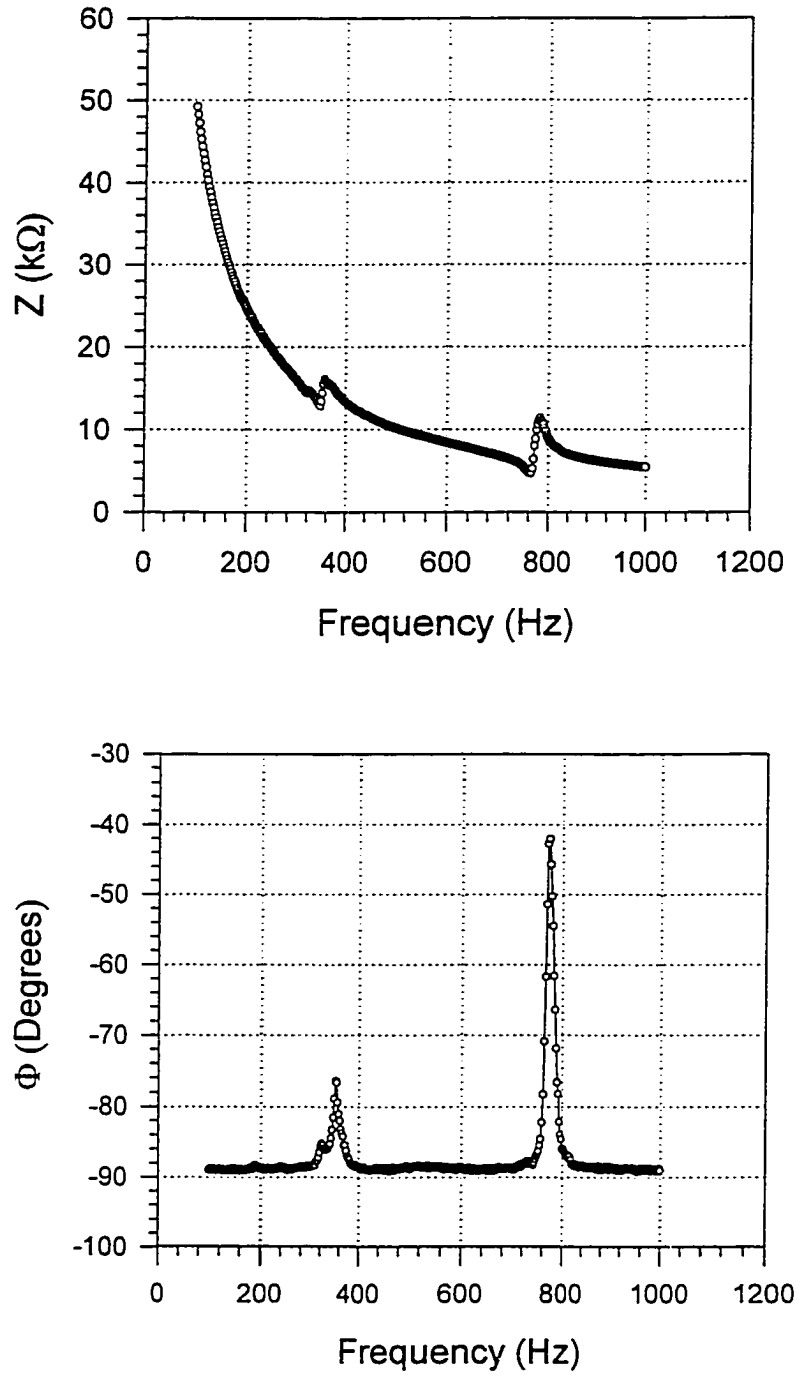


Figure 3.73 Impedance and Phase Angle vs Frequency for Case 7a

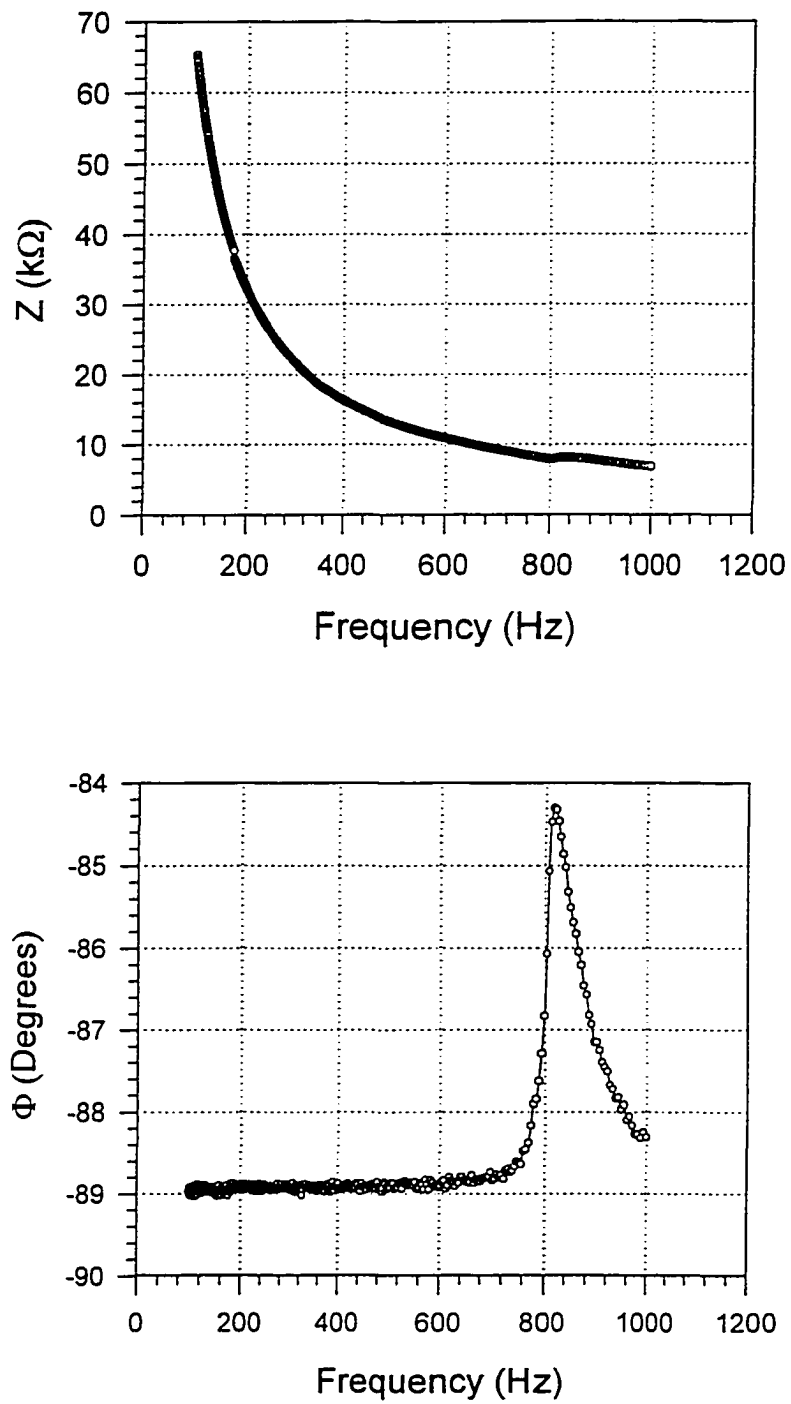


Figure 3.74 Impedance and Phase Angle vs Frequency for Case 1b

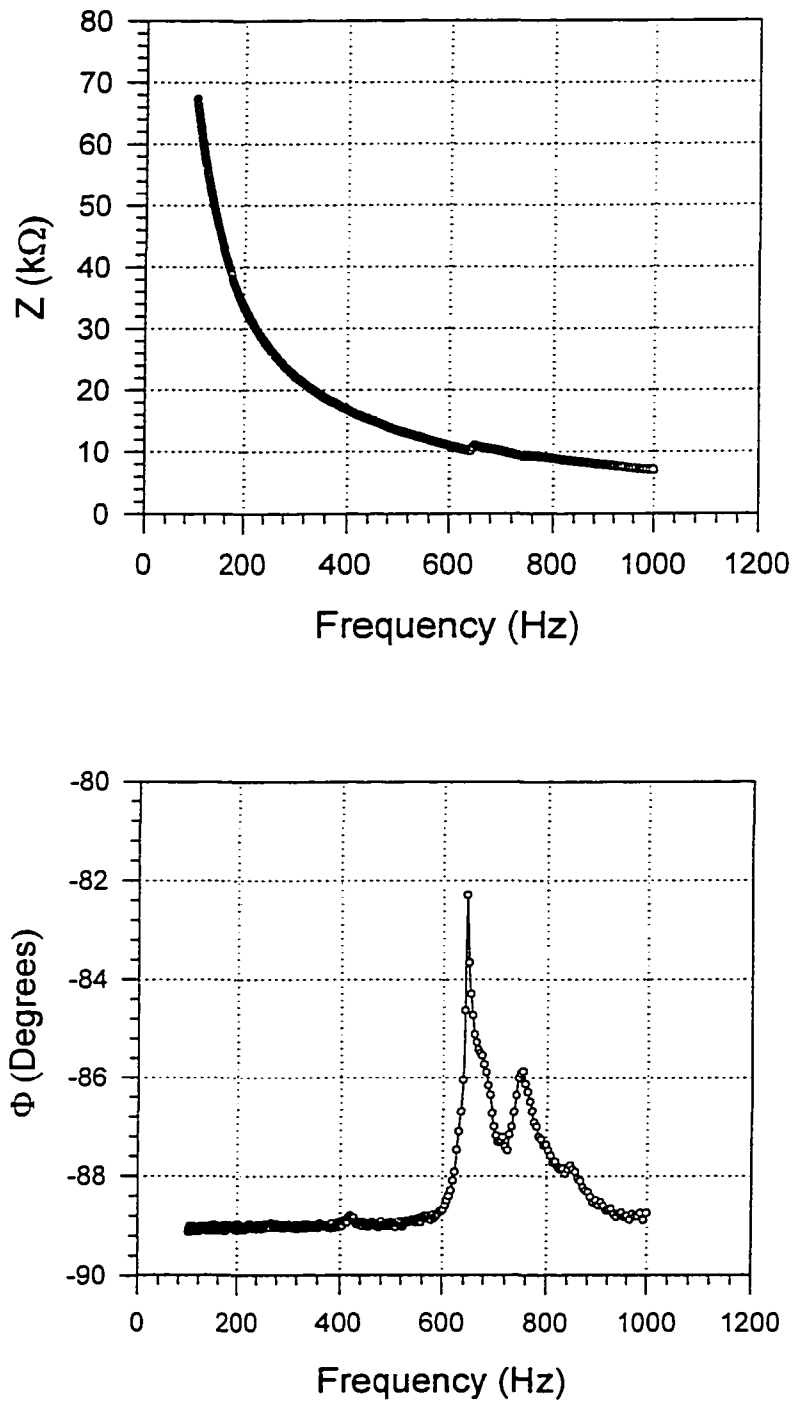


Figure 3.75 Impedance and Phase Angle vs Frequency for Case 2b

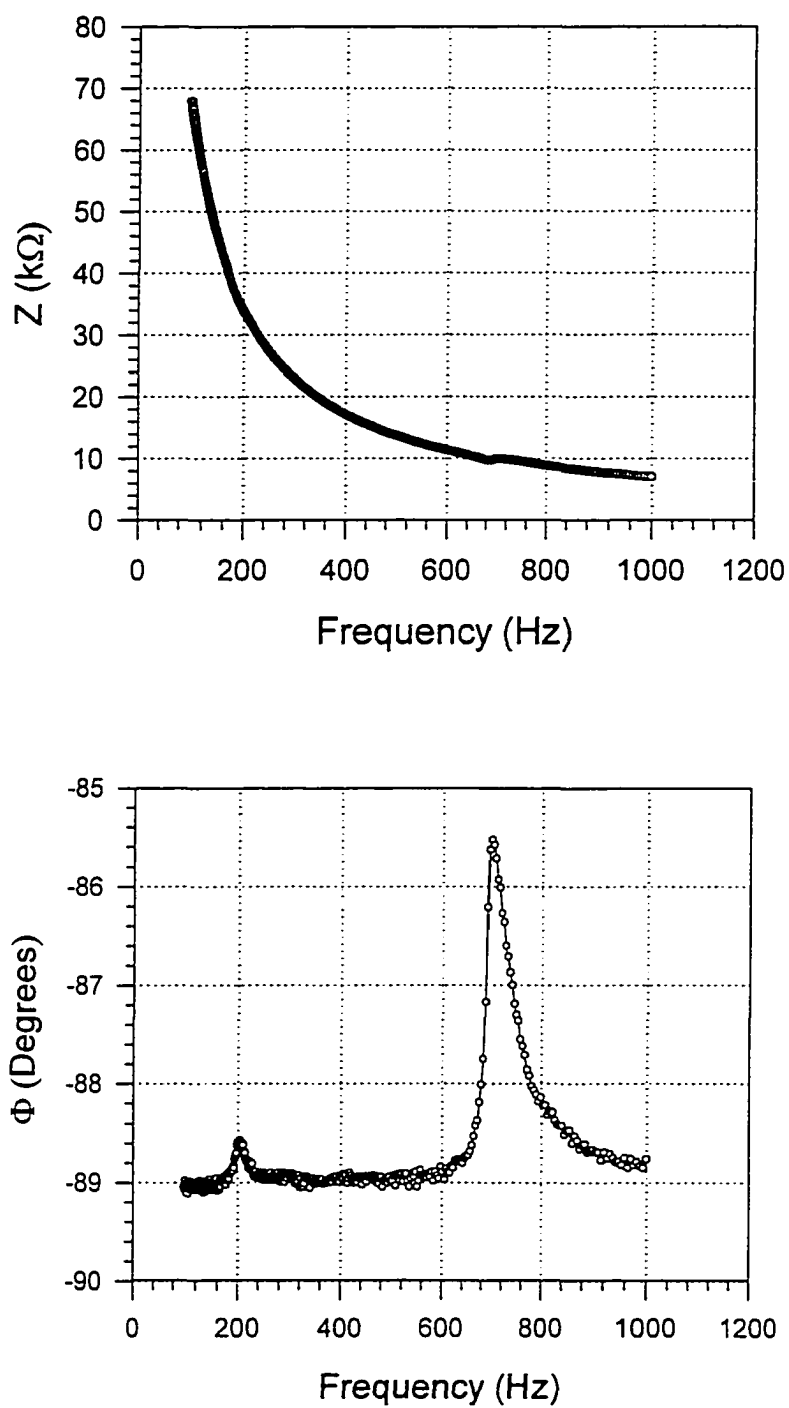


Figure 3.76 Impedance and Phase Angle vs Frequency for Case 3b

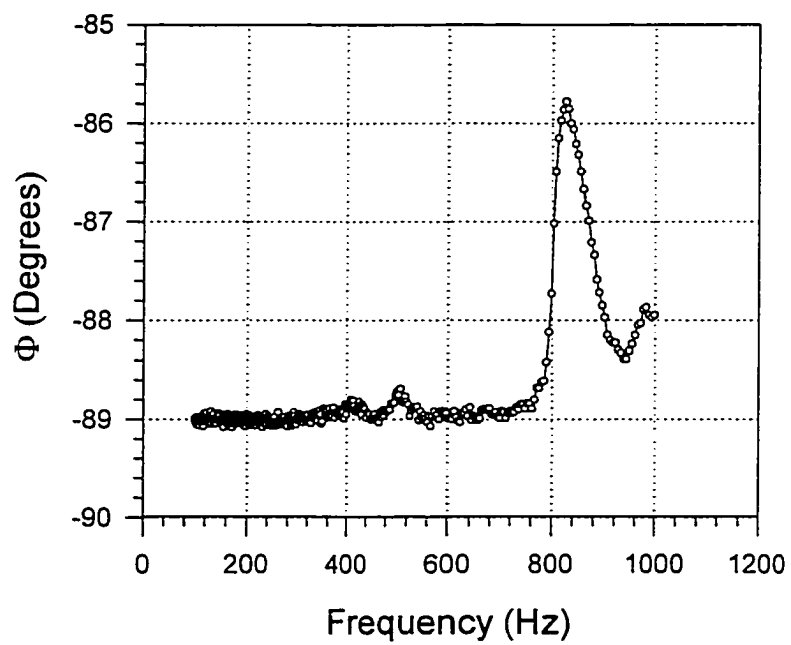
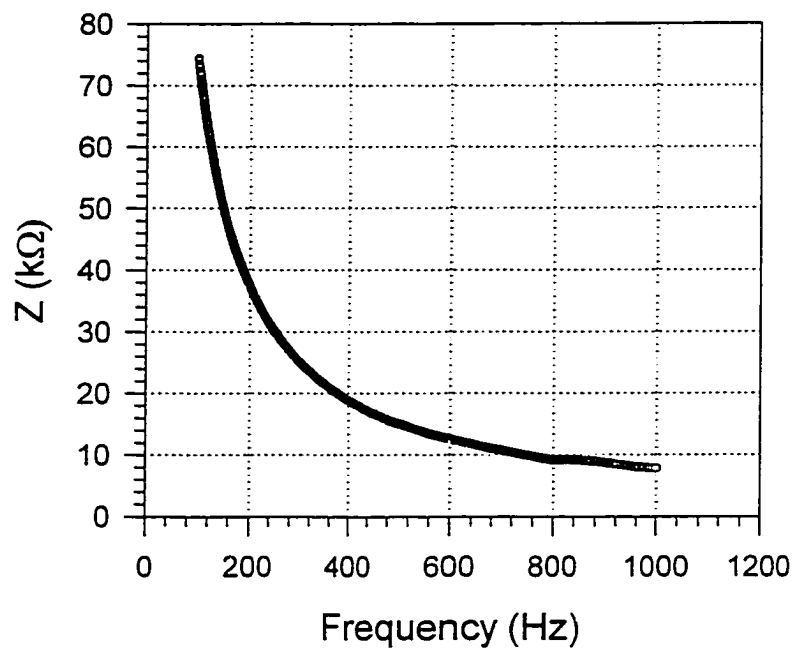


Figure 3.77 Impedance and Phase Angle vs Frequency for Case 4b

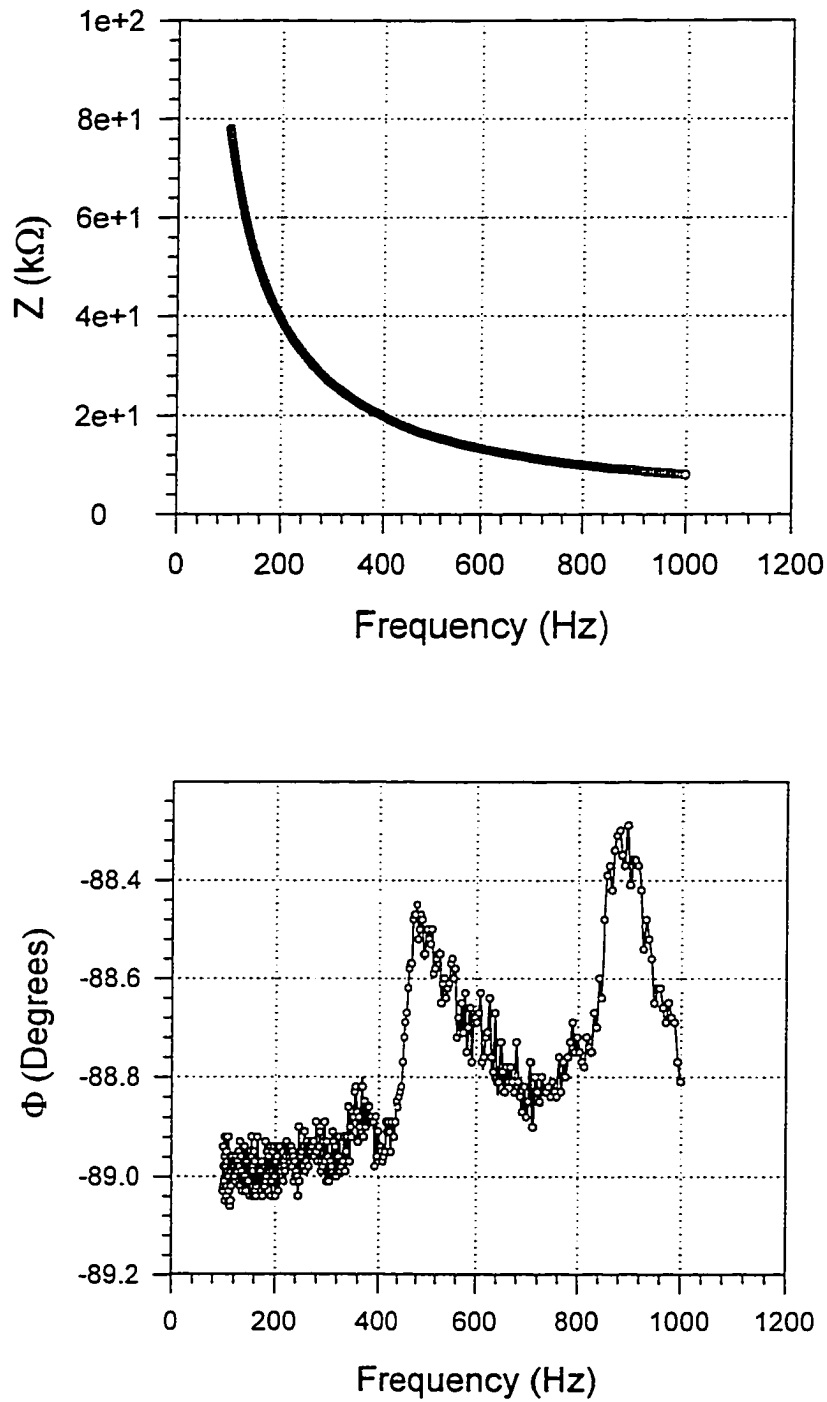


Figure 3.78 Impedance and Phase Angle vs Frequency for Case 4b

CHAPTER IV

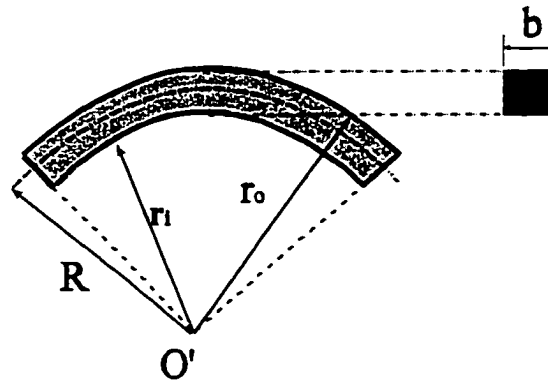
THEORETICAL FORMULATIONS

In order to explain the relationship between the number of backing layers of metal foil and displacement performance, a theory based on the neutral axis of a curved beam is suggested. Furman, Li, and Haertling [93] presented a similar theory for a different class of pre-stressed piezoelectric actuators (RAINBOW™). The actuator they analyzed was composed of an active layer (oxide layer) and an inactive one (reduced layer). They predicted that the maximum displacement should occur for an active over inactive layer thickness ratio of approximately one. This theory is based on neutral axis location and the fact the active and inactive layers of ceramic have the same modulus.

To identify the parameters that affect the piezoelectric device, curved beam theory is applied as an approximation. When a curved beam is bent in the plane of initial curvature, plane sections remain plane, the distribution of unit strain, and stress is not linear, and the neutral axis does not pass through the centroid of the section. [94] The location of the neutral axis is found by using the following, [95]

$$R = \frac{A}{\int_A \frac{dA}{r}} \quad (4.1)$$

where R is the location of the neutral axis from the center of curvature (O') of the member, A is the cross-sectional area, and r is the arbitrary position of the element dA from the center (O'). See schematic on the next page for more details.

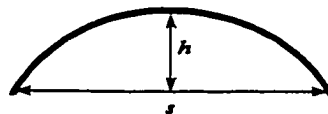


Since all the specimens tested have the same cross-sectional area, the equation above becomes:

$$R = \frac{A}{b \ln \left[\frac{r_o}{r_i} \right]} = \frac{b(r_o - r_i)}{b \ln \left[\frac{r_o}{r_i} \right]} = \frac{(r_o - r_i)}{\ln \left[\frac{r_o}{r_i} \right]} \quad (4.2)$$

This equation shows that the neutral axis depends only on the radius of curvature and not the cross-sectional area.

The radius of curvature of each specimen, was calculated using the formula below, where h and s were measured as shown in the schematic below.



$$r_i = \frac{h}{2} + \frac{s^2}{8h} \quad (4.3)$$

In order to compare all the cases, two ratios are defined. First, the "active to inactive" ratio is defined as used for the RAINBOW devices. For simplicity, this ratio is defined as:

$$\alpha = \frac{\textit{Active layer thickness}}{\textit{Inactive layer thickness}} \quad (4.2)$$

or,

$$\alpha = \frac{\textit{top layers + ceramic thickness}}{\textit{backing layers total thickness}}$$

Then, a second ratio is defined, which refers to the location of the neutral axis of the element, as:

$$\beta = \frac{(R - r_i)}{\textit{Inactive layer thickness}} \quad (4.5)$$

Using the above relations, the neutral axis of each specimen can be calculated. Only configurations after re-poling were considered, since there is more uniformity in these results. The results for the x/Al configurations can be seen in Table 4.1.

The active to inactive ratio was calculated using the ceramic layer as the active layer and the metal as the inactive, which predicts the 0/7-x/Al configuration as the one that produces the most displacement under no-load. To examine this result, the ratio defined as β (See equation 4.5) was calculated. If β is less than one, the neutral axis is located in the "inactive" layer, and if the ratio is greater than one, the neutral axis is in the "active" layer.

Values for β further show that when the neutral axis is just below the active layer, a large displacement is obtained from the piezoelectric device. This agrees with the theory presented by Furman, et al.[93]

The present piezoelectric devices, however, have additional material added between the layers (LaRC-SI film). Since the thickness of this adhesive material is difficult to determine, the total thickness of the device was measured using a micrometer. This value was defined as measured thickness. In this manner, an approximate thickness of adhesive layers can be determined. Using this approach, the theory does not predict configuration 0/7-x/Al as the best, but 0/3-x/Al. The results obtained are presented in Table 4.2

For this case, the neutral axis shifts, and the theory no longer agrees with the measurements performed. The inaccuracy in measuring real thickness of the devices, as well as the estimation of the thickness of the adhesive may explain the discrepancies between the results.

The same calculations were performed for the Al/Al configurations. The results presented in Table 4.3, which clearly show the neutral-axis theory to be inaccurate, were obtained using theoretical thickness values. However, if values of measured thickness are used, the theory proves to be correct. (See Table 4.4) These results again show that the configuration producing the most displacement was the one with a ratio of "active" layer to "inactive" layer close to one.

Some of the piezoelectric devices measured do not maintain a constant radius of curvature for various reasons (handling, poling, etc.), and therefore the neutral axis position also changes, with an unknown effect on displacement performance. Such an effect may be

favorable for some configurations, like the cases where the displacement measurements increased by approximately 33% after re-poling.

The values of the modulus of elasticity of aluminum (aluminum alloy 3003, ASTM B221, 68.95GPa)[96] and the ceramic wafer (69GPa)[92] are almost equal, making the stresses equally distributed [94]. Since the stiffness is the same for both materials, the piezoelectric devices with this configuration are easily deformable, especially if the voltages applied to the piezoelectric devices are relatively high (e.g., during poling). To illustrate the change in curvature for such devices, measurements of radius of curvature before and after poling were performed for all the configurations (Table 4.5). Note that some of the devices were not tested because they broke in handling or during poling. This is due to the brittleness of some of the samples, especially the ones that had no protective layer above the ceramic (i.e., x/Al-5 configuration).

Stainless steel (Type 304, 193.1GPa) [96] has a modulus of elasticity twice as high as the ceramic. Hence, the stresses are concentrated in the metallic layer (higher modulus of elasticity) leaving the ceramic free to move.

To further explore the concept presented above, THUNDER™ types I and II were analyzed in two different categories, since the formulas developed before (97) apply only to homogeneous curved beams. Applying the theory previously discussed to composite THUNDER™ devices required a transformation which led to an effective device composed of a single material with a common modulus. First, for a beam composed of two materials, (THUNDER™ model type I) with different moduli, a transformation factor, n , is defined [94]:

$$n = \frac{E_1}{E_2} \quad (4.6)$$

where E_1 is the modulus of elasticity of the bottom layer of a THUNDER device and E_2 is the modulus of the top material (the ceramic layer and the aluminum layer for the type I THUNDER™ actuators). This transformation factor indicates that the cross section having an original width b , must be increased by nb . In this case, model type I THUNDER™ actuators are essentially composed of two materials, since the modulus of aluminum is almost the same as the ceramic (69 GPa). Hence, the above expression indicates that the width of each component parallel to the principal axis of bending is increased in the same proportion that the modulus of elasticity of that component makes with the modulus of the assumed material of the equivalent beam. [96] For a curved beam composed of two different materials the equivalent beam structure is shown in Figure 4.1. In this figure, t_1 and t_2 are the respective bottom and top thicknesses and r_0 is the inner radius of curvature of the beam. If $E_1 > E_2$ then, the cross sectional area becomes as shown in Figure 4.1, which has a cross section of different size but the same modulus of elasticity. These areas are defined as,

$$A_1 = nb t_1 \quad \text{and} \quad dA_1 = nb dr \quad (4.7)$$

$$A_2 = bt_2 \quad \text{and} \quad dA_2 = b dr \quad (4.8)$$

which transforms the location of the neutral axis, R , into,

$$R = \frac{n t_1 + t_2}{n \ln [(r_o + t_1)/r_o] + \ln [(r_o + t_1 + t_2)/(r_o + t_1)]} \quad (4.9)$$

Using the above equation, the ratio defined as alpha can be calculated again using (97),

$$\alpha = \frac{(R - r_o)}{\text{inactive layer thickness}} \quad (4.10)$$

where r_o is the radius of curvature of the sample and the *inactive layer thickness* reflects the additional material placed below the ceramic layer (i.e., stainless steel). It was experimentally determined that the thickness of the adhesive layer for this THUNDER™ model type I was 1.5 mil (0.00381 cm) after the actuator was constructed. Hence, the inactive layer thickness was calculated by adding the adhesive layer under the PZT ceramic, the 1 mil (0.00254 cm) aluminum layer, the next adhesive layer, and the bottom layer (stainless steel of varying thicknesses). Results presented in Table 4.6 show these parameters as well as β and α . This table shows α to be a better parameter than β , defined as equation (4.11) below.

$$\beta = \frac{\text{top layer + ceramic thickness}}{\text{total thickness of bottom layers}} \quad (4.11)$$

When $\alpha=1.01$ (1% of the ideal case, $\alpha=1.0$) case 3a is again predicted as the configuration that will produce the most displacement, while $\beta=1.04$ (4% of the ideal case, $\beta=1.0$) predicts case 6a as the best performer, which Figure 3.53 clearly shows to be inaccurate.

The same theory was applied to THUNDER™ type II models, which are composed of materials with three different moduli of elasticity. In this case two parameters need to be defined, n_{1-2} and n_{3-2} :

$$n_{1-2} = \frac{E_1}{E_2} \quad (4.12)$$

$$n_{3-2} = \frac{E_3}{E_2} \quad (4.13)$$

where the subscript three refers to a material with the modulus of elasticity of the top layer (brass), two refers to the ceramic modulus, and one to the material below the ceramic (stainless steel). Again the material is transformed into a homogeneous specimen with different cross-sectional areas, as shown in Figure 4.2, where t_1 , t_2 , and t_3 , are the bottom layer, ceramic layer, and top layers thicknesses, respectively.

Hence, the neutral axis location is defined as,

$$R = \frac{n_{1-2}t_1 + t_2 + n_{3-2}t_3}{n_{1-2} \ln \left[\frac{r_o + t_1}{r_o} \right] + \ln \left[\frac{r_o + t_1 + t_2}{r_o + t_1} \right] + n_{3-2} \ln \left[\frac{r_o + t_1 + t_2 + t_3}{r_o + t_1 + t_2} \right]} \quad (4.14)$$

where r_o refers to the inner radius of curvature of the THUNDER™ device. For this type of THUNDER™ device, the adhesive thickness was 2 mil (0.00508 cm), so that the inactive layer thickness is the stainless steel thickness (variable) plus one layer of adhesive. Then, the parameters α and β can be calculated using Equations 4.10 and 4.11 . The results are presented in Table 4.7, which shows that configuration or model 2b is the device with the most displacement as the experimental results show in Figure 3.54. The value of β , on the

other hand, predicts configuration 4b as to be the best performer, however, for loads below 0.5 Kg, this is not true. With an applied load of 1 Kg, conclusions based on the value of α seem to match the experimental results.

These results clearly show that the neutral axis theory predicts the configuration with the best performance for a particular class of THUNDER™ devices under load and no-load conditions at 1 Hz. At higher frequencies, these results are not valid because of the mass attached to the device (which will decrease the device's natural resonant frequency as well as the instability of the measurement system used). A different mechanism is needed for measurements at higher frequencies.

It has been clearly demonstrated that the best design is configuration 3a. Hence, this is the design that has been developed into an actuator for the vortex generator mechanism. As can be seen in Figure 3.53, a displacement of approximately 0.4064 mm (0.016 in) was produced with this design with no load at 200 Vpp. In the next chapter, an aerodynamic application based on configuration 3a is presented.

Table 4.1
Location of Neutral Axis for x/Al Configurations Using Theoretical Thickness

Conf.	r_i (in)	Theoretical Thickness (mils)				R (in)	$R-r_i$ (mils)	β	α
		Top	Ceramic	Bottom	Total				
0/1-x/Al	6.0	0	7	1	8	6.004	4	7.00	4.0
0/3-x/Al	6.5	0	7	3	10	6.500	5	2.33	1.7
0/5-x/Al	5.4	0	7	5	12	5.400	6	1.40	1.2
0/7-x/Al	6.2	0	7	7	14	6.200	7	1.00	1.0
0/9-x/Al	6.3	0	7	9	16	6.300	8	0.78	0.89

Table 4.2
Location of Neutral Axis for x/Al Configurations Using Measured Thickness

Conf.	r_i (in)	Estimated Thickness of the "Active" Layer(mils)	Measured Total Thickness (mils)	R (in)	$R-r_i$ (mils)	β	α
0/1-x/Al	6.0	7	11.0	6.005	5.5	1.37	1.8
0/3-x/Al	6.5	7	16.0	6.508	8.0	0.89	0.8
0/5-x/Al	5.4	7	17.5	5.409	8.7	0.83	0.7
0/7-x/Al	6.2	7	18.5	6.209	9.2	0.80	0.6
0/9-x/Al	6.3	7	22.0	6.311	11.0	0.73	0.5

Table 4.3
Location of Neutral Axis for Al/Al Configurations Using Theoretical Thickness

Conf.	r_i (in)	Theoretical Thickness in mils				R (in)	$R-r_i$ (mils)	β	α
		Top	Ceramic	Bottom	Total				
1/3-x/Al	6.0	1	7	3	11	6.029	5.5	2.67	1.80
1/5-x/Al	4.7	1	7	5	13	4.731	6.5	1.60	1.30
1/7-x/Al	7.3	1	7	7	15	7.291	7.5	1.14	1.07
1/9-x/Al	5.9	1	7	9	17	5.914	8.5	0.88	0.94

Table 4.4
Location of Neutral Axis for Al/Al Configurations Using Measured Thickness

Conf.	r_i (in)	Estimated Thickness of the "Active" Layer(mils)	Measured Total Thickness (mils)	R (in)	$R-r_i$ (mils)	β	α
1/3-x/Al	6.00	9.9	17	6.009	8.5	1.39	1.20
1/5-x/Al	4.72	9.6	21	4.740	10.5	0.84	0.90
1/7-x/Al	7.28	9.4	24	7.290	12.0	0.67	0.80
1/9-x/Al	5.91	9.2	25	5.920	12.5	0.58	0.79

Table 4.5
Radius of Curvature before and after Re-Poling Flat Elements

<i>Conf.</i>	<i>Designation</i>	<i>R (cm)</i>		<i>% Difference</i>
		<i>Before Poling</i>	<i>After Poling</i>	
1	0/1-x/Al	15.03	15.15	+0.8
2	0/3-x/Al	16.01	16.50	+3.1
3	0/5-x/Al	13.11	13.60	+3.6
4	0/7-x/Al	17.85	15.70	-11.8
5	0/9-x/Al	14.70	16.02	+8.3
6	1/3-Al/Al	14.10	15.30	+16.0
7	1/5-Al/Al	12.00	12.50	+4.0
8	1/7-Al/Al	15.00	18.50	+19.2
9	1/9-Al/Al	17.00	15.00	-11.9
10	0/1-x/Al-5	broke	—	—
11	0/1-x/SS	13.86	9.87	-27.8
12	0/1-x/SS-3	8.13	12.50	+53.8
13	0/1-x/BeCu-2	broke	—	—

Table 4.6 Location of Neutral Axis for Cases 1a thru 7a

Case	r_o (in)	Thickness (mils)				R (in)	R- r_o (mils)	β	α
		Material		Inactive Layer	Total				
		I	II						
1a	3.05	16.5	2	6	18.5	3.058	0.008	2.08	1.32
2a	8.17	16.5	3	7	19.5	8.178	0.008	1.79	1.14
3a	7.97	16.5	4	8	20.5	7.978	0.008	1.56	1.01
4a	12.53	16.5	6	10	22.5	12.539	0.009	1.25	0.86
5a	7.97	16.5	7	11	23.5	7.979	0.009	1.14	0.81
6a	7.97	16.5	8	12	24.5	7.979	0.009	1.04	0.77
7a	7.54	16.5	9	13	25.5	7.550	0.010	0.96	0.73

Table 4.7 Location of Neutral Axis for Cases 1b thru 5b

Case	r_o (in)	Material Type Thickness (mils)					R (in)	R- r_o (mils)	β	α
		1	2	3	Total	Inactive				
1b	18	1	12	4	17	6	18.007	6.8	1.83	1.13
2b	18	1	12	5	18	7	18.007	7.0	1.57	1.00
3b	18	1	12	6	19	8	18.007	7.3	1.38	0.92
4b	18	1	12	9	22	11	18.008	8.4	1.00	0.76
5b	18	1	12	12	25	14	18.010	9.6	0.79	0.69

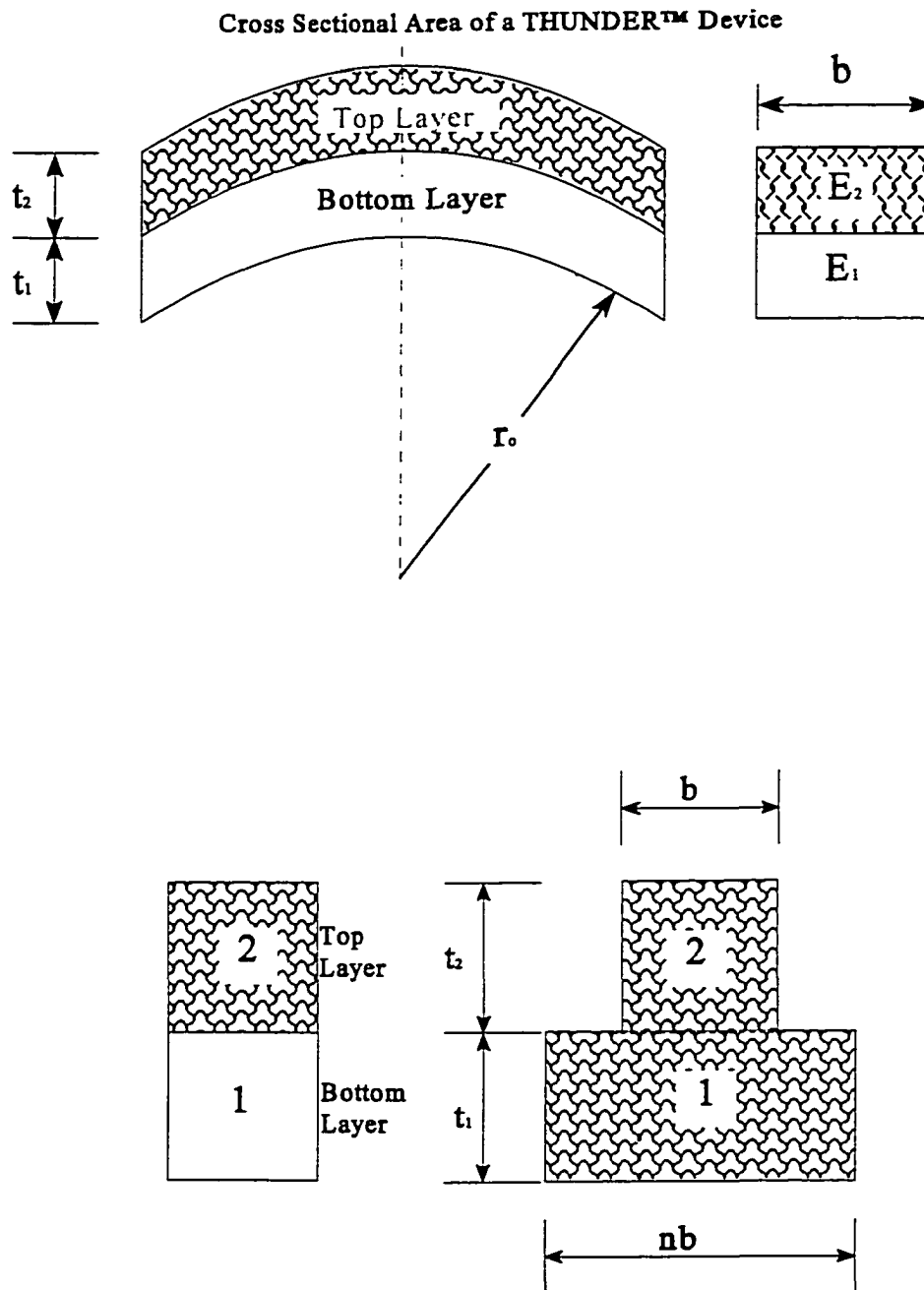


Figure 4.1 Equivalent Cross Sections for THUNDER™ Type I

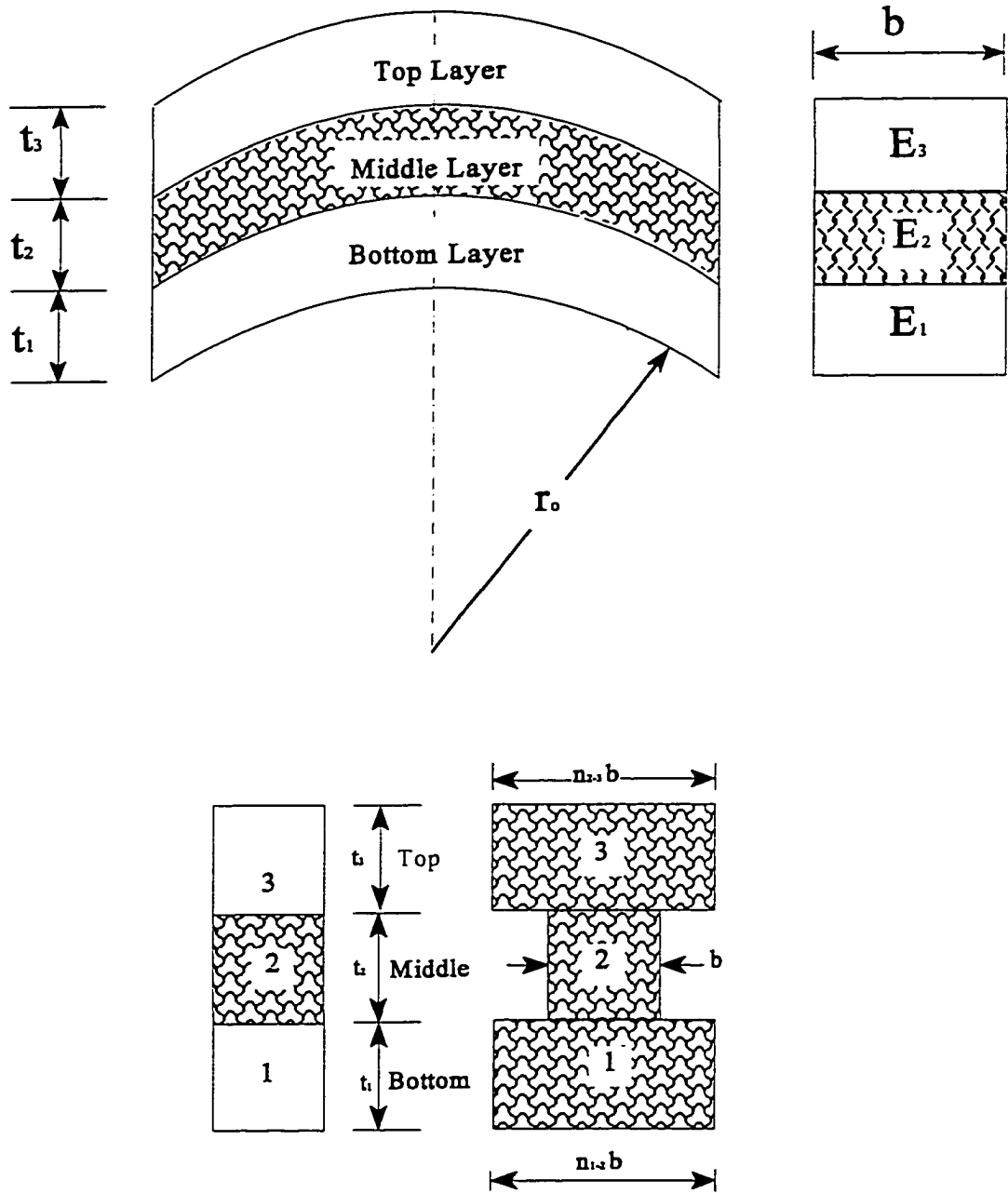


Figure 4.2 Equivalent Cross Sections for THUNDER™ Type II

CHAPTER V

APPLICATIONS TO FLOW CONTROL

5.1 General

Flow control, using vortex generators of various types have proven to be effective by many researchers, and the possibility of actively deploying them has been suggested in the past. However, many of the deployment systems considered involved mechanical parts or actuators that required large amounts of power. Hence, considerable additional weight and sophisticated control mechanisms are needed, which may not be feasible to add to existing designs of aircraft, cars, submarines, etc., without a significant performance penalty.

A THUNDER™-based actuator, used to deploy a vortex generator, has the advantage over most piezoelectric actuators in terms of weight, volume, power consumption, durability, and ruggedness. The greatest advantage over other piezoelectric actuators, however, is that the "shape" of a THUNDER™ device can be designed to fit a specific purpose. For example, a THUNDER™ device can be designed with a delta-wing shape, or any other simple geometry. Furthermore, THUNDER™ devices can be built in almost any size and with many different metals, to facilitate use under harsh environmental conditions. Considering all the advantages mentioned above, a submerged vane-type vortex generator was designed using a THUNDER™ device as an actuator. In order to test this concept, a two dimensional backward-facing ramp, with vane-type submerged vortex generators embedded in its surface, was constructed and tested. In this manner, vortex generators could be actively deployed at a particular height (e.g., adjustable to some percentage of the boundary-layer height) and frequency (variable), and be controlled remotely.

Several tests were conducted using the backward-facing ramp model which consisted of a two-dimensional ramp with an 20.32 cm radius (Figure 2.18). First, the baseline separation line was established using a model without vortex generators. Then, using conventional methods (with vortex generators attached to the model surface using an adhesive), an optimal location for the vortex-generators was found. Using this location as a reference point, a THUNDER™ device was embedded in the model so that vortex generators could be deployed at the optimum location. Finally, using the above setup, pressure measurements were acquired and the extent of the separation region was determined for the two conditions (with and without vortex generators deployed). To further illustrate the effectiveness of the THUNDER™-actuated vortex-generator system, smoke flow-visualization photographs were taken. A detailed description of the measurements acquired and all related results are given below.

5.2 Boundary-Layer Parameters

All tests were conducted at a constant flow speed of 24 m/s to insure a significant separated-flow region. The centerline flow was monitored along the length of the model with boundary-layer and pitot-static probes. The boundary-layer probe measured the differential pressure between the boundary-layer stagnation and the freestream static pressures, and the pitot-static probe measured the differential pressure between the freestream stagnation and static pressures. Using these data, the boundary-layer velocity at any point was evaluated with the following equation:

$$u = \sqrt{\frac{2 \cdot (P - P_{\infty})}{\rho}} \quad (5.1)$$

where P is the boundary-layer pressure, P_{∞} is the freestream static pressure, and ρ is the density of air at standard conditions. In this manner, the velocity profiles along the model can be obtained. To ensure turbulent flow, a velocity profile was compared with a theoretical turbulent velocity profile for flow over a flat plate at $x/h=5.0$ location (See Figure 5.1). The theoretical profile with a correlation coefficient of 90% with an equation of the form, [99]

$$\frac{u}{U_{\infty}} = \left(\frac{y}{\delta} \right)^{\frac{1}{7}} \quad (5.2)$$

The boundary layer thickness, δ , was determined experimentally as the normal distance from the wall to the location where the velocity reaches 99% of the freestream value. Furthermore, parameters, such as the displacement thickness, as well as the momentum thickness, can be calculated using the following expressions, [98, 54]

$$\delta^* = \int_0^{\delta} \left(1 - \frac{u}{U_{\infty}} \right) dy \quad (5.2)$$

$$\theta = \int_0^{\delta} \frac{u}{U_{\infty}} \left(1 - \frac{u}{U_{\infty}} \right) dy \quad (5.3)$$

where δ^* is the displacement thickness, and θ is the momentum thickness.

The physical meaning of the boundary-layer displacement thickness is demonstrated when considering the mass flow in a typical laminar and turbulent boundary layer flow. Since mass flow for incompressible flow is defined as the area under a boundary layer velocity profile, for a laminar velocity profile, the value of mass flow is larger than a turbulent flow (making the value of δ^* for turbulent flow smaller than a laminar flow). Similarly, the momentum thickness may be explained as the thickness that displaces the boundary of the wall by the distance θ . However, the growth of θ is negligible compared to δ^* . [53] Hence, the ratio of displacement to momentum thickness, called the dimensionless-profile shape factor, [99] can be defined as,

$$H = \frac{\delta^*}{\theta} \quad (5.4)$$

can be used to specify the onset of separation. The closer the value is to separation, the larger the value of H becomes for attached turbulent flow. [53] For example, if H reaches a value of 1.8 to 2.6 in a short distance, then turbulent flow separation is expected. This makes H a good indicator of the pressure gradient. [99]

In order to obtain values of δ , δ^* and, θ , velocity profiles were measured using a boundary-layer probe mounted on a height gage that was positioned at distances between $x = 127$ mm (5 in) to $x = 229$ mm (9 in) and y -increments of 0.254 mm (0.010 in). The origin of the frame of reference was chosen at the base of the model, see Figure 2.18. In this manner, $y=0.0$ mm corresponds to the area downstream of the ramp. One thousand measurements of velocity were made at each y -position to define the mean local boundary-

layer velocity. (See Figure 2.19 for a schematic of the relevant experimental set-up). In this manner, velocity profiles were generated along the length of the floor downstream of the ramp. Results of the velocity profile survey for the baseline model at various streamwise locations along the model are presented in Figure 5.2. Note that when the flow was reversed, the pressure measurements were negative, so that velocity values based on these results should only be used as an indication of reversed flow, since the boundary layer probe can not detect flow directions. So that, when $x/\delta=34.7$ ($x/h=16.9$), the flow is separated (reversed flow) due to the adverse pressure gradient that has been developing, and the fluid particles are slowed down. Then, due to the decrease in kinetic energy, a region of flow reversal is observed, which is called the separation region. [100] This region continues to increase until $x/\delta=8.9$ ($x/h = 26.9$), where the flow is not reversed and is considered re-attached flow.

Parameters that were calculated (such as δ , δ^* , and θ , and their variation in the freestream direction) are shown in Figure 5.3. Note that at the onset of separation, the boundary-layer thickness remained almost constant at a value of 5.37 mm. The same trend (constant values) is observed on displacement thickness, momentum thickness, and shape factor.

5.3 Submerged Vane - Type Vortex Generators

Based on the extensive results presented by Lin, submerged vane-type vortex generators produced the best results, in terms of reduction of the separation region associated with a rearward-facing ramp, and the least drag penalty.[54] The vortex generators in the present research (rectangular plates that projected normal to the wall) were arranged in a single row with adjacent generators set at alternating angles of incidence (± 15 deg.) to the

flow to produce an array of streamwise counterrotating vortices. (See Figure 5.4) The vortex generator height, η , was chosen according to the results provided by Lin, who concluded that $\eta \sim 0.1\delta$ to 0.2δ reduces the extent of separation by almost 90%. Hence, the chosen value for these surveys was $\eta = 0.1\delta$, based on the boundary layer thickness at the onset of separation, $\eta = 0.53$ mm (21 mils). Furthermore, the location of the row of vortex generators was 15δ upstream of the baseline separation region ($x = 115$ mm), consistent with Lin's experiments. Other relevant values of parameters include aspect ratio $\eta/l = 0.5$ ($l = 1.06$ mm or 42 mils), and a spanwise distance of $\lambda/s = 4$ ($\lambda = 2.12$ mm or 83 mils) between each pair of devices. Once the location for the vortex generators was determined, the THUNDER™ device was installed in the model. Since the device height was required to be 0.53 mm (20 mils), the voltage used to activate the vortex generator was between 250-300VDC. This range of voltages was determined by using the results obtained in chapter 3, and since the load of the vortex generator is less than the actuator weight, the load was neglected. Once the vortex generators were installed, velocity surveys were conducted and boundary-layer parameters calculated.

Measured velocity profiles with vortex generators deployed are shown in Figure 5.5, and again when the velocity was reversed, the flow was considered to be separated. Note that with vortex generators deployed, the flow is separated at $x/h = 25.9$ ($x/\delta = 24.4$) and it is attached at $x/h = 26.9$ ($x/\delta = 18.7$). Comparing these values to the baseline results, a delay in the onset of separation, as well as a reduction to the extent of the separated-flow region [approximately 30% ($\pm 5\%$)] is clearly shown.

To further illustrate the changes to flow parameters due to the deployed vortex generators, δ , δ^* , and θ were calculated. Variation in parameter values with streamwise location is similar to that observed for the baseline flow. (See Figure 5.6). This trend helps determine the extent of the separation region. Furthermore, the results shown coincide with the value suggested by White, where for a turbulent flow, separation occurs approximately at $H=2.4$. [99] For the baseline flow, a shape factor of 2.4 occurs at $x=291$ mm. When the vortex generators are deployed, this value of shape factor occurs at $x=329$ mm, indicating that the separation location has moved downstream, as shown in Figure 5.7. This parameter, however, does not predict the location of reattachment, for which more detailed measurements need to be performed.

5.4 Pressure Distribution

Static pressure orifices were located along the centerline of the top surface of the wind tunnel test section in the vicinity of the separation ramp. All surface static pressure measurements were referenced to the freestream static pressure measured at the beginning of the test section.

The measured pressure distributions for the two cases, baseline and with vortex generators deployed, are shown in Figure 5.8. It can be seen that the pressure distribution along the wall is altered when the vortex generators are deployed, confirming the results observed above. The "filling in" of the "valley" in the baseline pressure distribution with the vortex generators deployed is indicative of a weaker separation region of lesser extent. The extent of separation can be defined as the distance between the point where the pressure coefficient levels off and the point where maximum C_p occurs. Defined in this manner, the

baseline separation region starts at $x/h=26.1$ and ends at $x/h=36.1$. With VGs deployed, the separation region starts at $x/h=28.6$ and ends at $x/h=35.1$. These data indicate a reduction of 35% in the extent of the separation region, which agrees with the estimated value using the velocity profiles and the shape factor as previously discussed. In order to further validate these results, flow visualization experiments were conducted and a discussion of the results is presented below.

5.5 Flow Visualization Results

Using the same model, and the setup described on chapter 2, smoke-flow visualization pictures were taken at two different situations, activated and de-activated vortex generators. These results show a dramatic difference between the two cases. A sample of these cases is shown in Figure 5.9 (a) and (b).

These photographs were taken under the same conditions, in order to facilitate a direct comparison. The original photographs were digitized, thus enabling an accurate determination of the separation region in both cases. This was accomplished by overlaying a grid on the original photograph. The grid was formed by 2.54×2.54 mm (0.1×0.1 in.) divisions, so that a scale was provided. (See Figures 5.10 (a) and (b).) According to Figure 5.10(a), the baseline separation region, is 71.1 mm (2.8 in.) long and with the vortex generators deployed, Figure 5.10 (b) indicates that the separation region is 40.6 mm (1.6 in.) long. These results show a decrease of 43 % in the separation region. Thus, the effectiveness of a THUNDER™-based actuator for an array of vortex generators has been demonstrated, such that the vortex generators can be deployed only when necessary.

Further experiments were attempted with the vortex generators deployed at different frequencies. Pressure measurements or velocity profile measurements were taken, however the results were inconclusive. Such results were expected since the measurements made were time-averaged and time-dependent measurement were needed. Flow visualization was attempted and the results are shown in Figure 5.11 for vortex generators deployed at 12 Hz. The technique previously described was used and the extent of the separation is reduced by approximately 20%. Again time-dependent measurements need to be acquired in order to obtain a more accurate measurement. However, this further reduction in the separation region suggests that there may be a particular frequency of deployment that results in an optimum reduction to the extent of separated flow.

Experiments described in this section show the effectiveness of a "smart actuator" (THUNDER™) for submerged vane-type vortex generators. This actuator can be easily controlled and its versatility provides many different possibilities in the flow-control field.

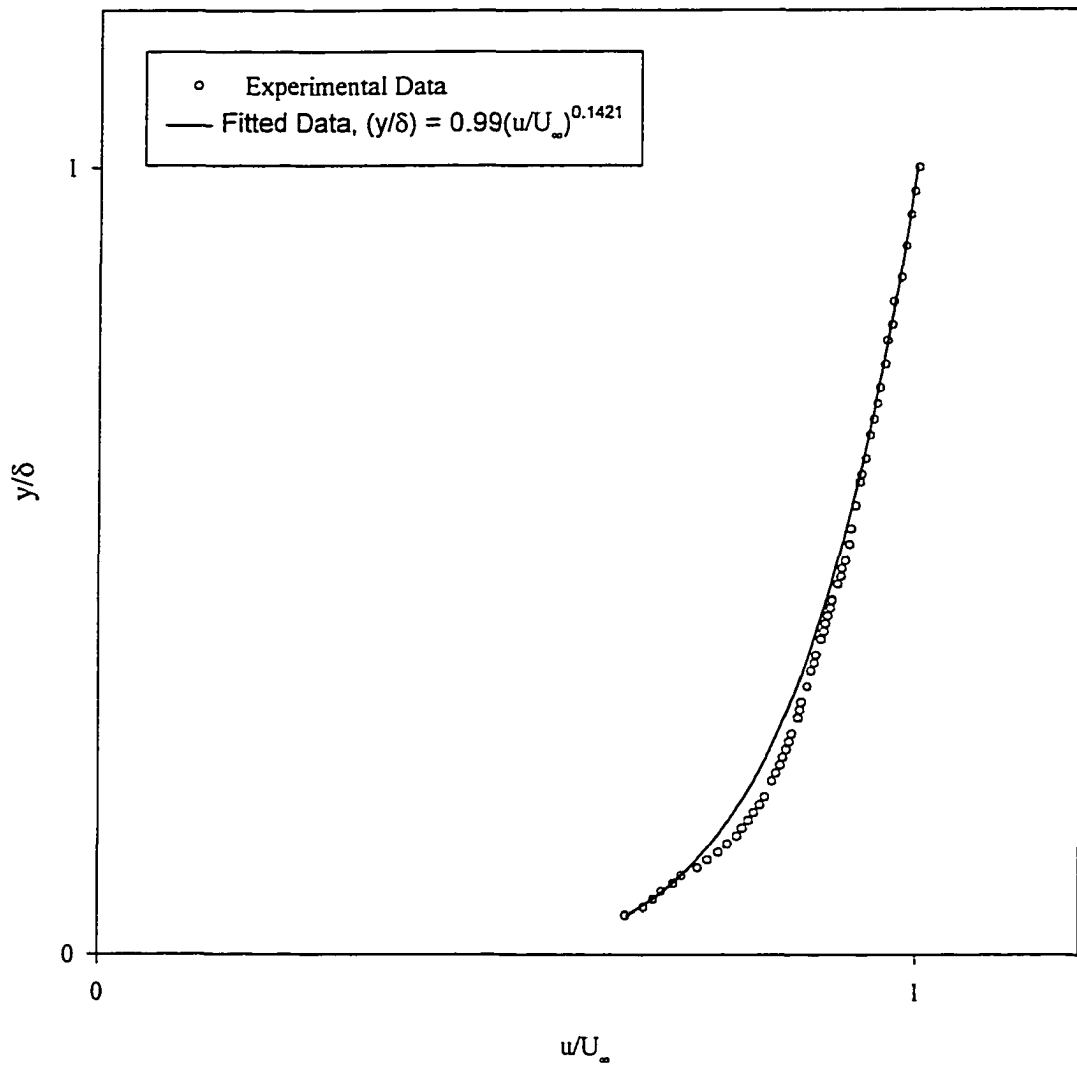


Figure 5.1 Velocity Profile for Turbulent Flow Over a Flat Plate, $x/h=5.0$

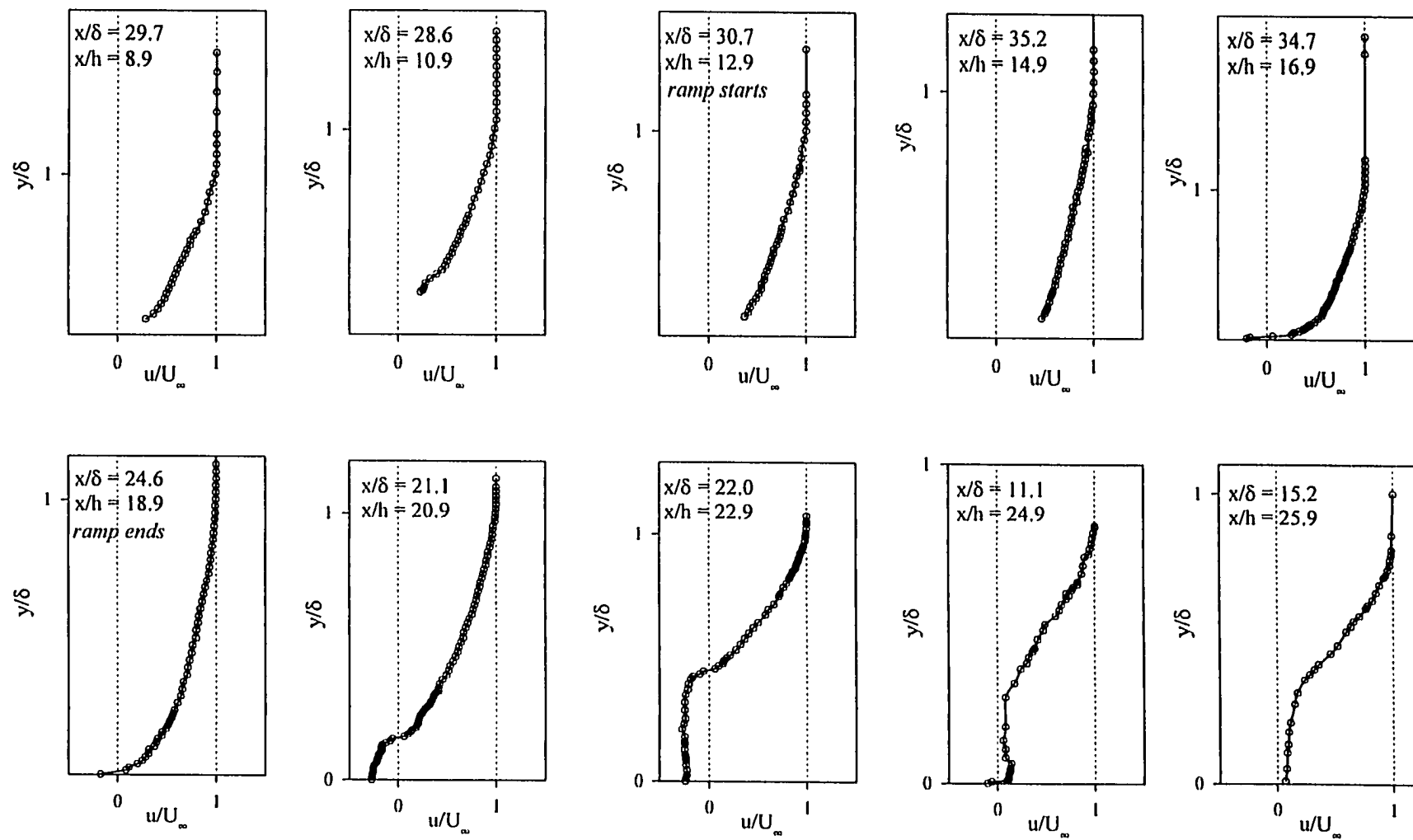


Figure 5.2 Baseline Velocity Profiles for a Backward-Facing Ramp

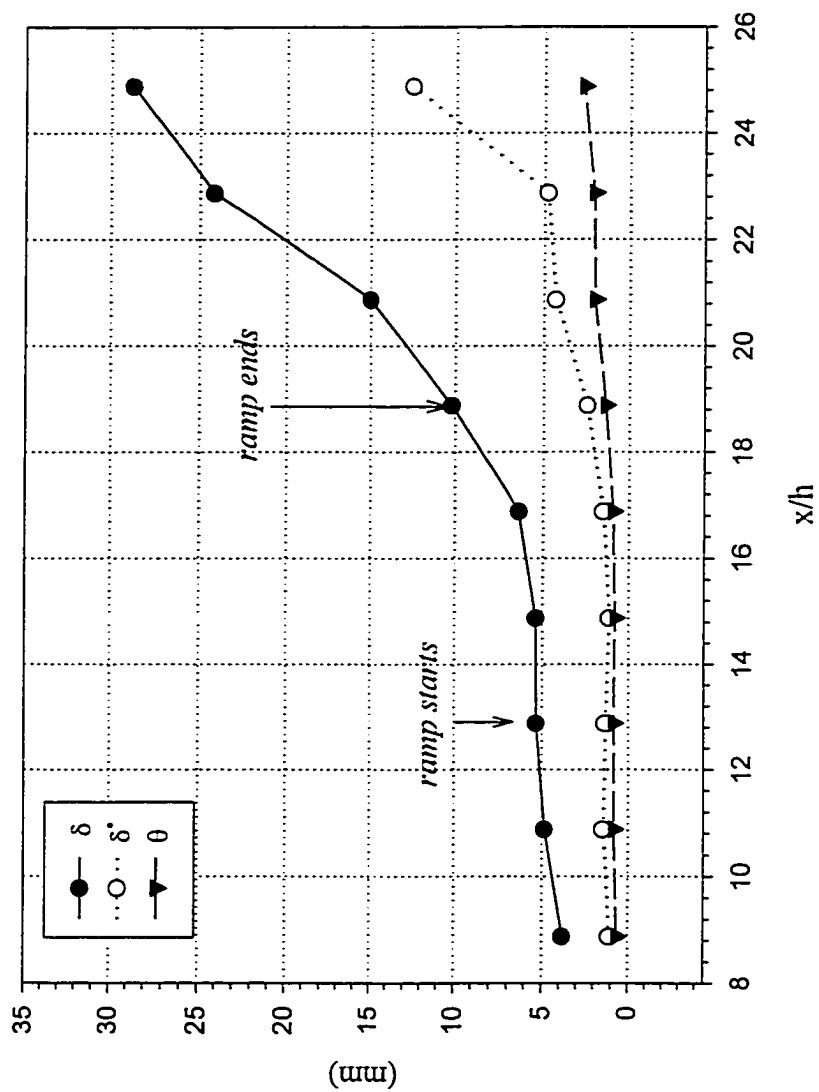


Figure 5.3 Baseline Boundary-Layer Parameters

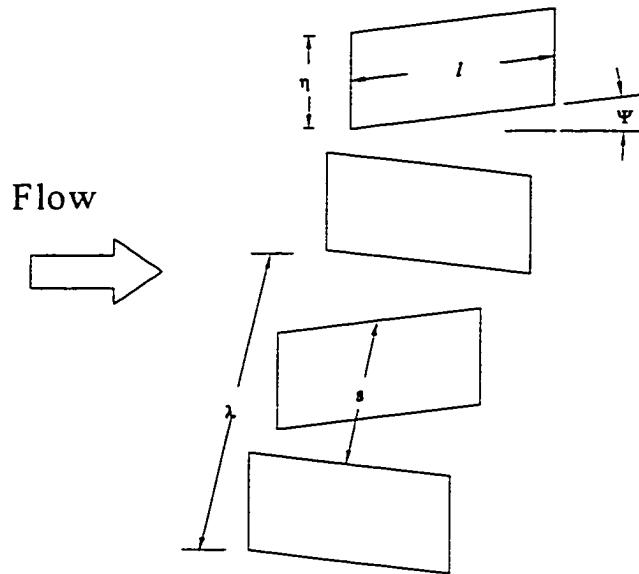


Figure 5.4 Schematic of Submerged Vane-Type Vortex Generators

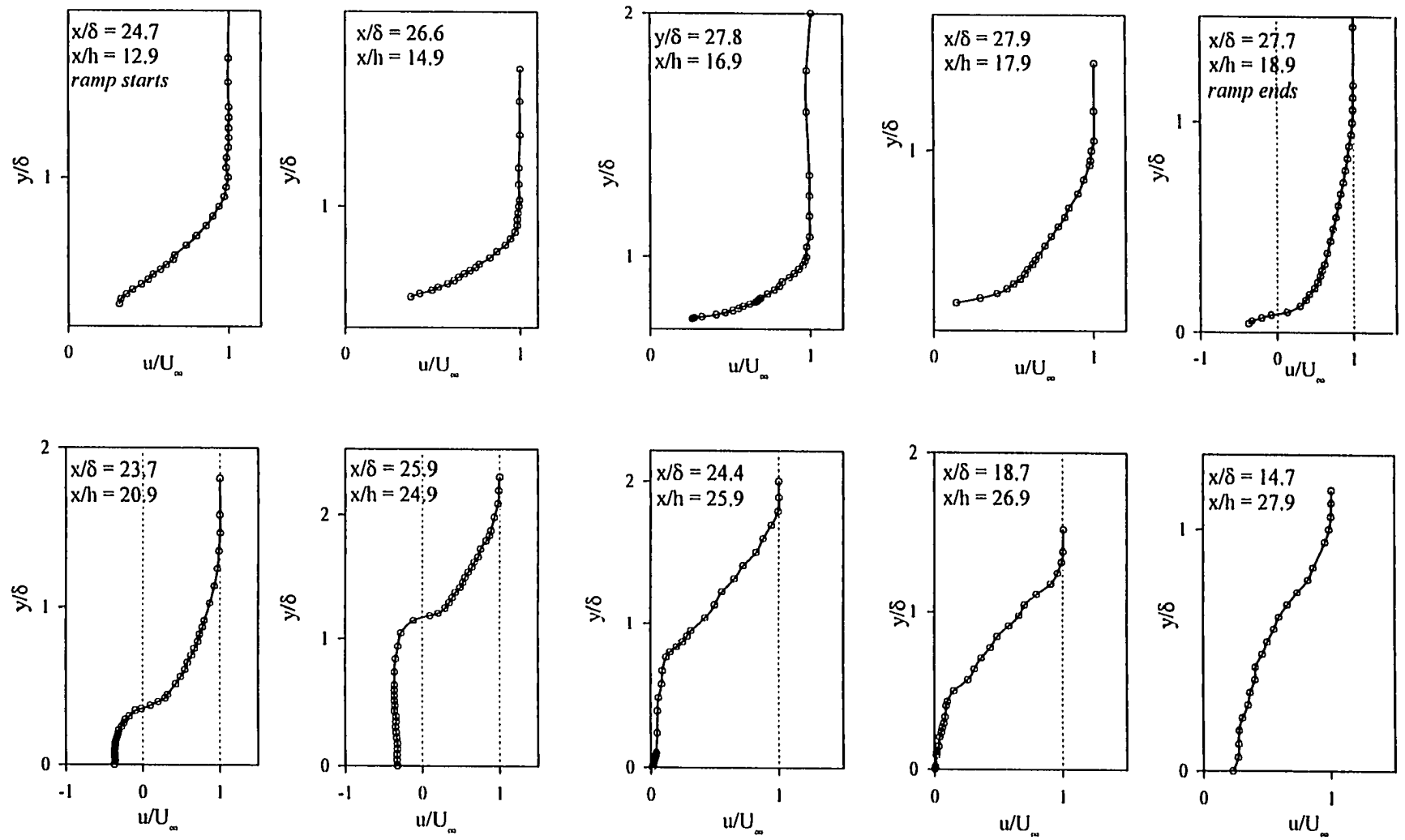


Figure 5.5 Velocity Profiles for a Backward-Facing Ramp with Deployed Vortex Generators

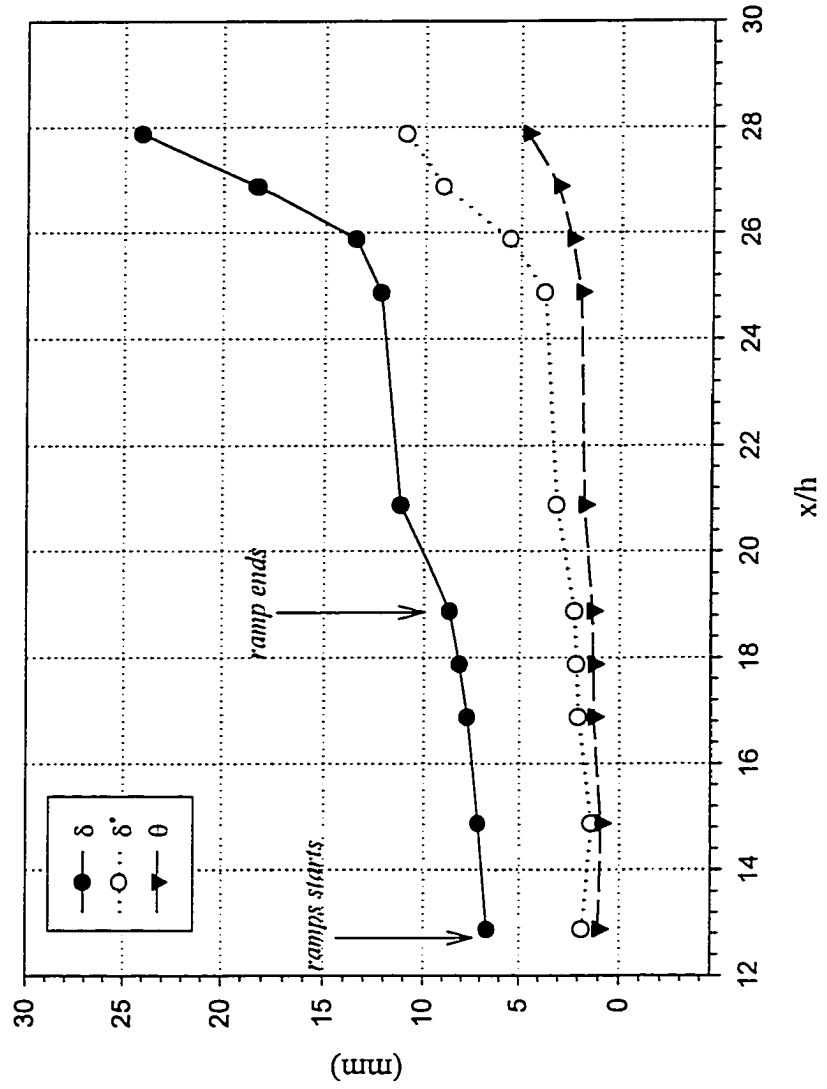


Figure 5.6 Boundary-Layer Parameters for Deployed Vortex Generators

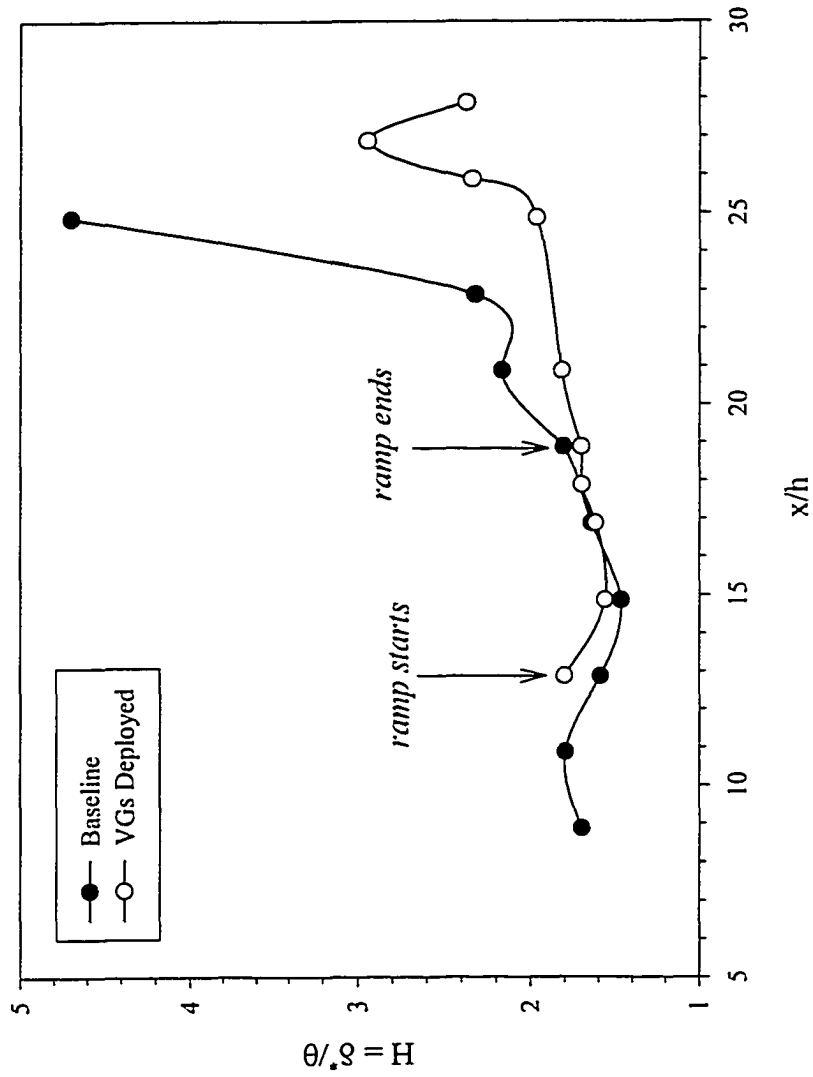


Figure 5.7 Boundary-Layer Shape Factor (Baseline and with Vortex Generators Deployed)

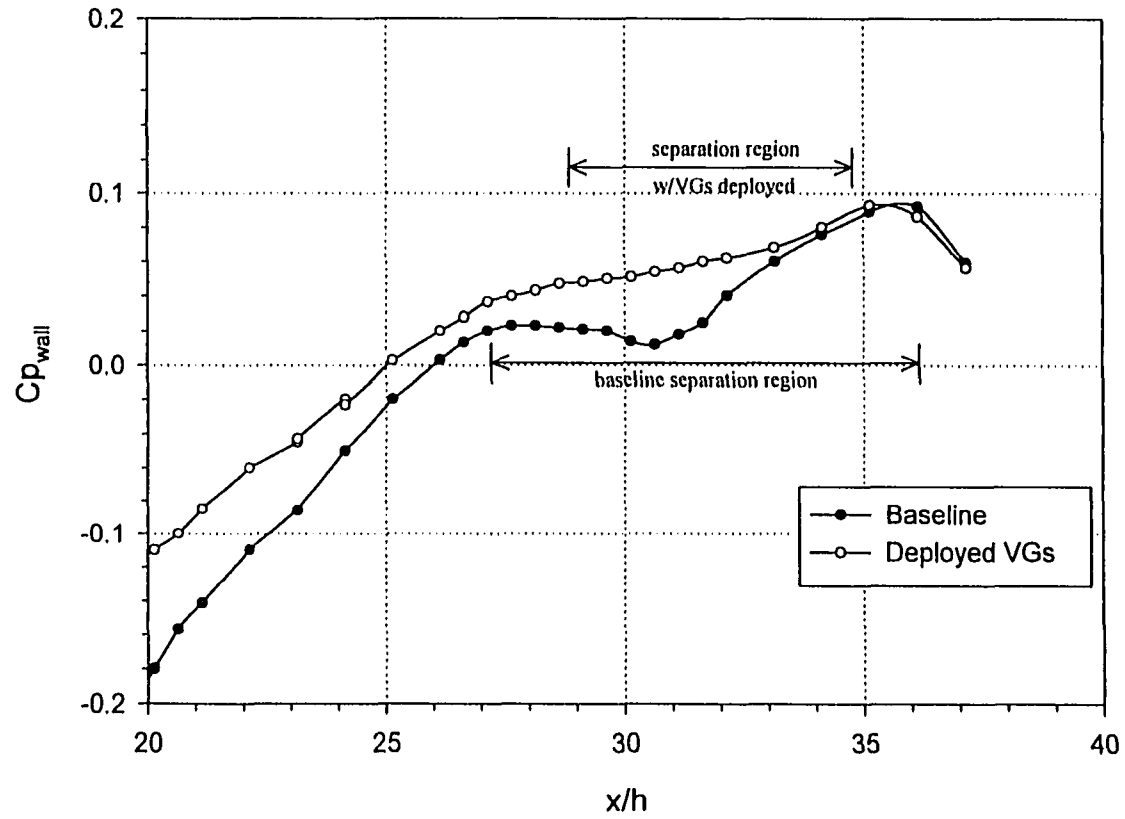


Figure 5.8 Wall Pressure Coefficient Distribution over a Backward-Facing Ramp (Baseline and with VGs Deployed)



(a) Baseline



(b) Vortex Generators Deployed

Figure 5.9 Smoke-Oil Flow Visualization over a Backward-Facing Ramp (Baseline and with VGs Deployed)

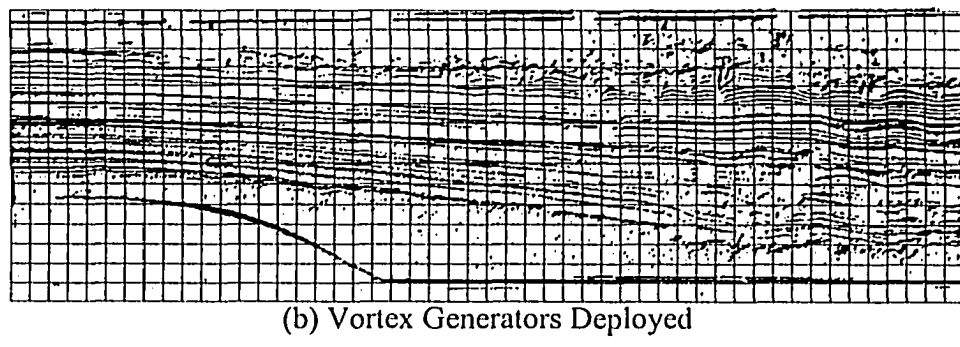
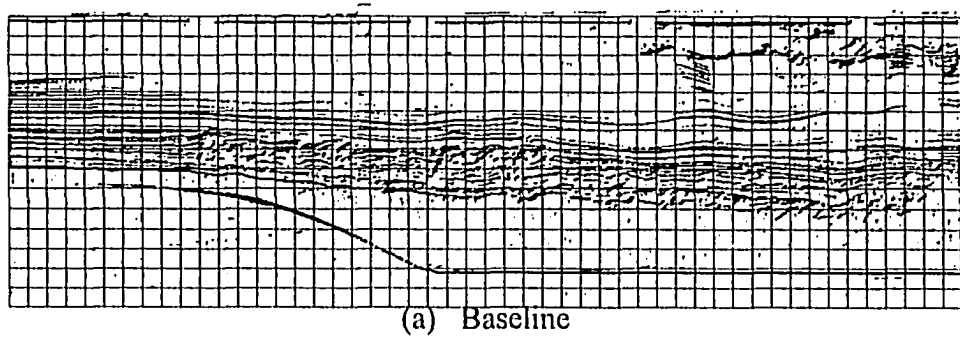


Figure 5.10 Method of Quantifying Flow Separated Region

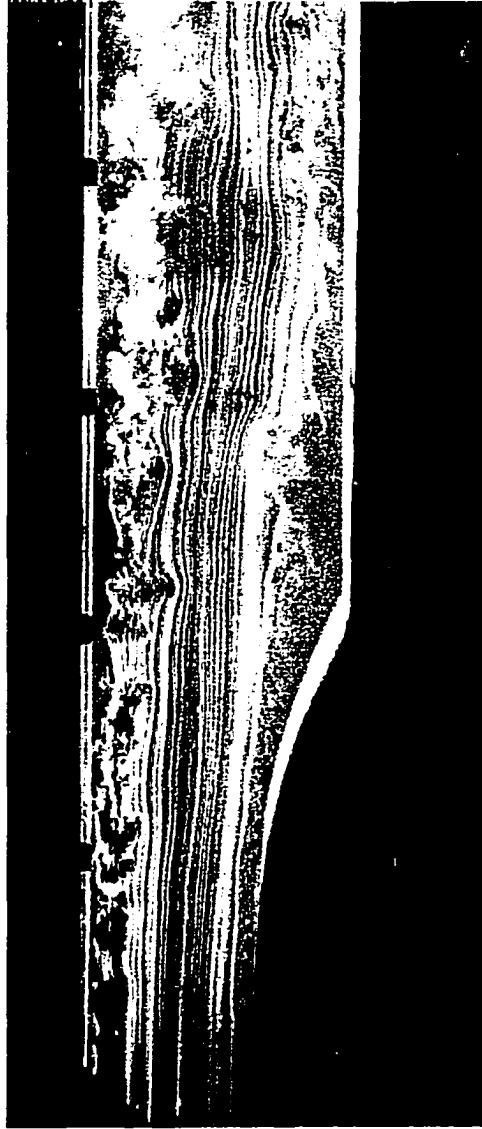


Figure 5.11 Smoke-Oil Flow Visualization for Vortex Generators Oscillating at 12 Hz

CHAPTER VI

SUMMARY, CONCLUSIONS AND RECOMMENDATIONS

Experiments were conducted to characterize the performance of a new piezoelectric device, THUNDER™, which was used as an actuator for submerged vane-type vortex generators, which controlled turbulent separated flow associated with a backward-facing ramp. This study was performed in three phases.

The first phase involved the testing of different configurations of THUNDER™ actuators constructed with different thicknesses and combinations of materials. The tests involved characterizing actuator performance under different operating voltages, frequencies, poling voltages, and capacitance, using state-of-the-art hardware and software. The results from this phase of testing indicated that in order to obtain accurate displacement measurements for THUNDER™ devices, they should be poled after processing, even though the ceramic wafer may have been poled at the manufacturer. One of the possible causes of depoling might be a result of the PZT-5A Curie point. This temperature which causes a dielectric breakdown is 350°C, compared to the processing temperature for the piezoelectric devices of 320°C. This may make the properties of the ceramic (K_{33}^T , etc.) less stable.

The experiments also demonstrated that the present clamping procedure for the piezoelectric devices is not appropriate near the resonant frequency, due to the large displacements obtained. A more compliant clamping device is needed at or near the resonant frequency, which appears to be independent of the configuration tested (approximately 250 Hz).

Further analysis of the data has shown that the movement of the piezoelectric device is restricted when a metallic layer is placed on top of the ceramic layer. This phenomenon can be explained by both the location of the neutral axis and the increased tension the additional metallic layer places on the device. A parameter, α , was defined such that $\alpha < 1$ indicated that the neutral axis of the static device was in the lower section of the device (the inactive layer (metal)) and when $\alpha > 1$, the neutral axis was in the active (ceramic) layer. Then, the configuration that provided the best performance had $\alpha = 1$. However, when the total thickness of the device was taken into account (including the adhesive) when calculating α , the theory appeared to fail for the x/Al cases (with measured backing thickness), although it held for Al/Al configurations.

The second phase of the experiments included more detailed tests of configurations composed of materials with higher moduli of elasticity (stainless steel, etc.). The important parameters in this phase of tests included voltage, frequency, equivalent circuit parameters and performance under load/no-load conditions. These results confirmed that the neutral-axis theory for a composite curved beam was appropriate for predicting the best design for THUNDER™ actuators under load/no-load conditions at 1 Hz. A value near one of the relevant parameter proposed in the first phase, α , correlates well with optimum actuator performance for a particular combination of materials. This relationship appears to be independent of the length, width, and the manufacturer of the ceramic wafer used in constructing a particular THUNDER™ based actuator.

Since the neutral-axis theory presented above can be applied to any combination of materials, other tests were designed with stiffer materials on the top and bottom of the ceramic. The results indicated that a material with a high modulus of elasticity (higher than

the PZT wafer) as a top layer of a THUNDER™ actuator, produced less displacement than one built with a material with a lower modulus than the ceramic wafer. At the same time, inactive layers with higher moduli than the wafer produced more displacement under particular loading conditions.

The third test phase involved the demonstration of the use of a THUNDER™-based actuator for deploying submerged-vane-type vortex generators to provide flow separation control over a backward-facing ramp. It was demonstrated that these vortex generators can be deployed using a relatively simple control mechanism with low power consumption. Furthermore, it was demonstrated that the flow separation region was reduced by 35-40%, using vortex generators deployed by a piezoelectric actuator.

Results from the last test phase also suggested the possibility of providing flow control with different levels of voltage applied to the actuator, thus providing the vortex generators with a mechanism to adjust their height (and frequency), depending on the flow conditions. That is, if the angle-of-attack of a wing changed, and hence the boundary-layer height, the vortex generator could be easily adjusted without making any modifications to the wing itself. All that would be required would be a different remote command.

Future work recommended for successful flow-control devices includes the use of THUNDER™ devices simultaneously functioning as sensors and vortex generators to detect and control flow separation. That is, pursue frequency performance of vortex-generators, investigate the potential for a THUNDER™-based device as a sensor to detect the onset of separation, and determine the feasibility of designing a closed-loop interactive flow-control system with THUNDER™-based devices as flow separation sensor and vortex generator actuator. In this manner, active flow separation control with appropriate sensor devices and

vortex generators deployed using piezoelectric devices can be designed so that the piezoelectric devices would serve as an active vortex generator that can be deployed “on demand.”

REFERENCES

1. Marshall, N. B., "The Life of Fishes," Weidenfield & Nicholson, London, 1965, pp. 402.
2. Lighthill, Sir James, "Mathematical Biofluidynamics," University of Cambridge, Society for Industrial and Applied Mathematics, Philadelphia, Pennsylvania, 19103, 1989.
3. Dehart, D., and Griffin, S., "Astronautical Laboratory Smart Structure/Skins Overview," *Proceedings of the First Joint U.S./Japan Conference on Adaptive Structures*, Maui, Hawaii, Nov 13-15, 1990, pp. 3-10.
4. Ha, S. K., Keilers, C., and Chang, F., "Finite Element Analysis of Composite Structures Containing Distributed Piezoceramics Sensors and Actuators," *AIAA Journal*, Vol. 30, No.3, March 1992.
5. Tzou, H.S., and Ye, R., "Analysis of Piezoelectric Structures with Laminated Piezoelectric Triangle Shell Elements," *AIAA Journal*, Vol. 34, No.1, January, 1996.
6. Chang, S.H., and Wang, H., "A high Speed Impact Actuator Using Multilayer Piezoelectric Ceramics," *Sensors and Actuator A*, 24, 1990, pp. 239-244.
7. Saka, T., Terai, Y., and Ishikiryama, M., "Improvement is Durability of Piezoelectric Ceramics for Actuator," *Jpn. Journal of Applied Physics*, Part 1, No. 9B, Vol. 34, September, 1995, pp. 5276-5278.
8. Kolm, H., and Kolm, E., "Piezoelectric Snap Actuator," United States Patent No. 4,383,195, May 10, 1983.
9. Suplee, C., "Is the Sky the Limit in the Future?" *The Virginian-Pilot*, Business News, P D-1, Wednesday, January 8, 1997.
10. Zuckerwear, A. J., Pretlow, R.A., Stoughton, J. W., and Bakeer, D.A., "Development of a Piezopolymer Pressure Sensor for a Portable Fetal Heart Rate Monitor," *IEEE Transactions on Biomedical Engineering*, Vol. 40, No. 9, September 1993, pp. 963-969.
11. Wada, B.K., Fanson, J. I., and Miauram K., "First Join U.S./Japan Conference on Adaptive Structures," Maui, Hawaii, U.S.A, November 13-15, 1990.
12. Studt, T., "Smart Materials, Creating Systems that React," *R & D Magazine*, April, 1992.

13. Wise, S.A., and Hooker, M. W., "Characterization of Multilayer Piezoelectric Actuators for Use in Active Isolation Mounts," Langley Research Center, Hampton Virginia, Science and Technology Corporation, Hampton, Virginia, National Aeronautics and Space Administration, Langley Research Center, Hampton, Virginia, Mar 1997.
14. Lai, Z, "Vibration Control with Piezoelectric Actuation Applied to Nonlinear Panel Flutter Suppression," Department of Mechanical Engineering and Mechanics, Old Dominion University, Norfolk, VA, 1994 pp.1-5.
15. Ehlers, S. M., and Weisshaar, T. A., "Static Aerolastic Behavior of an Adaptive Laminated Piezoelectric Composite Wing," *Proceedings of the 31st AIAA/ASME/ASCE/HS/ASC Structures, Structural Dynamics, and Materials Conference*, Long Beach, CA, 1990, pp. 1611-1623.
16. Vipperman, J. S., Clark, R. L., "Implementation of an Adaptive Piezoelectric Sensoriactuator," *AIAA Journal*, Vol 34, No.10, October, 1996, pp. 2102-2109.
17. Zhou, S., Liang, C., and Rogers C. A., "An Impedance-Based System Modeling Approach for Induced Strain Actuator-Driven Structures," *Journal of Vibration and Acoustics*, Vol. 118, July, 1996, pp. 323-331.
18. Cottrell, B.H., "Evaluation of Weigh-in-Motion Systems," Virginia Transportation Research Council, 1991.
19. Fanshawe, et al., "Snap Action Mechanical-Electrical Piezoelectrical Transducer," United States Patent 3,976,899, August 24, 1976.
20. Robbins, W. P., Polla, D. L., and Glumac, D. E., "High-Displacement Piezoelectric Actuator Utilizing a Meander-Line Geometry - Part I," *Experimental Characterization, IEEE Transactions on Ultrasonics, Ferroelectrics and Frequency Control*, Vol. 38, No. 5, September, 1991.
21. Schlichting, H, *Boundary-Layer Theory*, Seventh Edition, McGraw-Hill Publishing Company, 1979, pp. 43.
22. Huai X., Joslin R. D., and Piomelli U., "Large-Eddy Simulation of Boundary Layer Transition on Swept Wings," Department of Mechanical Engineering, University of Maryland, College Park, MD 20742.
23. Lin J. C., Howard F. G., and Selby, G. V., "Turbulent Flow Separation Control Through Passive Techniques," *AIAA 2nd Shear Flow Conference*, AIAA-89-0976, March 13-16, 1989.

24. Wada, B.K., Fanson, J. L., and Crawley, E. F., "Adaptive Structures," *J. of Intelligent Material System and Structure*, Vol. 1, April, 1990, pp. 157-174.
25. Haertling, G. H., "Intelligent Processing for Smart Materials," NASA-LaRC Smart Materials & Structures Workshop, May 1-17, 1994.
26. Warketin, D. J., Crawley, E.F., and Senturia, S. D., "The Feasibility of Embedded Electronics for Intelligent Structures." *J. of Intelligent Material Systems and Structures*, Vol. 3, July, 1992, pp. 462-482.
27. Barsoum, M., "Fundamentals of Ceramics," *Materials Science and Engineering*, 1st ed., Mc Graw- Hill, 1997, pp. 592-595.
28. Active Structures Technical Committee, A State-of-the-Art Assessment of Active Structures, NASA Technical Memorandum 107681, September, 1992.
29. Hansen, T., "Advanced Techniques for Terfenol-D Devices," *International Conference on Electronic Materials*, Materials Research Society, Fall Meeting, December 2-6, 1996.
30. O'Connor, L., "Memory Alloys Remember Two Shapes," *Mechanical Engineering*, Vol. 117, No.12, December, 1995.
31. Jaffe, B., Cook, W. R., and Jaffe, H., "*Piezoelectric Ceramics*," Academic Press, New York, 1971.
32. Kawai, H., "The Piezoelectricity of Poly (vinylidene fluoride)," *Japanese J. Applied Physics*, Vol. 8, No. 7, 1979, pp. 975-976.
33. Lee, C. K., "Theory of Laminated Piezoelectric Plates for the Design of Distributed Sensors/Actuators, Part I. Governing Equations and Reciprocal Relationships," *J. of Acoustical Society of America*, Vol. 87, No. 3., 1990, pp. 1144-1158.
34. Wersing, W., Schnöller, and Wahl, H., "Monolithic Multilayer Piezoelectric Ceramics," *Ferroelectrics*, Vol. 68, 1986, pp. 145-146.
35. Ounaies Z., "Sol-Gel and Microwave Processing of PZT materials for Sensor and Actuator Applications," Ph.D. Thesis, The Pennsylvania State University, December, 1995, pp. 1-10.
36. Giurgiutiu V., Chaudhry Z., and Rogers C. A., "Energy-Based Comparison of Solid-State Actuators," *Center for Intelligent Material Systems & Structures*, Virginia Polytechnic Institute and State University, Blacksburg, VA 24061-0261, Report No. CIMSS 95-101, September, 1995.

37. Lalande, F., Chaudhry, Z., and Rogers, C., "A Simplified Geometrically Nonlinear Approach to the Analysis of the Moonie Actuator," *IEEE Transactions on Ultrasonics, Ferroelectrics, and Frequency Control*, Vol. 42, No.1, January, 1995.
38. Haertling, G. H., "Method for Making Monolithic Prestressed Ceramic Devices," United States Patent, 5,471,721, Dec. 5, 1995.
39. Haertling, G. H., "Monolithic Prestressed Ceramic Devices and Method for Making Same," United States Patent 5,589,725, Dec. 31, 1996.
40. Ashley, S., "Smart Skis and Other Adaptive Structures," *Mechanical Engineering*, Vol. 117, No.11, November, 1995, pp. 76-81.
41. Wise, S.A., "Properties and Applications of RAINBOW High Displacement Actuators," *Enabling Technologies for Smart Aircraft Systems Workshop*, NASA-Langley Research Center, May 16, 1996.
42. Haertling, G. H., "Rainbow Actuators and Sensors: A New Smart Technology," The Gilbert C. Robinson Department of Ceramic Engineering, Clemson, SC 29634-0907, *SPIE*, Vol. 3030, pp. 81-92.
43. Near, C., "Piezoelectric Actuator Technology," *SPIE Smart Structures and Materials Conference*, February 27, 1996.
44. Hellbaum, R., Bryant, R. G., and Fox, R. L., "Thin Layer Composite Unimorph Ferroelectric Driver and Sensor," United States Patent No. 5,632,841, 1997.
45. Bryant, R. G., "LaRC™-SI: A Soluble Aromatic Polyimide," *High Performance Polymers*, Vol. 8, 1996, pp. 607-615.
46. Siochi, E. J., Young, P. R., and Bryant, R. G., "Effect of Molecular Weight on the Properties of A Soluble Polyimide," *Proceedings of the 40th International SAMPE Symposium*, May, 1997, pp. 11-17.
47. Brute Force Chip, "*Popular Mechanics*," March, 1997, pp. 16.
48. THUNDER is Booming, "Technology Transfer," *InTech, NASA News*, August, 1996, pp. 23.
49. Henry, K., "NASA Rolls Out Award-Winning THUNDER," *News Researcher*, Vol. 10, Issue 19, September, 20, 1996.
50. THUNDER Actuators Move a Lot, *R&D Magazine*, Vol. 38, No. 10, September, 1996, pp. 44.

51. NASA Langley Develops Piezoelectric Material, *Aviation Week & Space Technology*, Vol. 145, No. 15, October, 1996, pp. 10.
52. Bishop, D., Mossi, K., Swain, B., Rose, N., "Rugged, Robust, Reliable, New Multi-Function, High-Sensitivity Sensor," *Technology 2007 Conference*, Boston, Massachusetts, September, 1997.
53. Chang, P. K., "*Control of Flow Separation*," McGraw-Hill Book Company, 1976, pp. xiii, 10-12, 84-85.
54. Lin, John C., "Control of Low-Speed Turbulent Separated Flow Over a Backward-Facing Ramp," Old Dominion University, Ph.D. Dissertation, May, 1992.
55. Gad-el-Hak, M, Ho, Ch. M., "Unsteady Vortical Flow Around Three-Dimensional Lifting Surfaces Lifting Surfaces," *AIAA Journal*, Vol. 24, No 5, May, 1986, pp. 713-721.
56. Weibust, E., Bertelud, A., and Ridder, S.O., "Experimental Investigation of Laminar Separation Bubbles and Comparison with Theory," *J. Aircraft*, Vol. 24, No. 5, May 1987, pp. 291-297.
57. Bandyopadhyay, P. R., "Instabilities and Large Structures in Reattaching Boundary Layers," *AIAA Journal*, Vol. 29, No. 7, July, 1991, pp. 1149-1155.
58. Holmes, B. J., Developments in Flow Visualization Methods for Flight Research," *Fifth International, Flow Visualization Symposium*, Prague, Czechslovakia, August, 1989.
59. Mangalam, S. M., Stack, J. P., and Sewall, W. G., "Simultaneous Detection of Separation and Transition in Surface Shear Layers," AS&M Inc., pp. 12-1 - 12-10.
60. Mangalm, S. M., Balister, R. L., and Kubendran, L. R., "Advanced PC-based Instrumentation system for flow diagnostics," *Proceedings of the Thirty-Sixth International Instrumentation Symposium*, Denver, CO, May 6-10, 1990.
61. Seifert, A., Zilberman, M., and Wagnaski, I., "On the Simultaneous measurements of the two velocity components in the turbulent spot," *Journal of Engineering Mathematics*, Vol. 28, No. 1, February, 1994, pp. 43-54.
62. Patterson, A., Rymarz, P., and Ramaprian B. R., "Surface Pressure Measurements on a Pitching Swept Wing in a Water Channel," *AIAA Journal*, Vol. 33, No. 10, October, 1995.

63. Montividas, R. E., Acharya, M., and Metwally, H. M., "Reactive Control of an Unsteady Separating Flow," *AIAA Journal*, Vol. 30, No. 4, Technical Notes, pp. 1133-1134.
64. Thangam, S., and Speziale C. G., "Turbulent Flow Part a Backward-Facing Step: A Critical Evaluation of Two-Equation Models," *AIAA Journal*, Vol. 30, No. 5, May, 1992, pp. 1314 - 1320.
65. Schrek, S. J., Faller, W. E., and Luttges, M. W., "Neural Network Prediction of Three-Dimensional Unsteady Separated Flow Fields," *AIAA Applied Aerodynamics Conference*, AIAA-93-3426-CP, Monterey, CA, 1993.
66. Siefert, A., et al., "Oscillatory Blowing, A tool to delay boundary-layer separation," *AIAA Journal*, V. 31, No. 11, Nov., 1993, pp. 2052-2060.
67. Gittner, N. M., Chokani, N., "An Experimental Study of the Effects of Aft Blowing on a 3.0 Caliber Tangent Ogive Body at High Angles of Attack," *AIAA 91-3252, AIAA 9th Applied Aerodynamics Conference*, September 23-25, 1991, Baltimore, Maryland.
68. Bushnell, D. M., "Flow separation Control," Invited Lecture at University of Kansas, 1986.
69. Gad-el-Hak, M. and Bushnell, D.M., "Separation Control: Review," *Journal of Fluids Engineering*, Vol. 113, 1991, pp. 5-30.
70. Gad-el-Hak, M., and Ho C., "The Pitching Delta Wing," *AIAA Journal*, Vol. 23, No. 11, November, 1985, pp. 1660-1665.
71. Livine, E., Schmidt, L. A., and Friedmann, P. P., "Exploratory Design Studies of Actively Controlled Wings Using Integrated Multidisciplinary Synthesis," *AIAA Journal*, Vol. 30, No. 5, May, 1992.
72. Schreck, S. J., Faller, W. E., and Lutges, M. W., "Neural Network Prediction of Three-Dimensional Unsteady Separated Flow Fields," *AIAA-93-3426-CP*, pp. 227-240.
73. Selby, G. V., Lin, J.C., and Howard, F.G., "Control of Low-speed Turbulent Separated Flow Using Jet Vortex Generators," *Experiments in Fluids*, Springer-Verlag, Berlin, January, 1992, pp. 1-7.
74. Johnston, J., and Nishi, M., "Vortex Generator Jets - A Means for Passive and Active Control of Boundary-Layer-Separation," *AIAA 89-0564*, 1989.

75. Wallis, R., "The Use of Air Jets for Boundary-Layer Control," Australia: Aerodynamics Research Laboratories, Aero Note 110. 1952.
76. D'Andrea, R., Behnken, R. L., and Murray, R. M., "Active Control of Rotating Stall Using Pulsed Air Injection: A Parametric Study on a Low-Speed, Axial Flow Compressor," *SPIE*, Vol. 2494, pp.152-165.
77. Bertelrud, A., and Watson, R.D., "Use of Lebu-Devices for Drag Reduction at Flight Conditions," *The Royal Aeronautical Society*, London, September 15-17, 1987, pp. 1-37.
78. Lynn, T.B., Behert, D.W., and Gerich, D.A., "Direct Drag Measurements in a Turbulent Flat-plate Boundary Layer Turbulence Manipulators," *Experiments in Fluids*, 19 (1995), Springer-Verlag, 1995, pp. 405-415.
79. Wendt, B. J., and Hingst, W. R., "Flow Structure in the Wake of a Wishbone Vortex Generator," *AIAA Journal*, Vol. 32, No. 11, November, 1994.
80. Taylor, H. D., "United Aircraft Research Department Summary Report on Vortex Generator," United Aircraft Corp. Research Dept., Report R-05280-9, March 7, 1950.
81. Selby, G. V., "Passive Control of Three-Dimensional Separated Vortical Flow Associated With Swept Rearward-Facing Steps," *Journal of Fluids Engineering*, March, 1989, Vol. 111, pp. 99-101.
82. Gittner N.M. and Chokani N., "The Effects of Nozzle Exit Geometry of Forebody Vortex Control using Blowing," *10th AIAA Applied Aerodynamics Conference*, June 22-24, 1992, Palo Alto, CA.
83. Bare, E.A., Reubush, D.E., and Haddad, R.C., "Flow Field Over the Wing of a Delta-Wing Fighter Model With Vortex Control Devices at Mach 0.6 to 1.2," NASA Langley Research Center, Hampton, VA, 23665-5225, NASA TM-4296, April, 1992, pp. 1-124.
84. Lin, J. C., Robinson, S. K., McGhee, J., and Valarezo, W. O., "Separation Control on High-Lift Airfoils via Micro-Vortex Generators," *Journal of Aircraft*, Vol. 31, No. 6, pp. 1317-1323.
85. Reichert B. A., and Wendt, B. J., "Improving Diffusing S-Duct Performance by Secondary Flow Chart," National Aeronautics and Space Administration, Lewis Research Center, Cleveland, Ohio 44135.
86. Nam Kim, Kyoong B., and Chung, M., "Experimental Study of Roughness Effects of the Separated Flow over a Backward-Facing Step," *AIAA Journal*, Vol. 33, No.1, Technical Notes, 1994.

87. Lee, T., Fisher M., and Schwarz, "Investigation of the effects of a compliant surface on boundary-layer stability," *J. Fluid Mech.* (1995), Vol. 288, Copyright 1995, Cambridge University Press, pp. 37-58.
88. Alving, A. E., and Freeberg, P., "The Effect of Riblets on Sails," *Experiments in Fluids*, 19 (1995), Springer-Verlag 1995, pp. 937-404.
89. Reichert, B. A., and Wendt, B. J., "Improving Diffusing S-Duct Performance by Secondary Flow Control," NASA Lewis Research Center, Cleveland Ohio.
90. Miao, J.J., Chen, M. H, and Chou, J. H., "Frequency Effect of an Oscillating Plate Immersed in a Turbulent Boundary Layer," National Cheng University, Taiwan, China, *AIAA Journal*, Vol. 29, No. 7, July, 1991, pp. 1068-1074.
91. Gursul, I., Srinivas, S., and Batta, G., "Active Control Vortex Breakdown over a Delta Wing. University of Cincinnati," *AIAA Journal*, Vol. 33, No. 9, Technical Notes, 1995, pp. 1743-1745.
92. MOTOROLA, "PZT Piezoelectric Materials," Technical Data, 1996.
93. Furman, E., Li, G., and Haertling, G. H., " Electromechanical Properties of RAINBOW Devices," *Proceedings of the Ninth IEEE International Symposium on Applications of Ferroelectrics*, Aug. 7-10, 1994, IEEE Catalog Number 94CH3416-5.
94. Hibbeler, R. C., "*Mechanics of Materials*," Prentice Hall, New Jersey, 07458, pp. 319.
95. Young, W. C., "*Roark's Formulas for Stress and Strain*," McGraw Hill, 6th ed. 1989, pp. 80, and 117.
96. Pilkey, W. D., "*Formulas for Stress, Strain, and Structural Matrices*," John Wiley & Sons, Inc. 1994, p. 174.
97. Mossi, K., Selby, G., and Bryant, R., " Electromechanical Characterization of a Thin-Layer Unimorph Driver and Sensor," *Materials Letters*, To be published April, 1998.
98. Janna, W. S., "*Introduction to Fluid Mechanics*," Third Edition, PWS Publishing Company, Boston, 1993, p. 297.
99. Fox, W. R., and McDonald A. T., "*Introduction to Fluid Mechanics*," Fourth Edition, John Wiley & Sons, Inc., 1992, p. 414.
100. White, F. M., "*Fluid Mechanics*," Third Edition, McGraw-Hill, Inc. 1994, p. 398.

APPENDIX A

THUNDER™ Manufacturing Process

Materials. The raw materials needed to manufacture the present THUNDER™ devices are a piezoelectric ceramic wafer, metallic backing material, and an adhesive in spray and film form, and the a dielectric fluid. Two types of wafers were used in this study - Motorola 3195HD and a Morgan Matroc PZT Type 5A nickel poled and plated. Each set had several different thicknesses of stainless steel as backing material (from commercial vendors), with aluminum or brass as a top protective layer. The adhesive film was 25µm LaRC™-SI (Imitec, Inc.) And the primer was a LaRC™-SI/N-methylpyrrolidione solution 10%(w) (Imitec, Inc.) The construction of the piezoelectric devices required additional equipment which included an air brush, an oven with a vacuum fixture (an operating temperature of 350°C), and an autoclave with a minimum capability of 207 kPa (30 psi) and 350°C. The dielectric fluid HFE-100 (3M Corporation) and the N-methylpyrrolidione (Fisher) were used as received.

Procedure for the fabrication of THUNDER™. There are five basic steps involved in manufacturing the present class of piezoelectric devices: (1) spray coating of the ceramics, (2) construction of layers, (3) assembly, (4) bonding process in an autoclave, and, (5) poling.

Spray coating of the ceramics. LaRC™-SI/N-methyl-pyrrolidinone 10%(w) solution (Imitec, Inc.), is sprayed using an air brush. Both sides of the piezoelectric ceramic are cleaned using

alcohol. Two coats are then sprayed on each side of the ceramic, which is then dried in an oven for 2 hours at 70°C.

Construction of the layers. The backing material is first cleaned using alcohol, roughened with sandpaper, and sprayed with the LaRC™-SI solution, except in the case of stainless steel where only cleaning with alcohol is used. The materials (backing and LaRC™-SI film, 3% offset) are cut to the desired size. The spraying of the backing materials is the same as above.

Assembly. The materials are assembled in the required order and thermally processed to produce the piezoelectric devices. The order of the layers, starting from the bottom for a particular device, is metal, LaRC™-SI film, metal, LaRC™-SI film, ceramic wafer, LaRC™-SI film, and top metallic layer (optional). See Figure A.1 for an example of a typical laminate assembly.

Autoclave. An aluminum plate with a layer of fiberglass cloth covered with Kapton™ polyimide film is coated with Frekote™ release agent and concentrically put on the plate, leaving a border of approximately 2.54 cm. The laminate is carefully placed on the plate and covered with coated Kapton™ film followed by fiberglass cloth. Around the outer edge of the plate, heat resistant sealant tape is applied and a vacuum port is attached inside the tape perimeter. Kapton™ film is placed over the sealant tape, covering the entire surface of the plate and pressed around the tape to ensure a good seal. The plate is then put into an autoclave. The temperature is raised to 320°C at 5°C/min under a full vacuum. At 320°C,

a pressure of 207 kPa (30 psi) is generated for 30 minutes and then the plate is cooled at a rate of 5°C/min until the temperature reaches 200°C. The vacuum is then released and the fixture is allowed to cool to ambient temperature.

Poling. After the fixture is removed from the autoclave, the actuators are removed and immersed in HFE-100(3M) and using a clip for leads, a DC voltage of 35.4 kV/cm (90 V/mil) is applied for a full minute.

THUNDER™ Assembly

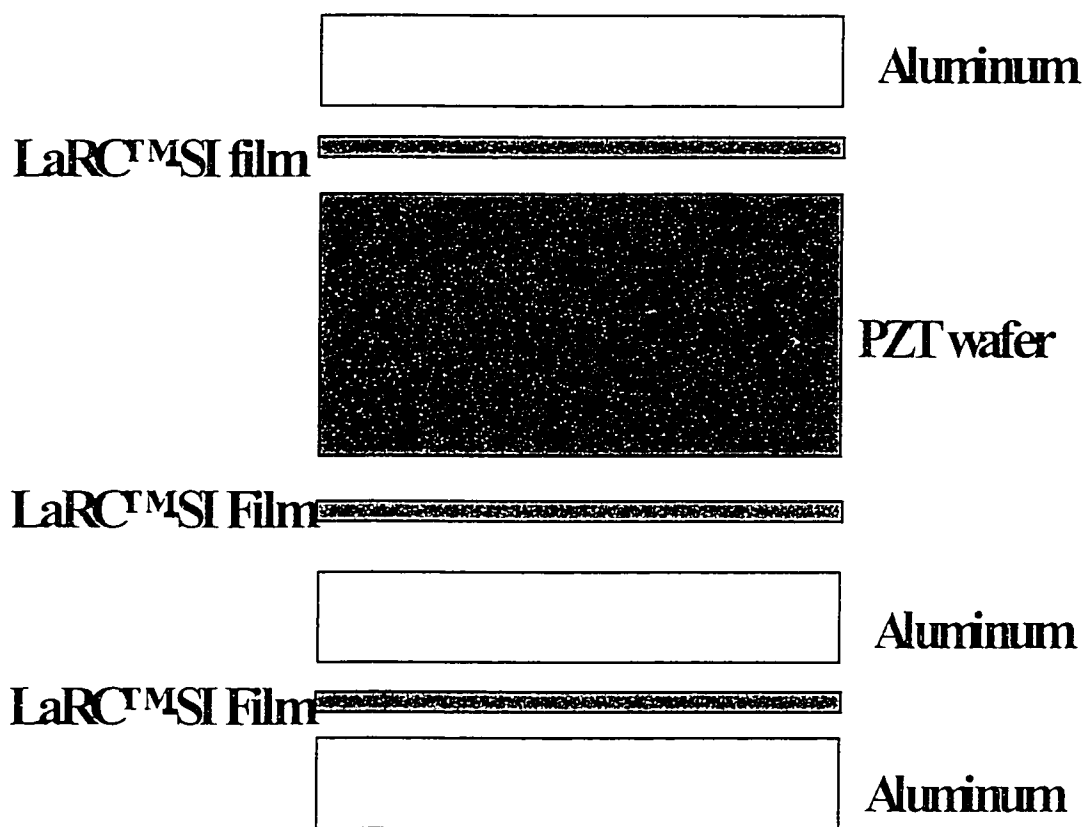


Figure A.1 Schematic of THUNDER™ Assembly

APPENDIX B

EQUIVALENT CIRCUIT

A piezoelectric crystal has an equivalent circuit which essentially consists of a capacitor. Its value depends on the dielectric constant of the PZT used. In this study, the dielectric constant, K_{33}^T , is given by [92]:

$$K_{33}^T = \frac{5.67 \cdot C \cdot t}{l \cdot w} \quad (\text{B.1})$$

where C is the capacitance (nF), t is the thickness ($\times 10^{-3}$ in), and l and w are the length and width respectively (in). As it can be seen in Equation 2.1 above, the capacitance depends on the geometry of the piece. Therefore, in order to classify some of the differences between the dielectric properties of the raw material (the PZT), and the final product (THUNDER™), impedance curves were produced for a series of devices. In this manner, an equivalent circuit was calculated, and hence, the capacitance. The equivalent circuit that produced the best results is shown in Figure B.1.

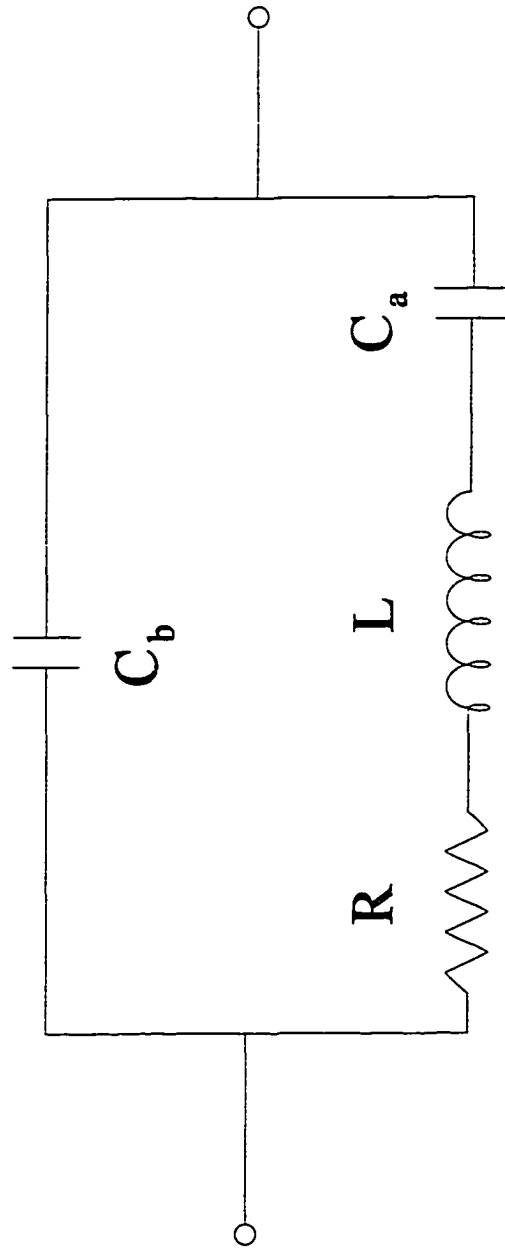
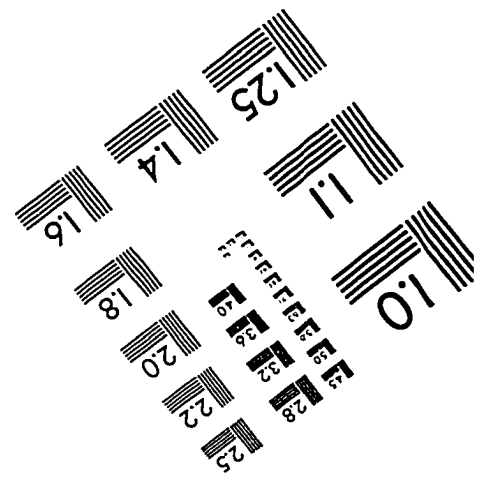
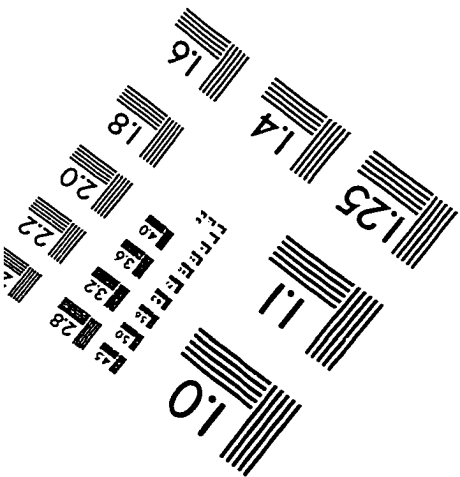
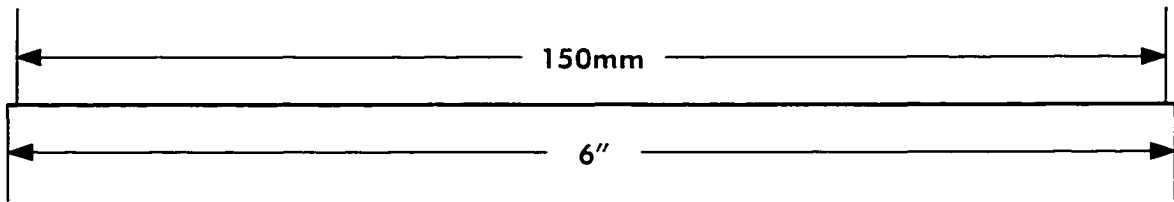
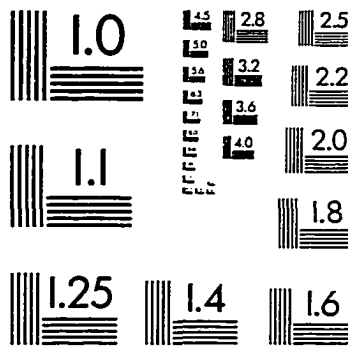
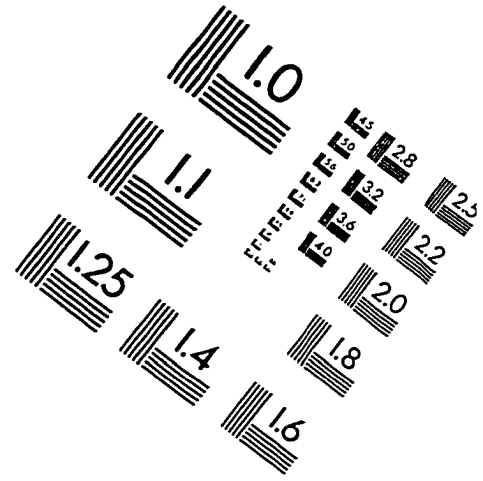
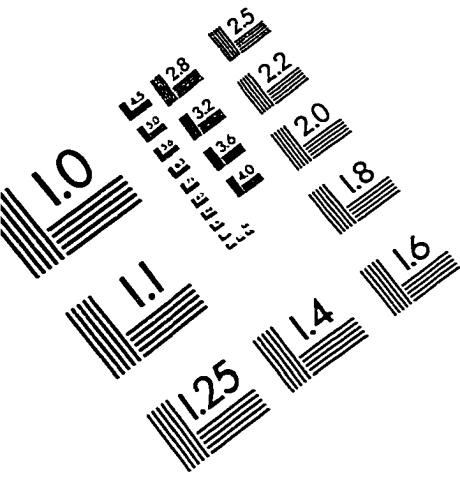


Figure B.1 THUNDER™ Equivalent Circuit

VITA

Karla Mossi was born in Tegucigalpa, Honduras on November 10, 1966. She attended the National Autonomous University of Honduras where she obtained a Bachelor of Science in Mechanical Engineering in May 1988. Her thesis title was "Fabrication of Briquettes Using Rice Husk." In May 1992, she obtained a master's degree in Mechanical Engineering and Mechanics from Old Dominion University. Her thesis was performed under a NASA grant and the title was "Characterization of Trailing Line Vortices". While pursuing her doctoral degree, Ms. Mossi worked as a senior computer consultant, as well as a Lecturer for courses such as fluid mechanics, gas dynamics, boundary layer theory, and introduction to engineering. Furthermore, she developed data acquisition systems for the mechanical engineering laboratories as well as revised and edited the thermo-fluids laboratory manual. For her work, Ms. Mossi was awarded the Outstanding Award for Laboratory Instruction by Old Dominion University in 1995-96 academic year. Then, while pursuing her doctoral degree in the area of piezoelectric actuators in cooperation with NASA Langley Research Center, she began working for the Face[®] International Companies where she supervised the development of their research laboratory which she now directs.

IMAGE EVALUATION TEST TARGET (QA-3)



APPLIED IMAGE, Inc
 1653 East Main Street
 Rochester, NY 14609 USA
 Phone: 716/482-0300
 Fax: 716/288-5989

© 1993, Applied Image, Inc., All Rights Reserved